Isotope dependent interactions in a mixture of ultracold atoms

Inaugural-Dissertation

zur

Erlangung des Doktorgrades der

Mathematisch-Naturwissenschaftlichen Fakultät

der Heinrich-Heine-Universität Düsseldorf

vorgelegt von

Florian Baumer

aus Lauingen a.d Donau

März 2010

Aus dem Institut für Experimentalphysik
der Heinrich-Heine-Universität Düsseldorf

Gedruckt mit der Genehmigung der
Mathematisch-Naturwissenschaftlichen Fakultät der
Heinrich-Heine-Universität Düsseldorf

Referent:	Prof. Dr. Axel Görlitz
Koreferent:	Prof. Dr. Georg Pretzler
Tag der mündlichen Prüfung:	29.04.2010

Summary

Within the scope of this thesis, comprehensive experimental studies on interspecies interactions between ^{87}Rb and various isotopes of Yb at temperatures in the μK regime have been performed. The interactions between Yb and ^{87}Rb manifested themselves through interspecies thermalization and – in the case of ^{174}Yb and ^{87}Rb – through phase separation.

Both, Yb and Rb, are well suited for the application of laser cooling, and quantum degeneracy has been reached for Yb as well as for Rb [1, 2]. In the context of mixtures of ultracold atoms, the combination of Yb and Rb is an interesting system, which has not been investigated so far. Due to the availability of several stable Yb isotopes, Bose-Bose mixtures as well as Bose-Fermi mixtures can be realized. The goal of the research project within which this PhD thesis has been carried out is the production of ultracold heteronuclear YbRb molecules in such a quantum degenerate mixture. YbRb molecules are an interesting system with significantly different physical properties than the alkali-alkali combinations, which are investigated in most experiments [3, 4, 5, 6]: YbRb molecules posses an electric as well as a magnetic dipole moment, which can for example be exploited for the study of spin lattice models [7].

Experiments described within this thesis were carried out at an apparatus, which has been used in previous studies on mixtures of Yb and Rb [8, 9, 10, 11]. However, the experiments presented here, required a significant improvement in stability and precision of the existing setup. Hence, in the course of this work, a number of components were changed or added to the existing system: Large parts of the laser systems were redesigned and improved detection methods were introduced to the experimental setup.

Due to the particular magnetic properties of Rb and Yb, a unique combination of trapping potentials, which allows for independent trapping and manipulation of ultracold ^{87}Rb and Yb atoms was used. The combined trap setup consisted of a Ioffe-Pritchard-type magnetic trap (MT) for ^{87}Rb and a bichromatic optical dipole trap (BIODT) for Yb. In the experimental sequence, Yb was pre-cooled in a MOT and transferred to the conservative BIODT. Subsequently, ^{87}Rb was prepared and evaporatively cooled in the MT. As a result, atomic samples consisting of typically $\approx 10^7$ ^{87}Rb atoms at a temperature of $\approx 1\,\mu$K and, depending on the isotope, $(0.3 \ldots 1.5) \times 10^5$ Yb atoms at temperatures of $5 \ldots 8\,\mu$K, were produced.

After the two atom clouds were brought into contact, thermalization of Yb with the colder ^{87}Rb cloud was observed. Measurements of the thermalization rate were performed using ^{87}Rb and the Yb isotopes ^{170}Yb, ^{172}Yb, ^{173}Yb, ^{174}Yb and ^{176}Yb, allowing the comparison of their relative scattering properties. Two Yb isotopes exhibited exceptional characteristics in combination with ^{87}Rb: On the one hand, almost no thermalization between ^{170}Yb and ^{87}Rb could be observed. Based on a quantitative analysis of thermalization data, the interspecies scattering length for this isotope combination could be determined to be

$|a_{87-170}| = 6.6^{+3.5}_{-2.9}\,a_0$. On the other hand, ^{174}Yb atoms thermalized almost instantaneously with the colder ^{87}Rb atoms, indicating a large elastic interspecies cross section.

In addition, we have observed phase separation in a mixture of ^{174}Yb and ^{87}Rb for certain trap geometries.

Phase separation has been studied before in mixtures of ultracold gases [12, 13, 14]. However, in contrast to those experiments, which are performed with degenerate quantum gases, phase separation between ^{174}Yb and ^{87}Rb as described in this PhD work is observed with purely thermal samples at temperatures in the μK regime.

For a quantitative understanding of the observed phase separation between ^{174}Yb and ^{87}Rb, it was essential, to have detailed knowledge of the characteristic parameters of the involved trapping potentials. With the knowledge of measured of trap frequencies for the MT and the BIODT, it was possible to simulate the potentials corresponding to the experimental situation. Interspecies interaction was accounted for by an additional interaction potential, which, in a first approach, was assumed to have a linear dependence on the ^{87}Rb density.

The quantitative results on the interaction potential are interpreted in terms of two-body scattering properties of the respective atoms. A "naive" mean field approach and thermal averaging of the energy dependent scattering length lead to conclusions inconsistent with experimental observations.

In the light of this discrepancy between observations and theory, possible experimental issues, which may lead to incorrect results for the interspecies interaction potential were carefully analyzed. Subsequently, the validity of the standard mean field theory in the present case was discussed on the basis of a simple comparison of relevant length scales. A more sophisticated theoretical model, which involves nonlinear density dependent corrections to the interaction potential, was introduced. Based on this approach, a low energy s-wave interspecies scattering length for ^{174}Yb and ^{87}Rb, $a_{87-174} = 4710^{+3970}_{-1520}\,a_0$ could be inferred. Furthermore, the description of the observed phase separation by diffusion dynamics and three-body recombination, as proposed by E. Tiesinga and S. Maxwell from the atomic theory group at NIST [15], is discussed.

The experimental results presented in this PhD thesis, allow conclusions on the YbRb ground state molecular potential and the energetic positions of weakly bound levels. In this context, E. Tiesinga and S. Maxwell [15] determined a Lennard-Jones potential, which quantitatively reproduces the experimental observations.

The experimental studies on interspecies interaction between different Yb isotopes and ^{87}Rb, which are described in the present PhD work, have greatly increased the knowledge of low energy properties of the respective mixtures. This is a major step towards the long term goal of this research project, which is the production of ultracold rovibronic ground state YbRb molecules. The future developments required to achieve this goal can be divided into two areas: One will be the continuation of studies on the YbRb molecular potentials, which already resulted in the successful production of excited state YbRb* molecules by photoassociation [16]. The other will be to realize a quantum degenerate mixture of both species, which would be an ideal starting point for the creation of ground state YbRb molecules. Based on new insights on the low energy scattering properties of

Yb and ^{87}Rb, a promising pathway towards a combined degenerate mixture of ^{87}Rb and Yb has been developed.

Zusammenfassung

Im Rahmen dieser Doktorarbeit wurden umfassende experimentelle Untersuchungen zu heteronuklearen Wechselwirkungen zwischen ^{87}Rb und verschiedenen Yb Isotopen im μK-Temperaturbereich durchgeführt. Die Wechselwirkung zwischen beiden Atomsorten äußerte sich dabei durch Thermalisierung und – im Fall von ^{174}Yb und ^{87}Rb – durch Phasenseparation beider Spezies.

Sowohl Yb als auch Rb sind gut geeinet für die Anwendung von Laserkühlverfahren. Das Regime der Quantenentartung wurde daher mit beiden Elementen bereits realisiert. [1, 2]. Das bislang noch nicht näher untersuchte System Yb-Rb is eine interessante Elementkombination mit vielseitigen Perspektiven im Bereich der ultrakalten gemischten Gase. Aufgrund der Verfügbarkeit 7 stabiler Ytterbiumisotope sind sowohl Boson-Boson- als auch Fermion-Boson-Gemische realisierbar. Zudem stellen ultrakalte YbRb Moleküle ein viel versprechendes System mit deutlich unterschiedlichen physikalischen Eigenschaften im Vergleich zu den in bisherigen in Experimenten untersuchten Alkali-Alkali-Kombinationen dar [3, 4, 5, 6]: YbRb Moleküle besitzen sowohl ein elektrisches als auch ein magnetisches Dipolmoment, was z.B. Untersuchungen zu Spin-Gitter-Modellen erlaubt.

Die in dieser Arbeit beschriebenen Experimente wurden an einer bereits früher eingesetzten Apparatur durchgeführt [8, 9, 10, 11], die jedoch in Bezug auf Stabilität und Präzision signifikant verbessert wurde. In diesem Zusammenhang wurden während dieser Arbeit zahlreiche Komponenten, wie etwa große Teile des Lasersystems neu aufgebaut.

Eine Besonderheit des Systems Yb-Rb ist die Kombination einer diamagnetischen (Yb) mit einer paramagnetischen (Rb) Spezies. Die unterschiedlichen magnetischen Eigenschaften erlauben eine Kombination von Fallenpotentialen, die eine (weitgehend) unabhängige Kontrolle über beide Atomsorten ermöglicht. Die kombinierte Falle besteht aus einer Ioffe-Pritchard Magnetfalle für ^{87}Rb und einer bichromatischen otpischen Diopolfalle (BIODT) für Yb. Im typischen Experimentierablauf wird Yb zunächst in einer magneto-optischen Falle vorgekühlt und schließlich in die BIODT geladen. Anschließend wird ^{87}Rb in die Magnetfalle geladen und evaporativ gekühlt. Damit können in der kombinierte Falle gleichzeitig $\approx 10^7$ ^{87}Rb Atome bei Temperaturen von $\approx 1\,\mu$K und, je nach verwendetem Isotop, $(0.3 \ldots 1.5) \times 10^5$ Yb Atome bei $5 \ldots 8\,\mu$K präpariert werden.

Nachdem beide Atomwolken in räumlichen Kontakt gebracht werden, thermalisiert Yb mit den kälteren ^{87}Rb Atomen. Im Rahmen der vorliegenden Arbeit wurden Thermalisierungsraten zwischen ^{87}Rb und den Yb-Isotopen ^{170}Yb, ^{172}Yb, ^{173}Yb, ^{174}Yb und ^{176}Yb im Temperaturbereich unterhalb von $10\,\mu$K gemessen, woraus man Rückschlüsse auf relative Streueigenschaften der jeweiligen Yb-Isotope ziehen kann. Dabei wiesen zwei Yb-Isotope außergewöhnliche Eigenschaften auf: Zum einen konnte nahezu keinerlei Thermalisierung zwischen ^{170}Yb und ^{87}Rb beobachtet werden. Eine quantitative Analyse dieser Daten erlaubt die Abschätzung der s-Wellen Streulänge für diese beiden Spezies

zu $|a_{87-170}| = 6.6^{+3.5}_{-2.9}\,\mathrm{a_0}$. Zum anderen themalisierten ^{174}Yb Atome nahezu instantan mit den kälteren ^{87}Rb Atomen, was auf einen großen elastischen Streuquerschnitt hindeutet.

Darüber hinaus konnte in bei veränderter Fallengeometrie Phasenseparation zwischen ^{174}Yb und ^{87}Rb beobachtet werden.

Im Feld der gemischten ultrakalten Quantengase wurde Phasenseparation bereits in verschiedenen Systemen untersucht [12, 13, 14]. Im Gegensatz zu diesen Experimenten, die alle im quantenentarten Regime durchgeführt wurden, trat die im Rahmen dieser Arbeit beschriebene Phasenseparation zwischen thermischen Atomwolken bei Temperaturen im μK-Bereich auf.

Für ein quantitavies Verständnis der beobachteten Effekte ist die genaue Kenntnis der harmonischen Eigenschaften aller beteiligter Fallenpotentiale nötig. Mit Hilfe ausführlicher Messungen zu Fallenfrequenzen der Magnetfalle und der BIODT war es möglich, Modellpotentiale zu simulieren, die die experimentelle Situation beschreiben. Die Wechselwirkung auf ^{174}Yb durch die ^{87}Rb Atome wurde dabei als zusätzliches repulsives Wechselwirkungspotential angenommen, das in erster Näherung proportional zur ^{87}Rb-Dichte ist.

Quantitative Ergebnisse zum heteronuklearen Wechselwirkungspotential zwischen ^{174}Yb und ^{87}Rb konnten in Bezug auf Zweikörper-Stoßparameter interpretiert werden. Ein "naiver" Mean-Field Ansatz führte bei thermischer Mittelung der energieabhängigen Streulänge dabei jedoch zu Ergebnissen, die den experimentellen Beobachtungen widersprachen.

Im Zusammenhang mit dieser Unstimmigkeit, wurden zunächst mögliche experimentelle Probleme untersucht, die zu falschen Ergebnissen für das gemessene Wechselwirkungspotential führen könnten. Zudem wurde die Gültigkeit der Mean-Field Theorie im vorliegenden Fall von großen Streulängen bei gleichzeitig hohen ^{87}Rb-Dichten diskutiert und ein nichtlinearer Korrekturterm eingeführt. Dieser berücksichtigt dichteabhängige Mehrteilchen-Wechselwirkungen. Mit Hilfe dieser Korrektur ergibt sich schließlich eine heteronukleare s-Wellen Streulänge zwischen ^{174}Yb und ^{87}Rb von $a_{87-174} = 4710^{+3970}_{-1520}\,\mathrm{a_0}$. Eine weitere theoretische Beschreibung der beobachteten Phasenseparation wurde von E. Tiesinga und S. Maxwell [15] aus der theoretischen Atomphysik-Gruppe am NIST vorgeschlagen: Sie beruht auf einem Diffusions-Modell und Dreikörperverlusten und wird im Rahmen dieser Arbeit ebenfalls diskutiert.

Die experimentellen Ergebnisse dieser Arbeit lassen Rückschlüsse auf das Grundzustandspotential des YbRb Moleküls und auf Bindungsenergien schwach gebundener Zustände zu. In diesem Zusammenhang haben E. Tiesinga und S. Maxwell [15] ein Lennard-Jones Potential berechnet, das die hier vorgestellten experimentellen Befunde korrekt wiedergibt.

Die im Zusammenhang mit der vorliegenden Arbeit durchgeführten Untersuchungen führten zu einer Reihe von neuen Erkenntnissen über die Wechselwirkungen zwischen verschiedenen Yb-Isotopen und ^{87}Rb. Diese Informationen können entscheidend dazu beitragen, das langfristige Ziel dieses Forschungsvorhabens, nämlich die Produktion von ultrakalten YbRb Molekülen im Grundzustand, zu erreichen. Die dazu nötigen weiteren Entwicklungen beziehen sich zum einen auf die Fortsetzung der experimentellen Unter-

suchungen der YbRb Molekülpotentiale, die bereits zur erfolgreichen Erzeugung angeregter YbRb* Moleküle durch Photoassoziation geführt haben [16]. Zum anderen besteht die Aufgabe, ein kombiniertes Quantengas zu erzeugen, da dieses einen idealen Ausgangspunkt für die Erzeugung von YbRb-Grundzustandsmolekülen darstellt. Ein möglicher Weg zur gemeinsamen Quantenentartung von Yb und ^{87}Rb wird am Ende dieser Arbeit aufgezeigt.

Contents

1

Introduction

The work presented here was carried out within a research project, whose long term goal is the creation of ultracold rovibrational ground state molecules of ytterbium (Yb) and rubidium (Rb). Detailed studies on the interaction between ^{87}Rb and various isotopes of Yb are required to achieve this goal. This PhD work focuses on the effect of phase separation between ^{174}Yb and ^{87}Rb resulting from strong interspecies interactions between these isotopes.

The following chapter motivates the present work by briefly introducing the field of ultracold atoms and molecules with special emphasis on the system YbRb. In addition, it focuses on interactions in two-component quantum gases and places the present experiments in the context of current developments.

Ultracold atoms and molecules

Since the first observation of slowing [17, 18] and cooling [19] of sodium atoms by the use of lasers in the 1980s, the field of ultracold atoms and molecules has virtually exploded. In 1997, the Nobel Prize was awarded to Claude Cohen- Tannoudji, William Phillips and Steven Chu for the development of techniques of laser cooling [20]. In the meantime, additional cooling methods were designed, which led to temperatures in the nano-Kelvin (nK) regime, where macroscopic quantum phenomena could be explored experimentally. The most prominent effect in this regime is the Bose-Einstein condensation (BEC), a new state of matter made accessible through the success of laser cooling and trapping. It was experimentally realized in 1995 [2, 21, 22]. Consequently, Eric Cornell, Wolfgang Ketterle and Carl Wieman were awarded the Nobel Price in Physics in 2001 "for the achievement of Bose-Einstein condensation in dilute gases of alkali atoms, and for early fundamental studies of the properties of the condensates" [23].

Ever since the field of ultracold atomic gases has developed, there has been great interest in adapting the success of measurements on ultracold atoms to the field of (heteronuclear) molecules, which offers exciting new possibilities:

First of all, ultracold molecules provide an ideal platform for ultrahigh-resolution molecular spectroscopy. Due to the low temperatures and long coherence times, molecular transitions can be studied at the highest spectral resolution limited only by the natural lifetimes of relevant molecular energy levels [24]. This increases the knowledge of molecular structure, which is crucial for understanding and control of dynamics in the emerging field of

cold molecule chemistry (see below). Additionally, the high resolution capability offers possibilities for stringent tests of fundamental physical laws and symmetries: Measurements on nuclear spin-dependent parity violation related to weak interactions between electrons and nucleons [25] as well as tests on possible changes of the fine structure constant [26] are proposed using ultracold molecules. Furthermore, experiments on the presence (and magnitude) of an elementary permanent electron dipole moment (EDM) make use of the large internal electric field in polar molecules. Ongoing EDM measurements use a beam of YbF molecules [27], a recent proposal discusses the system of ultracold YbRb [28], whose properties are investigated in the present PhD work.

Due to the large electric dipole moment of most heteronuclear molecules, they also allow the extension of recently achieved atomic dipolar quantum gases [29] with a relatively weak magnetic dipolar interaction to the molecular regime [30, 31], where electric dipolar interaction can be very strong. This points towards the possibility of manipulating the strong and long-range dipole-dipole interactions between molecules with external electric fields and simulating condensed matter systems.

In addition, paramagnetic heteronuclear molecules , e.g. YbRb, stored in optical lattices, provide the potential of realizing lattice-spin models, which were proposed as the basis for a new class of quantum computation [32, 7].

Finally, experiments with ultracold molecules allow fundamental insights into how chemical reaction processes may be governed by quantum mechanics. For example, as molecules are prepared in their lowest electronic, vibrational and rotational ground state, the only possible degree of freedom left is the orientation of the nuclear spin, which then plays an important role in molecular collisions. This allows quantum-state selective measurements of elastic, inelastic, and chemically reactive collisions: Recent studies using a mixture of ultracold Cs_2 molecules and Cs atoms in defined hyperfine sublevels report on the observation of a controllable exchange process [5] between the constituents. The control parameter in these experiments is the magnetic field, which changes the two-body interaction through a Feshbach resonance. As a result, it determines, whether the exchange reaction is endoenergetic or exoenergetic. An independent experiment demonstrates, that the chemical reaction $2\,{}^{40}K^{87}Rb \rightarrow {}^{40}K_2 + {}^{87}Rb_2$ using ultracold rovibronic ground-state ${}^{40}K^{87}Rb$ molecules shows a clear dependence on quantum statistics, angular momentum barriers, and threshold laws [33].

Note that the highlighted examples only represent a tiny fraction of experimental and theoretical studies in the growing field of ultracold molecules. A more comprehensive presentation of recent developments can be found in the review article by Carr et al. [34].

In the context of ultracold molecules, the alkali-rare earth system YbRb is an interesting combination with significantly different physical properties than the alkali-alkali combinations investigated in most experiments: Besides its strong dipolar character, the paramagnetic ${}^2\Sigma_{1/2}$ ground state would allow stable ground state YbRb molecules to be held in a magnetic trap.

All of the experiments described above require an effcient method of creating ultracold molecules, preferably in the rovibrational ground state. An overview of the different approaches to this problem is presented in [35]. Unlike many atomic species, molecules can

not be cooled and trapped using the methods of laser cooling, due to their complex internal structure. The most promising method for ultracold molecule production, which also represents one of the the long term goals of the experiment described in this PhD work, is to apply the well known techniques of laser cooling to the corresponding constituent atoms and subsequently connect them to molecules. The latter can be achieved either by the use of magnetically tunable Feshbach resonances [36] or by photoassociation [37]. After the application of these methods to an ultracold gas of atoms, the resulting diatomic molecules are typically in a high rotational, extremely weakly bound state. It is then a considerable challenge to efficiently transfer these molecules to the desired low-lying rovibronic states without allowing the binding energy to heat the gas. The method of stimulated Raman adiabatic passage (STIRAP) [38], which is a two-photon process, allows a coherent transfer to defined quantum states. Recently, ultracold rovibronic ground state molecules of Rb_2 [3], Cs_2 [4] and KRb[6] have successfully been created using the described path.

Interactions in two-component quantum gases – phase separation

An important step towards the experimental realization of ultracold molecules is the production of an ultracold mixture. However, this is not only a technological step, as the study of ultracold gases consisting of more than one component has been one of the intriguing developments in the field of ultracold atomic gases. It enables the study of Bose-Bose, Fermi-Bose, and Fermi- Fermi mixtures. The interactions, which determine the stability and the dynamics of the mixed-gas system, can be tuned by changing the combination of atomic species or by using magnetic and optical Feshbach resonances.

One aspect in experiments with mixed quantum systems is the occurrence of phase separation, which, in the case of a thermal mixture of ^{174}Yb and ^{87}Rb, is also the major scientific matter of the PhD work presented here. Generally, the problem of miscibility or phase separation of two different components in a thermal system is related to the question, whether the interspecies interaction energy is small or large compared to the thermal energy $k_{\mathrm{B}}T$. The experiments discussed in the following, however, are performed in the regime of quantum degeneracy, where the thermal energy plays a minor role with respect to particle interactions. Thus, the condition for phase separation depends on the interspecies interaction energy in the mixed system in comparison to the (intra-species) interactions of the respective constituents in the separated phases. The following paragraphs briefly summarize the developments in experiments with ultracold mixtures with special emphasis on the observation of phase separation.

Soon after the experimental realization of BECs in 1995, first degenerate mixtures consisting of ^{87}Rb atoms in the $|F = 1, m_F = -1\rangle$ and $|2, 2\rangle$ spin states, trapped in magnetic potentials were investigated experimentally [39] and theoretically [40]. These experiments demonstrated the possibility of producing long-lived multiple condensate systems. They also showed, that the condensate wave function is dramatically affected by the presence of interspecies interactions. In subsequent studies on ^{87}Rb $|1, -1\rangle$ - $|2, 1\rangle$ BEC mixtures, spatial separation was observed and the relative phase between both condensates [12, 41] was measured. Further experiments on partially condensed spin mixtures of ^{87}Rb exhibited

dramatic transient nondiffusive spin polarizations, which were attributed to longitudinal spin waves [42].

More recent studies involving a quantum degenerate mixture of ^{85}Rb and ^{87}Rb atoms in optical traps also exhibit interesting physics related to phase separation [13]: Depending on the relative intra- and interspecies interaction, which can be controlled by a magnetically tunable Feshbach resonance, the dual BEC showed either miscible or immiscible behavior. The latter lead to a dramatic spatial separation of the two species, resulting in counterintuitive density distributions: The robust formation of multiple, non-overlapped, single-species BEC "cloudlets" were observed, which was theoretically explained by the onset of modulation instability during the transition from the miscible to the immiscible phase [43].

The effect of phase separation was also observed in a strongly interacting Bose-Fermi mixture created from a two-component Fermi mixture with population imbalance. The experiment is based a degenerate gas of fermionic ^{6}Li atoms [44, 14] in the BEC-BCS crossover regime at a Feshbach resonance. On the "BEC-side" of the Feshbach resonance, the fermions with different spin polarization become bound as molecular Li_2 bosons and form a BEC. Depending on the initial population imbalance, the spatial distribution is represented by a core of Bose condensed Li_2 dimers surrounded by a shell of normal unpaired fermions, indicating strong interactions between the two components.

Another important step in the field of two-component quantum gases was the production and study of a degenerate mixture composed by two Bose-Einstein condensates of different atomic species, ^{41}K and ^{87}Rb [45, 46]. Simultaneous condensation is achieved by means of two-species sympathetic cooling in a magnetic trap and strong interspecies interactions could be observed.

This thesis

The experiments presented in this thesis have been performed within a research project involving the study of ultracold mixtures of Rb and Yb. Both atomic species are well suited for the application of laser cooling, and quantum degeneracy has been reached for Yb as well as for Rb [1, 2]. As discussed above, ultracold heteronuclear YbRb molecules are promised to be an interesting system, mainly due to their strong (electric and magnetic) dipolar character.

The pathway to ultracold YbRb molecules, which will be followed in the present experiment, requires the preparation of spatially overlapping clouds of ultracold Yb and Rb atoms. For efficient production of rovibronic ground state YbRb molecules it is planned to perform two consecutive two-photon processes. The first step in this direction, i.e. the formation of excited state YbRb* molecules by photoassociation, has already been successfully observed at the present apparatus [16] at higher temperatures.

Due to the particular magnetic properties of Rb and Yb, a unique combination of trapping potentials, which allows for independent trapping and manipulation of ultracold ^{87}Rb and Yb atoms is implemented in the experimental setup. The combined trap consists of a Ioffe-Pritchard-type magnetic trap (MT) for ^{87}Rb and a bichromatic optical dipole trap

for Yb. The present approach for the simultaneous preparation of ^{87}Rb and Yb at temperatures low enough to reach quantum degeneracy involves sympathetic cooling of Yb by evaporatively cooled ^{87}Rb atoms. This method has been successfully demonstrated in a previous work [9] in the temperature regime of $20 \ldots 50\,\mu$K for different Yb isotopes.

Within the present thesis, interactions of ^{87}Rb and Yb have been investigated at temperatures of $1 \ldots 5\,\mu$K, where the underlying scattering properties differ significantly from results obtained at higher temperatures. In order to enter successfully into this temperature regime, the experimental setup required a significant improvement in stability and precision. Hence, large parts of the laser- and atom imaging system have been redesigned in the course of this work.

The main scientific results of this PhD work are comprehensive studies on phase separation between ^{174}Yb and ^{87}Rb in the μK regime. Analysis of the experimental observations required accurate modeling of the trapping potentials in order to extract quantitative results on the interspecies interaction. These results can be related to the ^{174}Yb ^{87}Rb interspecies s-wave scattering length, using an approach, which not only describes mean field effects but also includes multiple-particle interactions. In contrast to the phase separation experiments in other systems, which are performed with degenerate quantum gases (see above), phase separation between ^{174}Yb and ^{87}Rb as described in this PhD work is observed with purely thermal samples at temperatures in the μK regime. To our knowledge, this phenomenon has not yet been observed in this regime before.

Furthermore, thermalization measurements in the $1 \ldots 5\,\mu$K regime using ^{87}Rb and various isotopes of Yb have been performed, allowing the comparison of relative scattering properties between the respective species.

Conclusions from the presents studies on interspecies interactions between ^{87}Rb and Yb have been used for model calculations on the Yb Rb molecular ground state potential. E. Tiesinga and S. Maxwell from the atomic theory group at NIST [15] determined a Lennard-Jones potential, which quantitatively reproduces the present experimental observations. This knowledge will significantly help to provide a strategy for the controlled transfer of excited state YbRb* molecules to a selected ground state that will be developed in future work of the group.

This thesis is organized as follows: Chapter 2 gives an introduction to the collision theory with a special emphasis on the low temperature aspect of these interactions and Chap. 3 provides the theoretical background for the laser cooling and trapping techniques employed. The experimental setup used in this PhD work including the vacuum chamber, the laser systems and the atom detection system is described in Chap. 4. Chapter 5 introduces the unique combination of magnetic and optical trapping potential present in these experiments and outlines the experimental procedure for simultaneous preparation of ultracold ^{87}Rb and Yb. Detailed measurements required for a comprehensive characterization of the trapping potentials are described in Chap. 6, before the following Chap. 7 and 8 focus on the central interspecies interaction experiments: Chapter 7 describes thermalization experiments in the $1 \ldots 5\,\mu$K range using ^{87}Rb and various Yb isotopes and Chap. 8 presents measurements, data analysis and interpretation of phase separation experiments between ^{87}Rb and ^{174}Yb.

The results of these studies are summarized and discussed in Chap. 9 and Chap. 10 closes with proposals for the future development of the research project.

2

Atom-atom interaction in dilute ultracold gases

Interactions in ultracold gases manifest themselves through collisions between particles. Hence, collision physics plays a crucial role in understanding the properties of ultracold gases. First, collisions ensure thermalization in trapped atomic samples, which is essential for successful evaporative cooling (see Sec. 3.2.2). Furthermore, sympathetic colling, i.e. thermalization of one atomic species with another, as described in Chap. 7 is based on interspecies collisions. Finally, strong interaction effects like the observed phase separation of ^{87}Rb and ^{174}Yb (see Chap. 8) are directly related to the respective collisional parameters.

In dilute ultracold gases, temperatures do not exceed a few μK and densities are below $10^{15}\,cm^{-3}$. Here, the intrinsically elaborate quantum mechanical description of collisions becomes relatively simple: Despite an arbitrarily complex atom-atom interaction potential, a single parameter sufficiently characterizes the scattering properties of the gas (see Sec. 2.1.4). In addition, to the lowest order, only two-body collisions have to be taken into account due to the low density.

The following section gives a basic introduction to collision physics with a special emphasis on the low temperature aspect of these interactions. In particular the essential concept of scattering length will be introduced and different aspects of low energy scattering are discussed with the help of a simple model potential. Subsequently, two-body collision properties are extended to a mean-field potential describing the macroscopic behavior of atomic clouds. This chapter ends with a basic introduction of Feshbach resonances and inelastic collisions.

The following approach is based on [47, 48, 49], further details of scattering theory can be found in [50, 51].

2.1 Basic principles of scattering theory

2.1.1 Definition of the scattering problem

Here we consider a non-relativistic, elastic collision process between two particles with position vectors $\vec{r}_1$ and $\vec{r}_2$ and masses m_1 and m_2, interacting through the scalar potential $V(\vec{r}_1, \vec{r}_2)$. By transforming the collision process into the center of mass system, the problem is reduced to an effective single-particle process: A particle with reduced mass $m_r = \frac{m_1 m_2}{m_1+m_2}$

is scattered by the potential $V(\vec{r}) = V(\vec{r}_1 - \vec{r}_2)$. In this coordinate system, the problem is defined by the relative velocity $\vec{v}$, the relative momentum $\vec{p} = m_r\vec{v}$ and the relative wave vector $\vec{k} = \vec{p}/\hbar$ with $k = |\vec{k}|$.

The incident particle is described by a wave packet $\psi(\vec{r})$, consisting of a superposition of plane waves $e^{i\vec{k}\vec{r}}$. For the case of elastic scattering, the problem is defined by the time independent Schrödinger equation

$$\left(\frac{\hbar^2}{2m_r}\vec{\nabla}^2 + V(\vec{r})\right)\psi_{\vec{k}}(\vec{r}) = E_k\psi_{\vec{k}}(\vec{r})\,, \tag{2.1}$$

where $E_k = \hbar k^2/(2m_r)$ is a well defined positive energy and the potential $V(\vec{r}) \to 0$ for $|\vec{r}| \to \infty$. Outside the range of $V(\vec{r})$, the asymptotic solution consists of two components:

$$\lim_{|\vec{r}|\to\infty} \psi_{\vec{k}}(\vec{r}) \propto e^{-i\vec{k}\vec{r}} + f_k(\theta,\phi)\frac{e^{ikr}}{r}\,. \tag{2.2}$$

The plane wave $e^{-i\vec{k}\vec{r}}$ represents the unperturbed transmitted part of the incident wave and $f_k(\theta,\phi)\frac{e^{ikr}}{r}$ is a scattered spherical wave. The *scattering amplitude* $f_k(\theta,\phi)$ depends on the relative wave vector of the particle, and generally on the azimuthal and polar angles θ and ϕ. Experimentally more accessible parameters are the differential and total *scattering cross section*. The differential cross section $\frac{d\sigma}{d\Omega}$ defines the number of particles dn scattered per unit time into the solid angle Ω about the direction (θ,ϕ) relative to the incident particle flux F_i:

$$\frac{dn}{d\Omega} = F_i\frac{d\sigma}{d\Omega}(k,\theta,\phi)\,. \tag{2.3}$$

The scattering amplitude connects the scattering wave function (2.2) with the experimentally observable differential and total scattering cross section:

$$\frac{d\sigma}{d\Omega}(k,\theta,\phi) = |f_k(\theta,\phi)|^2 \qquad \text{and} \qquad \sigma_{\text{tot}}(k) = \int |f_k(\theta,\phi)|^2\, d\Omega\,. \tag{2.4}$$

2.1.2 Partial wave expansion

In general, the exact determination of the scattering amplitude $f_k(\theta,\phi)$ requires the solution of the three dimensional Schrödinger equation, which is rather complex except for very particular cases. The situation is considerably simplified for the case of a spherically symmetric potential $V(\vec{r}) = V(r)$. From symmetry arguments, it is clear that in this case the scattering amplitude depends only on the angle θ between the incident direction and the observation direction. To take advantage of the symmetry of the problem, it is convenient to expand the incident and scattered wave functions in a basis set of spherical harmonic functions $Y_{lm}(\theta,\phi)$. In the given ϕ-independent case, these functions are reduced to Legendre polynomials $P_l(\cos\theta)$ depending on the angular momentum quantum number l. Using the ansatz

$$\psi_{\vec{k}}(\vec{r}) = \sum_{\ell=0}^{\infty}\frac{u_{k,\ell}(r)}{r}P_\ell(\cos\theta)\,, \tag{2.5}$$

the Schrödinger equation for the radial wave function $u_{k,\ell}(r)$ is given by

$$-\frac{\hbar^2}{2m_\mu}\frac{d^2}{dr^2}u_{k,\ell}(r) + \Bigg(-E_k + \underbrace{V(r) + \frac{\hbar^2\ell(\ell+1)}{2m_r r^2}}_{\equiv V_{\text{eff}}} \Bigg) u_{k,\ell}(r) = 0\,. \tag{2.6}$$

Note that the effective potential V_{eff} includes a *centrifugal term*, which describes the system's rotational energy.

The far-field asymptotic solution for the scattering wave is obtained by performing a partial wave expansion of the incoming plane wave $e^{-i\vec{k}\vec{r}}$ in Eq. 2.2 and comparing the coefficients of Eq. 2.5 and 2.2 in the $r \to \infty$ limit. A detailed description of this approach can be found in [49, 52]. The following asymptotic solution for the scattering wave function is obtained:

$$\lim_{|\vec{r}|\to\infty} \psi_{\vec{k}}(\vec{r}) = \frac{1}{k}\sum_{\ell=0}^{\infty} P_\ell(\cos\theta) A_\ell \left((-1)^{l+1}\frac{e^{-ikr}}{r} + e^{2i\delta_\ell(k)}\frac{e^{ikr}}{r} \right) . \tag{2.7}$$

This description represents again a superposition of the incident and outgoing wave function for each of the partial waves $\ell = 0, 1, 2, \ldots$. The outgoing wave function differs from the free particle case ($V(r) = 0$) only by a phase shift δ_ℓ. Hence, in the far field, the collision process is fully described by the *scattering phase* δ_ℓ for each partial wave. The coefficients A_ℓ have to be chosen so that at large distances this function has the asymptotic form of Eq. 2.2 (see e. g. [53] for details on this derivation). As a result, the scattering amplitude in partial wave expansion can be written as:

$$f(k,\theta) = \frac{1}{2ik}\sum_\ell (2\ell+1)\left(e^{2i\delta_\ell(k)} - 1\right) P_\ell(\cos\theta) \tag{2.8}$$

$$= \frac{1}{k}\sum_\ell (2\ell+1)\, e^{2i\delta_\ell(k)} \sin\delta_\ell(k) P_\ell(\cos\theta)\,. \tag{2.9}$$

Finally the total scattering cross section can be obtained by integrating over all scattering angles:

$$\sigma_{\text{tot}}(k) = \sum_\ell \sigma_\ell(k) = \frac{4\pi}{k^2}\sum_\ell (2\ell+1)\sin^2\delta_\ell(k)\,. \tag{2.10}$$

The maximum contribution of each partial wave to the total scattering cross section is

$$\sigma_{\ell,\text{max.}} = 4\pi(2\ell+1)/k^2\,. \tag{2.11}$$

This value is reached for $\sin^2\delta_\ell(k) = 1$ in the so-called *unitarity limit*.

The partial wave expansion reduces the scattering problem to the determination of the scattering phase for each angular momentum contribution. The situation is further simplified for ultracold collisions ($k \to 0$), where all contributions to the scattering amplitude except the s-wave ($\ell = 0$) vanish (see Sec. 2.1.4).

The scattering amplitude (2.9) for pure s-wave collisions ($\ell = 0$) can be separated in its real and imaginary part according to:

$$\begin{aligned} f_0(k) &= \frac{1}{k} e^{2i\delta_0(k)} \sin\delta_0(k) \\ \Rightarrow \mathrm{Im}\frac{1}{f_0(k)} &= -k \qquad \text{and} \qquad \mathrm{Re}\frac{1}{f_0(k)} = k\cot\delta_0(k)\,. \end{aligned} \tag{2.12}$$

From the last two equations it follows immediately that the s-wave scattering amplitude can be rewritten as

$$f_0(k) = \frac{1}{g_0(k) - ik}, \tag{2.13}$$

where the function $g_0(k) = k\cot\delta_0(k)$. This expression for the scattering amplitude will be used to derive the energy dependence of the s-wave scattering cross-section in Sec. 2.3.

2.1.3 Identical particles

The previous discussion is based on distinguishable particles assuming that the two scattering diagrams of Fig. 2.1, corresponding to a scattering amplitude $f(k,\theta)$ and $f(k,\pi-\theta)$, respectively, could be discriminated. For the case of identical particles, however, the two

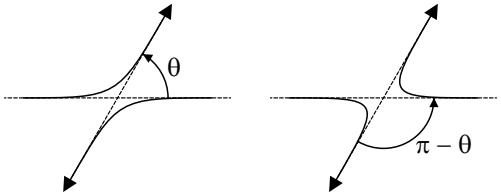

Figure 2.1: *Two scattering processes leading to the same final state for indistinguishable particles.*

processes result in the same scattering state. Taking into account the (anti)symmetrisation principle for bosons (fermions), the ansatz for the scattering wave function (2.2) has to satisfiy the condition $\Psi(\vec{r}_1,\vec{r}_2) = \epsilon\cdot\Psi(\vec{r}_2,\vec{r}_1)$ with $\epsilon = +1$ ($\epsilon = -1$) for bosons (fermions):

$$\psi_{\vec{k}}(\vec{r}) \propto e^{i\vec{k}\vec{r}} + \epsilon e^{-i\vec{k}\vec{r}} + \Big(f(k,\theta) + \epsilon f(k,\pi-\theta)\Big)\frac{e^{ikr}}{r}\,. \tag{2.14}$$

The differential cross section then reads

$$\frac{d\sigma}{d\Omega} = \left|f(k,\theta) + \epsilon f(k,\pi-\theta)\right|, \tag{2.15}$$

where θ varies in this case between 0 and $\pi/2$. The Legendre polynomials have to be multiplied by $(-1)^l$ under particle commutation leading to destructive interference off all odd (even) partial wave contributions for bosons (fermions). he (anti)symmetrization principle therefore doubles the contribution of the even partial waves for bosons (the odd partial waves for fermions) and cancels the contribution of the odd ones (the even ones for

fermions):

$$\text{bosons}: \quad \sigma_{\text{tot}} = \frac{8\pi}{k^2} \sum_{\ell \text{ even}} (2\ell+1) \sin^2 \delta_\ell(k) \tag{2.16}$$

$$\text{fermions}: \quad \sigma_{\text{tot}} = \frac{8\pi}{k^2} \sum_{\ell \text{ odd}} (2\ell+1) \sin^2 \delta_\ell(k) \tag{2.17}$$

2.1.4 The low energy limit

Suppression of higher partial waves

For the partial wave $\ell = 0$, the potential entering into the Schrödinger equation (2.6) is simply the interatomic potential $V(r)$ with a long range part typically described by a term $-C_n/r^n$. For higher partial waves, this potential is superimposed by the centrifugal term $\hbar^2 l(l+1)/(2m_r r^2)$, resulting in an effective potential

$$V_{\text{eff}}(r) = -\frac{C_n}{r^n} + \frac{\hbar^2 \ell(\ell+1)}{2m_r r^2}\,. \tag{2.18}$$

At large particle distances, the interaction between two ground state atoms in the electronic S-state is limited to Van-der-Waals interaction. The Van-der-Waals interaction results from a short-lived spontaneous electric dipole moment in one atom creating a matching dipole moment in the other, thus leading to an attractive force. The corresponding potential scales with the inter atomic distance r as C_6/r_6, where C_6 is the so called C_6 *dispersion coefficient*[1]. Values for the C_6 coefficient can be obtained from theoretical calculations based on the molecular potentials [54] or by comparison of theoretical predictions with experimental results [55, 56, 57].

The potential (2.18) represents a *centrifugal barrier* at $r = r_c$ for approximating particles: If the approaching unbound atoms do not have sufficient energy to cross the barrier, they will be repelled before they can reach the interaction region of $V(r)$ for $r < r_c$. The centrifugal barrier height is given by

$$E_c(\ell) = 2\left(\frac{\hbar^2 \ell(\ell+1)}{6m_r}\right)^{3/2} C_6^{-1/2}\,. \tag{2.19}$$

Quantitatively, the highest contributing partial wave ℓ_{max} can by determined from [58]

$$E_c(\ell_{\text{max}}) = \frac{3}{2} k_{\text{B}} T, \tag{2.20}$$

assuming a mean collision energy $\frac{3}{2}k_{\text{B}}T$.

[1] The C_6 dispersion coefficient is usually given in atomic units [a.u.]. It can be converted into the SI-system by $C_6\,[\text{SI}] = C_6\,[\text{a.u.}]\frac{e^2 a_0^5}{4\pi\varepsilon_0}$ with the elementary charge e and the Bohr radius a_0.

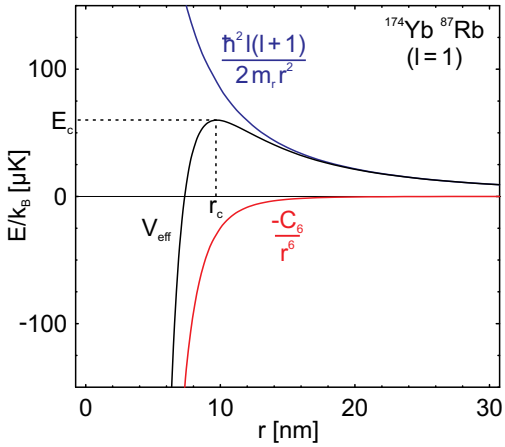

Figure 2.2: *Effective potential V_{eff} according to Eq. 2.18 (black), consisting of the pure van-der-Waals potential (red) and the centrifugal term (blue). Calculations are based on an ^{174}Yb - ^{87}Rb collision ($C_6 = 3186$ a.u.) with angular momentum $\ell = 1$ resulting in a centrifugal barrier height $E_c \approx 63\,\mu K$.*

Centrifugal barrier in the system Yb-Rb For the case of Rb and Yb, the respective C_6 dispersion coefficients are given by

$$C_6^{\text{Rb}} = (4703 \pm 9)\,\text{a.u.}\ [56] \qquad \text{and} \qquad C_6^{\text{Yb}} = (1932 \pm 30)\,\text{a.u.}\ [57]\,.$$

However, an exact value for the C_6 coefficient of the YbRb ground state molecular potential is so far unknown. Photoassociation experiments [16] performed at this apparatus probe only the excited state and the ab-initio potentials do not extend to long ranges [59]. Hence an approximation based on [60] is used to determine the interspecies dispersion coefficient:

$$C_6^{\text{YbRb}} \approx \frac{1}{2}\sqrt{C_6^{\text{Yb}} C_6^{\text{Rb}}}\left(\frac{\Delta E_{\text{Yb}} + \Delta E_{\text{Rb}}}{\sqrt{\Delta E_{\text{Yb}} \Delta E_{\text{Rb}}}}\right) \approx 3186\,\text{a.u.}\,. \tag{2.21}$$

Here, $\Delta E_{\text{Yb,Rb}}$ represent the energies of the main electronic transitions (Yb: $^1S_0 \rightarrow {}^1P_1$ transition with $\Delta E_{\text{Yb}} = {}^{hc}/_{399\,\text{nm}}$, Rb: D_1- and D_2 line with $\Delta E_{\text{Rb}} = {}^{hc}/_{\frac{1}{2}(780\,\text{nm}+795\,\text{nm})}$).

Using this approximation for C_6^{YbRb}, Fig. 2.2 shows a calculation of the effective potential V_{eff} for ^{174}Yb - ^{87}Rb p-wave ($\ell = 1$) collisions. The Yb-Rb centrifugal barrier height (2.19) gives a p-wave ($\ell = 1$) and d-wave ($\ell = 2$) threshold of $E_c(\ell = 1)/k_{\text{B}} \approx 63\,\mu$K and $E_c(\ell = 2)/k_{\text{B}} \approx 326\,\mu$K. At collision energies below these thresholds, the respective partial waves do not contribute to the scattering amplitude. All relevant experiments described in the scope of this thesis are carried out at temperatures below $10\,\mu$K, where Eq. 2.20 results in $\ell_{\text{max}} < 0.51$. Hence, in this regime, only the s-wave contributes significantly to the scattering process, while all other partial waves do not overcome the centrifugal barrier.

Shape resonances An exception to the situation described above occurs for so called *shape resonances*: For $\ell \neq 0$, it is possible, that quasi-bound states exist in the potential well close to $r = 0$. There will then be a scattering resonance if the incident relative particle has an energy close to the energy of such a quasi-bound state. The particle is able to tunnel through the centrifugal barrier and couple to the quasi-bound state. These shape resonances may enhance strongly the contribution of $\ell \neq 0$ partial waves in an energy domain where a pure $\ell = 0$ scattering would be expected [47].

s-Wave scattering – the scattering length

In the regime of pure s-wave collisions, the scattering cross section (2.10) for distinguishable particles is given by

$$\sigma_0(k) = \frac{4\pi}{k^2} \sin^2 \delta_0(k) \,. \tag{2.22}$$

For low energies (relative wave vector $k \to 0$), the scattering phase shift scales as $\delta_\ell \propto k^{2\ell+1}$ [48, 49], resulting in an s-wave phase shift proportional to k. Hence the low energy limit for the scattering cross section is k-independent and can be written as

$$\sigma_0 = 4\pi a^2 \qquad \text{with} \qquad a = -\lim_{k\to 0} \frac{\tan \delta_0(k)}{k} \,. \tag{2.23}$$

The parameter a is hereby defined as the *(s-wave) scattering length*. Its physical meaning is related to the zero crossing of the scattered radial wave function $u_{k,0}(r)$ (see definition in Eq. 2.5), which has the form $u_{k,0}(r) \propto \sin(kr + \delta_0(k))$ outside the interaction region of $V(r)$. For $kr \ll 1$, $u_{k,0}(r)$ has the form of a straight line:

$$u_{k,0}(r) \propto kr \cos \delta_0(k) + \sin \delta_0(k) \,. \tag{2.24}$$

This line crosses the axis of abscissa at

$$r_0 = -\frac{\tan \delta_0(k)}{k} \,. \tag{2.25}$$

Hence the scattering length a corresponds to the zero crossing of the (asymptotic) radial wave function for $k \to 0$. In this description, the scattering potential $V(r)$ simply leads to a phase shift of the (asymptotic) wave function in the radial direction. A pure repulsive potential always results in a positive scattering length, as the probability distribution is reduced within the potential region. The situation for an attractive potential with increasing potential depth is discussed on the basis of Fig. 2.3: A weak attractive potential without any bound state shifts the radial wave function in the negative direction, leading to a negative scattering length (a). For the case, that the potential supports a bound state, which coincides with the dissociation limit, the horizontal asymptote of $u_{k,0}(r)$ leads to a diverging scattering length (b). The radial wave function is "bent" stronger for deeper potentials, resulting in positive values for a (c). Despite the attractive interatomic potential, the process of s-wave scattering can be seen as an effective repulsion of the particles. Finally, a further increase of the potential depth may also result in a vanishing scattering length (d).

Generally, the scattering length is of great importance in the physics of ultracold gases, as it describes the elastic interaction between atoms an thus determines their collective behavior in a simple and intuitive way. Its sign and magnitude defines the characteristic properties of degenerate quantum gases [62]. Furthermore, for certain atomic species, (almost) arbitrary values of the scattering length for trapped atoms can be adjusted using magnetically tunable Feshbach resonances, which provides new possibilities in ultracold physics [63].

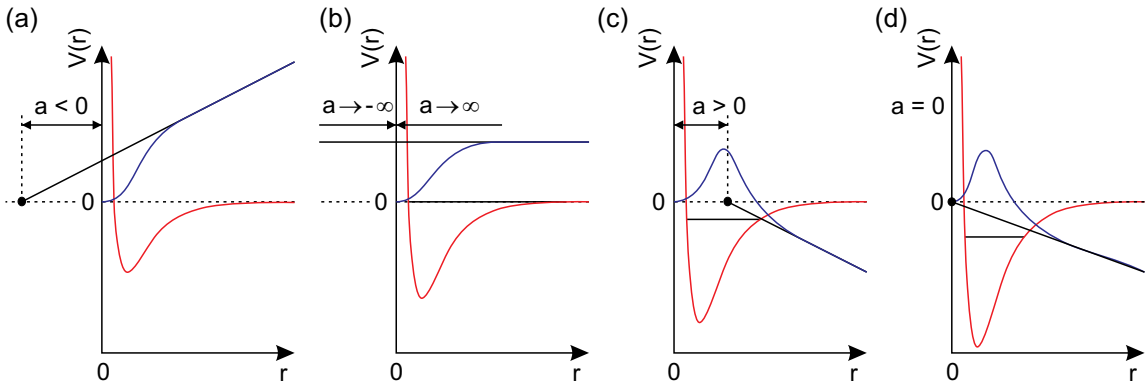

Figure 2.3: *Qualitative characteristics of the scattering length for an attractive scattering potential in relation to the zero crossing of the asymptotic radial wave function: (a) If the potential does not support a bound state, the scattering length is negative. (b) It diverges for the case, that a bound state coincides with the dissociation limit. (c) Deeper potentials result in stronger "bending" of the wave function $u_{k,0}(r)$, which is represented by the blue line, leading to positive- or (d) zero scattering length. Adapted from [61].*

2.2 Scattering by a square well potential

The example of scattering by a square well potential allows deeper insight in potential scattering, especially at low collision energies. This problem can be solved analytically for the different scattering parameters and illustrates many characteristic properties of scattering by attractive potentials at low energies.

2.2.1 Solution for scattering phases $\delta_\ell(k)$

The square well potential is defined by

$$V(r) = \begin{cases} -V_0 & \text{for } r < R_0 \text{ and} \\ 0 & \text{for } r \geq R_0\,, \end{cases} \tag{2.26}$$

where R_0 defines the range of $V(r)$. The solution of this problem can be found in various quantum mechanics textbooks, a very detailed approach is presented in [52]. The square well can support N_b bound states, where N_b is given by

$$N_b = \left[\frac{1}{\pi}\sqrt{\frac{2m_r V_0 R_0^2}{\hbar^2}} - \frac{1}{2}\right]\,. \tag{2.27}$$

The symbol $[x]$ represents the next integer greater than or equal to x. Hence, the potential depth has to be at least

$$V_{\min} = \frac{\pi^2\hbar^2}{8m_r R_0^2} \tag{2.28}$$

in order to support one bound state. Scattering by this potential is possible only for particles with energy $E > 0$. The stationary solution of the free particle problem ($V(r) =$

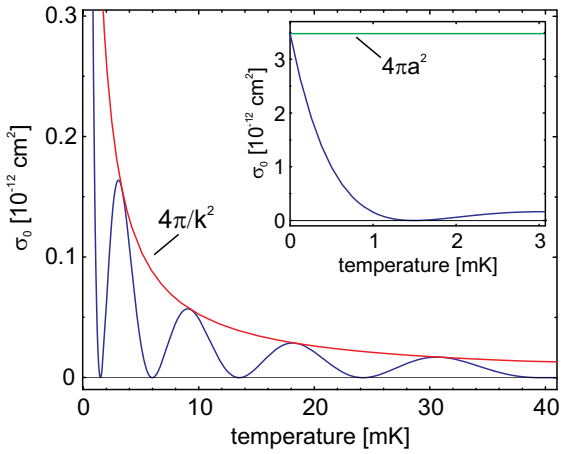

Figure 2.4: *Calculated energy dependence of the s-wave scattering cross section σ_0 based on a square well potential with $R_0 = 100\ a_0$ and 100 bound states. σ_0 oscillates between 0 and the unitarity limit $4\pi(\ell+1)/k^2$. At low energies (see inset), the scattering cross section reaches the limit $4\pi a^2$.*

0) obtained from the Schrödinger equation (Eq. 2.6) is given by a linear combination of spherical Bessel $j_\ell(kR_0)$ and von Neumann functions $n_\ell(kR_0)$. Within the potential ($r < R_0$), the only regular solution is the spherical Bessel function. At the distance $r = R_0$, boundary conditions for the inside- and outside wave functions have to be met. The asymptotic ($r \to \infty$) phase shift between the unperturbed and the scattered solution is a direct consequence of this boundary condition [52]:

$$\delta_\ell(k) = \arctan\left(\frac{kj'_\ell(kR_0)j_\ell(k_0R_0) - k_0 j'_\ell(k_0R_0)j_\ell(kR_0)}{kn'_\ell(kR_0)j_\ell(k_0R_0) - k_0 j'_\ell(k_0R_0)n_\ell(kR_0}\right) . \tag{2.29}$$

Here, $k = \sqrt{2m_rE/\hbar^2}$ is the relative wave vector outside the potential ($r \geq R_0$), $k_0 = \sqrt{2m_r(E+V_0)/\hbar^2}$ is the wave vector for $r < R_0$ and the dash $'$ denotes the derivative with respect to the complete argument. The following discussion will be focused on pure s-wave scattering. In this regime, the scattering phase shift given by

$$\delta_0(k) = \arctan\left(\frac{k\tan k_0R_0}{k_0}\right) - kR_0 . \tag{2.30}$$

Figure 2.4 shows the energy dependence of the s-wave scattering cross section calculated according to to Eq. 2.30. The energy E is given in units of temperature T using the following conversion: $k = \sqrt{2m_rE/\hbar^2} = \sqrt{2m_rk_BT/\hbar^2}$. The scattering cross section shows an oscillation between zero and the corresponding unitarity limit $4\pi(\ell+1)/k^2$. This behavior is known as the "Ramsauer-Townsend effect" [50] and can be understood in relation to the scattering phase. Each time the incident relative particle energy is such that an integer multiple of half the wavelength fits inside the potential region, no scattering occurs. In that case, the solutions for the wave with and without potential have an integer phase shift of π and the scattering cross-section vanishes. In between, the phase shift reaches odd multiples of $\pi/2$ which corresponds to unitarity scattering (see Eq. 2.11).

Note that in the temperature regime shown in Fig. 2.4, higher partial waves ($\ell > 0$) significantly contribute to the scattering amplitude. However, as they show a similar temperature dependence as the s-wave, they are excluded from this plot. At low scattering

temperatures, all $\ell > 0$ partial waves tend towards zero with an energy dependence $k^{4\ell}$ (*Wigner threshold law*, [48]). For sufficiently small values of k, only the s-wave remains, reaching the constant limit $4\pi a^2$, where a represents the scattering length.

In the case of scattering by a square well potential, the s-wave scattering length can be derived analytically: using the definition Eq. 2.23 and Eq. 2.30, it is given by

$$a = -\lim_{k\to 0} \frac{\tan\delta_0(k)}{k} \underset{\text{square well}}{=} \left(1 - \frac{\tan k_0 R_0}{k_0 R_0}\right) R_0 \tag{2.31}$$

2.2.2 Zero energy resonances

Keeping in mind that $k_0 = \sqrt{2m_r(E+V_0)/\hbar^2}$, Eq. 2.31 shows that the scattering length periodically diverges depending on the potential depth V_0. The condition for these poles is:

$$\begin{aligned} k_0 R_0 &= (n - \frac{1}{2})\pi \qquad , n \in \mathbb{N} \\ \Rightarrow V_0 &= \frac{\pi^2\hbar^2}{8m_r R_0^2}\,(2n-1)^2 = V_{\min}\,(2n-1)^2 \qquad , n \in \mathbb{N} \end{aligned} \tag{2.32}$$

This relation shows, that the position of the resonance poles coincide with a potential depth which supports exactly n bound states.

Generally, the energies E_b of bound states are obtained by solving the Schrödinger equation (2.6). In the present case of a square well potential, E_b is determined by the following equation [64]:

$$\sqrt{\frac{2m_r|E_b|}{\hbar^2}} = -\sqrt{\frac{2m_r(V_0-|E_b|)}{\hbar^2}}\,\cot\left(\sqrt{\frac{2m_r(V_0-|E_b|)}{\hbar^2}}\right) \tag{2.33}$$

Figure 2.5 shows the scattering lengths and the energetic positions of bound states as a function of the potential depth V_0, calculated according to Eq. 2.31 and Eq. 2.33. The potential depth as well as the binding energies are displayed in units of $V_{\min}$, the scattering length in units of R_0. This plot reconfirms the characteristic behavior of a, which has been discussed in terms of the zero crossing of the asymptotic radial wave function in Sec. 2.1.4: If no bound state is supported by the potential ($V_0 < V_{\min}$), the scattering length is negative. Just before the condition (2.32) is reached, a is large and negative and the potential is said to have a *virtual state* close to the dissociation energy. The scattering length has a pole with a change in sign as a new bound state enters the square well. As the potential depth is further increased, the scattering length remains positive and finally becomes zero, before the potential supports an additional bound state.

The behavior is repeated for each new bound state, which is related to the more general *Levinson's theorem* [48]. It connects the number of bound states of a given potential with the low energy limit of the scattering phase: $\delta_\ell(k=0) = (n + 1/2\xi_0)\pi$. Here, n is the number of bound s-states and $\xi_0 = 0$ except at a potential depth coinciding with a bound state at $E_b = 0$, where $\xi_0 = 1$.

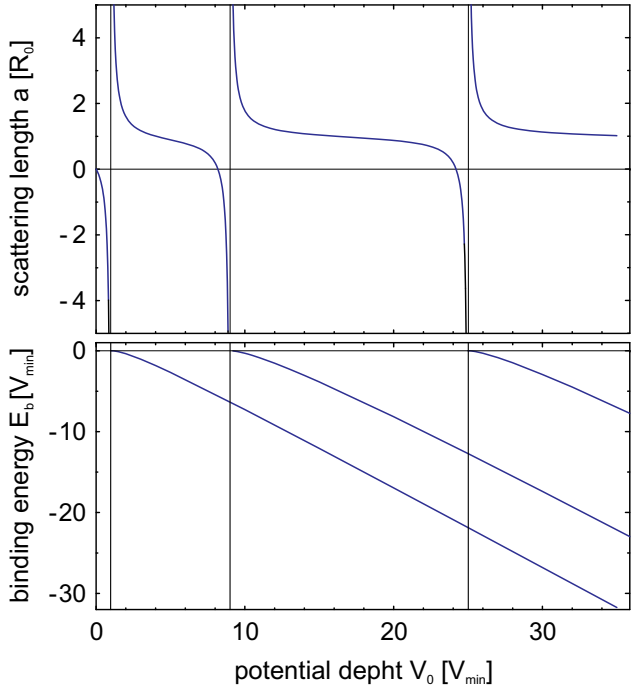

Figure 2.5: *Calculated scattering lengths and binding energies as a function of the potential depth in units of* $V_{\min} = \pi^2\hbar^2/(8m_rR_0^2)$. *Each time a new bound state enters the spectrum, the scattering length diverges.*

The resonances leading to a pole in the s-wave scattering length are known as *zero energy resonances*. Note that despite the diverging scattering length, the scattering cross section is still limited to $4\pi/k^2$ by the unitarity limit.

In the region of large positive scattering lengths, which is related to a weakly bound state, the binding energy E_b of this state can be directly connected to the s-wave scattering length. The two equations 2.33 and 2.31 lead to the relation:

$$E_b \cong \frac{\hbar^2}{2m_r a^2} \tag{2.34}$$

Although this result is explicitly obtained here for the square well potential, it is valid generally [65].

Mass dependent zero energy resonances

In the previous discussion, the condition (2.32) for poles in the scattering length is met by altering the potential depth V_0. The same characteristic behavior of a is also obtained for fixed V_0 and a variation of the reduced mass m_r. This situation is experimentally realized for collisions between one atomic species with different isotope of another species.

Figure 2.6 shows calculated scattering length using a square well potential and the species ^{87}Rb and ^{x}Yb with a varied Yb isotope mass x. In this model, the potential depth is chosen to support 6 bound states for ^{87}Rb-^{174}Yb with the last bound state close to zero resulting

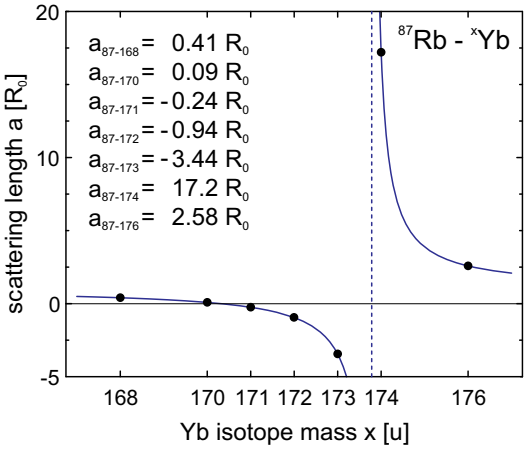

Figure 2.6: *Calculated mass dependence of the s-wave scattering length based on the system ^{87}Rb-^{x}Yb and a square well potential with 6 bound states for ^{87}Rb-^{174}Yb. Depending on the Yb isotope mass x, the interspecies scattering length varies over an arbitrary range of values.*

in a large scattering length a_{87-174} for this combination. In the presence of a zero energy resonance, the interspecies scattering length $a_{87-\mathrm{x}}$ can take on arbitrary values depending on the Yb isotope mass x. Of course, a continuous mass scaling is not possible in this system due to the discrete mass numbers of Yb isotopes (indicated by the black dots in Fig. 2.6).

Note that this basic square well potential calculation only qualitatively illustrates the characteristic relation between a_{YbRb} and the relative mass m_r. The parameters of this model potential do not represent the "real" system (e.g. the real number of bound states $n_b \gg 6$, see Chap. 9). They are chosen to give results qualitatively matching the observations on Rb-Yb interaction described in this thesis. Chap. 9 discusses experimental results presented here with respect to more sophisticated calculations based on realistic Yb-Rb ground state molecular potentials.

2.3 Temperature dependence at low energies

In the previous general approach, presented in Sec. 2.1.4, the s-wave scattering cross section

$$\sigma_0(k) = \frac{4\pi}{k^2} \sin^2 \delta_0(k) \tag{2.35}$$

is given only in the limit $k \to 0$:

$$\sigma_0 = 4\pi a^2 \tag{2.36}$$

$$\text{with} \qquad a = -\lim_{k\to 0} \frac{\tan \delta_0(k)}{k} \,. \tag{2.37}$$

In the interesting regime of low but non-zero energies, the general temperature dependence of the s-wave scattering cross-section can be approximated, which is discussed in the following.

In order to abide to the definition of the scattering length (2.37), which implies the limit $k \to 0$, we define a new parameter, the energy dependent scattering length a_E according

to

$$a_E(k) = -\frac{\tan\delta_0(k)}{k} \qquad \Leftrightarrow \qquad a = \lim_{k\to 0} a_e(k)\,. \tag{2.38}$$

Constant scattering length

Equation 2.36 represents a zero-order approximation of the scattering cross section for $k \to 0$. Using the basic assumption of an energy independent scattering length $a_E(k) = a$ as a first approach, the scattering cross section (2.35) becomes k-dependent:

$$\sigma_0^{(1)}(k) = \frac{4\pi a^2}{k^2a^2 + 1} \tag{2.39}$$

Effective range expansion

A more sophisticated approximation for the temperature dependence is based on the effective range expansion of the scattering amplitude [48, 50]. Starting point is the scattering amplitude in the form of Eq. 2.13. It can be shown that $g_0(k) = k\cot\delta_0(k)$ is analytical over a wide range of collision energies provided the potential $V(r)$ vanishes faster than $\propto 1/r^5$ [51]. Hence, for small collision energies $g_0(k)$ can be expanded in even powers of k:

$$g_0(k) = -\frac{1}{a_E(k)} = k\cot\delta_0(k) \approx c_0 + c_1k^2 + \cdots\,. \tag{2.40}$$

Here, the first parameter can be identified as $c_0 = -1/a$ (see the definition of the scattering length in Eq. 2.37) and $c_1 \equiv 1/2r_{\text{eff}}$ includes the *effective range* r_{eff}:

$$\frac{1}{a_E(k)} \approx -\frac{1}{a} + \frac{1}{2}r_{\text{eff}}k^2 + \cdots\,. \tag{2.41}$$

Including the effective range expansion in the scattering cross section for low energies, one obtains:

$$\sigma_0^{(2)}(k) = \frac{4\pi a^2}{k^2a^2 + (\frac{1}{2}k^2r_{\text{eff}}a - 1)^2} \tag{2.42}$$

In a basic picture, the effective range expansion term is a second order correction to the scattering phase shift, reducing or enlarging the "effective width" of the potential.

The effective range parameter r_{eff} generally depends on the specific potential. For the case of a square well potential, $r_{\text{eff}} = R_0 - R_0^3/(3a^2)$ can be found analytically. In contrast, the van der Waals interaction potential $-C_6/r^6$ requires a more sophisticated approach. Both a semi-classical approximation [65] and, independently, a quantum-defect theory approach [66] obtain the following relation for r_{eff} to the C_6 coefficient and the scattering length a:

$$r_{\text{eff}} = \frac{\sqrt{2}\beta_6}{3}\left[\frac{\Gamma\left(\frac{1}{4}\right)}{\Gamma\left(\frac{3}{4}\right)} - \frac{2\sqrt{2}\beta_6}{a} + \frac{\Gamma\left(\frac{3}{4}\right)}{\Gamma\left(\frac{1}{4}\right)}\frac{4\beta_6^2}{a^2}\right]\,. \tag{2.43}$$

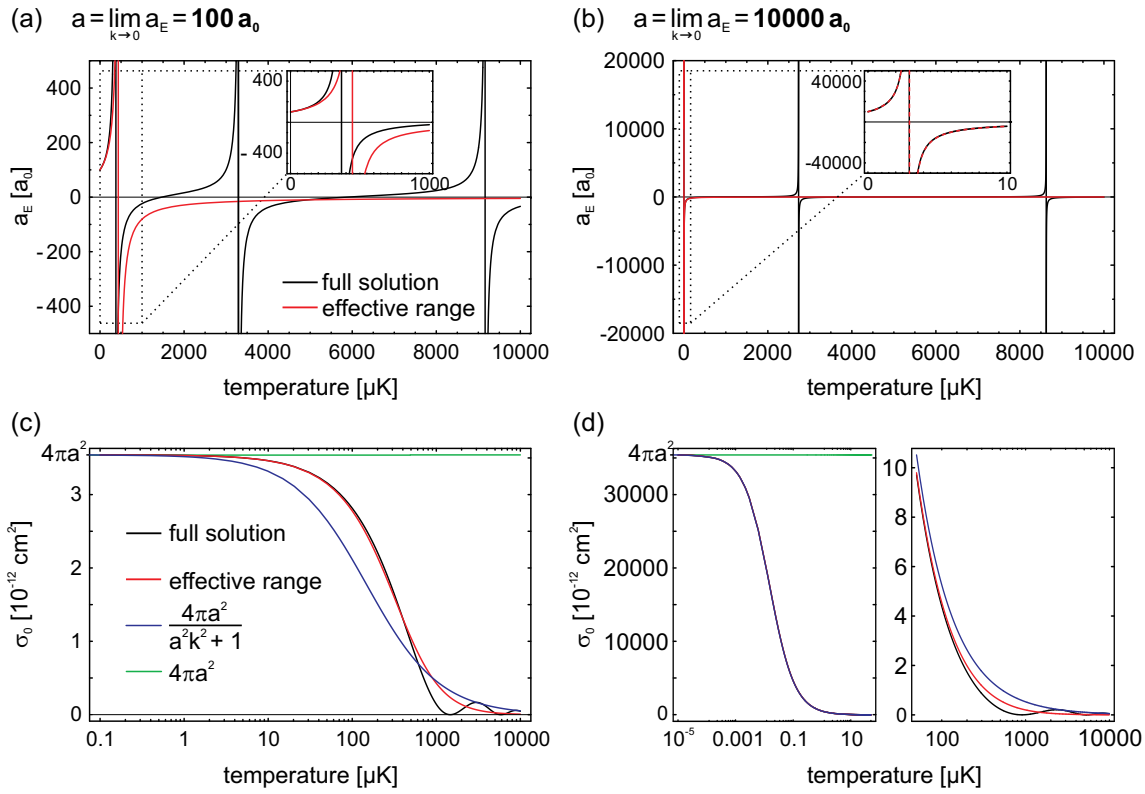

Figure 2.7: *Calculated temperature dependent scattering lengths a_E (a,b) and s-wave cross sections σ_0 (c,d) for a square well potential with $R_0 = 100\,\mathrm{a_0}$ and 100 bound states. V_0 is chosen to yield zero energy scattering length $a \approx 100\,\mathrm{a_0}$ for (a, c) and $a \approx 10000\,\mathrm{a_0}$ for (b, d). See text for details.*

In this representation, $\beta_6 = (2m_r C_6/\hbar^2)^{1/4}$, $\Gamma(x)$ is the Gamma function and r_{eff}, a, β_6 and C_6 are given in atomic unit. Note that for $a \to 0$, the effective range parameter given by (2.43) diverges, which indicates that this approximation is limited to large values of a. In the experimentally typical regime of $50\,\mathrm{a_0} < a < \infty$, and for a wide parameter range of C_6 and m_r, Eq. 2.43 yields effective range parameters $r_{\mathrm{eff}} \approx 100 \ldots 250\,\mathrm{a_0}$.

Square well potential

The example of scattering by a square well potential allows the discussion of different approximations for the low energy scattering parameters as described above: Figure 2.7 (a, b) compares the calculated temperature dependencies of $a_E(k)$ for the square well potential ($R_0 = 100\,\mathrm{a_0}$) with the effective range solution. Sub-figures (c, d) show different orders of approximation (Eq. 2.36, 2.39, 2.42) and the exact solution (2.30) for the s-wave scattering cross section. These results are based on a model potential with a potential depth V_0 chosen to set the last bound state energetically far from (a, c) or close to (b, d) the dissociation energy. The latter case simulates the situation close to a zero energy resonance. As a result, the zero energy scattering length $a = \lim_{k\to 0} a_e(k) \approx 100\,\mathrm{a_0}$ in the

case (a, c) and $a \approx 10000\,a_0$ for (b, d).

These calculations reconfirm, that the effective range approximation simulates the low energy part of $a_E(k)$ very well for a zero energy resonance (large a, Fig. 2.7 (b)), while it fails for smaller a (a). In terms of the scattering cross section, none of the different approximations reproduces the Ramsauer-Townsend oscillations occurring at higher temperatures (see Chap 2.2.1). At lower temperatures and small a, the inclusion of the effective range provides a much better agreement than the first order approximation $\sigma_0^{(1)}(k)$ from Eq. 2.39. For large a, both approximations $\sigma_0^{(1)}(k)$ and $\sigma_0^{(2)}(k)$ eventually reach the unitarity limit $4\pi/k^2$.

2.4 Pseudo potential and mean field theory

The previous sections already highlighted the importance of the scattering length, which characterizes the interaction between two atoms at low energies. It also plays a key role in the statistical physics description of cold gases, which is discussed in the following:

The Fermi pseudo potential The aim of the method of pseudo potentials is to replace the "real" interatomic potential responsible for low-energy collisions by an effective potential, which correctly reproduces the scattering properties. The simplest interaction between two particles is the contact interaction given by the potential

$$V(\vec{r}) = g\,\delta(\vec{r})\,. \tag{2.44}$$

Here, $\delta(\vec{r})$ represents the 3-dimensional delta-function depending on the relative position vector $\vec{r}$. A formally unambiguous way to describe the contact interaction in scattering theory is to use the so called *Fermi pseudo-potential* [67]

$$V(\vec{r})\Psi(\vec{r}) = g\,\delta(\vec{r})\frac{\partial}{\partial r}(r\Psi(\vec{r}))\,, \tag{2.45}$$

which leads to the following cases depending on the form of $\Psi(\vec{r})$:

$$V(\vec{r})\Psi(\vec{r}) = \begin{cases} g\,\Psi(0)\delta(\vec{r}) & \text{if } \Psi(\vec{r}) \text{ is regular in } r=0\,, \\ g\left(\frac{\partial u}{\partial r}\right)_{r=0}\delta(\vec{r}) & \text{if } \Psi(\vec{r}) \text{ is of the form } \Psi(\vec{r}) = \frac{u(\vec{r})}{r}\,. \end{cases} \tag{2.46}$$

The solution of the Schrödinger equation including the pseudo potential (2.45) results in a relation between the pseudo potential and the s-wave scattering length [47]:

$$g = \frac{4\pi\hbar^2 a}{m} \tag{2.47}$$

This result is valid for distinguishable particles with equal mass m. Using the description by the pseudo potential, low energy collisions depend only on the scattering length and not on the detailed interatomic potential. Hence, two interatomic potentials corresponding to the same scattering length lead to the same scattering properties, although they may have completely different microscopic properties, even for the case that one is attractive and the other one repulsive.

Mean field theory Given the case that the gas is in the dilute regime ($n|a|^3 \ll 1$) where n represents the spatial density), and assuming it is cold enough that the limit (2.23) is valid, the two-body description using the pseudo potential can be extended to determine the collective behavior of the gas. In the ultracold, dilute regime, the thermal de Broglie wavelength is on the order of the interparticle separation and much larger than the potential range. Therefore, the atoms "probe" an effective interaction integrated over many particles. This interaction has the form of a contact potential and can be correctly described by the pseudo potential given in Eq. 2.45. The additional potential energy on a given particle created by the presence of all other particles with density n is then simply:

$$U = g\,n = \frac{4\pi\hbar^2 a\,n}{m}\,. \tag{2.48}$$

A detailed derivation of this result based on a refractive index approach can be found in [47].

The mean field concept has proven to be very successful and describes many features of Bose- Einstein condensates (BECs). The particle interaction term (2.44) is simply included in the Schrödinger equation resulting in the well known *Gross-Pitaevskii equation* [68] for Bose- Einstein condensates:

$$\left[-\frac{\hbar^2}{2m_r}\nabla^2 + V_{\text{trap}}(\vec{r}) + 2g|\psi(\vec{r})|^2\right]\psi(\vec{r}) = i\hbar\frac{\partial}{\partial t}\psi(\vec{r}). \tag{2.49}$$

Note that $\psi(\vec{r})$ represents here the BEC wave function. The collective behavior of a BEC described by this equation is governed by the scattering length a: a positive scattering length results in an effective repulsion of the atoms , whereas a negative scattering length leads to attraction and eventually the collapse of the BEC[2].

The treatment of atom-atom interaction by the mean field potential is a simple description of intrinsically complex effects. Hence, its application requires careful consideration, which is pointed out by the following remarks:

- The pseudo potential defined above correctly reproduces the far field scattering phase when it is used to replaces the exact interatomic potential in scattering events in the limit $k \to 0$. It can not be used as a real potential between atoms.
- In contrast to the scattering cross section σ_0, there is no directly correspondent unitarity limit for the mean field pseudo potential: The scattering length $a = \lim_{k\to 0} -\tan\delta_0(k)/k$ can take on values between $\pm\infty$ and directly enters the pseudo potential. However, if the underlying condition ($n|a|^3 \ll 1$) is violated for large values of a, the description by the mean field theory based on a two-body pseudo potential is questionable.
- For low energies, the scattering length can be replaced by the energy dependent form $a_E(k)$, using e.g. the effective range expansion (2.41). Hence the pseudo potential

[2] A BEC with attractive interactions can exist in a trap for a limited particle number and has been observed e.g. with ^{7}Li, which has a negative scattering length [69].

becomes energy dependent [67, 70]:

$$V_E(\vec{r}, k) = \frac{4\pi\hbar^2 a_E(k)}{m}\delta(\vec{r})\frac{\partial}{\partial r}r\,. \tag{2.50}$$

Note that in this description k represents the relative wave vector long before and long after the scattering event. The change in k during the interaction process, which (in a simple classical picture) results from the atoms moving in the "real" interatomic potentials is not relevant in this approach.

2.5 Feshbach resonances

Resonance enhancement of collision cross sections depends on the existence of bound- or metastable states. While a weakly bound molecular state is responsible for zero energy resonances (see Sec. 2.2.2), the metastable state may be described in terms of tunneling across a potential energy barrier (shape resonances, see Sec. 2.1.4) or coupling a bound level of a subsystem to its environment. The latter effect is known as *Feshbach resonances* and its basic physical properties can be understood in the following way: Figure 2.8 illustrates the two channel situation including a molecular potential $V_{bg}(r)$, which represents an energetically open channel in a collision process with small collision energy E. In addition, the potential $V_c(r)$ representing the closed channel[3] is required, as it can support bound molecular states near the energy threshold of the open channel. A Feshbach resonance occurs when the bound molecular state in the closed channel comes energetically into resonance with the scattering state in the open channel.

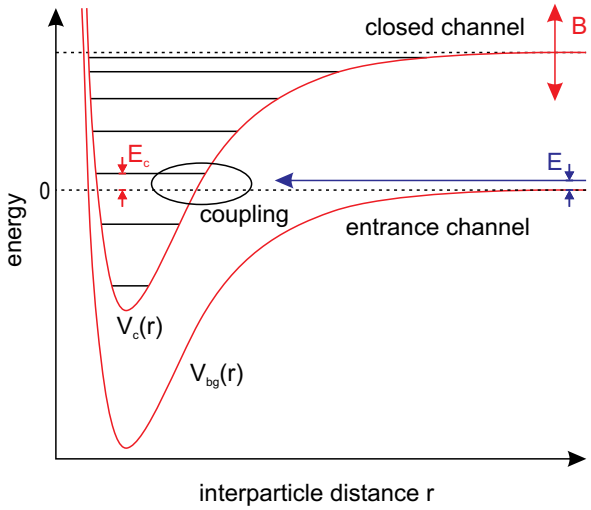

Figure 2.8: *Basic mechanism of Feshbach resonances: The effect occurs when two atoms colliding at energy E in the entrance channel V_{bg} resonantly couple to a molecular bound state with energy E_c supported by the closed channel. Magnetic shifting of the molecular potentials with respect to each other allows the adjustment of the coupling.*

For the case that the magnetic moment of the involved channels are different, their energy difference can be controlled via a magnetic field. This leads to a *magnetically tuned*

[3] A channel is closed, if the total (kinetic and internal) energy of the colliding particles is lower than the internal energy for the collision on the closed channel.

Feshbach resonance. In this case, the scattering length $a_{\mathrm{Fb}}(B)$ depends on the magnetic field B according to [71]

$$a_{\mathrm{Fb}}(B) = a_{bg}\left(1 - \frac{\Delta}{B - B0}\right) . \tag{2.51}$$

Here a_{bg} is the background scattering length associated with $R_{bg}(r)$, which gives the off-resonant value. The parameter B_0 denotes the resonance position, where the scattering length diverges ($a \to \pm\infty$), and the parameter Δ is the resonance width. Experimentally accessible magnetic fields reach up to $B_0 \approx 1000\mathrm{G}$ and the resonance width Δ, which strongly depend on the coupling strength between the scattering and resonance state, is typically in the range of $\Delta = 0.01 \ldots 10\,\mathrm{G}$ [72].

Typical experimental methods used to detected Feshbach resonances include inelastic loss spectroscopy [73], which makes use of the strong 3-body recombination rate dependence on the scattering length (see Sec. 2.6). Furthermore, the change of elastic collision properties (e.g. the thermalization rate [74]) or radiatively induced trap loss [75] around a Feshbach resonance can be observed. All methods described here require temperatures in the regime of a few μK in order to observe a clear resonant structure.

Tuning the scattering length close to a Feshbach resonance enables many fascinating experiments with ultra-cold atoms [73]. More details on recent developments in this field can be found in the review article [72].

2.6 Inelastic collisions

Besides elastic scattering, which is discussed above, inelastic collisions determine the properties of ultracold gases significantly. In inelastic collision processes, internal energy of the scattering particles is converted to kinetic energy. This additional energy is usually sufficient for the colliding atoms to leave the trapping potential in ultracold atom experiments. The probability of a scattering event in a gaseous cloud of atoms apparently depends on the density. In the density regime of $n = 10^{12} \ldots 10^{15}$ typically achieved in ultracold atomic samples, three inelastic processes have to be considered:

Background gas collisions Each collision process of cooled and trapped atoms with atoms from the "hot" background gas ($T_{\mathrm{bg}} \approx 300\,\mathrm{K}$) directly leads to atom loss from the trapping potential. The background-limited lifetime τ_{bg} at a given pressure p [mbar] can be approximated by the relation $\tau_{\mathrm{bg}} \approx 1.3 \times 10^{-8}/p$ [76]. Hence, vacuum conditions with $p < 10^{-10}\,\mathrm{mbar}$ are required to achieve lifetimes of several minutes.

Two-body spin- and dipolar relaxation In magnetic potentials, trapped atoms are not residing in the energetically lowest state (see Sec. 3.2.1). Hence, collisions between atoms can be accompanied by a transition into energetically more favorable levels: One or both atoms flip their spin and the Zeeman-energy is converted into kinetic energy. Depending on the coupling mechanism, this inelastic process is either called *spin relaxation* [77] (collision between atoms in different m_F sub levels) or *dipolar relaxation* [78] (higher order coupling

between spin and angular momentum during the collision). Both processes may result in loss of atoms from a magnetic trap (spin-flip to an untrapped state) and heating of the atomic sample. The rate for spin relaxation and dipolar relaxation collisions depends on the density n with event rates in alkali atoms typically on the order of $\gamma_{\mathrm{sr}} \approx n \cdot 10^{-11}\,\mathrm{cm^3/s}$, and $\gamma_{\mathrm{dr}} \approx n \cdot 10^{-15}\,\mathrm{cm^3/s}$ respectively.

If the atomic sample is spin polarized (all atoms residing in the same spin state), spin relaxation is suppressed and the significantly less frequently occurring dipolar relaxation remains. In optical dipole potentials (see Sec. 3.2.3), atoms can be trapped in their lowest hyperfine level, which completely prevents inelastic tws-body loss.

In the case of Yb in the $6^1\mathrm{S}_0$ ground state, spin- and dipolar relaxation processes are intrinsically suppressed as no electronic spin is present.

Three-body recombination The event of three trapped atoms being close enough to interact, offers another possibility for an inelastic process: Two atoms form a weakly bound molecule and the third takes up the excess binding energy of the molecule. The probability for a three-body event scales with the square of the density and the rate constants for this process depend strongly on the details of the interaction potential. However, for the recombination to a weakly bound s level, a universal relation between the event rate constant α_{rec} and the s-wave scattering length a is given by

$$\alpha_{\mathrm{rec}} \approx C\,\frac{\hbar a^4}{m}\,. \tag{2.52}$$

Here, C is a dimensionless factor, which is predicted to be in the range between 1 and ≈70 [79, 80]. For typical experimental values of the scattering length $a \approx 100\,\mathrm{a_0}$, three-body recombination plays a role only for very dense samples ($n = 10^{14} \ldots 10^{15}$), since the event rates are typically very small ($\gamma_{\mathrm{rec}} = n^2\alpha_{\mathrm{rec}} \approx n^2 \cdot 10^{-29}\,\mathrm{cm^6/s}$). The situation however drastically changes for larger scattering length: Close to Feshbach resonances or zero energy resonances (see Sec. 2.5 and 2.2.2), three-body recombination is the dominating loss mechanism.

3

Preparation of ultracold atomic samples

This chapter briefly describes the relevant methods of cooling gaseous atoms down to temperatures in the nK regime and trapping them in optical and magnetic potentials. It includes the basic principles of laser cooling and their application in Zeeman slowers and magneto optical traps (MOTs). These methods are used as a first cooling stage in the present experiment, where temperatures in the several $10 \ldots 100\,\mu K$*-range are reached. Furthermore, this section discusses conservative traps that are created by magnetic- and optical dipole potentials. These potentials are used in the main experiments presented in the scope of this work. For a quantitative analysis of the observed effects, it is crucial to have detailed knowledge and control of the trapping potentials which are theoretically described in this section.*

The following approach does not make the claim to be complete, it rather focuses on the basic methods used in the present experiments. For an extensive derivation of this theory and a more detailed description of its applications, see e.g. [76, 81].

3.1 Principles of laser cooling

The basic idea of laser cooling is that photon scattering transfers momentumd in $\hbar\vec{k}$ increments to atoms. The wave vector $\vec{k}$ with magnitude $|\vec{k}| = k = {}^{2\pi}/_{\lambda}$ depends on the wavelength λ of the involved light field. If enough photons are scattered, the atomic velocity can be changed significantly as a result of the scattering force F that depends on the scattering rate Γ [76]:

$$\vec{F} = \hbar\vec{k}\,\Gamma \qquad \text{with} \qquad \Gamma = \frac{\gamma}{2}\,\frac{s_0}{1 + s_0 + \left({}^{2\delta}/_{\gamma}\right)^2}\,. \tag{3.1}$$

Here, $\gamma = {}^{1}/_{\tau}$ is the natural line width of the excited atomic state, determined by its lifetime τ. The saturation parameter $s_0 = I/I_{\text{sat}}$ is connected to the incident light intensity I and the saturation intensity $I_{\text{sat}} = (\pi hc\gamma)/(3\lambda^3)$. The scattering rate Γ also depends on the detuning

$$\delta = \delta_0 - \vec{k}\cdot\vec{v} - \frac{\mu' B}{\hbar} = \omega - \omega_0 - \vec{k}\cdot\vec{v} - \frac{\mu' B}{\hbar}\,, \tag{3.2}$$

which generally consists of three contributions: $\delta_0 = \omega - \omega_0$ is the frequency difference between the laser light frequency ω with respect to the atomic resonance frequency ω_0.

For atoms in motion, the Doppler shift $-\vec{k}\cdot\vec{v}$ has to be taken into account, whereas the term $-\mu' B/\hbar$ considers the Zeeman shift in the presence of a magnetic field with magnitude B. The Zeeman shift of the relevant atomic transition depends on the effective magnetic moment $\mu' = (g_e m_e - g_g m_g)\mu_B$ consisting of the Landé g-factors g_i and the magnetic quantum numbers m_i of the involved ground- and excited atomic state (μ_0 is the Bohr magneton).

The scattering rate Γ and hence the force on the atoms saturate for high intensities $I \gg I_{sat}$ and zero detuning $\delta = 0$ at maximum values of $\Gamma_{max} = \gamma/2$ and $\vec{F}_{max} = \hbar\vec{k}\,\gamma/2$. The model which is sketched here assumes an ideal two-level system with a closed cycling transition that allows for continuously repeated absorption- and spontaneous emission cycles. In the experiment, the complex level structure of atoms often requires additional repumper lasers, that prevent atoms from leaving the cycling transition (see Sec. 4.2.1 and Sec. 5.3.1).

3.1.1 Zeeman slowers

Historically, the first steps in the field of laser cooling involved the one-dimensional deceleration of an atomic beam using the scattering force [82, 83, 17]. In this configuration, a laser beam is directed opposite to an atomic beam, which results in a maximum deceleration

$$|a_{max}| = \frac{F_{max}}{m} = \frac{\hbar k}{m}\frac{\gamma}{2} \tag{3.3}$$

of atoms with mass m. In order to achieve maximum deceleration, the used light frequency has to be kept on resonance with the atomic transition during the slowing process at all times. As can be seen from Eq. 3.2, the velocity-dependent Doppler-shift has to be accounted for.

The basic idea of a Zeeman-slower is, to use a spatially varying magnetic field to compensate the Doppler-shift while atoms are being slowed. For atoms moving in the z-direction, this condition is given by

$$\delta = \omega - \omega_0 - \vec{k}\cdot\vec{v} - \frac{\mu' B}{\hbar} = \omega - \omega_0 + kv(z) - \frac{\mu' B(z)}{\hbar} \stackrel{!}{=} 0\,. \tag{3.4}$$

At a given initial atom velocity v_0, the deceleration with magnitude $|a_{max}|$ leads to a trajectory according to $v(z) = \sqrt{v_0^2 - 2|a_{max}|z}$. Under this condition, the required magnetic field has the form

$$B(z) = -\frac{\hbar}{\mu'}\left(\omega_0 - \omega - kv(z)\right) = \frac{\hbar}{\mu'}\left(\delta_0 + k\sqrt{v_0^2 - 2a_0 z}\right)\,. \tag{3.5}$$

This solution describes a Zeeman slower with an increasing field geometry, as it is used in our experimental setup. In this configuration, the laser is operated at a detuning $\delta_0 = -kv_0$, in order to be on resonance with fast atoms of velocity v_0 entering the Zeeman slower at zero magnetic field. In order to address only a transition between defined Zeeman substates, polarized light is used. In the increasing field geometry, the effective magnetic moment μ' of the slowing transition has to be negative. This leads to a decrease of the

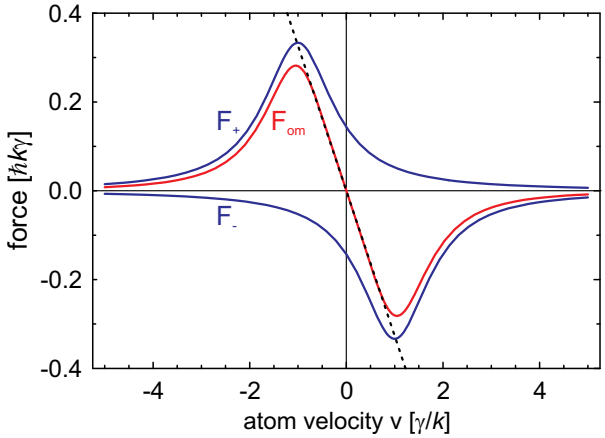

Figure 3.1: *Velocity dependence of the optical damping forces for one-dimensional optical molasses. The blue lines show the individual forces from each beam, while the red line is their sum. The dashed line indicates the linear behavior that results in a pure damping force over a restricted velocity range.*

transition frequency along the slower that compensates for the decreasing Doppler shift of the decelerated atoms.

Experimentally, atomic properties as well as parameters like the maximum initial velocity v_0 and minimum final velocity v_{end} determine the required magnetic field $B(z)$, the initial detuning δ_0 and the length L of a Zeeman slower. The typical atom deceleration is in the range of $|a| = 10^4 \ldots 10^5\,\text{m/s}^2$. Atoms are slowed from initial velocities of $v_0 = 100 \ldots 300\,\text{m/s}$ to final values of $v_{\text{end}} = 5 \ldots 30\,\text{m/s}$ over a distance of $L = 30 \ldots 100\,\text{cm}$. Details on the parameters of the Zeeman slowers used in the present experiment can be found in [84, 8, 9].

3.1.2 Optical molasses and magneto optical trap (MOT)

With three mutually orthogonal intersecting laser beams a region of space can form an optical molasses of atoms [85]. The essential idea is that in the optical molasses, atoms experience a force proportional to the velocity which can be considered a viscous damping force. Although this force can not actually trap atoms, it can cool them: in a one-dimensional view, the forces from the two counter propagating light beams are added to give the total force $\vec{F}_{\text{om}} = \vec{F}_+ + \vec{F}_-$ with the individual forces

$$\vec{F}_\pm = \hbar\vec{k}_\pm \frac{\gamma}{2} \frac{s_0}{1 + s_0 + \left(\frac{2(\delta_0 \mp kv)}{\gamma}\right)^2}\,. \tag{3.6}$$

For small velocities, a linear approximation is justified and the total force $\vec{F}_{\text{om}}$ can be written as

$$\vec{F}_{\text{om}} \approx \frac{8\hbar k^2 \delta_0 \cdot s_0 \cdot \vec{v}}{\gamma\left(1 + s_0 + (2\delta_0/\gamma)^2\right)^2} = -\beta\vec{v}\,. \tag{3.7}$$

For the case of red detuned laser beams ($\delta_0 < 0$), this force points in the opposite direction of the atomic velocity and therefore viscously damps the atomic motion. This process is referred to as *Doppler cooling* of atoms. Figure 3.1 shows the velocity dependence of the individual forces (blue) and the resulting force (red) for $s_0 = 2$ and a detuning $\delta_0 = -\gamma$.

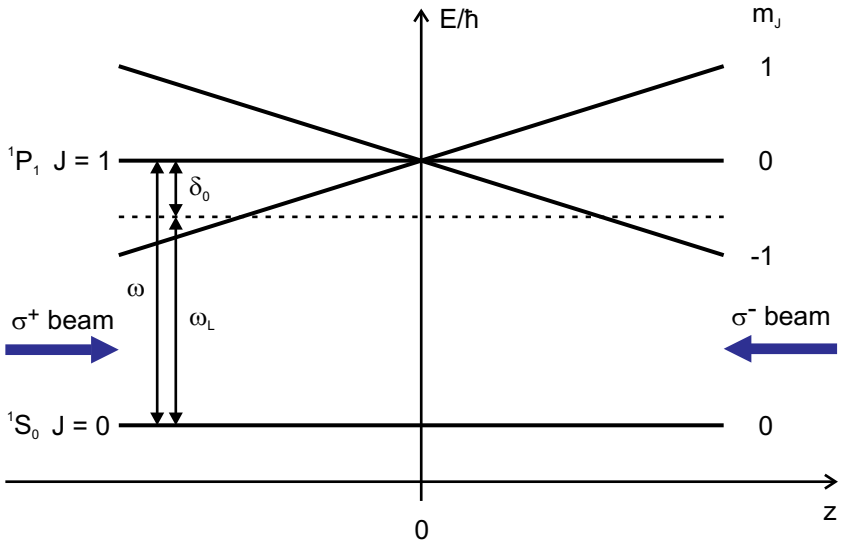

Figure 3.2: *Schematic arrangement for an Yb MOT in the one-dimensional case. Adapted from [9].*

The dashed line shows how this force corresponds to a pure damping force over a restricted velocity range. around zero. Doppler cooling is limited by a heating process resulting from the randomness of momentum steps the atoms undergo with each emission or absorption. The competition between this heating and the damping force leads to an equilibrium temperature, called *Doppler temperature* or *Doppler cooling limit* [76]:

$$T_{\mathrm{D}} = \frac{\hbar\gamma}{2k_{\mathrm{B}}}\,. \tag{3.8}$$

This temperature limit depends only on the transition line width and is typically on the order of $\approx 100\,\mu$K. Further details and a more extensive approach on the theory of optical molasses can be found in [86, 87, 88]

It is a small step from optical molasses to the magneto-optic trap (MOT). With the addition of a magnetic quadrupole field, typically applied using a pair of anti-Helmholtz coils, an optical molasses can be cleverly arranged so that the net photon scattering always adds up to drive the atoms into the trapping region. Figure 3.2 describes the basic principle of a one dimensional MOT in the case of Yb. Here, the MOT transition uses the ground state $|^1S_0, J = 0\rangle$ and the excited state $|^1P_1, J = 1\rangle$. In the presence of a linear magnetic field $B(z) = B_0 z$, the latter splits into three Zeeman sub-states with magnetic quantum number $m_J = -1, 0, 1$. Circularly polarized light with opposite orientation is used in the counter propagating laser beams to address defined magnetic sub-states. Additionally, the MOT beams are red detuned ($\delta_0 < 0$) with respect to the atomic transition at zero magnetic field (represented by the dashed line in Fig. 3.2). Because of the Zeeman shift, the excited state with $m_J = 1$ ($m_J = -1$) is shifted up (down) for $B > 0$. At the position $z > 0$ ($z < 0$) in Fig. 3.2, the magnetic field therefore tunes the $\Delta m = -1$ ($\Delta m = +1$) transition closer to resonance and the $\Delta m = +1$ ($\Delta m = -1$) transition further out of

resonance. Hence, at a position $z > 0$ ($z < 0$) more light is scattered from the σ^- beam (σ^+ beam), driving the atoms towards the trap center. In this configuration, the scattering force results in $\vec{F}_{\mathrm{MOT}} = \vec{F}_+ + \vec{F}_-$ with the individual contributions

$$\vec{F}_\pm = \hbar\vec{k}_\pm \frac{\gamma}{2} \frac{s_0}{1 + s_0 + \left(\frac{2(\delta_0 \mp kv \pm (\mu' B_0/\hbar)z)}{\gamma}\right)^2}. \tag{3.9}$$

Analogous to Eq. 3.7, a linear approximation for small velocities and position displacements ($|\vec{k}\vec{v}|$, $|(\mu' B_0/\hbar)z| \ll |\delta_0|$) is applied, which gives the total force [76]

$$\begin{aligned} \vec{F}_{\mathrm{MOT}} &\approx \frac{8\hbar k^2 \delta_0 \cdot s_0 \cdot \vec{v}}{\gamma\left(1 + s_0 + (2\delta_0/\gamma)^2\right)^2} + \frac{\mu' B_0}{\hbar} \frac{8\hbar k \delta_0 \cdot s_0 \cdot \vec{r}}{\gamma\left(1 + s_0 + (2\delta_0/\gamma)^2\right)^2} \\ &= -\beta\vec{v} - \kappa\vec{r}. \end{aligned} \tag{3.10}$$

In addition to the velocity dependent damping force, a position dependent trapping force is present in the MOT.

The dissipative force $\vec{F}_{\mathrm{MOT}}$ is able to capture all atoms in a MOT that are slower than a maximum capture velocity v_c. Assuming a constant maximum acceleration $a_{max} = \hbar k\gamma/2$ across the MOT diameter $2r_c$, which is defined by the beam radii r_c, v_c is given by[76]:

$$v_c = \sqrt{\frac{2\, r_c \hbar k \gamma}{m}} \tag{3.11}$$

In general, MOTs can be loaded from a background gas of thermal atoms. However, only a tiny fraction of the atoms in a thermal Maxwell Boltzmann velocity distribution feature velocities within the maximum capture range. Therefore, many experiments – including the one presented in the scope of this thesis – use Zeeman slowers to increase the fraction of trappable atoms.

As a result, up to 10^{10} atoms can be trapped in a MOT at peak densities of $10^{11}\mathrm{cm}^{-3}$. For the density distribution, it is important do distinguish between two different regimes [89]: In the limit of small atom numbers (often called *temperature limited regime*), atom interactions can be neglected. In this regime, the atomic spatial and momentum distributions are close to Gaussian and are characterized by the temperature and the trap spring constant κ. On the contrary, in the limit of large atom numbers (*density limited regime*), interactions between atoms play an important role as the reabsorption of scattered atoms (radiation trapping) [90] causes a repulsive force between them. At a certain atomic density, the outward radiation pressure of the fluorescence light balances the confining forces of the trapping laser beams. In this regime, a further increase of the number of trapped atoms leads to larger atoms clouds, but not to higher peak densities.

For the case that the MOT is not operated on a cycling transition, this density limit can be overcome. In the configuration of a so called *dark SPOT MOT* [91], atoms in the trap center are optically pumped into a "dark" hyperfine level that is not addressed by the trapping beams. In this "dark" region, repulsive forces between atoms due to rescattered radiation are suppressed and trap loss due to excited state collisions is reduced. The present

experiment uses such a dark SPOT MOT configuration for ^{87}Rb in order to achieve higher peak densities (see Sec. 4.2.1 and 5.3.1).

The temperature limit in a MOT is the Doppler temperature, which is typically in the regime of $\approx 100\,\mu$K. However, more advanced cooling methods like *polarization gradient cooling* [92, 93] are able to provide lower temperatures, at least for some atomic species. Further details on laser cooling techniques and magneto-optic traps can be found in [94, 89, 95].

3.2 Conservative traps for neutral atoms

Generally, the MOT is a universal tool in cold atom physics. Many experiments can be performed directly in the MOT (e.g. photoassociation spectroscopy as in our previous work [16]) but more often the MOT is used nowadays as a tool for loading conservative type traps. In these traps, limitations in temperature and density due to scattering of near-resonant light are overcome. The following describes two types of conservative type traps, which are used in the present experiment: The (purely) magnetic trap (MT) uses the interaction of neutral atoms with the gradient of a static magnetic field. This interaction can form a trapping potential in the absence of lasers [96, 97]. It relies however on the atom's state-dependent magnetic moment and therefore limits the applicability of magnetic traps to atoms with a paramagnetic ground state. On the contrary, the optical dipole trap (ODT) is based on the electric dipole interaction of atoms with far-detuned light and can be used for any atomic species. Inhomogeneous light fields, realized for example by the focus of a high power laser beam, create the corresponding trapping potential [98]. Atoms trapped in conservative traps can be further cooled to the nK regime by the method of evaporative cooling, which is also described in this section.

3.2.1 Magnetic traps

The energy shift of an atom with magnetic moment $\vec{\mu}$ residing in a spin state $|F, m_F\rangle$ in the presence of a magnetic field $\vec{B}$ is given by:

$$\Delta E = -\vec{\mu}\vec{B} = g_F\, m_F\, \mu_\mathrm{B}\, |\vec{B}|. \tag{3.12}$$

Here, g_F is the Landé g-factor of the state with a total angular momentum quantum number F and m_F is the magnetic quantum number. Atoms are generally trapped in a potential minimum. For atomic states $|F, m_F\rangle$ with $g_F\, m_F > 0$ ($g_F\, m_F < 0$), a potential energy minimum coincides with a magnetic field minimum (maximum). According to this, atoms in the corresponding states are called *low field seeker* (*high field seeker*). Maxwell's equations fundamentally allow only magnetic field minima in free space [99]. Hence, only atoms in low field seeking states ($g_F\, m_F > 0$) are trapped by static magnetic traps. On the contrary, $m_F = 0$ states as well as strong field seeking states ($g_F\, m_F < 0$) are not trapped. In order to suppress atom loss from a MT, uncontrolled transitions between Zeeman sub-states of trapped atoms have to be avoided. The probability of these so called *Majorana-spin-flips* increases for small magnetic fields, where the atoms' quantization axes

is not able to follow the external magnetic field adiabatically [100]. Thus, stable magnetic traps require a magnetic field with nonzero magnitude all across the trapping region.

The magnetic field configuration realized in a *Ioffe-Pritchard-trap* [101] fulfills the requirements stated above. In our experiment, the corresponding magnetic fields are created by coils arranged in a clover-leave-configuration [102]. Details on the experimental implementation can be found in [8, 9]. The magnetic field configuration is characterized by an offset B_0, a radial field gradient B' and an axial field curvature B'' [97]:

$$\vec{B}(\vec{r}) = B_0 \begin{pmatrix} 0 \\ 0 \\ 1 \end{pmatrix} + B' \begin{pmatrix} x \\ -y \\ 0 \end{pmatrix} + \frac{B''}{2} \begin{pmatrix} -xz \\ -yz \\ z^2 - \frac{1}{2}(x^2+y^2) \end{pmatrix} . \tag{3.13}$$

This results in the following trapping potential:

$$U_{\mathrm{MT}}(\vec{r}) = \mu |B(\vec{r})| = \tag{3.14}$$
$$\mu \sqrt{\left(B_0 + \frac{B''}{4}\left(2z^2 - x^2 - y^2\right)\right)^2 + \left(B'y + \frac{B''}{2}yz\right)^2 + \left(B'x - \frac{B''}{2}xz\right)^2} .$$

For the case of small energies, a harmonic approximation of this potential leads to:

$$U_{\mathrm{MT,harm}}(\vec{r}) = \mu B_0 + \frac{\mu}{2}\left[\left(\frac{B'^2}{B_0} - \frac{B''}{2}\right)\left(x^2+y^2\right) + B''z^2\right] . \tag{3.15}$$

Figure 3.3 (a) illustrates the MT potential calculated according to Eq. 3.14 for ^{87}Rb in the ground state $|F=1, m_F=-1\rangle$-sublevel using a typical experimental field configuration. (a) shows the potential in the x-z-plane and Fig. 3.3 (b) compares radial and axial cuts of U_{MT} (red) with the harmonic approximation $U_{\mathrm{MT,harm}}$ (blue dashed). In the z-direction, U_{MT} is intrinsically harmonic, while in the x,y-directions, the harmonic regime is limited to energies $k_{\mathrm{B}}T \ll \mu B_0$. The magnetic potential in harmonic approximation is characterized by the trap frequencies

$$\omega_x = \omega_y = \sqrt{\frac{\mu}{m}\left(\frac{B'^2}{B_0} - \frac{B''}{2}\right)} \qquad \text{and} \qquad \omega_z = \sqrt{\frac{\mu}{m}B''} . \tag{3.16}$$

In general, the density distribution $n(\vec{r})$ of a thermal atomic cloud with a temperature T in the presence of a potential $U(\vec{r})$ is given by [67]:

$$n(\vec{r}) = n_0 \exp\left(-\frac{U(\vec{r})}{k_{\mathrm{B}}T}\right) . \tag{3.17}$$

The peak density n_0 is determined by the normalization condition

$$\int n(\vec{r})\, d^3r \overset{!}{=} N , \tag{3.18}$$

where N is the atom number. For the case of the magnetic potential in harmonic approximation, this leads to a Gaussian density distribution

$$n_{\mathrm{MT,harm}}(\vec{r}) = n_0 \exp\left(-\frac{U_{\mathrm{harm}}(\vec{r})}{k_{\mathrm{B}}T}\right) = n_0 \exp\left(-\frac{x^2}{2\sigma_x^2} - \frac{y^2}{2\sigma_y^2} - \frac{z^2}{2\sigma_z^2}\right) , \tag{3.19}$$

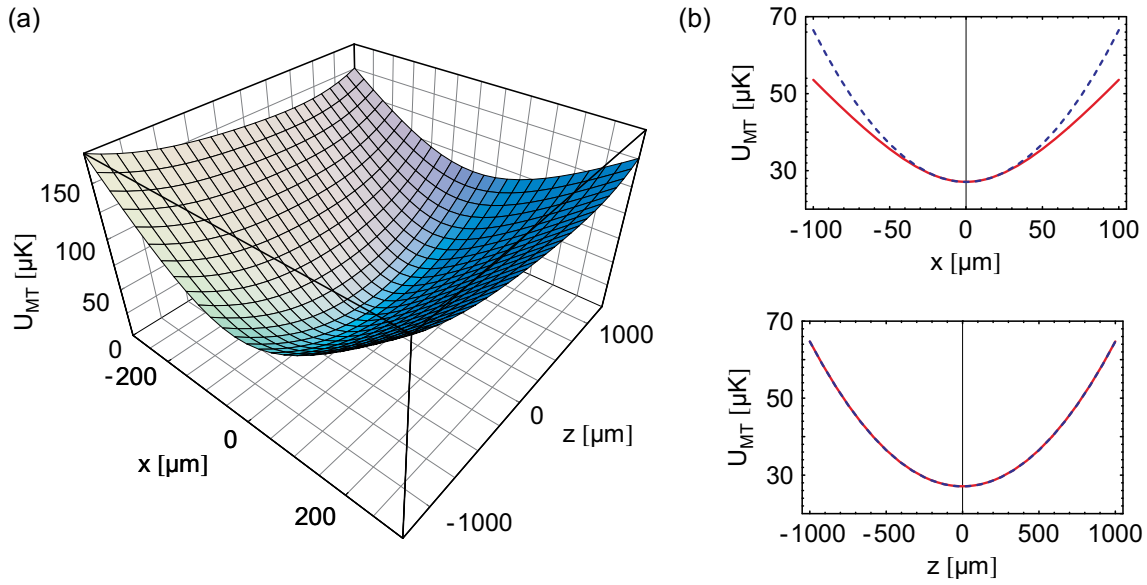

Figure 3.3: *Calculated ^{87}Rb MT potential for typical experimental values: $B_0 = 0.81\mathrm{G}$, $B' = 138\mathrm{G/cm}$ and $B'' = 224\mathrm{G/cm^2}$. (a) shows the x-z-plane, while (b) compares radial and axial cuts of U_{MT} (red) with the harmonic approximaton $U_{\mathrm{MT,harm}}$ (blue dashed).*

characterized by the $1/\sqrt{e}$-widths

$$\sigma_x = \sigma_y = \sqrt{\frac{k_{\mathrm{B}}T}{\mu\left(\frac{B'^2}{B_0} - \frac{B''}{2}\right)}} = \frac{1}{\omega_x}\sqrt{\frac{k_{\mathrm{B}}T}{m}} \qquad \text{and} \qquad \sigma_z = \sqrt{\frac{k_{\mathrm{B}}T}{\mu B''}} = \frac{1}{\omega_z}\sqrt{\frac{k_{\mathrm{B}}T}{m}}\,. \tag{3.20}$$

The peak density of an atomic cloud with N atoms trapped in this potential is given by

$$n_0 = \frac{N}{(2\pi)^{3/2}\,\sigma_x\sigma_y\sigma_z}\,. \tag{3.21}$$

The present trap configuration, which is displayed in Fig. 3.3, leads to an elongated, cigar shaped atom cloud with an aspect ratio of $\sigma_z/\sigma_{x,y} \approx 10$.

3.2.2 Evaporative cooling

Evaporative cooling is an effective method to reach the nK regime as it is not subject to limitations induced by near resonant light. It was used for the first time with spin-polarized hydrogen [103] and finally led to the observation of Bose-Einstein condensation of alkali atoms (^{87}Rb:[2], ^{23}Na: [22], ^{7}Li: [21]). The essential idea is that by clever control of the trap depth, hot atoms can be preferentially ejected and the remaining atoms will rethermalize at a lower temperature. Figure 3.4 demonstrates this method for to a cloud of atoms in thermal equilibrium at an initial temperature T_1. Its thermal energy E follows

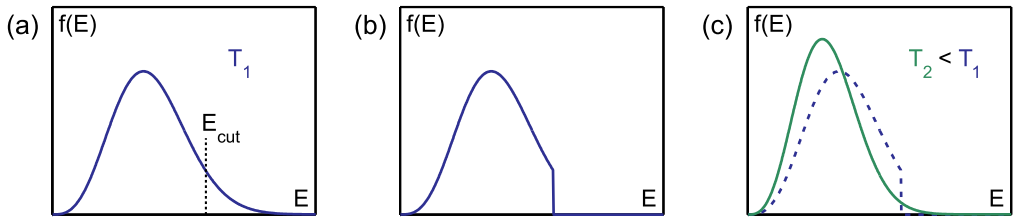

Figure 3.4: *Principle of evaporative cooling. Starting from a thermal equilibrium T_1 (a), hot atoms with $E > E_{\mathrm{cut}}$ are ejected (b). Finally, the system rethermalizes at a lower temperature $T_2 < T_1$ (c). From [9].*

the Maxwell-Boltzmann distribution [67]:

$$f(E)\mathrm{d}E \propto \sqrt{E}\, e^{-E/k_{\mathrm{B}}T_1}\, \mathrm{d}E \tag{3.22}$$

For evaporative cooling, atoms with an energy $E > E_{\mathrm{cut}}$ are removed from the trap, leaving behind a thermal disequilibrium (b). Finally, elastic collisions lead to a rethermalization of the system resulting in a lower temperature $T_2 < T_1$. The evaporation rate per atom depends on the density n, the elastic scattering cross section σ_0, the mean thermal velocity $\langle v \rangle$ and the parameter $\eta = E_{\mathrm{cut}}/(k_{\mathrm{B}}T)$ [104]:

$$\tau_{\mathrm{evap}}^{-1} = \frac{\dot{N}}{N} = n \langle v \rangle \sigma_0 \eta\, e^{-\eta} \tag{3.23}$$

In a trap with finite potential depth, atoms with energies above the trap depth are permanently created by elastic collisions leading to a continuous evaporation (so called *plain evaporation*). However, as the temperature decreases, less atoms with sufficient energy are produced and plain evaporation is suppressed. Quantitatively, the parameter η increases and the evaporation rate (Eq. 3.23) exponentially decreases. Hence, in order to effectively reduce the temperature, the trap depth has to be reduced keeping η constant (*forced evaporation*). The efficiency of evaporative cooling, which is defined as the relative temperature reduction over relative atom loss rate ($\dot{\mathrm{T}}/\mathrm{T}/\dot{\mathrm{N}}/\mathrm{N}$), depends only on the parameter η. If the trap depth is reduced slowly enough (η large), it is possible that the atom density rises despite atom loss. For the case that the increase in density is large enough, the elastic collision rate $\Gamma_{\mathrm{el}} \propto n \langle v \rangle \propto n T^{1/2}$ increases despite the temperature reduction. Thus, the evaporation efficiency increases during the cooling process, which is called *runaway evaporation*. However, the maximum duration of an evaporation ramp is limited by atom loss processes such as background gas collisions or inelastic two- and three-body collisions (see Sec. 2.6). Therefore, if the evaporation ramp is too slow, the evaporative cooling rate is compensated by atom loss and heating processes. The timing sequence of an evaporation ramp is typically optimized experimentally.

For efficient cooling, the number of elastic collisions has to exceed the inelastic collision rate by many times over ($\Gamma_{\mathrm{el}}/\Gamma_{\mathrm{inel}} \gg 100$). For low energies, the ratio $\Gamma_{\mathrm{el}}/\Gamma_{\mathrm{inel}}$ decreases

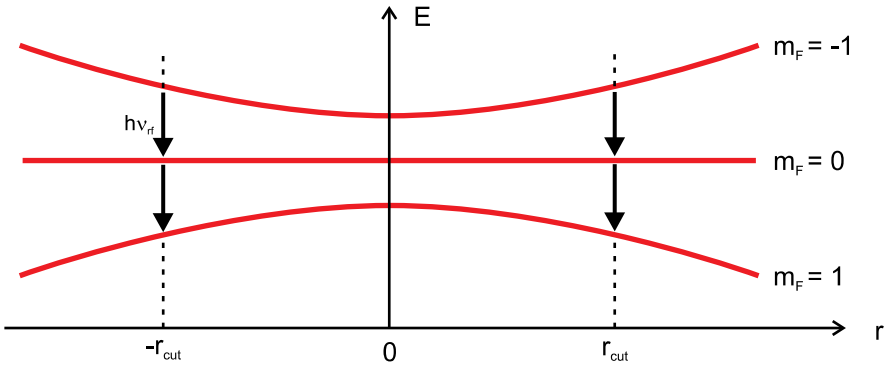

Figure 3.5: *Principle of radio frequency induced evaporation of ^{87}Rb in the $|5S_{1/2}, F = 1\rangle$ ground state. Note that $g_F = -1/2$. The red lines indicate the Zeeman energy shift of the m_F sub states as a function of the atom position in the trap. Only atoms with high enough thermal energies reach the position, where they are in resonance with the radio frequency photon. Here, a transition to an untrapped spin state is induced and the atoms are removed from the trap. Adapted from [9].*

(see [9] for details), which limits the minimum temperature to a level where $\Gamma_{\mathrm{el}}/\Gamma_{\mathrm{inel}} \approx 1$:

$$k_{\mathrm{B}} T_{\mathrm{min}} = \frac{\pi m \Gamma_{\mathrm{inel}}^2}{16 \sigma_0^2} \tag{3.24}$$

As this temperature limit depends on the scatting cross section, effective evaporative cooling is restricted to certain atomic species and isotopes with amenable scattering properties.

Radio frequency induced evaporation In magnetic traps, atoms with an energy above a certain threshold can be removed by inducing a transition to a non trappable spin state. The position dependence of the Zeeman shift for the individual sub-states is shown in Fig. 3.5 for the case of ^{87}Rb in the ground state. Transitions between spin states are induced by applying an alternating electro-magnetic field with a frequency ν_{RF} in the radio frequency (RF) range. The resonance condition

$$\nu_{\mathrm{RF}} \left(\vec{B}(\vec{r}) \right) = \frac{g_F \, \mu_{\mathrm{B}} \, |\vec{B}(\vec{r})|}{h} \tag{3.25}$$

is connected to the potential energy through $E_{\mathrm{th}} = g_F \, m_F \, \mu_{\mathrm{B}} \, |\vec{B}(\vec{r})|$. Only atoms with a thermal energy that is larger than this threshold energy come into resonance with the RF field while oscillating in the trap and thus, transitions to untrapped spin states are induced. This allows an energy selective removal of "hot" atoms from the trap. The parameter η is connected to the induced radio frequency ν_{RF} through

$$\eta = \frac{|m_F| \, h \, \nu_{\mathrm{Rf}} - |g_F \, m_F \, \mu_{\mathrm{B}} \, B_0|}{k_{\mathrm{B}} T} = \frac{|m_F| \, h \, (\nu_{\mathrm{RF}} - \nu_{\mathrm{RF0}})}{k_{\mathrm{B}} T} \,, \tag{3.26}$$

which includes the magnetic field offset $B_0 = h \, \nu_{\mathrm{RF0}} / \mu_{\mathrm{B}}$, that defines the bottom of the trap. Experimentally, the ratio frequency ν_{RF} is continuously reduced during an evaporation ramp keeping η constant.

Note that RF induced evaporation in a MT selectively removes energetic atoms without varying the trapping potential. In contrast, lowering the height of the trapping potential in an optical trap (see below) is accompanied by a weaker confinement. This lowers the density slowing down the evaporation process.

3.2.3 Optical dipole traps

The basic idea of optical dipole traps is based on the interaction of atoms with inhomogeneous light fields. The optical dipole force arises from the dispersive interaction of the induced atomic dipole moment with the intensity gradient of the light field. In a simple oscillator model [105], an electric field

$$\vec{E}(\vec{r},t) = \vec{e}E(\vec{r})e^{i\omega t} + \vec{e}E^*(\vec{r})e^{-i\omega t} \tag{3.27}$$

with polarization vector $\vec{e}$ and frequency ω induces an atomic dipole moment

$$\vec{p}(\vec{r},t) = \alpha(\omega_\mathrm{L})\vec{E}(\vec{r})\,. \tag{3.28}$$

Here, α is the complex polarizability. The interaction potential of the induced dipole moment $\vec{p}$ with the driving field $\vec{E}$ is given by

$$U_\mathrm{dip} = -\frac{1}{2}\langle\vec{p}\vec{E}\rangle = -\mathrm{Re}(\alpha)|\vec{E}(\vec{r})|^2 = -\frac{1}{2\varepsilon_0 c}\mathrm{Re}(\alpha)I(\vec{r})\,, \tag{3.29}$$

where the angular brackets denote the time average over the rapidly oscillating terms. The dipole potential is hence proportional to the light intensity $I(\vec{r}) = 2\varepsilon_0 c|\vec{E}(\vec{r})|^2$ and the real part of the complex polarizability. This parameter describes the in-phase component of the dipole oscillation being responsible for the dispersive properties of the interaction. The conservative dipole force is in turn proportional to the intensity gradient of the driving field:

$$\vec{F}_\mathrm{dip}(\vec{r}) = -\nabla U_\mathrm{dip}(\vec{r}) = \frac{1}{2\varepsilon_0 c}\mathrm{Re}(\alpha)\nabla I(\vec{r})\,. \tag{3.30}$$

The accompanying photon scattering rate is given by

$$\Gamma_\mathrm{sc} = \frac{P_\mathrm{abs}}{\hbar\omega} = \frac{1}{\hbar\varepsilon_0 c}\mathrm{Im}(\alpha)I(\vec{r})\,. \tag{3.31}$$

It is proportional to the light intensity and the imaginary part of the polarizability, which describes the out-of-phase component of the dipole oscillation. The dipole potential (3.29) and the scattering rate (3.31) are the main quantities, which determine the properties of a dipole trap.

A Lorentz's model of a classical oscillator can be used to calculate the complex polarizability (see [105] for details):

$$\alpha(\omega_\mathrm{L}) = 6\pi\varepsilon_0 c^3 \frac{\gamma/\omega_0^2}{\omega_0^2 - \omega^2 - i\left(\omega^3/\omega_0^2\right)\gamma}\,. \tag{3.32}$$

The model is based on an ideal two-level atomic system, where ω_0 is the oscillation eigenfrequency corresponding to the optical transition frequency. The classical damping rate γ corresponds to the spontaneous decay rate of the excited level. In a full quantum mechanical approach, γ is replaced by the dipole matrix element between ground and excited state. However, for the relevant case of large detuning $|\delta| = |\omega - \omega_0| \gg \gamma$ and a small scattering rate $\Gamma_{\mathrm{sc}} \ll \gamma$, the classical result (3.32) provides an excellent approximation for the quantum-mechanical oscillator. Thus, the dipole potential (3.29) and the corresponding scattering rate (3.31) are given by

$$U_{\mathrm{dip}}(\vec{r}) = -\frac{3\pi c^2}{2\omega_0^3}\left(\frac{\gamma}{\omega_0-\omega}+\frac{\gamma}{\omega_0+\omega}\right) I(\vec{r})\,, \tag{3.33}$$

$$\Gamma_{\mathrm{sc}}(\vec{r}) = \frac{3\pi c^2}{2\hbar\omega_0^3}\left(\frac{\omega}{\omega_0}\right)^3\left(\frac{\gamma}{\omega_0-\omega}+\frac{\gamma}{\omega_0+\omega}\right)^2 I(\vec{r})\,. \tag{3.34}$$

The basic physics of dipole trapping in far-detuned laser fields can be understood on the basis of these two equations.

Experimentally, the sign of the detuning $\delta = \omega - \omega_0$ determines the nature of this potential: Below an atomic resonance ("red" detuning, $\delta < 0$), the dipole potential is negative and the interaction thus attracts atoms into the light field. Potential minima are therefore found at positions with maximum intensity. Above resonance ("blue"detuning, $\delta > 0$) the dipole interaction repels atoms out of the field, and potential minima correspond to intensity minima.

In the case of small detuning $\delta \ll \omega_0$, the second term in the equations 3.33 and 3.34 can be neglected, leading to the so called *rotating-wave approximation*. Under this assumption, the dipole potential scales as I/δ, whereas the scattering rate scales as I/δ^2. As photon scattering is accompanied by a heating rate (see below), optical dipole traps usually use large detunings and high intensities to keep the scattering rate as low as possible for a given potential depth.

Note that the conservative optical dipole force and the dissipative scattering force, which was introduced in Sec. 3.1, both originate from interaction of a light field with atoms. Which force has the dominating effect, depends on the actual parameters: If the light field is a plane wave, the dipole force vanishes as $\nabla I(\vec{r}) = 0$. For inhomogeneous light fields ($\nabla I(\vec{r}) \neq 0$), the dominating force depends on the detuning δ: The scattering force can be neglected, if $\delta \gg \gamma$ which is typically used in optical dipole traps. A general theoretical approach on the atom-light interaction using optical Bloch equations can be found in [106, 81, 76]. In a quantum mechanical description, the dipole potential is created by an intensity-dependent shift of atomic energy levels ("dressed atom picture", [107]), which is induced by the coupling of the light field to the atom.

Multi-level atoms

In real atoms, a multitude of electronic transitions are possible, including complex fine- and hyperfine structure. The main consequence is that the dipole potential in general

depends on the particular sub-structure of the atom and all electronic states coupling to the ground state have to be taken into account. In terms of the oscillator model discussed before, multi-level atoms can be described by state-dependent atomic polarizabilities. The dressed atom picture sums over dipole matrix elements between the ground state and all possible excited states for the calculation of the ground state energy shift [105].

However, the situation simplifies, if the light field detuning with respect to all relevant transitions exceeds their fine- and hyperfine structure splitting ($\delta_0 \gg \Delta_{\mathrm{FS}} \gg \Delta_{\mathrm{HFS}}$). This case applies to the experimental situation described in the scope of this thesis. Fine-, hyperfine-, and magnetic substructure can be neglected and the multi-level problem is reduced to simply summing up the light shift potenials corresponding to transitions to all relevant atomic levels. The dipole potential and the scattering rate are then given by

$$U_{\mathrm{dip}}(\vec{r}) = \sum_i -\frac{3\pi c^2}{2\omega_{0i}^3}\left(\frac{\gamma_i}{\omega_{0i}-\omega}+\frac{\gamma_i}{\omega_{0i}+\omega}\right) I(\vec{r}) \qquad \text{and} \tag{3.35}$$

$$\Gamma_{\mathrm{sc}}(\vec{r}) = \sum_i \frac{3\pi c^2}{2\hbar\omega_{0i}^3}\left(\frac{\omega_{\mathrm{L}}}{\omega_{0i}}\right)^3\left(\frac{\gamma_i}{\omega_{0i}-\omega}+\frac{\gamma_i}{\omega_{0i}+\omega}\right)^2 I(\vec{r})\,, \tag{3.36}$$

with transition frequencies ω_{0i} and line widths γ_i of all relevant atomic transitions.

For atomic states with fine structure splitting, the individual contributions of each fine structure transition are weighted by the corresponding oscillator strength in order to calculate a mean effective transition frequency and line width according to

$$\omega_{0i} = \sum_j \frac{f_j\,\omega_{0j}}{f_j} \qquad \text{und} \qquad \gamma_i = \sum_j \frac{f_j\,\gamma_j}{f_j}\,. \tag{3.37}$$

The oscillator strengths f_j of the individual fine structure transitions can be calculated for allowed electric dipole transition according to [108]

$$f_i = \frac{m_{\mathrm{e}}\,c\,\epsilon_0\,\lambda^2}{2\pi\,e^2}\,\frac{g_i}{g_j}\,A_{ij} \qquad \text{with} \qquad g_{i,j} = 2J_{i,j}+1\,. \tag{3.38}$$

Here, the weighting factors $g_{i(j)}$ are related to the ground state (excited state) angular momenta $J_{i(j)}$ and $A_{ij} \equiv \gamma$ is the transition probability. Due to the much smaller energy shifts, hyperfine splitting is not taken into account:

Dominant contributions for the dipole potential (3.35) and the scattering rate (3.36) are characterized by large line widths and small detuning with respect to the light field.

Red detuned dipole traps

The dipole force points towards intensity maxima if the light field is tuned below the atomic transition frequency ("red" detuning). Therefore, already the focus of a red detuned laser beam constitutes a stable dipole trap for atoms. The spatial intensity distribution of a focused Gaussian beam with power P propagating in the z-direction is described by

$$I(r,z) = \frac{2P}{\pi w^2(z)}\exp\left(-\frac{2r^2}{w^2(z)}\right)\,, \tag{3.39}$$

where r denotes the radial coordinate ($r^2 = x^2 + y^2$). The $1/e^2$ radius $w(z)$ depends on the axial coordinate z via

$$w(z) = w_0 \sqrt{1 + \left(\frac{z}{z_\mathrm{R}}\right)^2} \,. \tag{3.40}$$

The laser beam is characterized by the minimum radius w_0, which is called the *beam waist* and the *Rayleigh length* $z_\mathrm{R} = \pi w_0^2/\lambda$. This length depends on the wavelength λ and describes the distance from the focus along the z-axis, where the beam radius reaches the magnitude $w_0\sqrt{2}$. The maximum intensity in the focus is given by

$$I_0 = \frac{2P}{\pi w_0^2} \,. \tag{3.41}$$

The resulting dipole potential created by a focused "red" detuned laser beam can be calculated from equations 3.35, 3.39 and 3.40:

$$U_\mathrm{dip}(r,z) = U_0 \frac{1}{1-(z/z_\mathrm{R})^2} \exp\left(-\frac{2r^2}{w_0^2\left(1+(z/z_\mathrm{R})^2\right)}\right) \quad \text{with} \tag{3.42}$$

$$U_0 = \sum_i -\frac{3\pi c^2}{2\omega_{0i}^3}\left(\frac{\gamma_i}{\omega_{0i}-\omega} + \frac{\gamma_i}{\omega_{0i}+\omega}\right) I_0 \,. \tag{3.43}$$

The potential in the trap center $U_0 = U_\mathrm{ODT}(0,0)$ is called *trap depth*. Figure 3.6 (a) shows the $1/e^2$ radius of a focused laser beam and the resulting optical dipole potential for Yb for typical experimental beam parameters.

If the thermal energy $k_\mathrm{B}T$ of an atomic ensemble is much smaller than the trap depth U_0 , the extension of the atomic sample is radially small compared to the beam waist and axially small compared to the Rayleigh range. In this case, the optical potential can be well approximated by a simple cylindrically symmetric harmonic oscillator

$$U_\mathrm{ODT,harm}(r,z) = -U_0\left(1 - 2\left(\frac{r}{w_0}\right)^2 - \left(\frac{z}{z_\mathrm{R}}\right)^2\right) \,. \tag{3.44}$$

Figure 3.6 (b) compares radial and axial cuts of the calculated potential U_ODT (red line) with the harmonic approximation $U_\mathrm{ODT,harm}$ (blue dashed line).

In the harmonic approximation, the oscillation frequencies of a trapped atom are given by

$$\omega_r = \sqrt{\frac{4U_0}{mw_0^2}} \qquad \text{and} \qquad \omega_z = \sqrt{\frac{2U_0}{mz_\mathrm{R}^2}} \tag{3.45}$$

in radial and axial direction respectively. In the case of the harmonic approximation, the density distribution of a thermal cloud of N atoms is Gaussian:

$$n_\mathrm{ODT}(\vec{r}) = n_0 \exp\left(-\frac{U_\mathrm{ODT,harm}(\vec{r}) - U_0}{k_\mathrm{B}T}\right) = n_0 \exp\left(-\frac{r^2}{2\sigma_r^2} - \frac{z^2}{2\sigma_z^2}\right) \tag{3.46}$$

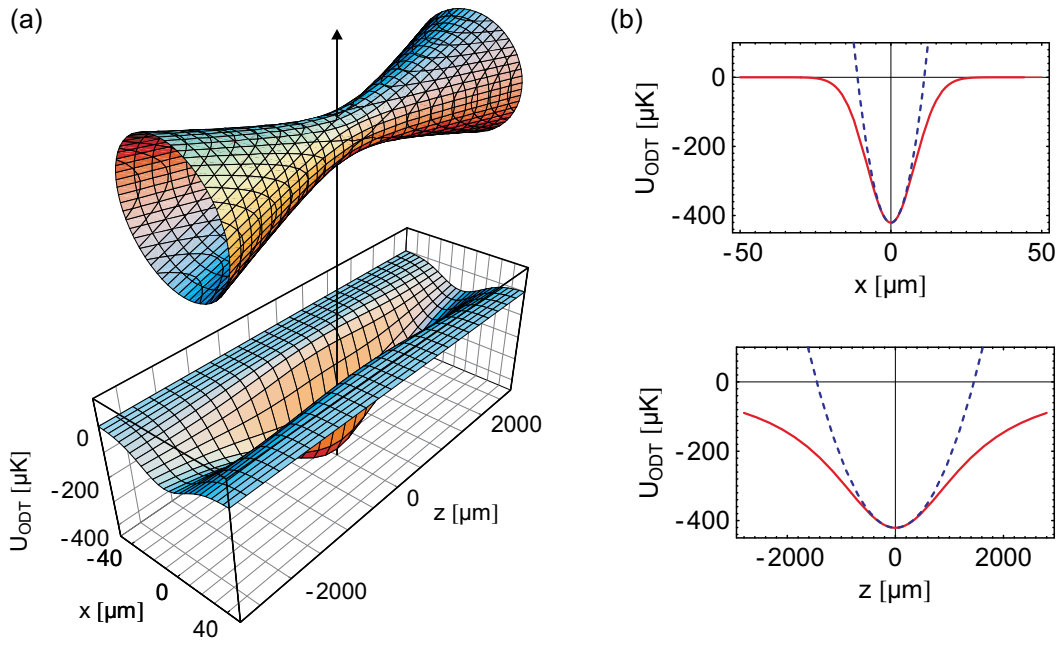

Figure 3.6: *Red detuned optical dipole trap created by a focused Gaussian laser beam: (a) shows the $1/e^2$ radius around the focus and the resulting optical potential for Yb for typical experimental values: $\lambda = 532\,\mathrm{nm}$, $P = 3\,W$, $w_0 = 15\,\mu\mathrm{m}$. (b) compares radial and axial cuts of the potential U_{ODT} (red) with the harmonic approximation $U_{\mathrm{ODT,harm}}$ (blue dashed).*

The characteristic radial and axial $1/e^2$-widths are

$$\sigma_r = \sqrt{\frac{w_0^2 k_\mathrm{B} T}{4U_0}} = \frac{1}{\omega_r}\sqrt{\frac{k_\mathrm{B}T}{m}} \qquad \text{and} \qquad \sigma_z = \sqrt{\frac{z_\mathrm{R}^2 k_\mathrm{B} T}{2U_0}} = \frac{1}{\omega_z}\sqrt{\frac{k_\mathrm{B}T}{m}} \tag{3.47}$$

and the peak density is given by

$$n_0 = \frac{N}{(2\pi)^{3/2}\,\sigma_r^2 \sigma_z}\,. \tag{3.48}$$

For optical dipole traps created by a red detuned focused laser beam, the axial confinement typically exceeds the radial confinement by a large factor, as $z_\mathrm{R} \gg w_0$. The aspect ratio

$$\frac{\sigma_z}{\sigma_r} = \frac{\omega_r}{\omega_z} = \frac{z_\mathrm{R}}{w_0}\sqrt{2} = \frac{w_0}{\lambda}\pi\sqrt{2} \tag{3.49}$$

depends only on the beam waist w_0 and the wavelength λ. In the present experiment, the chosen parameters lead to nearly one-dimensional density distributions with aspect ratios on the order of $\sigma_\mathrm{r}/\sigma_z \approx 1/100$.

Light induced heating mechanisms

Heating by the trap light is an issue of particular importance for optical dipole trapping. A fundamental source of heating is the spontaneous scattering of trap photons, which due to

its random nature causes fluctuations of the scattering force. Each photon absorption- and re-emission process is accompanied by a momentum transfer from a photon to an atom. This increases the system energy in increments of the so called *recoil energy*,

$$E_{\mathrm{R}} = \frac{\hbar^2 k^2}{2m}\,, \tag{3.50}$$

which can be related to the so-called *recoil temperature* by:

$$T_{\mathrm{R}} = \frac{2E_{\mathrm{R}}}{k_{\mathrm{B}}} = \frac{\hbar^2 k^2}{k_{\mathrm{B}} m}; \tag{3.51}$$

Both absorption and spontaneous re-emission processes show fluctuations and thus both contribute to the total heating power, which is defined as the mean thermal energy change $\dot{\bar{E}}_{\mathrm{th}}$ [105]:

$$P_{\mathrm{heat}} = \dot{\bar{E}}_{\mathrm{th}} = 2E_{\mathrm{R}}\langle\Gamma_{\mathrm{sc}}\rangle = k_{\mathrm{B}} T_{\mathrm{R}}\langle\Gamma_{\mathrm{sc}}\rangle\,. \tag{3.52}$$

This heating power is proportional to the mean scattering rate $\langle\Gamma_{\mathrm{sc}}\rangle$.

In thermal equilibrium, the mean kinetic energy per atom in a three-dimensional trap is $\bar{E}_{\mathrm{kin}} = 3k_{\mathrm{B}}T/2$. In a harmonic trapping potential, the potential energy is equal to the kinetic energy and thus the mean thermal energy is given by $\bar{E}_{\mathrm{th}} = \bar{E}_{\mathrm{kin}} + \bar{E}_{\mathrm{pot}} = 3k_{\mathrm{B}}T$. Using this relation between mean energy and temperature, the heating power resulting from photon scattering can be reexpressed as a heating rate

$$\dot{T}_{\mathrm{heat}} = \frac{1}{3}\frac{\dot{\bar{E}}_{\mathrm{th}}}{k_{\mathrm{B}}} = \frac{1}{3} T_{\mathrm{R}}\langle\Gamma_{\mathrm{sc}}\rangle\,. \tag{3.53}$$

describing the corresponding increase of temperature with time.

In a dipole trap created by a red detuned focused laser beam, the maximum scattering rate $\langle\Gamma_{\mathrm{sc,max}}\rangle = \langle\Gamma_{\mathrm{sc}}\rangle(I_0 = {}^{2P}/_{\pi w_0^2})$ is present in the focus leading to a maximum heating rate $\dot{T}_{\mathrm{heat,max}} = {}^{1}/_{3}\, T_{\mathrm{R}}\,\langle\Gamma_{\mathrm{sc,max}}\rangle$. In multi-level atoms, the total heating rate is calculated by summing up the individual contributions according to Eq. 3.36. Here, the respective transition-dependent recoil temperatures have to be taken into account:

$$\begin{aligned}\dot{T}_{\mathrm{heat,max}} &= \frac{1}{3}\sum_i T_{\mathrm{R},i}\,\langle\Gamma_{\mathrm{sc,max}}\rangle_i \\ &= \frac{1}{3}\sum_i \frac{\hbar^2 k_i^2}{k_{\mathrm{B}} m}\,\frac{3\pi c^2}{2\hbar\omega_{0i}^3}\left(\frac{\omega}{\omega_{0i}}\right)^3\left(\frac{\gamma_i}{\omega_{0i}-\omega} + \frac{\gamma_i}{\omega_{0i}+\omega}\right)^2 \frac{2P}{\pi w_0^2}\end{aligned} \tag{3.54}$$

Evaporative cooling in optical dipole traps

Generally, forced evaporative cooling in optical dipole traps is achieved by adiabatically ramping down the trapping beam power. In contrast to RF induced evaporation in magnetic traps, this not only lowers the trap depth, but also weakens the confinement. The method of evaporative cooling however requires high densities to assure fast thermalization rates. While this effect is disadvantageous for evaporative cooling in optical dipole

traps, the fact that arbitrary atomic states can be optically trapped, turns out to be an advantage.

Effective evaporative cooling requires, that the ratio between inelastic collisions causing losses and heating, and elastic collisions providing thermalization and evaporation, has to be large. In dipole traps, inelastic processes can be suppressed when the particles are prepared in their energetically lowest magnetic state. By using large laser detunings with respect to strong atomic transitions, heating effects caused by the trap light can be practically eliminated.

The use of dipole traps consisting of two crossed red detuned laser beams enhances the confinement in all three dimensions and allows effective evaporative cooling. In this configuration, an all optical formation of a BEC has been accomplished for the first time in ^{87}Rb [109]. More importantly, optical dipole traps are used to reach quantum degeneracy in elements that are not trappable in magnetic potentials. For an overview see [110]. Different isotopes of Yb are also cooled to quantum degeneracy using all optical methods [1, 111].

4

Apparatus

This chapter describes the apparatus, that was used for the experiments described in the present work. The complete setup is arranged on three optical tables: two of them host the laser systems designed for cooling and trapping of ^{87}Rb and Yb and the third one supports the the main vacuum chamber and the laser systems for the optical dipole traps. In addition, the relevant methods of atom detection and data processing are presented here. This apparatus was used in previous experiments and detailed technical description can be found in [8, 9, 11]. However, the experiments presented here, have required a significant improvement in stability and precision compared to the previous setup. Hence, in the course of this work, a number of components were changed or added to the existing system: Large parts of the laser systems were redesigned, which is described in Sec. 4.2. Additionally, improved detection methods as detailed in Sec. 4.3 were introduced to the experimental setup.

4.1 Vacuum system

All experiments presented here are performed inside the main vacuum chamber, which is illustrated in Fig. 4.1. It has a wheel-shaped geometry with 10 windows in a radial arrangement and 2 additional axial windows. The windows provide optical access for the Zeeman-slower, MOT- and optical dipole trap laser beams, as well as for the atom detection systems. Atom ovens, which prepare the Yb and Rb atoms in a gaseous form, are connected to the central chamber by the corresponding Zeeman-slower tubes. The Rb oven operates at a temperature of $\approx 120\,^{\circ}\mathrm{C}$, while Yb needs $\approx 430\,^{\circ}\mathrm{C}$ to provide enough atom flux for the Zeeman-slower.

Vacuum Ultracold atom experiments have to be carried out in an ultra high vacuum environment, as collisions with energetic atoms from the background gas lead to rapid atom loss in the ultracold sample (see Sec. 2.6). The pressure in the main chamber is at a level of $\approx 10^{-11}$ mbar, which is maintained by a titanium sublimation pump and an additional ion-getter pump. Both oven sections are also equipped with ion-getter pumps that keep the pressure at a level of $< 10^{-9}$ mbar, when the atom ovens are operating. Differential pumping tubes are connecting the ovens with the Zeeman slower tubes, allowing to maintain pressure difference of ≈ 3 orders of magnitude.

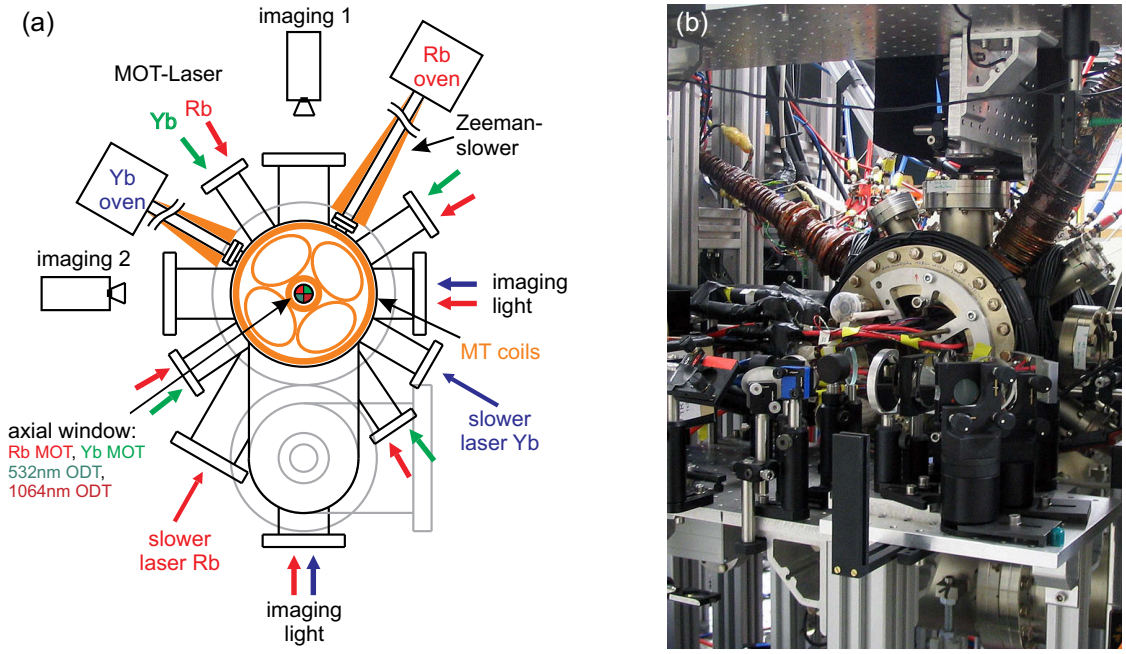

Figure 4.1: *(a) schematic diagram (adapted from [9]) and (b) photograph of the main vacuum setup*

Magnetic field Water cooled coils are attached to the main chamber and the Zeeman slower tubes providing the magnetic fields necessary for cooling and trapping of both atomic species. The 3-dimensional gradient field required for the MOT (see Sec. 3.1) is created by a single-sided configuration of two coils. The calculated field gradients in the trap center are $(\partial B/\partial z)/I = 0.44\ \mathrm{G/cm\,A}$ in axial direction and$(\partial B/\partial r)/I = 0.22\ \mathrm{G/cm\,A}$ in radial direction [9] for a given current I through the coils. Typical MOT currents used in the present experiments are $5 \ldots 90\,\mathrm{A}$. The magnetic trap (MT) potential for Rb is generated by additional coils arranged in a clover-leave-geometry (see [8] for details). At a current of 235 A, the resulting axial field curvature is $B'' = 231\,\mathrm{G/cm^2}$, the radial field gradient is $B' = 133\,\mathrm{G/cm}$ and typical offset fields are on the order of $B_0 = 0.8\,\mathrm{G}$ (see Sec. 3.2.1).

In addition to the MOT and MT coils, three pairs of compensation coils are attached to the vacuum chamber. They provide variable and nearly homogeneous magnetic fields in all three dimensions and are used for various purposes: First, they serve to compensate unwanted stray magnetic field caused by the earth magnetic field, the ion pumps and the Zeeman slowers. Second, additional magnetic fields created by the compensation coils shift the spatial position of zero magnetic field in the MOT or the minimum magnetic field in the MT. This allows a controlled movement of the trapped atoms. The accessible range is in the order of several mm for the Rb MOT and $\approx 1\,\mathrm{mm}$ for the MT, where movement is restricted to radial directions. Finally, defined magnetic quantization fields for absorptive or dispersive imaging of the atomic clouds are also provided by the compensation coils.

The current of all coils is independently controlled by the experiment control system.

Fast switching is provided either by insulated gate bipolar transistors (IGBTs) or high power MOS-FETs. Ring down circuits, which are integrated in the system to avoid large electromagnetic induction voltages, determine the minimum switching times to $\approx 1\,\mathrm{ms}$.

4.2 Laser systems

This section describes the laser systems required for cooling and trapping of ^{87}Rb and Yb atoms. It focuses on changes of various components, that occurred in the course of this work: For the Rb MOT lasers, an improved stabilization system was implemented in the existing setup. In addition, the "green" 556 nm light generation, which is used for the Yb MOT, was changed from the previously used dye laser to a frequency doubling system of 1112 nm light. Finally,the optical system used for the Yb BIODT was partly redesigned and the pointing stability- and pointing control system was highly improved.

4.2.1 Rb Cooling and trapping

The Zeeman-slower and the MOT for ^{87}Rb are operated on the atomic ^{87}Rb D2-line at 780nm. The main transition for cooling and trapping uses the $5^2\mathrm{S}_{1/2}$ ground state hyperfine level $|F = 2\rangle$ and the $5^2\mathrm{P}_{3/2}$ excited state hyperfine level $|F' = 3\rangle$, which is shown in Fig. 4.2. In different experimental stages, a variable MOT laser detuning δ_0 of $0 \ldots 60\,\mathrm{MHz}$ with respect to the $|F = 2\rangle \rightarrow |F' = 3\rangle$-transition is used. To maintain the necessary cycling transition for the ^{87}Rb-MOT, an additional repumper is required. Although the selection rule $\Delta F = 0, \pm 1$ prevents atoms, to enter the ground state $|F = 1\rangle$ level, off-resonant excitation to the $|F' = 2\rangle$ state can allow some atoms to end up in this level, removing them from the cycle. The repumper returns these atoms to the $|F = 2\rangle$ state through optical pumping so that they reenter the MOT cycle. In the present configuration, we work with two independent repumping beams. One of them is partially blocked by an obstacle to create a dark region for the dark-spot MOT configuration (see Sec. 5.3.1). The other one, denoted as repumper 2 is unchanged and provides repumping light for all trapped atoms.

The laser for the Zeeman-slower is detuned by -626 MHz with respect to the $|F = 2\rangle \rightarrow |F' = 3\rangle$-transition to compensate the Doppler shift for the fast atoms entering the increasing-field-slower. A separate repumper laser is also needed here. In addition to that, a beam denoted as depumper, which is resonant with the $|F = 2\rangle \rightarrow |F' = 2\rangle$ is needed, to prepare the atoms in a defined spin state for the MT. Furthermore, beams for the imaging system are required. Resonant imaging is carried out on the $|F = 2\rangle \rightarrow |F' = 3\rangle$ transition, while for off-resonant dark contrast imaging the slower repumper is used (see Sec.: 4.3.3). All relevant atomic levels and the laser beams for the ^{87}Rb MOT are summarized in Fig. 4.2.

Light generation The light required for the ^{87}Rb MOT is created by 4 diode lasers (diodes: Sharp GH0781JA2C, 120 mW, 784 nm). Two of them are designed as external cavity master diode lasers (ECDL) in Littrow-configuration [112] and are independently frequency-stabilized to atomic ^{87}Rb transitions. The other two lasers are injected with

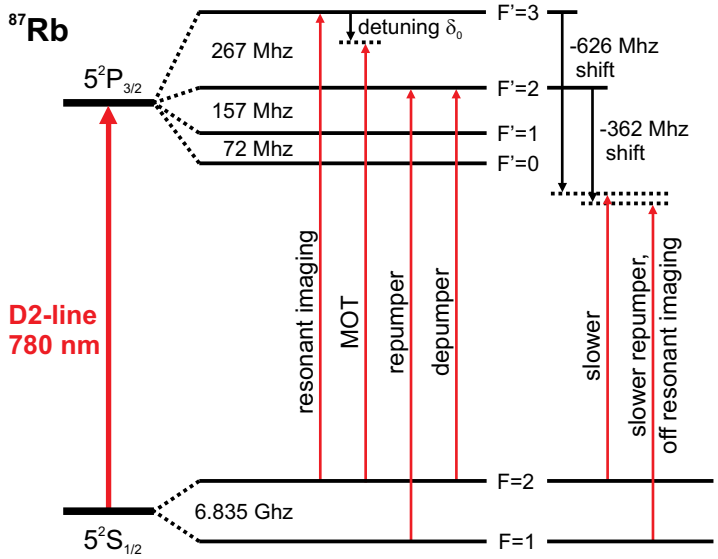

Figure 4.2: *Diagram of relevant atomic levels and laser beams used in the present experimental setup for ^{87}Rb cooling, trapping and detection.*

$\approx 100\,\mu$W derived from one of the master lasers and act as high power slave lasers. In order to generate the different beams described above, light frequency shifting is achieved with acousto-optic modulators (AOM). All laser beams can be switched on an off by mechanical beam shutters. Controllable AOMs provide fast switching, as well as power or frequency adjustments. The laser system for the Rb MOT was originally designed in a previous work and a detailed description can be found in [8]. However, in the course of this work some modifications were made and an updated scheme of the laser system is shown in Fig. 4.3

Frequency stabilization The MOT master and the repumper laser use an independent spectroscopy and frequency stabilization systems. The lock signal for each laser is generated by spectroscopy on the D2-transition in a Rb vapor cell. This signal is then fed back through a PI-loop to a controllable, frequency selective element of the laser. In the course of this work, both spectroscopy systems were changed from a configuration described as *dichroic-atomic-vapor laser lock* (DVALL) in [113], to Doppler-free saturation spectroscopy [114]. The DWALL-method directly provided a dispersive lock signal. However, this signal was subject to long term temperature-dependent offset drifts and hence did not provide enough stability. In the improved spectroscopy configuration, the branches of the laser beams entering the spectroscopy cells, are frequency-modulated by AOMs (in Fig.4.3: AOM 4 and 5). Absorption-signals are generated by photodiodes which measure the power of the laser beams going through the vapor cells. Through demodulation with lock-in amplifiers, dispersive lock signals are produced. Fig. 4.4 shows both the absorption spectra and the demodulated lock signals used to frequency stabilize the MOT master and the repumper laser. The measured linewidths of the lock signals for the MOT master laser and the repumper are ≈ 9MHz and ≈ 14MHz, respectively. The difference to the natural linewidth

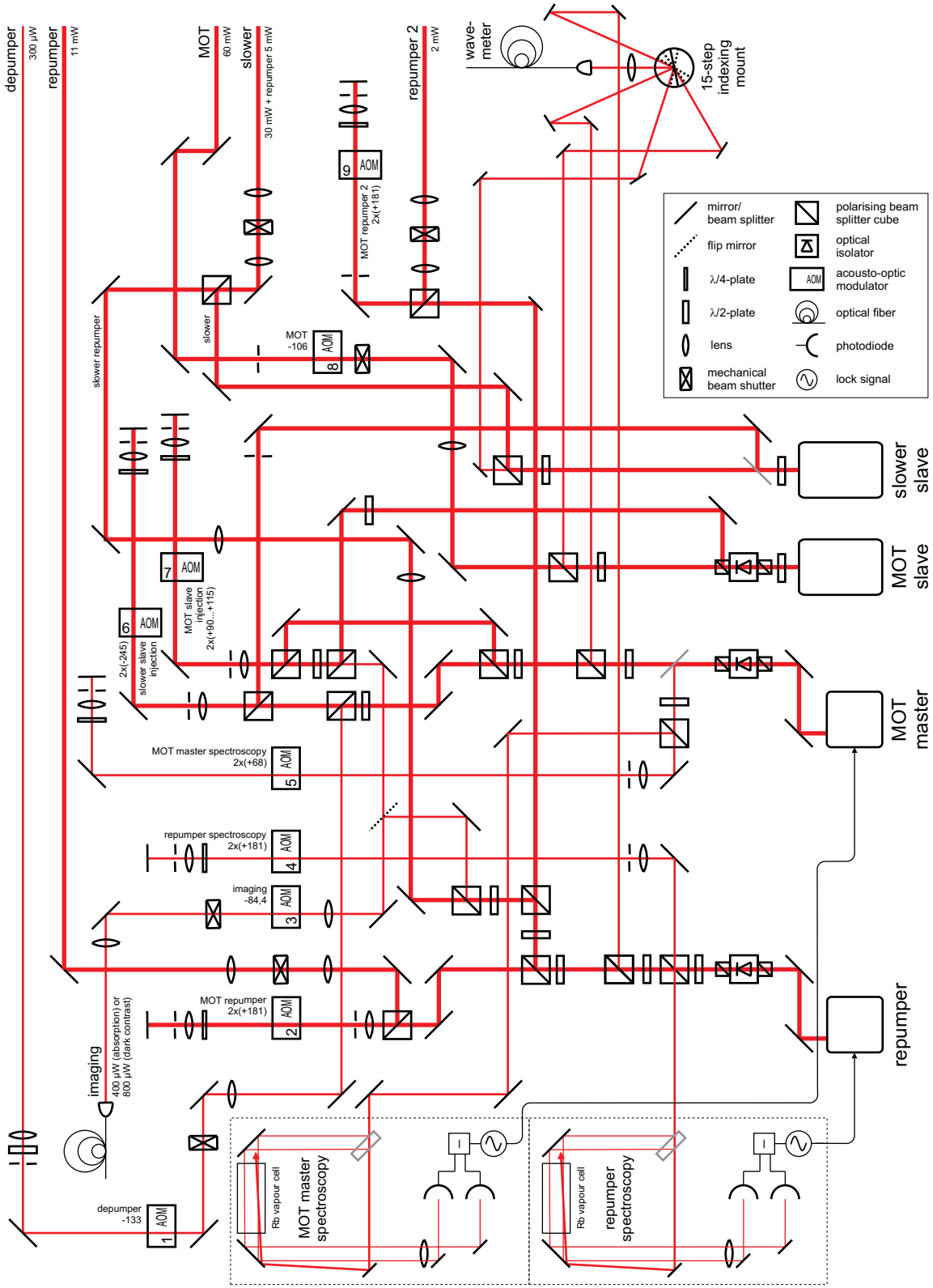

Figure 4.3: *Laser system for* ^{87}Rb.

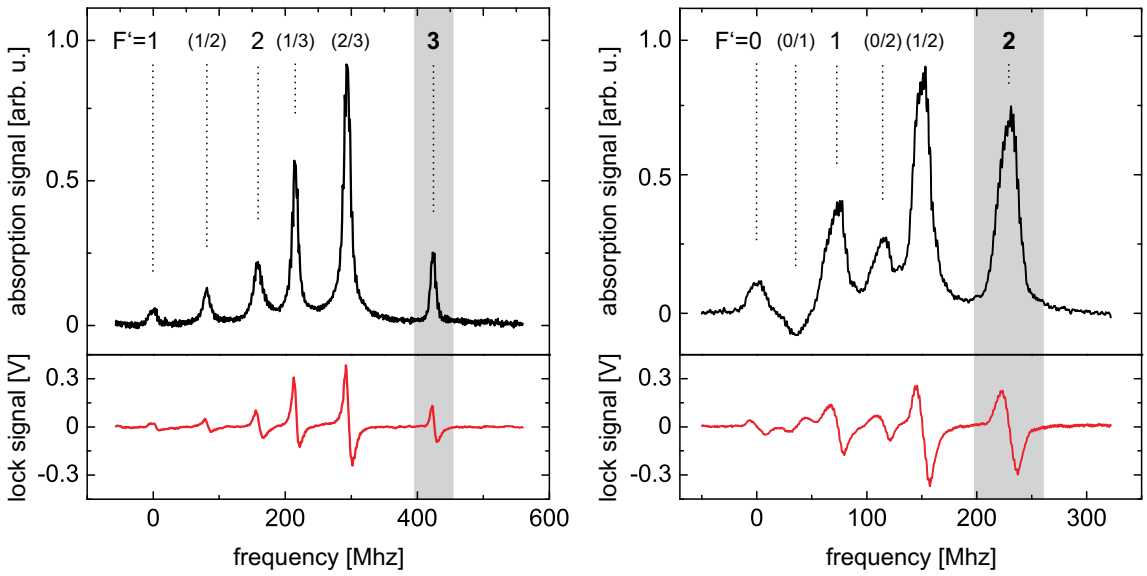

Figure 4.4: *Absorption spectra (black) and lock signals (red) for (a) the MOT master ($F = 2$) and (b) the repumper ($F = 1$) laser frequency stabilization. The hyperfine structure of the ^{87}Rb $5^2P_{3/2}$-level is well resolved and the peaks are labeled by the total angular momentum quantum number F' of the excited state. Additionally, so-called crossover peaks are located in the center between two hyperfine peaks and result from the characteristic spectroscopy method used here. They are labeled by (i/j), where i, j relate to the involved hyperfine levels. See [114] for details. The gray areas indicate the peaks used for laser frequency stabilization. The frequency axes are calibrated by the outermost peaks in each spectrum.*

of this transition, which is $\gamma/2\pi = 6.06$ MHz [115] results from saturation- and pressure-broadening effects. Due to the lock-in technology used here, the lock signals are free of offset drifts and are less susceptible to temperature changes.

The lock signals are passed to PI-loops and the resulting signals control the position of the external grating of the lasers through a piezo-crystal. Thus, frequency stabilization can be achieved as the external cavity, consisting of the laser diode and the grating, determines the actual laser frequency [112]. The bandwidth of the total locking loop however is limited by mechanical resonances of the external grating setup, that occur at acoustical frequencies in the range of ≈ 1 kHz. It turned out, that acoustical noise, for example created by mechanical beam shutters positioned on the same optical table as the lasers, led to short term laser frequency instabilities. Especially for the MOT master laser, which generates the light for resonant atom imaging, the lock system was not fast enough under mechanical noise.

To address this, the MOT master laser frequency stabilization has been refurbished to include two stages: The first stage is bandwidth limited by an electronic low-pass filter to ≈ 100 Hz and controls the external grating as described above. This stage provides long term stabilization and is able to compensate for large externally induced frequency

displacements. For the second stage, the lock signal is additionally used to control the MOT laser diode current, which is also a frequency selective parameter. The bandwidth of the diode current closed loop control is not subject to mechanical oscillations and can therefore be much higher, providing an improved short term stability. In the present setup, the bandwidth is limited to $\approx 5\,\mathrm{kHz}$ by the lock-in amplifier output lowpass, which results in sufficient short term frequency stability.

A quantitative estimation of the frequency stability can be made using the spectroscopy signals of the lasers in the locked state. For the repumper laser, a frequency stability of $\approx \pm 2.5\,\mathrm{MHz}$ is reached at a timescale of seconds, while the two stage MOT master system provides stability of $\approx \pm 0.85\,\mathrm{MHz}$.

Configuration of cooling laser beams The light generated by the MOT slave laser is split into 6 beams with beam diameters expanded to $\approx 15\,\mathrm{mm}$ before they enter the main vacuum chamber. The MOT repumper beam is superimposed to one of the MOT beams at the vacuum chamber. An obstacle is introduced into the repumping beam, to create the dark inner region for the dark spot-MOT (see Sec. 5.3.1).

The slower beam with the superimposed slower repumper is expanded to $\approx 30\,\mathrm{mm}$ before it enters the Zemann-slower and it is focused to the nozzle, where the atoms leave the Rb oven. The additional depumper- and repumper 2 beams are independently guided to the main chamber. In order to improve the pointing stability, the imaging light is guided through a optical single mode fiber while all other beams travel to the vacuum chamber through free space. The power of all independent beams entering the vacuum chamber, is specified in Fig. 4.3.

4.2.2 Yb MOT

In the present experimental configuration, the ytterbium MOT uses the atomic Yb $^1\mathrm{S}_0 \rightarrow {}^3\mathrm{P}_1$ intercombination line at 555.8 nm for cooling and trapping. Unlike in ^{87}Rb, there

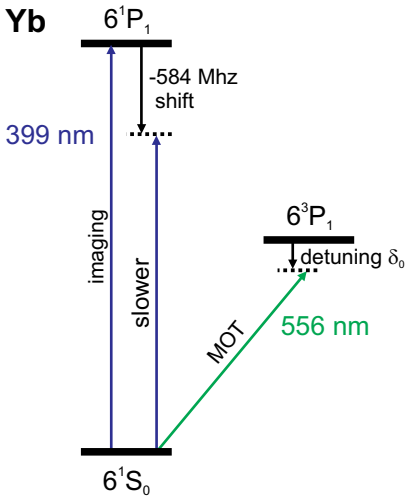

Figure 4.5: *Relevant atomic levels of Yb and laser beams used in the preset experimental setup for the Yb MOT and for Yb detection.*

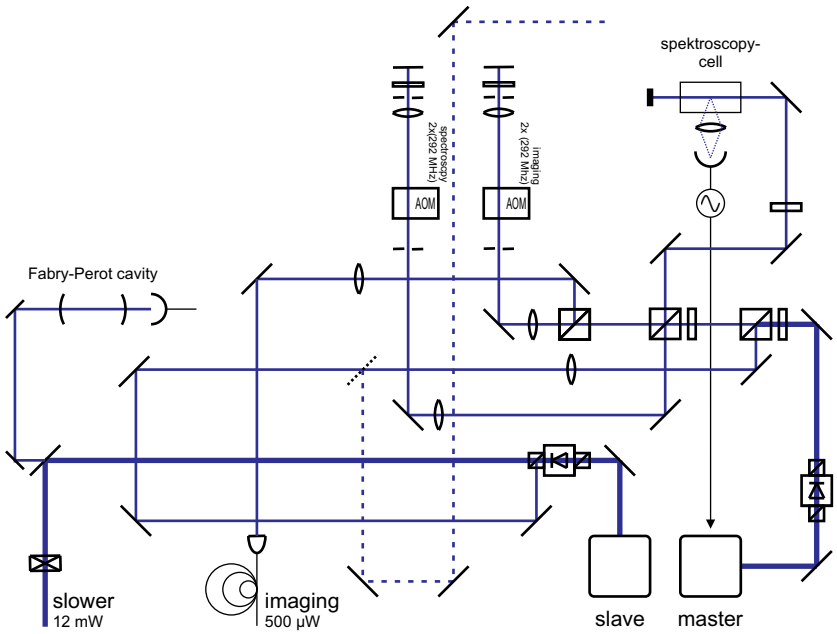

Figure 4.6: *399 nm laser system for the Yb Zeeman-slower and for resonant Yb imaging.*

are virtually no losses to other states and therefore no additional repumper is required. The intercombination transition is semi-forbidden, as it involves an electronic spin change from a singlet to a triplet configuration. This leads to a quite narrow line width of $\gamma_{556} = 2\pi \times 181\,\mathrm{kHz}$ [116].

The Zeeman-slower for Yb uses the $^1S_0 \rightarrow {}^1P_1$ transition at 398.9 nm. This transition has a line width of $\gamma_{399} = 2\pi \times 28\,\mathrm{MHz}$ and allows a fast deceleration of the atoms in the slower. Resonant imaging of Yb atoms is also performed at this wavelength. A diagram of the relevant atomic levels of Yb and the laser beams used for the Yb MOT and for Yb detection is shown in Fig. 4.5. In the course of this work, we were able to cool and trap ^{173}Yb in a MOT for the first time in the existing experimental setup, hence the necessary requirements for this specific isotope are highlighted in the following.

399 nm light

At 399 nm, two laser beams with different frequencies are required: First, the imaging beam, which is resonant with the Yb $^1S_0 \rightarrow {}^1P_1$ transition and second, the slower beam which is shifted by $\approx 584\,\mathrm{MHz}$ with respect to this transition. As in Rb, this detuning compensates the Doppler shift for the fast atoms entering the increasing field Zeeman slower.

Light generation The laser light at 399 nm is generated by a diode laser system in master-slave configuration (master diode: Nichia NDHV310ACAEI, 399 nm, 30 mW; slave diode: Nichia NDHV310APC, 401 nm, 60 mW). The master ECDL, whose setup is identical to

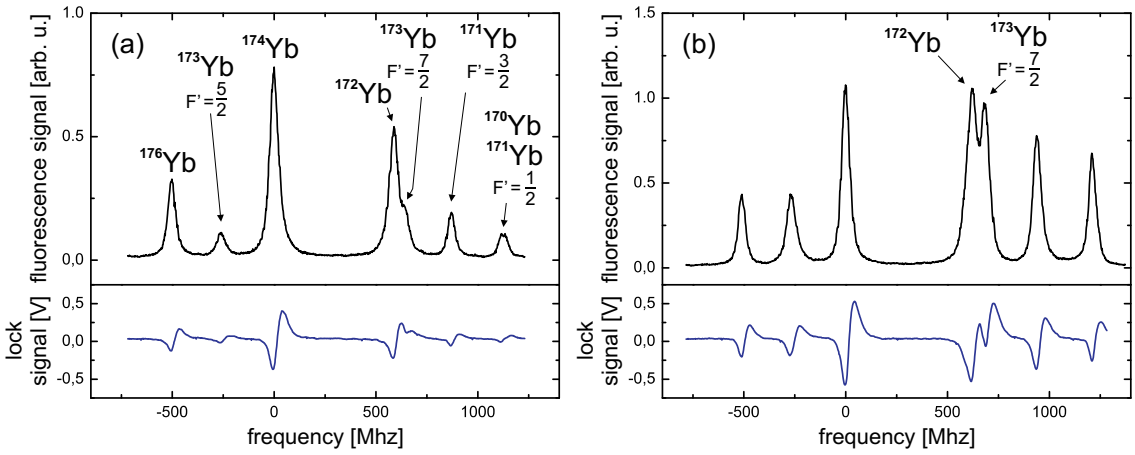

Figure 4.7: *Fluorescence spectra in natural isotopic mixture of Yb (black) and lock signals (blue) for the 399 nm master laser frequency stabilization. The peaks are labeled by the corresponding Yb isotope and in the case of fermionic isotopes by the excited state hyperfine level. (a) Linear polarization is used. (b) Circular polarization leads to a relative intensity change of the fermionic lines. Adapted from [9].*

the Rb MOT master and repumper laser, is frequency stabilized to a spectroscopy signal. A small portion of its light is injected into the slave laser, acting simply like an amplifier, which produces $\approx 12\,\mathrm{mW}$ of usable light for the slower. Another branch of the master laser beam, which is frequency-shifted to the $^1\mathrm{S}_0 \rightarrow {}^1\mathrm{P}_1$ transition and guided through a single mode optical fiber, is used for Yb imaging. In the current configuration, 500 μW of light are present after the fiber. A schematic of the 399 nm laser system is shown in Fig. 4.6. Further details on the 399 nm laser system can be found in [9, 11].

Spectroscopy at 399 nm For the 399 nm master laser frequency stabilization we carry out fluorescence spectroscopy on an collimated atomic Yb beam in a separate vacuum chamber [9]. The use of a simple vapor cell, similar to the Rb spectroscopy, is impractical for Yb due to its low vapor pressure at accessible temperatures. To generate a lock signal, the spectroscopy laser beam is frequency modulated and the fluorescence signal, which is recorded by a photo-multiplier tube (PMT), is demodulated by a lock-in amplifier. Like in the Rb repumper stabilization setup, the lock signal controls the external grating position of the 399 nm master laser to stabilize its frequency. The resulting frequency stability is $\approx$ 7 MHz on a timescale in the order of seconds. An additional diode-current lock, as implemented for the Rb MOT master laser is not required here, because the large natural line width of $\gamma_{399} = 2\pi \times 28.0\,\mathrm{MHz}$ [116] allows a less accurate frequency stabilization. Furthermore, no mechanical beam shutters, which could induce short term instabilities, are located on the same optical table as the 399 nm lasers. The fluorescence spectrum and the corresponding lock signal is shown in Fig. 4.7. The measured line widths are on the order of $\approx 50\,\mathrm{MHz}$, determined by Doppler-broadening due to nonzero transversal atom velocities in the slightly diverging atomic beam. The large number of observed lines in

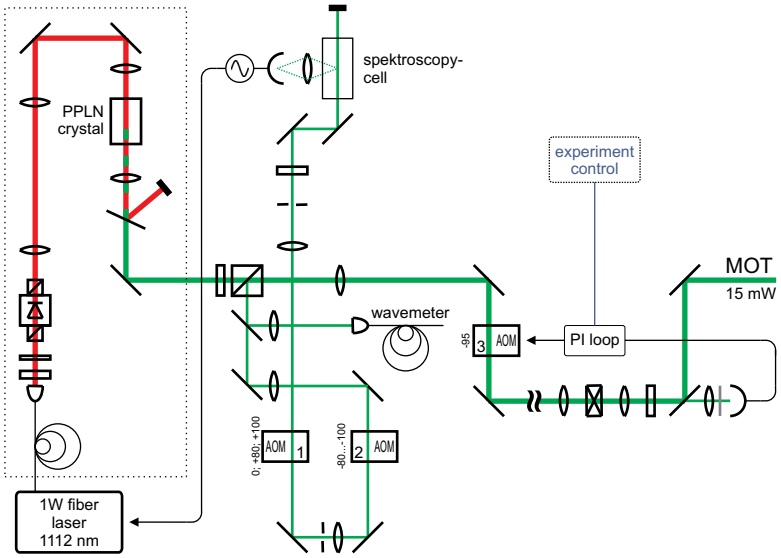

Figure 4.8: *556 nm laser system for the Yb MOT.*

the fluorescence spectrum is due to the individual isotopes in the natural isotope mix. Additionally, for fermionic isotopes, the hyperfine structure of the $^1P_1$ excited state is resolved. By changing the polarization of the spectroscopy light from linear (Fig 4.7 (a)) to circular (Fig 4.7 (b)), we observe a change in the relative intensity of the fermionic lines with respect to the bosonic lines. This effect is related to the angular dependence of the fluorescence of the Yb atoms. For circular polarization, the lines resulting from ^{172}Yb and ^{173}Yb $|F' = 7/2\rangle$ can be resolved.

The 399 nm master laser can be frequency stabilized to lines of 4 bosonic isotopes (^{170}Yb, ^{172}Yb, ^{174}Yb and ^{176}Yb) and 2 fermionic isotopes (^{171}Yb, $|F' = 3/2\rangle$ and ^{173}Yb $|F' = 7/2\rangle$). In the Zeeman-slower, only the corresponding isotope is addressed and filtered out of the natural isotopic mixture for further cooling and trapping in the MOT.

556 nm light

In the course of this work, the generation of light at 556 nm used for the MOT transition in Yb, was changed from a dye laser system to a configuration, where light at 1112 nm is frequency doubled to 556 nm. The infrared light is produced by a 1 W fiber laser (Koheras Boostik BoY10PztS, specified line width: < 40 kHz) and sent through a periodically poled lithium niobate (PPLN) crystal in a single pass configuration. The PPLN crystal is temperature stabilized to ≈ 180 °C and it is located at a focus of the 1112 nm light. For maximum conversion efficiency, the beam parameters are carefully adjusted to match the geometric properties of the PPLN crystal. Residual infrared light is separated from the 556 nm beam after the crystal by a dichroic mirror and sent to a beam block. With this setup, which is shown in Fig. 4.8, ≈ 25 mW of green light are produced.

In the 556 nm laser system, beams for spectroscopy and the wavemeter are branched

of, before the light is sent to the vacuum chamber. AOM 2 shifts the spectroscopy light, which is stabilized to the $^1S_0 \rightarrow {}^1P_1$-transition, by +97 MHz and frequency modulates it for lock-in detection. The additional AOM 1 is only used for fermionic isotopes (see below). The frequency shifts of AOM 1 and AOM 3 is compensated by AOM 3, which has a frequency range of $+88 \ldots +100$ Mhz leading to an adjustable MOT light detuning of $\delta_0 = -9 \ldots +3$ MHz. AOM 3 is also used for fast switching and is part of an adjustable power stabilization system, which additionally consists of a photodiode and a PI-loop control. For the power stabilization, residual light, which leaks through one of the mirrors, is used. The PI-loop electronic compares the photodiode level to the set point given by the experiment control system. It acts on the power input of AOM 3 to stabilize the 556 nm Yb MOT light power to an adjustable level.

Frequency stabilization We use the fluorescence signal of the Yb $^1S_0 \rightarrow {}^3P_1$ intercombination transition to stabilize the 556 nm light frequency. The spectroscopy is performed on the same atomic beam, which is used for the 399 nm diode laser. The green light, however enters the spectroscopy vacuum chamber through a different window and fluorescence is detected by an additional PMT. The observed peaks in the Yb $^1S_0 \rightarrow {}^3P_1$ spectrum have a line width of ≈ 5 MHZ. Although the atomic beam is further collimated before it enters the 556 nm spectroscopy region, Doppler broadening is still the dominating line-broadening effect here. When the laser is stabilized using the green spectroscopy signal, the stability is better than ± 0.08 MHz. The dispersive lock signal is generated by the same frequency modulation technique, which is used for the Rb lasers and for the 399 nm diode laser. The lock signal is sent to the internal piezo of the 1112 nm fiber laser, which controls its wavelength in a range of 18 pm when the full voltage range of $0 \ldots 200$ V is used. This translates to a total scan range of ≈ 8.7 GHz for the 556 nm light, allowing the $^1S_0 \rightarrow {}^3P_1$-lines of all isotopes to be observed in a single sweep. A recorded spectrum with magnified regions, that are relevant for frequency stabilization on the fermionic isotopes is shown in Fig. 4.9. In addition to the isotope shift and hyperfine splitting of fermionic isotopes, Zeeman-splitting of the fermionic lines can be resolved in this spectrum. The Zeeman-splitting results from a well-defined magnetic field, which is created by a permanent magnet sitting on top of the spectroscopy vacuum chamber. The field vectors are aligned with the atomic beam axis and with the polarization vector of the linearly polarized spectroscopy light. The additional magnetic field provides a well defined quantization axis and splits the spectroscopic lines into well separated Zeeman components.

Note, that for the states used in the following description, Russel-Saunders (or L - S) coupling of the individual orbital angular momenta and spins of the Yb 6s electrons can be used [118]. In the case of bosonic isotopes, the situation is simple: The $^1S_0$ ground-state has total angular momentum $J = 0$ and lacks magnetic sub-structure. In contrast, the $J = 1$ excited state has a magnetic moment with magnitude and the magnetic sub-states $m_J = \pm 1$ acquire a Zeeman shifted energy relative to the $m_J = 0$ sub-state. However, in the present configuration only the unshifted π-transition with a spin-change $\Delta m_j = 0$ is driven by the spectroscopy light and no additional peaks appear. Hence, in order to frequency stabilize the 556 nm laser for cooling and trapping of bosonic Yb isotopes, the

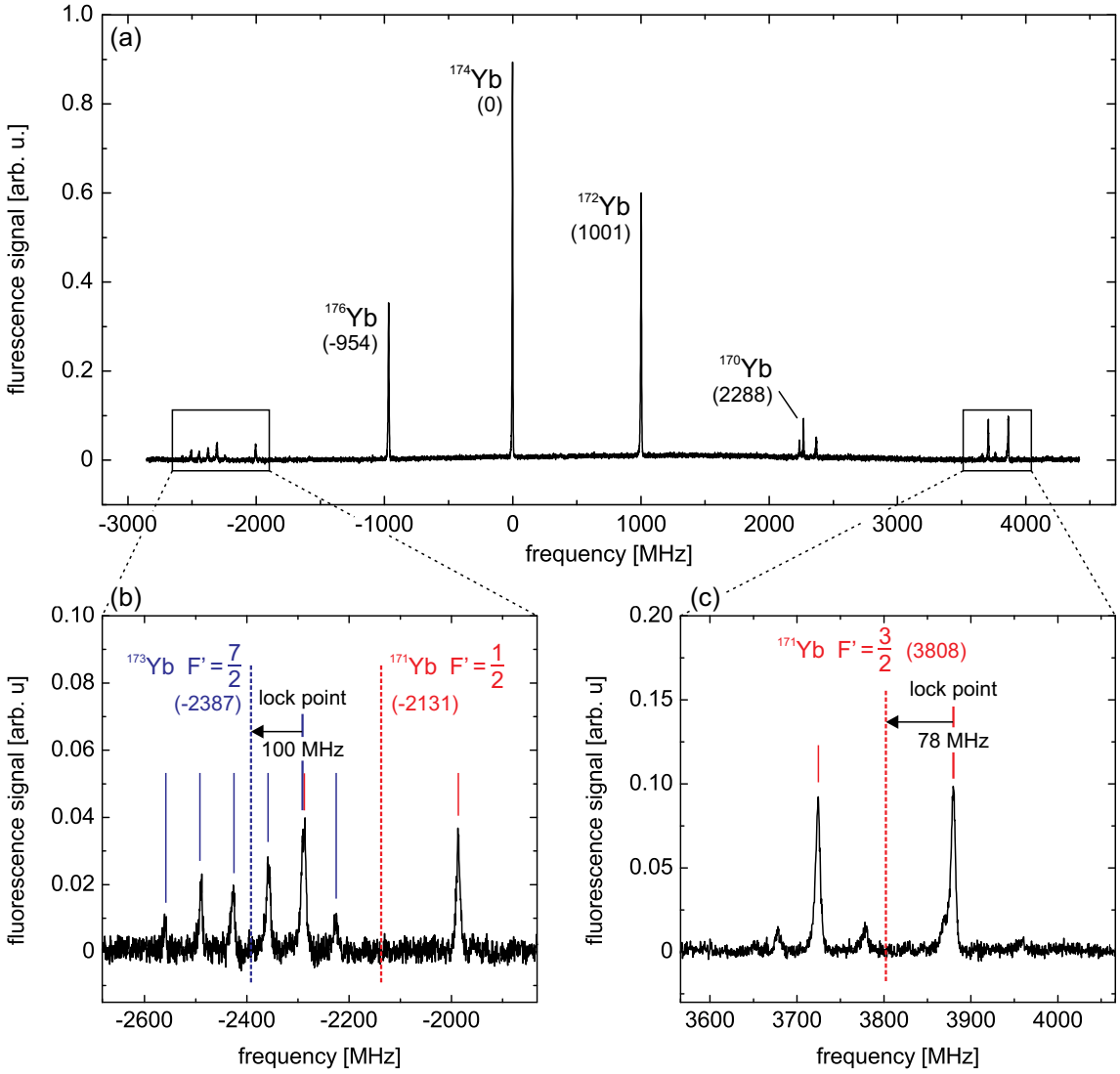

Figure 4.9: *Fluorescence spectrum of the Yb* $^1S_0 \rightarrow {}^3P_1$*-transition. The frequency-axis is calibrated with wavemeter data and shown with respect to the* ^{174}*Yb-line, which corresponds to a measured wavelength of 555.8049 nm. The lines, which are relevant for the present experiment, are labeled by the originating isotope, if necessary by hyperfine-sublevel and by the frequency difference in MHz relative to the* ^{174}*Yb-line (data from [117]). (a) shows the full sweep, while (b) and (c) are zoomed regions relevant for frequency stabilization on the fermionic isotopes.*

corresponding spectroscopy peaks can be directly used.

For fermionic isotopes, the situation is more complex, as a nonzero nuclear angular momentum leads to hyperfine splitting into states with total spin F. In the presence of a weak magnetic field[1], these states are split into sub-levels m_F with an energy shift [119]

$$E_Z = m_F \, g_F \, \mu_\mathrm{B} \, B, \tag{4.1}$$

with the Bohr Magneton μ_B and the hyperfine-structure Lande g-Factor

$$\begin{aligned} g_F = \; & g_J \frac{F\,(F+1) + J\,(J+1) - I\,(I+1)}{2\,F\,(F+1)} \\ & - g_I \frac{m_e}{m_p} \frac{F\,(F+1) + I\,(I+1) - J\,(J+1)}{2\,F\,(F+1)}. \end{aligned} \tag{4.2}$$

Here, I and J are the total nuclear- and electronic angular momentum quantum numbers, while m_e and m_p are the electron- and proton mass. Values for the nuclear g-factor g_I can be found in the literature and under the approximation that the electron g-factor $g_s = 2$, the fine-structure Lande g-Factor is

$$g_J \approx 1 + \frac{J\,(J+1) - L\,(L+1) + S\,(S+1)}{2\,J\,(J+1)}, \tag{4.3}$$

with L and S being the orbital angular momentum- and spin quantum numbers of the corresponding level.

Figure 4.10 summarizes the quantum-numbers, the Lande-g-factors and the resulting Zeeman-splitting of levels relevant for ^{171}Yb and ^{173}Yb frequency stabilization. Values for the nuclear g-factor g_I are taken from [116]. Note that for the ground-state, the first term in Eq. 4.2 vanishes and the second term is small due to the electron-proton mass-ratio of $\approx 1/1836$. Hence, the ground-state Zeeman-splitting is negligible.

Under the conditions described here, the spectrum shown in Fig. 4.9 can be explained as followed. For π-light, the ^{173}Yb $|F' = 7/2\rangle$-level splits into 6 equally separated Zeeman-lines (see Fig. 4.9 (b)) with a mean frequency difference of $\approx 66\,$MHz. According to Eq. 4.1, this line separation can be attributed to a magnetic field with magnitude $B_0 \approx 110\,$Gauss. The ^{171}Yb $|F' = 1/2\rangle$-level is energy shifted by 255.1 MHz [117] from the center of the ^{173}Yb $|F' = 7/2\rangle$-manifold. The magnetic field with magnitude B_0 leads to a splitting into two lines separated by $\approx 308\,$MHz (measured separation: $\approx 305\,$MHz). In the present configuration, the ^{171}Yb $|F' = 1/2, m'_F = -1/2\rangle$-line coincides with the $|F' = 7/2, m'_F = 3/2\rangle$-line leading to a increased joint peak, which is used for frequency stabilization on ^{173}Yb. The frequency difference of $\approx -100\,$MHz to the center of the ^{173}Yb $|F' = 7/2\rangle$-manifold is compensated by an additional AOM (in Fig. 4.8: AOM 1), which is operated at $+100\,$MHz, when ^{173}Yb is addressed.

Cooling and trapping of ^{171}Yb uses the ^{3}P$_1$ $|F' = 3/2\rangle$-level, which splits into 2 Zeeman-lines separated by $\approx 154\,$MHz at the presence of a magnetic field with magnitude B_0

[1] This description is valid only for the case, where the Zeeman energy E_Z is small compared to the energetic separation of hyperfine levels. Here, $\vec{I}$ and $\vec{J}$ are strongly coupled to $\vec{F}$, which precesses around the external magnetic field axis, resulting in linear Zeeman effect [119]

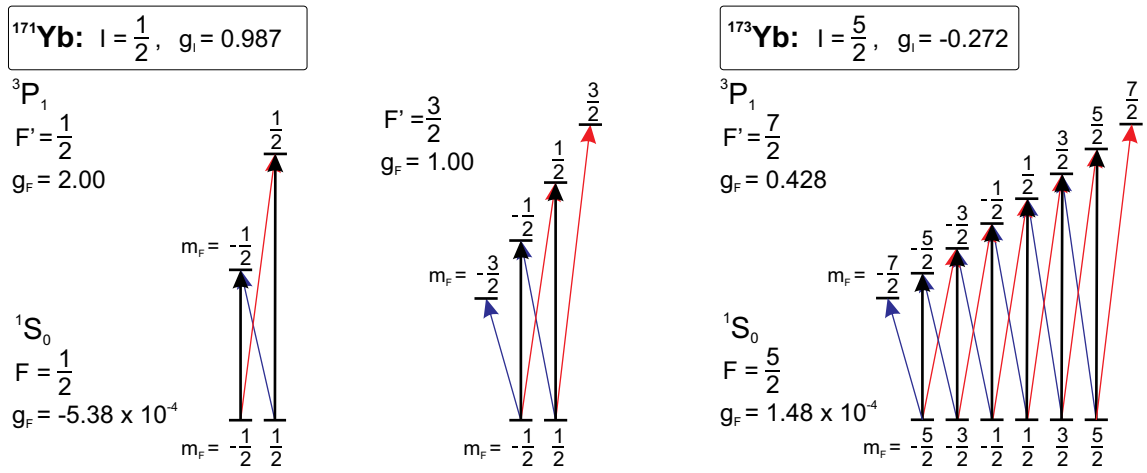

Figure 4.10: *Zeeman-splitting of the levels relevant for ^{171}Yb and ^{173}Yb frequency stabilization. Note that the relative energy shifts of excited state levels are drawn to scale. Black arrows indicate π-transitions, red and blue arrows show σ^+ and σ^- transitions.*

(measured separation: ≈ 155 MHz). The 556 nm light is frequency stabilized on the $|F' = 3/2, m_F = 1/2\rangle$-line and AOM 1 is run at +77 MHz to compensate for the Zeeman-shift.

In total, the Yb MOT can be operated with all stable Yb isotopes except ^{168}Yb (relative abundance only 0.13 % [116]). Switching between the different isotopes only requires, to change the 556 nm- and the 399 nm light frequency stabilization to the corresponding spectroscopy lines.

Configuration of the MOT and slowing beams

The 556 nm MOT light is split into three beams with beam diameters of ≈ 8 mm, which are then retro-reflected to complete the trap. This configuration complicates the process of adjusting the MOT, but it makes the best use of the limited amount of ≈ 15 mW of stabilized power. The Yb Zeeman-slower is operated with ≈ 12 mW of blue light at 399 nm, which is expanded to a beam diameter of ≈ 15 mm and focused onto the Yb oven nozzle. Blue Yb imaging light is superimposed to the ^{87}Rb imaging beam by a dichroic mirror to allow maximum flexibility in the imaging system (see Sec. 4.3 for details). All three beams described here can be independently switched on and off with mechanical beam shutters located on the optical table, which hosts the vacuum chamber.

4.2.3 Optical dipole trap

The bichromatic optical dipole trap (BIODT) used in this experiment provides the optical potentials for cold Yb and Rb atoms and is a powerful tool that allows independent trapping and manipulation of the two species. Details on the bichromatic approach as well as calculations and model potentials can be found in Chap. 5 and 6.

This section describes the experimental realization of the optical potentials.

Requirements

The BIODT consists of two parallel superimposed laser beams at 532 nm and 1064 nm, with the following beam parameter:

- 532 nm beam
  - Gaussian beam waist w_0: $\approx 15\,\mu$m
  - maximum light power: ≈ 3.5 W, minimum light power: ≈ 35 mW
  - relative power stability: better than 1% within the total range
- 1064 nm beam
  - Gaussian beam waist w_0: $\approx 15\,\mu$m
  - maximum light power: ≈ 200 mW, minimum light power: ≈ 10 mW
  - relative power stability: better than 1% within the total range
- relative lateral position control: $\approx 1\,\mu$m accuracy
- relative lateral position stability: $< 1\,\mu$m within the total power range

Setup

The light for the BIODT is generated by a diode pumped solid state (DPSS) laser (Coherent Verdi V10, 10 W, 532 nm) and a fiber laser (IPG PYL-20M-LP, 20W, 1064 nm). The complete laser system for the BIODT is outlined in Fig. 4.11.

The optical system for the infrared beam at 1064 nm was originally designed in a previous work and details can be found in [9]. It is left unchanged for the present experiments.

In contrast, the system for the green ODT at 532 nm was completely redesigned in the course of this work, in order to improve pointing- and power stability. As the 532 nm DPSS laser, which is located on the vacuum chamber table, produces more output than used in the present configuration, part of the light is branched of by a polarizing beam-splitter cube and sent to a beam dump. The beam diameter is first reduced by a telescope to a collimated beam that matches the geometric properties of the switching AOM and the power control electro optic modulator (EOM). Afterwards, the beam aspect ratio is adjusted with a telescope consisting of cylindrical lenses. By precisely changing their distance with a micrometer translation stage, it is also possible to compensate astigmatism. In the next stage, the beam radius is magnified to ≈ 5.5 mm, before it is focused into the vacuum chamber by a $f = 500$ mm-achromatic lens. One of the lenses in the magnifying telescope is also mounted on a micrometer translation stage, which allows precise adjustment of the axial focal position in the vacuum chamber. Under the assumption of Gaussian beam shapes, the specified beam radii w_L lead to a rough estimation of the beam waist $w_0 \approx 15\,\mu$m, according to $w_0 = \lambda f/\pi\, w_L$ [120]. A more precise determination of the beam parameters is presented in Sec. 6.1.2.

In the 532 nm ODT optical system, the AOM (Isomet 1205C-2) is only used for fast beam turn-off only, as power adjustment with this AOM led to uncontrollable beam pointing instabilities. We clearly observed a power dependent angle deviation of the beam with

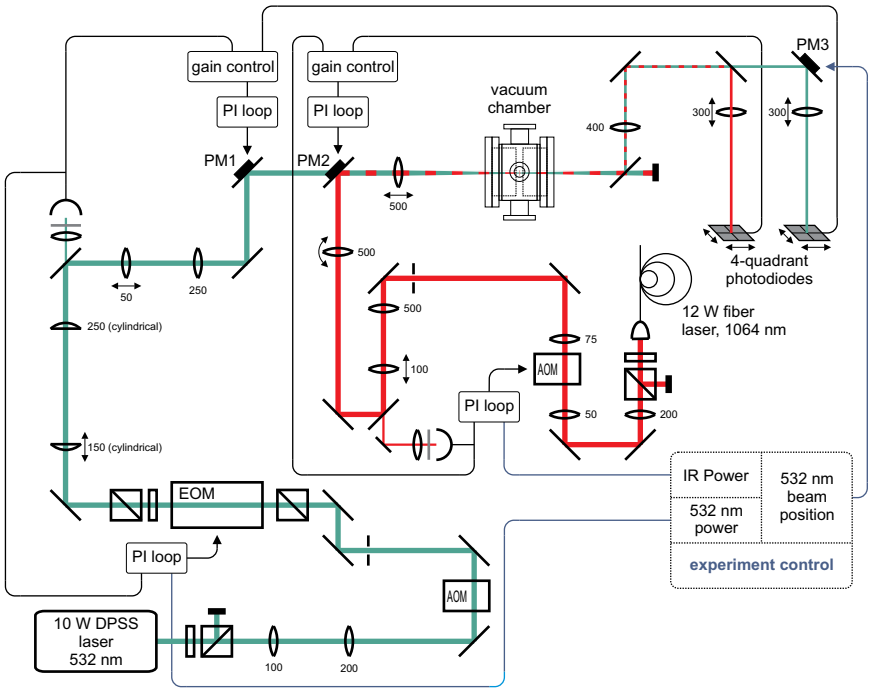

Figure 4.11: *Laser system for the BIODT and electronic equipment for position- and power-stabilization.*

respect to the optical axis. One solution to this problem, which is realized in the 1064 nm ODT system, is placing the AOM in the beam's focus. In this configuration, the focal point inside the vacuum chamber is an optical image of the focus inside the AOM. Therefore, angle deviations are compensated in a first order approximation for this exact point. In the green system, however, increased light absorption in the AOM crystal leads to thermal lensing effects for high optical densities, which excludes the option of using a focal point inside the 532 nm AOM.

In order to overcome this problem, we use an EOM (Linos LM 0202 VIS 5W), which is placed between two crossed thin-film polarizing cubes (Linos G335-713), to control the 532 nm power. This setup provides a measured extinction ratio of >1/200, meeting the specified requirements. For power stabilization, a photodiode, which is placed behind one of the mirrors, is used. An electronic circuit compares this value with a set point given by the experimental control board and a PI loop sends the resulting signal to the power control EOM. With this setup, a relative stability of better than 1% within the total range is provided. An identical power stabilization system is implemented in the 1064 nm ODT beam setup leading to similar results.

Position stabilization

As stated above, a continuous operation of the BIODT requires, that the beam foci are superimposed with a relative lateral stability of $< 1\,\mu$m. However, a free running system

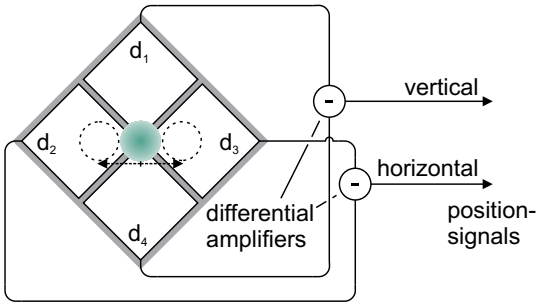

Figure 4.12: *Wiring scheme of the 4-quadrant photodiode used for the 532 nm ODT beam position stabilization. The dashed circles indicate a complete beam displacement to one of the diodes d_2 or d_3 leading to a maximum horizontal position-signal of* ± 12 V.

is subject to both short term instabilities such as mechanical vibrations or acoustical noise and long term drifts caused for example by thermal expansion of the whole setup.

In order to achieve the required stability, an active position stabilization system for both the 532 nm and the 1064 nm beams is implemented in the BIODT setup, which is shown in Fig. 4.11. Additionally, we included a piezo-driven position control for one of the beams, giving us the possibility, to adjust the relative beam position on a μm-level. The present configuration is a redesign of the original setup described in [9] with improved long-term stability and independence of the BIODT beam power. As the optical part is unchanged compared to the work of Tassy [9], I will emphasize the electronic part of the present system.

After the vacuum chamber, the beams are independently imaged on two 4-quadrant photodiodes (Hamamatsu S6695-01, 2x2 mm active area, 15 μm gap) to monitor their position. A careful adjustment procedure ensures, that the exact position of the focal plane and with it the center of the trapping potential is imaged on the 4-quadrant odiodes. The 4-quadrant photodiodes are rotated by 45° in a plane perpendicular to the beam axes. The difference signal of two opposit diodes is generated electronically, in order to create horizontal and vertical beam-position signals (see Fig. 4.12). The gain of this first stage is adjusted to span ± 12 V, when the light with maximum power is completely directed on one or the other of the oppositely arranged diodes (represented by the dashed circles in Fig. 4.12). When the optical power of the ODT beams is modified, the position-signals generated by the 4-quadrant photodiodes and hence the overall gain in the PI loop control changes. We observed, that especially for low BIODT powers (down to 1 % of the original magnitude), the position lock did not provide enough stability, causing the beams to drift apart. To compensate for that, we implemented a gain-control stage in the position stabilization, which controls the signal gain depending on the used optical power in the ODT beams. This gain-control works as a divider and it is realized digitally with a LabView-based progam on a PC. For fast input and output, we use a National Instruments I/O-card (NI PCI-6229), which provides 16 Bit analog-digital- and digital-analog-conversion at a total speed of 250 kS/s. The gain control simultaneously runs for 4 channels (2 directions for each ODT beam) and uses the power detection photodiode signal of each beam as a divider for the respective beam position signal. An actual signal delay of $\approx 100\,\mu$s is introduced by the digital gain-control stage. The maximum gain (minimum divisor) is limited, to avoid large amplification of signals with small signal-to-noise ratios.

After the gain-control and a PI-loop electronic stage, the signals are used to control the corresponding axis of piezo-equipped mirror mounts (in Fig. 4.11: PM1 and PM2), which determine the radial ODT beam focal position inside the vacuum chamber. We use Thorlabs KC1-T-PZ mirror mounts, which provide ±18 arcsec piezo adjustment at an input voltage range of 0 . . . 150 V (an amplification stage matches the signals to this voltage range). The stabilization system keeps the imaged focal points of the beams at the center of the 4-quadrant detector and thus the lateral trap positiosn at a fixed point. The bandwidth of this feedback loop is limited by mechanical oscillations of the piezo-mounted mirrors to ≈ 200 Hz. However, in the present configuration we electronically limit the bandwidth to ≈ 10 Hz, which is sufficient to compensate relevant pointing instabilities. The bandwidth limitation however enables us to increase the DC gain and at the same time prevent the system from oscillating.

The actual position stability can simply be estimated from the beam position signal provided by the 4-quadrant phododiodes: Assuming a beam radius of ≈ 12 μm (the focus is reduced by a factor 3/4 by the imaging system), and the maximum detector signal of 12 V, which is generated, when the beam is completely displaced to one of the diodes, the 4-quadrant phododiode output voltage can be translated into a position. In the present case, this estimate implies a short term stability on the order of ±0.1 μm for both ODT beams. A day-to-day long term drift of $< 1\,\mu$m is observed, which provides enough stability for a convenient operation of the experiment.

Position control The accuracy required to adjust the relative ODT beam position exceeds the precision, which is achieved by mechanical tuning on the corresponding mirror mounts. Hence, a piezo-driven position control system is included in the BIODT position stabilization system. One of the mirrors in the 532 nm beam stabilization imaging path is piezo-equipped (in Fig. 4.11: PM3), which allows a precise beam position adjusting on a sub-μm level. When the angle of PM3 is changed, the beam is dislocated from the 4-quadrant photodiode center. The position stabilization loop compensates this through PM1, leading to an effective lateral 532 nm ODT displacement inside the vacuum chamber. We measured the actual position of atom clouds trapped in the 532 nm ODT as a function of the corresponding piezo voltage on PM3, which is shown in Fig. 4.13. The ODT position is determined with absorption images that provide a resolution of ≈ 5 μm. The total displacement range is limited to ≈ 60 μm, determined by the maximum adjustment range of PM1. A pre-adjustment to this level is possible by mechanical tuning on the corresponding axis on PM3. Within this range, the beam position depends linearly on the corresponding piezo voltage, which is indicated by the red line in Fig. 4.13. The sensitivity of this position control is ≈ 1.1 μm/V horizontally and ≈ 0.88 μm/V vertically. The discrepancy between the two axes can be explained by asymmetries in the optical system caused by imperfect alignment. The piezo voltage is controlled at a level of ≈ 0.1 V, leading to a mean position accuracy of $\ll 1\mu$m for both directions.

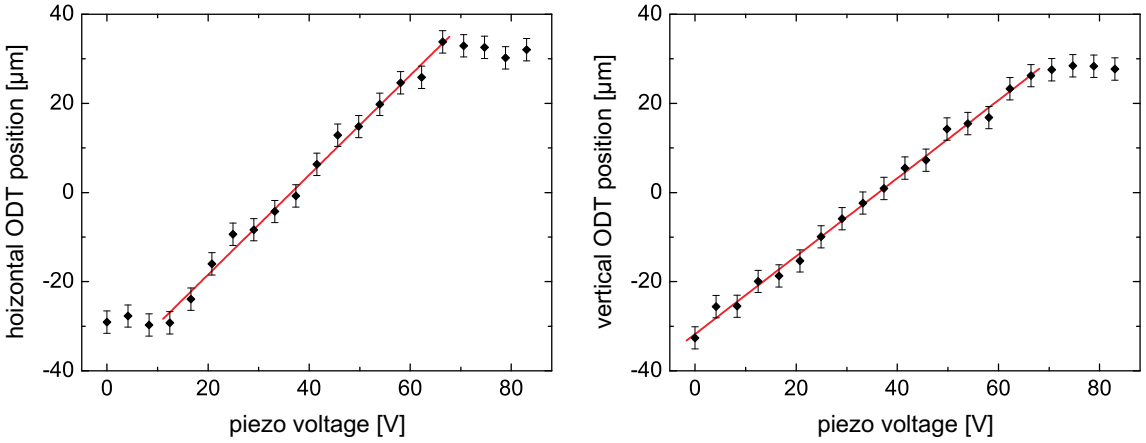

Figure 4.13: *Measured (a) horizontal and (b) vertical 532 nm ODT positions as a function of the corresponding piezo voltage on PM3. Outside the linear regions (indicated by the red lines), the beam displacement on the 4-quadrant photodiode can not be compensated by PM1, which limits the position adjustment range.*

4.3 Atom detection

The basic data obtained in our experiments, is the density distribution of ultracold Rb and Yb clouds. All further atomic cloud parameters, like atom number or temperature, are determined by elaborate analysis of these raw data. In order to gain the information about the atomic density distributions, optical methods are used. In general, interaction of atoms with a beam of light involves three processes, which are relevant for our detection schemes: absorption of photons, spontaneous re-emission of photons, and shifting the phase of the transmitted light. These properties are used in absorptive, fluorescence, and dispersive imaging methods, respectively.

In the following, the present configuration of the imaging system is described and the different imaging methods are introduced. Further information on technical details can be found in [8, 9]. In the course of this work, simultaneous imaging of both atomic species was performed for the first time in the existing setup. Furthermore, the method of dark contrast imaging was included in the setup, allowing the detection of high-density Rb clouds.

4.3.1 Imaging system

The imaging system used in the present experimental setup is shown in Fig. 4.14. It includes a photodiode and a PMT, which continuously monitor the Rb- and Yb MOT fluorescence and two cameras used for MOT alignment. Most importantly, the imaging system consists of three main charge-coupled-device (CCD) cameras used for atom detection in the actual experiments. Table 4.1 summarizes the camera and imaging properties as well as their operation methods in the present experiments. *Camera 3* has a different imaging scale than the other cameras and is able to image significantly larger clouds of atoms. In order to use this camera, an additional mirror is placed in the imaging path of *camera 1*. For

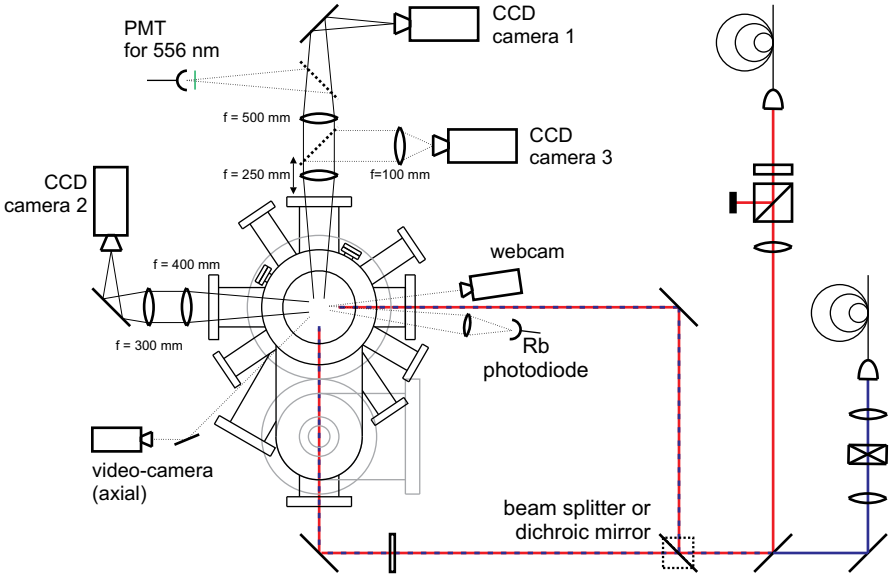

Figure 4.14: *Schematic diagram of the atom detection system.*

	camera 1	**camera 2**	**camera 3**
model	Finger Lakes Instrumentation MaxCam 7-E	ABS Jena UK1117	ABS Jena UK1117
CCD resolution	764×512 pixel	768×576 pixel	768×576 pixel
effective pixel size	4.37 × 4.37 μm/pixel	5.83 × 5.83 μm/pixel	20.3 × 20.3 μm/pixel
imaging region	3.34 × 2.24 mm	4.48 × 3.34 mm	15.6 × 11.7 mm
imaging method	absorption, dark contrast	absorption	fluorescence
atomic species	Yb/Rb	Yb/Rb	Rb

Table 4.1: *Cameras and imaging properties used in the present experimental configuration.*

precise focusing of this imaging path, the first lens in the imaging system is mounted on a micrometer translation stage. *Camera 2* is also mounted on a micrometer translation stage, which allows precise alignment of the horizontal imaging path. Imaging light at 399 nm and 780 nm, used for absorptive or dispersive imaging of Yb and Rb, is sent to the main chamber through single mode optical fibers before the two light fields are superimposed by a dichroic mirror. For imaging of either Yb or Rb by both cameras, the corresponding imaging beam is split into two branches by a beam splitting cube. On the other hand, if simultaneous imaging of both atomic species is performed, the beam splitting cube, which is mounted on a magnetic base is replaced by a dichroic mirror. It separates the 399 nm beam from the 780 nm beam. In this configuration, the Yb cloud is imaged in the horizontal plane by *camera 2*, while *camera 1* images Rb in the vertical plane.

4.3.2 Fluorescence imaging

For fluorescence imaging, resonant light is illuminating the atoms and the scattered light is detected. The scattering rate of an atom (given already in Eq.3.1) can be written as:

$$\Gamma = \frac{s_0\,\gamma/2}{1 + s_0 + \hat{\delta}^2}\,. \tag{4.4}$$

Here, the detuning $\hat{\delta} = \frac{\omega-\omega_0}{\gamma/2}$ of the laser light with frequency ω from the atomic resonance frequency ω_0 is given in units of half line widths $\gamma/2$. A total number of N atoms scatter light with a power $N\hbar\omega_0\Gamma$. Hence, by measuring the light power, which is scattered into a defined solid angle with a calibrated phododiode or camera, it is possible to determine the original atom number.

In the present experiment, we use *camera 3* for fluorescence imaging for temperature measurements of large and hot ^{87}Rb clouds trapped in the MT. Furthermore, ^{87}Rb atom number calibration also makes use of fluorescence images (see Sec. 4.3.5). We illuminate the atoms for a period of 100 μK with light from the MOT beams, which is tuned to resonance ($\hat{\delta} = 0$). The camera is triggered to take a picture with an exposure time that covers the illumination time. An additional picture without atoms is subtracted from the bright picture for background reduction. Note that resonant imaging of ^{87}Rb is performed using the $|F = 2\rangle \rightarrow |F' = 3\rangle$ transition of the D2 line. In the majority of experiments, however, the ^{87}Rb atoms reside in the $|F = 1\rangle$ ground state sublevel. Hence the repumper 2 beam is turned on for 0.7 ms before taking the first image in order to optically pump all ^{87}Rb atoms into the $|F = 2\rangle$ hyperfine level.

4.3.3 Absorptive and dispersive imaging

The method of absorption imaging uses resonant probe light and measures the absorption by the atomic cloud (see Fig. 4.15). On the other hand, for dark-contrast imaging, off resonant probe light is used and the phase-shift caused by the atoms is detected. In a general description, a cloud of atoms with density $n(x, y, z)$ attenuates and phase-shifts probe light with an incident amplitude $E_0(x, y)$, which propagates in the z-direction in the following way [121]:

$$E(x, y) \;=\; e^{-OD(x,y)/2} \cdot E_0(x, y)\, e^{i\,\phi(x,y)}. \tag{4.5}$$

The optical density $OD(x, y)$ and the phase shift $\phi(x, y)$ depend on the column density $\tilde{n}(x, y) = \int n(x, y, z)dz$ and the resonant cross section σ_0 according to

$$OD(x, y) \;=\; \tilde{n}(x, y) \cdot \sigma_0\, \frac{1}{1 + \hat{\delta}^2} \;=\; \tilde{n}(x, y) \cdot \sigma_\lambda \tag{4.6}$$

$$\phi(x, y) \;=\; -\tilde{n}(x, y) \cdot \sigma_0\, \frac{\hat{\delta}}{2(1 + \hat{\delta}^2)}. \tag{4.7}$$

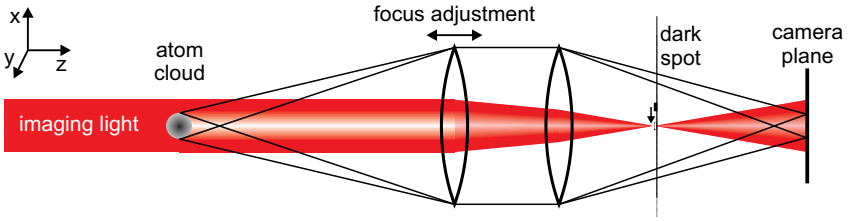

Figure 4.15: *Scheme of the absorptive and dispersive imaging. Resonant light is absorbed by the atom cloud and the residual light is imaged onto the camera plane (absorption imaging). For dark contrast imaging, off-resonant light is used and an opaque spot is introduced a focus of the imaging light to block unscattered light. The remaining scattered light is imaged on the camera plane.*

a) Absorption imaging For resonant probe light with an incident intensity $I_0(x, y)$, the measured intensity after passing the atoms is

$$\langle I_\mathrm{a}(x, y)\rangle = |E(x, y)|^2 = I_0(x, y) \cdot e^{-OD(x,y)} . \tag{4.8}$$

In order to determine the integrated column density $\tilde{n}(x, y)$ across the image and reduce background noise effects, more than one single image is collected: For absorption imaging, we measure an image of the probe light after passing through the atoms ($\equiv I_\mathrm{a}(x, y)$), a probe light image without atoms ($\equiv I_0(x, y)$), and a background image ($\equiv I_\mathrm{bg}(x, y)$). According to Eq. 4.6 and Eq. 4.8, these single images are processed as followed to obtain the density distribution:

$$\tilde{n}(x, y) \; = \frac{1}{\sigma_\lambda} OD(x, y) \underset{\hat{\delta}=0}{=} -\frac{1}{\sigma_0} \ln \frac{I_\mathrm{a}(x, y) - I_\mathrm{bg}(x, y)}{I_0(x, y) - I_\mathrm{bg}(x, y)} \tag{4.9}$$

In our experimental cycle, $\approx 400\,\mu$W of resonant imaging light for ^{87}Rb and Yb is turned on for $100\,\mu$s, and the three single images are taken consecutively within $\approx 5\,$s. The wait time between the single images is required to download the image data to the data acquisition PC. Absorption imaging is used in the present experiment for temperature and density distribution measurements of both atomic species. Note that analogously to the procedure for fluorescence imaging, ^{87}Rb atoms have to be optically pumped into the $|F = 2\rangle >$ ground state hyperfine level in order to be in resonance with the imaging light field.

A typical false color absorption image of $\approx 8 \times 10^6$ ^{87}Rb atoms at a temperature of $\approx 900\,$nK is shown in Fig. 4.16 (a). This image is taken 30 ms after the MT potential is switched off. During this time, a ballistic expansion occurs leading to the observed density distribution. The method of absorption imaging is sensitive enough to detect as few as $\approx 10^4$ Yb atoms trapped in the BIODT potential and extract their density distribution. However, when the optical density of the atomic sample becomes too large, like in high density ^{87}Rb clouds, absorption images become impractical for the following reasons: First, the signal-to-noise-radio in the light distribution $I_\mathrm{a}(x, y)$ decreases and saturation effects occur, as the incident probe light gets almost completely absorbed by the atoms. Second, probe light diffraction effects can not be avoided when the sample density is high, leading to artifacts in the measured image.

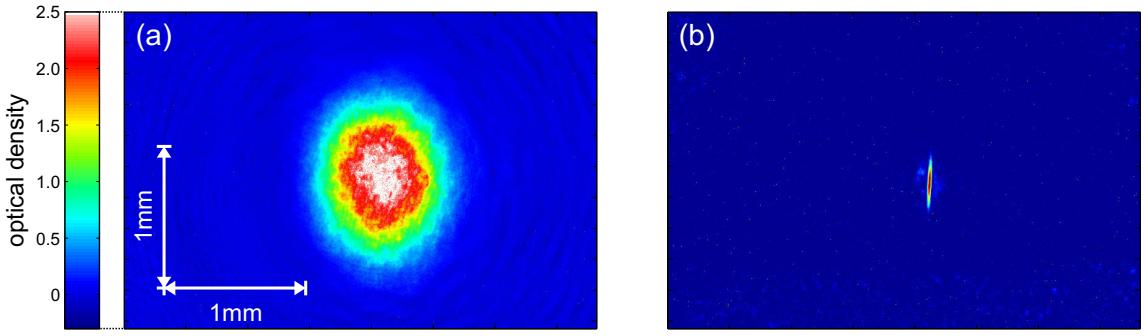

Figure 4.16: *False color (a) absorption- and (b) dark-contrast image of* $\approx 8 \times 10^6$ ^{87}Rb *atoms at a temperature of* ≈ 900nK. *The absorption image is taken after 30 ms of ballistic cloud expansion, while the dark contrast image shows the initial cloud distribution in the MT potential.*

b) Dark ground imaging The method of dark ground imaging uses a small opaque object, placed in the Fourier plane of the imaging system, to filter out unscattered probe light. In the experimental setup, this is realized by a gold spot with diameter of $\approx 500\,\mu$m, which is sputtered on a glass plate. The glass plate is mounted on a micrometer translation stage, allowing the opaque spot to be precisely placed in a focus of the imaging beam (see Fig. 4.15). To illustrate the method of dark ground imaging, the probe light field after passing through the atoms is separated into a scattered and an unscattered light field according to:

$$E(x,y)) \;=\; e^{-OD(x,y)/2}\, E_0(x,y) \cdot e^{i\,\phi(x,y)} \;=\; E_0(x,y) \;+ \Delta E(x,y). \tag{4.10}$$

Blocking of the unscattered light gives the dark-ground signal:

$$\begin{aligned} \langle I_{\mathrm{dg}}(x,y)\rangle \;&=\; |E(x,y) \;-\; E_0(x,y)|^2 \\ &=\; I_0(x,y)\left(1 + e^{-OD(x,y)} - 2e^{-OD(x,y)/2}\cos\phi\right) \\ &\underset{\phi\to 0}{\simeq}\; I_0(x,y)\left(1 + e^{-OD(x,y)} + e^{-OD(x,y)/2}(\phi^2 - 2)\right) \end{aligned} \tag{4.11}$$

For small phase shifts, the dark ground signal is quadratic in ϕ.

For dark contrast images, we obtain the actual dark ground distribution $I_{\mathrm{dg}}(x,y)$ and a background image $I_{\mathrm{bg}}(x,y)$. The images are processed as follows, to obtain a signal, which is proportional to the density distribution:

$$\tilde{n}(x,y) = c_{\mathrm{dg}} \cdot \sqrt{I_{\mathrm{dg}}(x,y) - I_{\mathrm{bg}}(x,y)} \tag{4.12}$$

The magnitude of the proportionality constant c_{dg}, which depends on σ_0 and $\hat{\delta}$ is not required in the present experiments, as this method is not used for absolute atom number

determination. For dark contrast imaging we also prepare the ^{87}Rb atoms in the $|F = 2\rangle >$ ground state sublevel. Successively, $\approx 800\,\mu$W of light, which is detuned from resonance by $\approx 6.2\,$GHz is used to illuminate the atoms for $100\,\mu$s. We are able to image ^{87}Rb atoms at peak densities of up to $10^{14}\,\mathrm{cm}^{-3}$, while they are still trapped in the MT potential. A typical intra-trap dark contrast image is shown in Fig. 4.16 (b).

The possibility of simultaneously taking intra-trap images of both atomic species allows direct observation of interspecies interaction processes (see Chap. 8).

4.3.4 Temperature determination

Under the assumption of a harmonic trapping potential, the density distribution $n(x, y, z)$ of an atomic cloud as well as the corresponding column density $\tilde{n}(y, z)$ is Gaussian:

$$\tilde{n}(y,z) = \int n(x,y,z)dx = n_0\sqrt{2\pi}\sigma_x \exp\left(-\frac{y^2}{2\sigma_y^2} - \frac{z^2}{2\sigma_z^2}\right). \tag{4.13}$$

The cloud dimensions σ_i $(i = x, y, z)$ depend on the respective trapping frequencies ω_i and the temperature T:

$$\sigma_i(t) = \sqrt{\frac{k_\mathrm{B}T}{m\omega_i^2}}, \qquad i = x, y, z \tag{4.14}$$

Without any trapping potential, ballistic expansion occurs and the cloud size as a function of the time of flight (TOF) is given by [121]:

$$\sigma_i(t_\mathrm{TOF}) = \sqrt{\sigma_i(0)^2 + \frac{k_\mathrm{B}T}{m}t_\mathrm{TOF}^2} = \sqrt{\frac{k_\mathrm{B}T}{m\omega_i^2} + \frac{k_\mathrm{B}T}{m}t_\mathrm{TOF}^2}, \qquad i = x, y, z \tag{4.15}$$

with the initial cloud size $\sigma_i(0)$. For $t_\mathrm{TOF} \gg \omega_i^{-1}$, the cloud size is independent of the initial size or shape and expands linearly in time.

For temperature measurements, the atom cloud is imaged after a defined TOF and its size is determined by applying a two-dimensional Gaussian fit to the data. When several images with a varied TOF are taken, Eq. 4.15 can be used as a fitting function for the measured time-dependent cloud sizes. The temperature and the initial cloud size $\sigma_i(0)$ can be extracted from this fit. This method is well known and accurate, but it requires 5…8 data points for a single temperature measurement. As this is experimentally time-consuming, the majority of the temperature data presented here, was obtained with a single-image method. To discuss this approach, Eq. 4.15 is rewritten in the following way:

$$T = \frac{m}{k_\mathrm{B}}\frac{\sigma_i(t_\mathrm{TOF})^2}{1/\omega_i^2 + t^2}. \tag{4.16}$$

An exact temperature determination requires the knowledge of the trap frequencies ω_i. However, for a long TOF ($t_\mathrm{TOF} \gg \omega_i^{-1}$), the term $1/\omega_i^2$ can be neglected in Eq. 4.16 allowing temperature determination, even when the trap frequencies are not exactly known.

In the experiments presented here, the radial trap frequencies for ^{87}Rb are in the range of $2\pi \times 140 \ldots 2\pi \times 1000$ Hz, while the radial Yb trap frequencies are $\approx 2\pi \times 1000$ Hz. Under these assumptions, the error caused by neglecting the term $1/\omega_i^2$ in Eq. 4.16 becomes $<1\,\%$ after a time of flight $t_{\mathrm{TOF}} > 1.1$ ms for Yb and $t_{\mathrm{TOF}} > 8$ ms for ^{87}Rb. Experimentally, images used for single-shot temperature measuremtns were taken at a TOF of 3.5 ms for Yb and 30 ms for ^{87}Rb, justifying the described approximation. The dominant uncertainty in temperature measurements is the error of the Gaussian fit to the atomic density distribution.

4.3.5 Atom number calibration

Generally, the number of atoms N can be extracted from an absorption image by summing the measured optical density over all camera pixels. From Eq. 4.9 follows

$$N = \frac{A}{\sigma_\lambda} \sum_{\mathrm{pixel}} \ln \frac{I_{\mathrm{a}}(x,y) - I_{\mathrm{bg}}(x,y)}{I_0(x,y) - I_{\mathrm{bg}}(x,y)}\,, \tag{4.17}$$

where A is the area in the atomic cloud that corresponds to one camera pixel. This sum depends on the cross-section $\sigma_\lambda = \sigma_0/(1+\hat{\delta}^2)$, which includes the saturation intensity I_{sat} via $\sigma_0 = \hbar\omega_0\gamma/(2I_{\mathrm{sat}})$. In the case of multi-level atoms, the saturation intensity I_{sat} of a specific transition generally depends on probe light polarization, the magnetic quantum number of the atom and the orientation of the magnetic field.

For absorptive imaging of Yb, we use the $^1\mathrm{S}_0 \rightarrow {}^1\mathrm{P}_1$-transition, which (for bosonic isotopes[2]) leads to the simplest case: The Clebsch-Gordan coefficients for the σ^+-, σ^-- and π- transition are identical and hence the resonant cross-section is independent of the probe light polarization. Thus, under the assumption of small laser linewidth ($\gamma_{\mathrm{laser}} < \gamma_{\mathrm{atom}}$), atom number calibration can be reliably carried out using absorption images.

Imaging light for ^{87}Rb clouds is resonant with the $|5^2\mathrm{S}_{1/2}\ \mathrm{F}{=}\ 2\rangle \rightarrow |5^2\mathrm{P}_{3/2}\ \mathrm{F}' = 3\rangle$ transition, where the transition strength for σ^+- and σ^--transitions differ by a factor of 15 [76]. In the experimental setup, we use σ^+-polarized light and apply a small magnetic field parallel to the probe light propagation axis. However, this configuration is subject to uncontrolled stray magnetic fields and it is very sensitive to imperfect light polarization. Light with the wrong polarization is absorbed much less by the atoms leading to an underestimation of the actual atom number.

Hence, we calibrate the ^{87}Rb absorption images using a different method based on fluorescence images. This method was applied in a previous work by Nemitz [11] and is not subject to the limitations stated above. The scattering rate of an atom, given in Eq. 4.4 can be rewritten in the form

$$\Gamma = \frac{s_0\,\gamma/2}{1 + s_0 + \hat{\delta}^2} = \frac{1}{1 + \frac{I_{\mathrm{eff}}}{I}} \frac{\gamma}{2} \qquad \text{with} \qquad I_{\mathrm{eff}} = (1+\hat{\delta}^2) I_{\mathrm{sat}}. \tag{4.18}$$

[2] Due to their non-vanishing nuclear magnetic moment, fermionic Yb isotopes have a more complex substructure. Ultimately, this leads to an underestimation in the detected atom number. However, the present experiments do not require an exact atom number calibration for fermionic Yb isotopes and this method is used as an rough approximation.

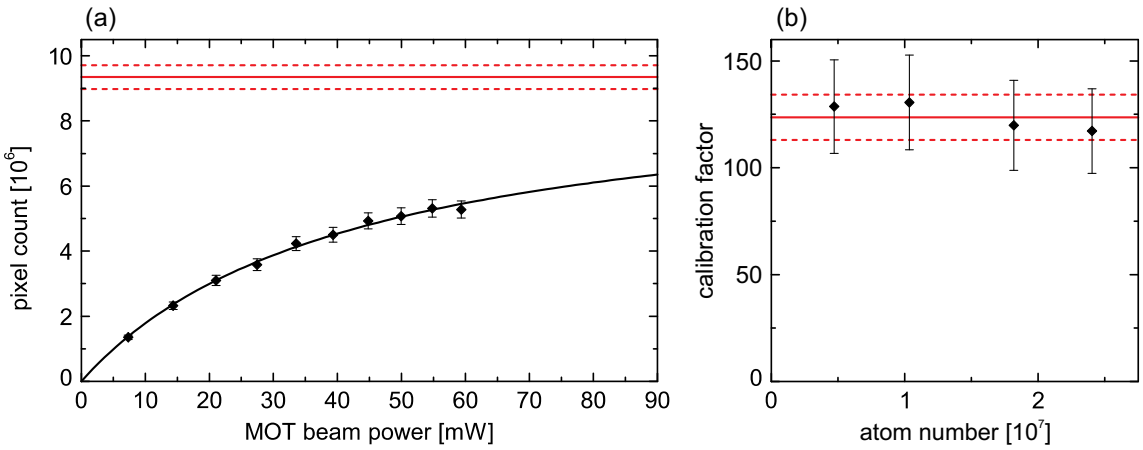

Figure 4.17: *(a) Measured fluorescence image pixel sums as a function of the imaging light power and extrapolated pixel count (red line). In this series,* $\approx 10^7$ ^{87}Rb *atoms at a temperature of* $\approx 1\,\mu$K *are imaged after 30 ms of ballistic cloud expansion. (b) Resulting calibration factors for absorption images together with their weighted mean (red line).*

If the incident intensity is high compared to the saturation intensity, the scattering rate will saturate at a maximum of $\Gamma_{\max} = \gamma/2$. Any detuning $\hat{\delta}$ from resonance simply increases the effective saturation intensity I_{eff} , while leaving the characteristic shape of the saturation curve intact. Imperfect light polarization, which include different Clebsch-Gordan coefficients for the specific transition, can be treated in the same way. The total number of photons scattered by N atoms over a time t, which are detected by the camera is given by

$$N_{\text{cam}} = a \cdot N_{\text{tot}} \cdot t = a \cdot N \frac{1}{1 + \frac{I_{\text{eff}}}{I}} \frac{\gamma}{2} \cdot t\,. \tag{4.19}$$

Here, a is a calibration factor that includes the solid angle of the imaging system, window and lens transmissions and the CCD's quantum efficiency at the corresponding wavelength. Those quantities have been measured by Nemitz and details can be found in [11]. For an absolute atom number calibration, a series of fluorescence images at different probe light intensities is obtained and the resulting saturation curve is fitted using Eq. 4.19. The extrapolated atom number for $I \to \infty$ is extracted from this fit. Figure 4.17 (a) shows typical saturation data together with the fit (black line) and the extrapolated pixel count (red line, error indicated by dashed red lines). Subsequently after each series with fluorescence images, absorption images of ^{87}Rb at the same experimental conditions are taken to obtain a corresponding atom number calibration factor. The calibration measurements are performed at $\approx 1\,\mu$K after a TOF of 30 ms, matching typical parameters of the present experiments. We tested the dependency of obtained calibration factors on the ^{87}Rb atom number in a range of $5 \times 10^6 \ldots 2.5 \times 10^7$, which is shown in Fig. 4.17 (b). Within their error bars, the scaling factors are atom number independent and the weighted mean of these data points results in a calibration factor of 123.6 ± 10.6 (indicated by the red line

in Fig. 4.17 (b)). This factor directly converts the sum of all optical density values in an absorption image into a ^{87}Rb atom number.

4.4 Experiment control

The experiment is controlled by a computer-based control system that was developed in the course of a previous work (details can be found in [11]). It consists of a PC with three National Instruments I/O boards (2× NI PCI-6229 M-series, each with 32 digital channels; 1× NI PCI-6723, 32 analog channels, 13 bit resolution) and an electronic connection board. The control system includes switching and power adjustment of laser beams and magnetic coils as well as triggering of the different imaging cameras.

The control software is LabView-based and allows the direct control over all experimental parameters (*steady state mode*). In addition, it is possible to program and run sequences of different experimental states at an output rate of 50 kHz (*pattern mode*). Typical sequences of experiments presented in this work consist of up to 40 single parameter states and take up to 50 s.

5

Preparation of ultracold ^{87}Rb and Yb in independent conservative potentials

The experimental investigations described in this thesis are carried out in an ultracold atom trap that allows for independent trapping and manipulation of ultracold ^{87}Rb and Yb atoms. The combined trap setup consists of a Ioffe-Pritchard-type magnetic trap (MT) for ^{87}Rb and a bichromatic optical dipole trap (BIODT) for Yb. In the experimental sequence, Yb is pre-cooled in a MOT and transferred to the conservative BIODT. Subsequently, ^{87}Rb is prepared and evaporatively cooled in the MT until the two species are brought into contact.

This section briefly describes the bichromatic approach and its realization. Furthermore, it highlights the experimental methods used to simultaneously prepare ultracold Yb and ^{87}Rb in their respective trapping potentials.

5.1 Independent trapping – the bichromatic idea

Almost all experiments that investigate heteronuclear interactions in ultracold mixtures use pure magnetic [122, 123] or pure optical traps [124, 125]. In either case, both atomic species are trapped in the same potential, which requires similar interactions with the used light- or magnetic fields for both species. Furthermore the flexibility in experiments, that probe interspecies interactions is limited.

The configuration presented here, is designed to widen the possibilities for the study of ultracold mixtures by providing independent trapping potentials for the used elements ^{87}Rb and Yb. More specifically, each atomic species does not interact with the trapping potential used for the other one (to the lowest order) and vice versa. This is possible due to the different magnetic characteristics: ^{87}Rb is an alkali atom with paramagnetic ground state whereas the rare earth metal Yb has a diamagnetic ground state. Hence, Yb does not interact with the magnetic field used for ^{87}Rb trapping, fulfilling the requirements for independent trapping. On the other hand, magnetically trapped ^{87}Rb atoms are generally affected by the light fields used for optical trapping of Yb. However, a cleverly arranged configuration of two optical dipole traps minimizes the effect on ^{87}Rb.

The bichromatic optical dipole trap (BIODT) used in our experimental setup is based on the fact that the magnitude and the sign of the dipole potential depend on the detuning of the trapping light frequency with respect to the main atomic transition (see Sec. 3.2.3).

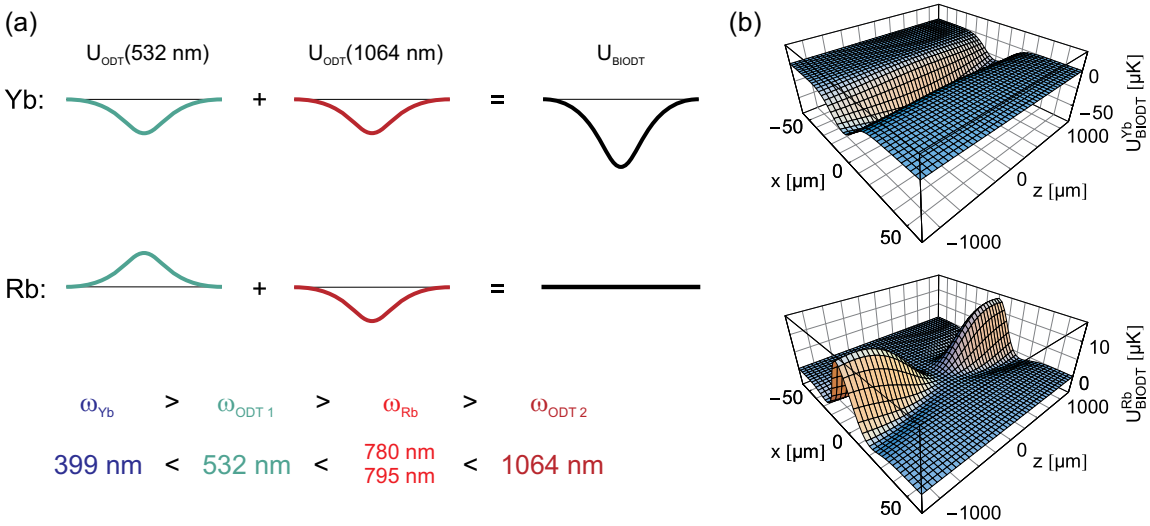

Figure 5.1: *Principle of the bichromatic optical dipole trap (BIODT). By superposition of two light fields with carefully chosen wavelength, two attractive potentials add up to a trapping potential for Yb. Due to its different main transition frequency, attractive and repulsive light fields cancel for ^{87}Rb. (a) outlines the basic principle and (b) shows calculated BIODT potentials for Yb (top) and Rb (bottom) using the following parameters: beam waists $w_{532} = w_{1064} = 15\,\mu$m; beam powers: $P_{532} = 340\,mW$, $P_{1064} = 0.382 \cdot I_{532}$*

Furthermore, in the limit of low excitation, dipole potentials created by more than one light field add up linearly to a total optical potential. Figure 5.1 (a) illustrates the basic idea for the case of a bichomatic single beam trap. The trapping laser wavelength are chosen to be 532 nm and 1064 nm. They are both "red" detuned from the main Yb transition wavelength of 399 nm. Hence, each beam focus forms an attractive potential for Yb and their superposition adds up to an even stronger trap. For ^{87}Rb, the 1064 nm light creates an attractive potential as well, as it is "'red" detuned from the main ^{87}Rb transition wavelength of 780 nm. In contrast, the 532 nm laser is "blue" detuned with respect to this transition, leading to a repulsive potential for ^{87}Rb. By choosing the same beam waist for both trapping beams and carefully adjusting the correct power ratio, both potentials cancel in the trap center, which is shown in Fig. 5.1 (b). Note that for a power ratio resulting in optimum potential cancellation for ^{87}Rb ($P_{1064} = 0.382 \cdot P_{532}$ for equal beam waists), the 1064 nm ODT contributes only $\approx 1/5$ to the total potential for Yb. Thus, small changes of the ODT beam power ratio have great effect on the ^{87}Rb potential while leaving the Yb trap practically unmodified.

The calculated potentials shown in Fig. 5.1 (b) demonstrate the limitation of this method: For equal beam waists w_0, the Rayleigh lengths $z_{\mathrm{R,i}} = \pi w_0^2/\lambda_i, (i = 1, 2)$ of the trapping beams differ by a factor of 2 for $\lambda_1 = 532$ nm and $\lambda_2 = 1064$ nm. This restricts the region of perfect potential cancellation for ^{87}Rb to the trap center. Outside the focus, attractive as well as repulsive regions for ^{87}Rb can not be avoided. Experimentally, this plays an important role and detailed potential calculations are presented in Sec. 6.2.

A related scheme, which uses only a bichromatic light field for the independent adjustment of the trapping strength for two species was proposed by Onforio et al. [126]. Similar BIODT potentials were also used in previous experiments at this apparatus [9]. A detailed discussion on the conceptual design of the BIODT can also be found in the thesis of Tassy [9].

In contrast to the previous measurements, the BIODT is reduced by a factor of ≈ 10 during the experimental sequence to achieve maximum potential cancellation for ^{87}Rb and minimize the influence of perturbing parts of the potential (see Chap. 7). In addition to that, for the study of phase separation (see Chap. 8), the relative trapping beam powers are adjusted in a way to intentionally create either repulsive or attractive potentials for ^{87}Rb. This allows a flexible and well-defined control of the ^{87}Rb density at the Yb cloud position.

5.2 Preparation of Yb atoms in the BIODT potentials

In the present configuration, the beam waists of the dipole trapping beam are set to a value of $\approx 15\,\mu$m and the maximum available light powers are $P_{532} \approx 3.5\,$W and $P_{1064} \approx 0.2\,$W. These parameters lead to a calculated BIODT trap depth of $U_0/k_\mathrm{B} \approx 550\,\mu$K.

In order to load atoms into this rather shallow BIODT potential, they are initially prepared and precooled in a MOT operating at the intercombination transition for Yb. For an efficient transfer, this process is split into two phases: First, the MOT is operated at parameters optimized for fast loading of atoms from the Zeeman slower. Second, the parameters are continuously changed to a compressed MOT state, where the density is increased and the temperature is reduced. Simultaneously, the BIODT is ramped up to its maximum potential depth and finally the MOT is turned off. In the next step, the BIODT potential is successively decreased by a total factor of ≈ 10 in order to minimize its effect on ^{87}Rb

5.2.1 "Green" Yb MOT

The "green" MOT used for Yb is operated on the $^1\mathrm{S}_0 \rightarrow {}^3\mathrm{P}_1$ intercombination line at 555.8 nm. Due to its narrow line width of $\gamma_{556} = 2\pi \times 181$ kHz [116], the theoretically obtainable Doppler temperature (Eq. 3.8) is as low as $T_\mathrm{D} = 4.4\,\mu$K. However, the drawback of the low scattering rate is that the maximum capture velocity (Eq. 3.11) is only $6.1\,\mathrm{m/s}$ assuming MOT beam radii of $\approx 4\,$mm. The Zeeman slower that feeds the MOT is hence designed for a final velocity of 5 m/s [9]. It operates on the $1^1\mathrm{S}_0 \rightarrow {}^1\mathrm{P}_1$ transition at 398.9nm. The broader line width of $\gamma_{399} = 2\pi \times 28\,$MHz allows for a much faster deceleration than the green transition, where a Zeeman slower would require an impractical length. Figure 5.2 shows a typical loading and decay curve and a photograph of a ^{174}Yb MOT. The "green" MOT fluorescence, which is recorded with a photomultiplier tube is proportional to the atom number. Typical MOT loading times are in the order of seconds and as the $^1\mathrm{S}_0 \rightarrow {}^3\mathrm{P}_1$ MOT transition is a closed cycling transition without any branching to other states, the MOT decay time – after turning off the Zeeman slower – is dominated by losses induced

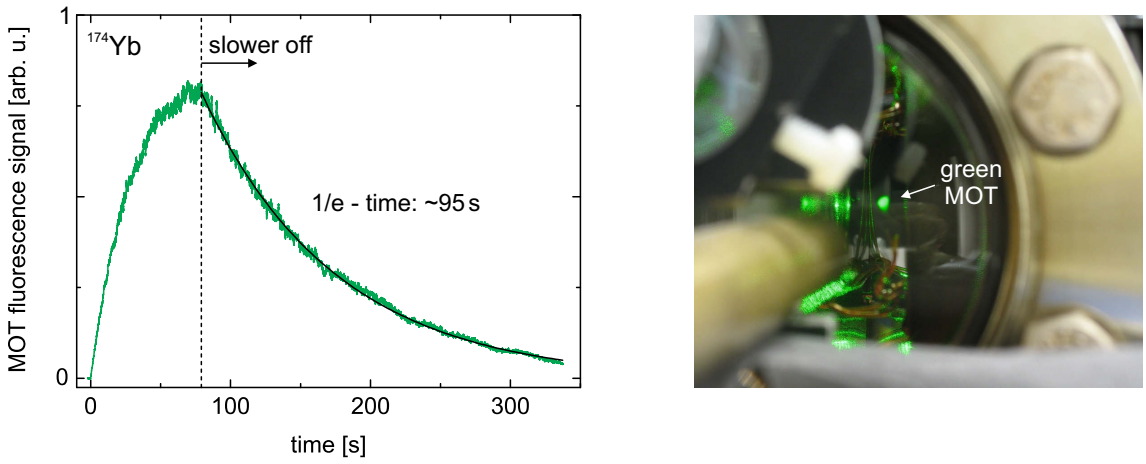

Figure 5.2: *(a) Loading and decay curve and (b) photograph of a ^{174}Yb MOT operated on the "green" transition at 556 nm. The MOT lifetime is predominantly determined by background gas collisions, which results in a large decay time.*

by background gas collisions (see Sec. 2.6). Due to the low pressure of $\approx 10^{-12}$ mbar this leads to exceptionally large MOT lifetimes > 1 minute, depending on the MOT beam adjustment.

For an efficient loading from the Zeeman-Slower we use a MOT laser detuning of $\delta_0 \approx -4\,\mathrm{MHz}$ ($\equiv -22.5\gamma$) and a small magnetic field gradient of $4.4\,\mathrm{G/cm}$ radially and $2.2\,\mathrm{G/cm}$ axially. The maximum available 556 nm MOT light of 15 mW is distributed over three retro reflected MOT beams with beam diameters of ≈ 8 mm. Due to additional losses in the optical system, the measured beam powers right in front of the vacuum chamber are ≈ 4 mW for the radial beams and ≈ 2 mW for the axial beams. The total peak intensity over all beams is $\approx 600\,I_\mathrm{s}$ in the MOT region. The MOT loading time depends on the used Yb isotope, as the atom flux in the Zeeman slower is determined by the relative isotopic abundance in the natural mix. Accordingly, the actual MOT loading phase in the experimental sequence ranges from 10 s (^{174,172}Yb) up to 30 s (^{170}Yb). Even longer loading times are impractical in the experimental cycle and do not yield larger BIODT atom numbers as soon as the density limited MOT regime is reached. Temperatures after the loading stage are in the range of several 100 μK and the atom number is $1 \ldots 2 \times 10^7$ depending on the isotope. The MOT size is approximated by fitting a Gaussian shaped function to the observed density distribution. The $1/e^2$-radius is ≈ 1.2 mm and the calculated peak density is $3 \ldots 6 \times 10^9\,\mathrm{cm}^{-3}$.

5.2.2 Transfer to the BIODT

The BIODT beam powers are ramped from zero to their maximum values of $P_{532} \approx 3.5$ W and $P_{1064} \approx 0.2$ W within 1 s at the end of the MOT loading phase. Simply turning off the MOT, however, does not provide enough atoms in the BIODT potential. For an efficient transfer to the BIODT, larger MOT densities and lower temperatures are required.

These conditions are achieved by linearly ramping the MOT parameters within 100 ms to a final compressed and cooled MOT state: The magnetic field gradient for the MOT is increased to 40 G/cm radially and 20 G/cm axially. This results in a stronger MOT confinement. Simultaneously, the MOT detuning is ramped to $\delta_0 \approx -0.5\,\mathrm{MHz}$ ($\equiv -2.8\gamma$) and the light power is linearly decreased to 0.1 mW, leading to a final intensity of $\approx 4\,I_\mathrm{s}$. Due to the lower photon scattering rate, the MOT temperature is significantly reduced under these conditions. The theory of Doppler cooling predicts a linear temperature dependence on the trapping light intensity [86]:

$$T(I) = \frac{\hbar\gamma^2}{8\,k_\mathrm{B}\,\delta_0}\left(1 + \frac{I}{I_\mathrm{s}} + 4\frac{\delta_0^2}{\gamma^2}\right) \tag{5.1}$$

Previous measurements on the "green" MOT presented in [9] are in qualitative agreement with this temperature dependence.

As a result from the MOT parameter change, the MOT size is reduced to a $1/e^2$-radius of $\approx$ 0.19 mm. Since almost no atoms are lost due to the compression of the MOT, the density is increased to $1\ldots2 \times 10^{11}\ \mathrm{cm}^{-3}$. We observe MOT temperatures in the range of $20\ldots50\,\mu$K depending on the actual MOT alignment. No significantly different temperatures are measured for bosonic and fermionic isotopes. This is in agreement with previous observations [9], where the effect of polarization gradient cooling for fermionic Yb is only observed at higher MOT light intensities. The general difference between the lowest obtainable temperatures and the theoretically predicted Doppler temperature can be explained by an imperfect MOT alignment that leads to imbalances in the light forces affecting the atoms in the MOT. The observed MOT temperatures are very similar to the temperatures in other Yb MOT experiments operating on the 556 nm transition [127, 128].

Subsequently after the MOT compression, this stage is held for 10 ms before the Yb MOT and slower lasers are turned off.

The settings used for the Yb atom transfer to the BIODT potentials are optimized experimentally, to obtain the best transfer efficiency which is shown in Fig. 5.3 for the most important parameters: In Fig. 5.3 (a), the initial laser detuning used in the MOT loading phase is changed and the optimum value is indicated by the dashed line. Figure 5.3 (b) and (c) demonstrate the optimization for the detuning and light power at the end of the parameter ramp described above. The fixed parameters in the respective measurement are set to their optimum value. Note that for zero final MOT power, atoms are still transfered to the BIODT, as the trapping lasers are already on during the "green" MOT ramp. In addition to the settings presented in Fig. 5.3, further parameters including the "green" MOT ramp time and the relative MOT position with respect to the BIODT potentials are also experimentally optimized. Due to long term drifts in the experimental setup, this process is repeated on a regular (≈weekly) basis ensuring a constant Yb atom number in the BIODT potentials.

5.2.3 BIODT ramp down

Depending on the Yb isotope, we initially trap about $0.5\ldots1 \times 10^6$ atoms in the BIODT. After $\approx$ 1 s of plain evaporation, the Yb cloud has reached its equilibrium temperature of

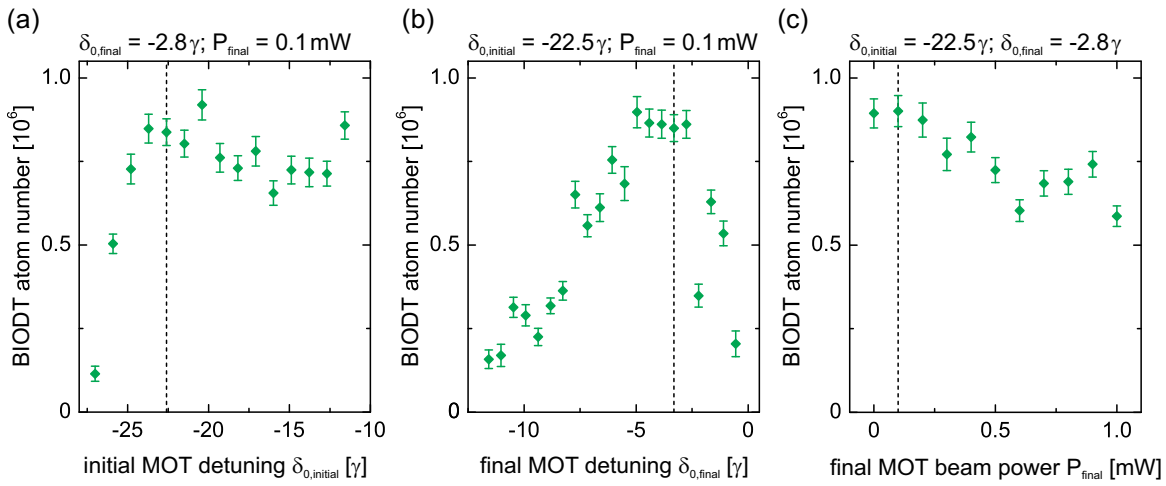

Figure 5.3: *Measured ^{174}Yb atom number in the BIODT as a function of different "green" MOT settings. The dashed lines indicate the values typically used in the present experiments.*

$\approx 40\,\mu$K. Assuming ideal Gaussian beams with beam waists $w_0 = 15\,\mu$m, the calculated trap frequencies of the BIODT potential for $P_{532} \approx 3.5\,$W and $P_{1064} \approx 0.2\,$W are $\omega_r \approx 2\pi \times 3.4\,$kHz radially and $\omega_z \approx 2\pi \times 28\,$Hz axially. An atomic cloud with a temperature of $\approx 40\,\mu$K has $1/e^2$-radii of $\sigma_r \approx 4.0\,\mu$m radially and $\sigma_r \approx 490\,\mu$m axially and the calculated peak density is $3 \ldots 6 \times 10^{13}\,$cm^{-3}. The lifetime in the BIODT of $\approx 40\,$s is limited by background gas collisions and three-body collisions.

After the BIODT loading phase, we prepare an ensemble of typically 10^7 ^{87}Rb atoms at a temperature of $\approx 1,5\,\mu$K in the MT, spatially separated from the Yb, which is still trapped in the BIODT (see below). During this process, which takes $\approx 35\,$s, we ramp down the power of the 532 nm ODT beam to a final level of $P_{532} = 340\,$mW and $P_{1064} = 90 \ldots 120\,$mW. This minimizes perturbations on the ^{87}Rb due to imperfections of the BIODT optical potential. The 532 nm ODT beam is ramped down in two stages which is illustrated in Fig.5.4. After a holding time of $\approx 8\,$s, the power is linearly reduced to 30 % of the original value within 9 s. This setting is kept constant for another 18 s before the second linear ramp to its final level is applied within 500 ms. The 1064 nm ODT is reduced to its final setting in a similar way. In two-species experiments, the cloud of cold ^{87}Rb, is moved on top of the Yb cloud simultaneously to the final BIODT ramp (see Fig.5.4).

The gradual reduction of the BIODT trap depth leads effectively to forced evaporative cooling and thus the Yb temperatures and atom numbers are lowered. This process is isotope dependent as it is connected to the respective atom-atom scattering cross section (see Sec. 3.2.2). Typical final Yb temperatures are summarized in Tab. 5.1 together with the zero energy s-wave scattering length a of the respective Yb isotope. This data is taken immediately after the final BIODT ramp down with no ^{87}Rb present. Qualitatively, a large scattering length $|a|$ allows a more efficient evaporation as the rethermalization rate is higher and thus the temperatures, which can be achieved by plain evaporation are lower.

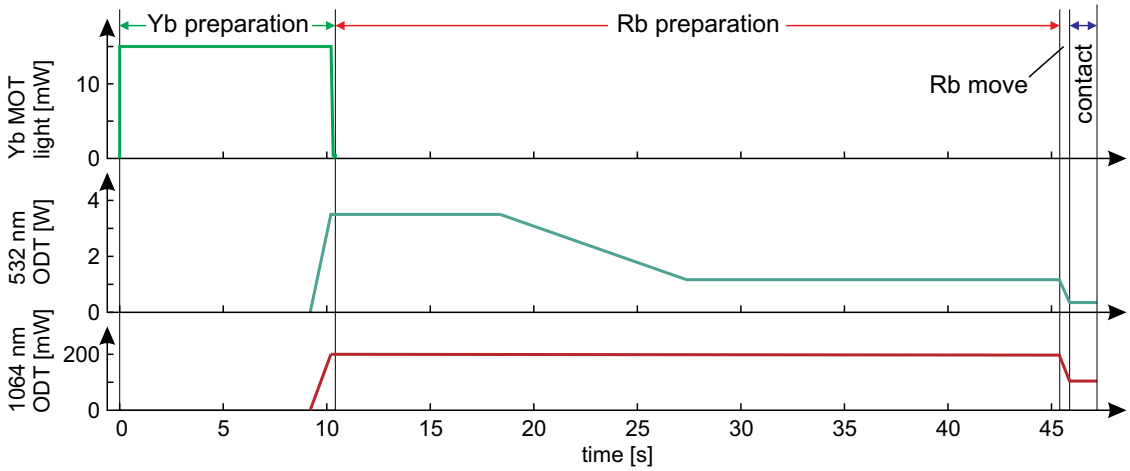

Figure 5.4: *Experimental sequence of the different Yb and ^{87}Rb atom preparation phases. Yb atoms are loaded in at MOT (upper graph) and transferred to the BIODT potentials (lower graphs). ^{87}Rb atoms are prepared in the MT while simultaneously the BIODT potentials are ramped to their final value. Subsequently, both species are brought into contact for interaction experiments.*

isotope	T_{final}	s-wave scatterin length a [57]
^{170}Yb	$\approx 7\,\mu$K	$(64 \pm 2)\,a_0$
^{172}Yb	$\approx 6\,\mu$K	$(-599 \pm 64)\,a_0$
^{173}Yb	$\approx 6\,\mu$K	$(199 \pm 2)\,a_0$
^{174}Yb	$\approx 5\,\mu$K	$(105 \pm 2)\,a_0$
^{176}Yb	$\approx 8\,\mu$K	$(-24 \pm 4)\,a_0$

Table 5.1: *Typical temperatures and atom numbers of different Yb isotopes after the BIODT ramp down to its final level*

However, recent calculations based on two-color photoassociation spectroscopy of Yb atoms show a strong energy dependence of the scattering cross section $\sigma(E)$, especially for ^{171}Yb and ^{176}Yb [57], which leads to a more complex situation.

Note that the distinctive form of the ramp down is optimized for ^{174}Yb, which shows strong interspecies interaction with ^{87}Rb. In typical interspecies experiments, a cloud of $\approx 1 \times 10^7$ ^{87}Rb atoms at a temperature of $T_{\mathrm{Rb}} \approx 1.5\,\mu$K is brought into contact with ^{174}Yb immediately after the final BIODT ramp. We observe almost instantaneous thermalization of ^{174}Yb with the colder ^{87}Rb (see Chap. 7). Using this effect, the final BIODT ramp is designed to be non-adiabatic with respect to the ^{174}Yb temperature. Due to the fast ramp, thermal disequilibrium in ^{174}Yb is created, which is resolved by thermalization with the cold ^{87}Rb cloud present at the end of the final ramp. Experimentally, we confirmed that this form of the BIODT ramp down leads to significantly higher ^{174}Yb atom numbers than a slow adiabatic ramp to the identical final level.

The final 1064 nm ODT power is also optimized experimentally in order to have minimum perturbing effects on ^{87}Rb (see Chap. 7). Due to the intrinsically small contribution of the 1064 nm light to the total BIODT for Yb, there are no significant changes to the Yb trapping potential.

For $P_{532} = 340\,\mathrm{mW}$ and $P_{1064} = 110\,\mathrm{mW}$ and equal beam waists $w_0 = 15\,\mu\mathrm{m}$ the calculated trap depth is $U_0/k_\mathrm{B} \approx 60\,\mu\mathrm{K}$ and trap frequencies are $\omega_\mathrm{r} \approx 2\pi \times 1.1\,\mathrm{kHz}$ radially and $\omega_\mathrm{z} \approx 2\pi \times 11\,\mathrm{Hz}$ axially. A typical cloud of 2×10^5 ^{174}Yb atoms at $5\,\mu\mathrm{K}$ in this potential has $1/e^2$-radii of $\sigma_r \approx 4.2\,\mu\mathrm{m}$ radially and $\sigma_r \approx 460\,\mu\mathrm{m}$ axially at a peak density of $1.3 \times 10^{13}\,\mathrm{cm}^{-3}$.

The numbers given here result from calculations based on ideal BIODT potential geometries and beam adjustment. A careful experimental trapping potential characterization resulting from trap frequency measurements is presented in Chap. 6.

5.3 Preparation of ^{87}Rb in the MT potential

While Yb is "stored" in the BIODT potential, a cloud of cold ^{87}Rb atoms in the $|F = 1, m_F = -1\rangle$-state is prepared in the MT potential (see Fig. 5.4). This process involves the accumulation of ^{87}Rb in a MOT, the transfer to the MT and finally RF induced evaporative cooling to temperatures of $\approx 1\,\mu\mathrm{K}$. Due to the diamagnetic ground state, Yb is not affected by the magnetic fields used during the different stages of the ^{87}Rb preparation. However, when the ^{87}Rb MOT spatially overlaps the Yb BIODT potentials, we observe strong Yb atom loss. This is explained by light induced inelastic collisions between excited ^{87}Rb- and ground state Yb atoms. To avoid this loss mechanism, the ^{87}Rb MOT is loaded $\approx 2\,\mathrm{mm}$ away from the Yb trap. The MT center is also spatially separated from the Yb atoms, which allows preparation of cold ^{87}Rb without interfering with the Yb cloud.

5.3.1 ^{87}Rb loading process

Similar to the Yb sequence, the ^{87}Rb loading process is divided into different phases: First, MOT parameters are chosen that allow efficient loading from the Zeeman slower. Afterwards, the atom density is increased by switching to a dark SPOT MOT configuration. Temperature reduction is achieved in a subsequent optical molasses phase. Finally, ^{87}Rb atoms are optically pumped to the the $|F = 1, m_F = -1\rangle$ state and the MT fields are turned on.

MOT loading phase

The MOT for ^{87}Rb uses the $|5^2\mathrm{S}_{1/2},\ F = 2\rangle \rightarrow |5^2\mathrm{P}_{3/2},\ |F' = 3\rangle$ transition at 780 nm, which has a line width of $\gamma_{780} = 2\pi \times 6.1\,\mathrm{MHz}$ resulting in a Doppler temperature of $146\,\mu\mathrm{K}$. An additional repumper laser operating on the $F = 1\rangle \rightarrow F' = 2\rangle$ transition is required to maintain a continuous cooling cycle (see Sec. 4.2.1).

Experimentally, we use $\approx 4\,\mathrm{mW}$ of light power for each of the 4 radial- and $\approx 2\,\mathrm{mW}$ for the 2 axial MOT beams. The beam diameters of $\approx 15\,\mathrm{mm}$ lead to a calculated total light

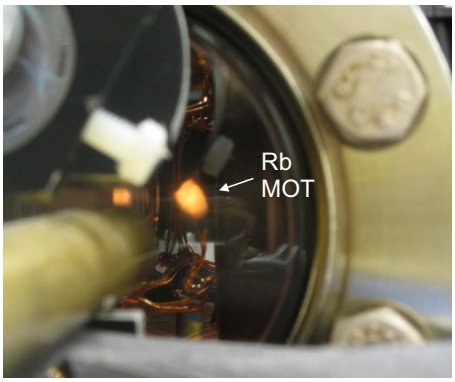

Figure 5.5: *Photograph of a few 10^9 ^{87}Rb atoms trapped in a MOT. The MOT size is significantly larger than the "green" Yb MOT shown in Fig. 5.2. Note that the color of the near infrared 780 nm light scattered by the ^{87}Rb atoms is reproduced incorrectly in this image.*

intensity in the MOT center of $\approx 14\, I_s$. In the loading phase, the MOT laser detuning is set to $-3\,\gamma$ and magnetic field gradients are $26\,^{\mathrm{G}}/_{\mathrm{cm}}$ radially and $13\,^{\mathrm{G}}/_{\mathrm{cm}}$ axially. The MOT is loaded from a Zeeman slower designed for final atom velocities of $20\,^{\mathrm{m}}/_{\mathrm{s}}$, which is well below the maximum MOT capture velocity $v_c \approx 60\,^{\mathrm{m}}/_{\mathrm{s}}$. The ^{87}Rb MOT, which is shown in Fig. 5.5, reaches its equilibrium atom number of $\approx 3 \times 10^9$ already $3 \ldots 5\,\mathrm{s}$ after it is turned on. However, the equilibrium state strongly depends on the actual beam alignment. Thus, the loading phase is aborted after a defined loading time of $1 \ldots 2\,\mathrm{s}$ in order to ensure a constant atom number over different experimental cycles. During the loading phase, the MOT density changes from the temperature limited regime to the density limited regime (see Sec. 3.1). In this transition phase, the MOT temperature depends on the absolute atom number and density as $T_{\mathrm{MOT}} \propto N^{1/3} \cdot n^{2/3}$ [95]. Typically, the temperature after $1 \ldots 2\,\mathrm{s}$ of MOT loading is in the range of 1 mK [8] and the atomic density is $\approx 10^{10}\,\mathrm{cm}^{-3}$. The MOT center in the loading phase is spatially shifted from the BIODT position by an additional offset magnetic field. Due to the large MOT beam radii, the MOT is operational over a range of several millimeters, without a change in the beam alignment.

Dark SPOT MOT

The present experimental configuration includes two separate ^{87}Rb repumping beams. The beam denoted as *repumper 2* in Fig. 4.3 illuminates the complete MOT volume whereas the main ^{87}Rb repumper has a dark center. This dark region has a diameter of $\approx 7\,\mathrm{mm}$ and it is created by an opaque obstacle in the beam path which is imaged to the center of the vacuum chamber. Figure 5.6 illustrates the optical path and shows a photograph of the repumping beam close to the main chamber.

During the MOT loading phase, both repumping beams are turned on to achieve maximum loading rate. For lower temperatures and higher peak densities we turn off *repumper 2* switching to a dark SPOT MOT configuration. Simultaneously, the Zeeman slower is turned off and the resulting change in the magnetic field is compensated by additional offset fields. Subsequently, the MOT is moved to the MT position by a 50 ms long, linear ramp of the magnetic compensation fields. At this stage, the density is increased to $4 \ldots 8 \times 10^{11}\,\mathrm{cm}^{-3}$ and the temperature is slightly reduced to $\approx 500\,\mu\mathrm{K}$.

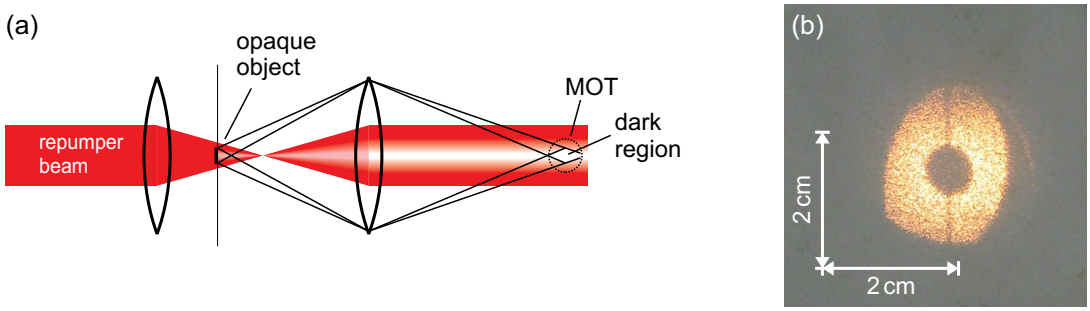

Figure 5.6: *(a) Schematic of the optical beam path and (b) photograph of the ^{87}Rb MOT repumper. The dark inner region is created by a bolt head soldered to a thin wire, which is imaged to the trap center.*

Optical molasses

For further cooling of the atomic sample, a short optical molasses phase is included in the the ^{87}Rb preparation process. To achieve this, the MOT magnetic fields are turned off after the atoms have been moved to the final position. To avoid the combination of uncontrolled magnetic fields and near-resonant trapping light in the turn-off process, the MOT lasers are blocked for 2 ms while the current in the MOT coils decays. Within the next 5 ms, the MOT laser detuning δ_0 is linearly ramped to $-10\,\gamma$, which leads to measured ^{87}Rb temperatures of only $50 \ldots 80\,\mu$K. The observation of sub-Doppler temperatures result from polarization-gradient cooling mechanisms present for ^{87}Rb. Unlike Doppler-cooling, the temperature obtained by this cooling mechanism decreases when the detuning increases [93]:

$$T_{\mathrm{pg}} \propto \frac{I}{\delta_0} \tag{5.2}$$

A reduction of the trapping laser power I is experimentally not possible in our setup, as it is accompanied by a movement of the light beams originating from the power control AOM. However, simultaneously to the MOT detuning shift, we ramp down the repumping beam to $\approx 1\,\%$ of its original power, which also reduces the photon scattering rate.

The measured $1/e^2$ cloud radii after the optical molasses phase are ≈ 2 mm, matching the volume of the MT.

Transfer to the MT

^{87}Rb atoms in the MT are trapped in the $|F = 1, m_F = -1\rangle$ state[1]. For an efficient transfer to the MT, we selectively populate this state by optically pumping the ^{87}Rb atoms using the *depumper* laser (see Sec. 4.2.1). This σ^- polarized field, which is resonant with the $|5^2\mathrm{S}_{1/2}, F = 2\rangle \rightarrow |5^2\mathrm{P}_{3/2}, F' = 2\rangle$ is turned on for $200\mu s$, after the MOT lasers are switched off. Simultaneously, the magnetic fields creating the MT potential are activated.

[1] The ^{87}Rb $|F = 1, m_F = -1\rangle$ state has a smaller magnetic-dipolar decay-rate constant compared to the $|F = 2, m_F = 2\rangle$ state [129] leading to an increased lifetime of atoms in the trap.

The radial confinement of the MT is initially loosened in order to better match the present ^{87}Rb cloud parameters by increasing the magnetic offset field B_0 in the Ioffe-Pritchard geometry, which reduces the radial trap frequencies (see Eq. 3.16 in Sec. 3.2.1). Within a 100 ms linear ramp, the MT potential is subsequently changed from this initial loading configuration to a radially tighter potential, which is used for the evaporative cooling process (see below). Measured trap frequencies in the MT are $\omega_r \approx 2\pi \times 134$ Hz radially and $\omega_z \approx 2\pi \times 13.7$ Hz axially (see Sec. 6.1.1 for details). Due to adiabatic compression [130] and imperfect mode matching of the trapping potentials, the ^{87}Rb temperature is increased by the MT loading process to $160 \ldots 180\,\mu$K and observed atom numbers are $\approx 7 \times 10^8$. The ^{87}Rb cloud in this potential has a $1/e^2$-radii of $\sigma_r \approx 0.29$ mm radially and $\sigma_r \approx 3.0$ mm axially and a peak density of $\approx 1.4 \times 10^{12}$ cm^{-3}.

5.3.2 Evaporative cooling of ^{87}Rb and MT position shift

In order to prepare ^{87}Rb atoms at a temperature of $\approx 1\,\mu$K for interspecies interaction experiments as described in this work, we use the method of RF induced evaporative cooling (see Sec. 3.2.2). The stepwise experimental optimization of the evaporation ramp was part of a Bachelor's thesis carried out at this apparatus and a detailed description can be found in [131]. The actual RF ramp sequence used in the present experiments together with measured temperatures, atom numbers and calculated peak densities is shown in Fig. 5.7. After 4 s of plain evaporation, the RF is gradually reduced from 27 MHz to 900 kHz at a measured trap bottom $B_0 = h\,\nu_{\mathrm{RF0}}/\mu$ with $\nu_{\mathrm{RF0}} \approx 550$ kHz. Within a total time of 31 s, the temperature and the number of ^{87}Rb atoms is reduced to $\approx 1\,\mu$K and $1 \ldots 1.5 \times 10^7$, depending on the starting conditions. Simultaneously, the $1/e^2$ cloud radii are shrunk to $\sigma_r \approx 22\,\mu$mm radially and $\sigma_r \approx 230\,\mu$m axially and the ^{87}Rb density is increased from $\approx 1.4 \times 10^{12}$ cm^{-3} to $4 \ldots 6 \times 10^{13}$ cm^{-3}.

Note that by further reducing the RF to ≈ 650 kHz within $1 \ldots 8$ s, large Bose-Einstein condensates of ^{87}Rb in the $|F = 1, m_F = -1\rangle$ state can reliably be produced. Measured transition temperatures are $\approx 300 \ldots 400$ nK and a condensate typically consists of $1 \ldots 2 \times 10^6$ atoms. However, besides the ^{87}Rb MT trap frequency measurement (see Sec. 6.1.1), characteristic properties of BECs are neither studied nor used within the scope of this work. Detailed investigations on BECs produced at this apparatus, which consist of ^{87}Rb atoms in the $|F = 2, m_F = 2\rangle$ state are presented in [8].

Creating spatial overlap between ^{87}Rb and Yb In order to avoid contact between magnetically trapped ^{87}Rb and Yb in the BIODT during the preparation process, the MT center is initially located at a position, which is ≈ 0.9 mm radially shifted from the Yb cloud. However, for the interspecies interaction experiments presented here, the MT is moved to the Yb position after the RF evaporation ramp (see Fig. 5.4).

Experimentally, the MT position is controlled by the horizontal and vertical magnetic compensation field settings. The actual dependence of the MT position on the magnetic field is carefully calibrated for the horizontal and vertical axes to a precision of $\approx 5\mu m$ [9].

For the majority of the present experiments, the MT is moved within 500 ms to the

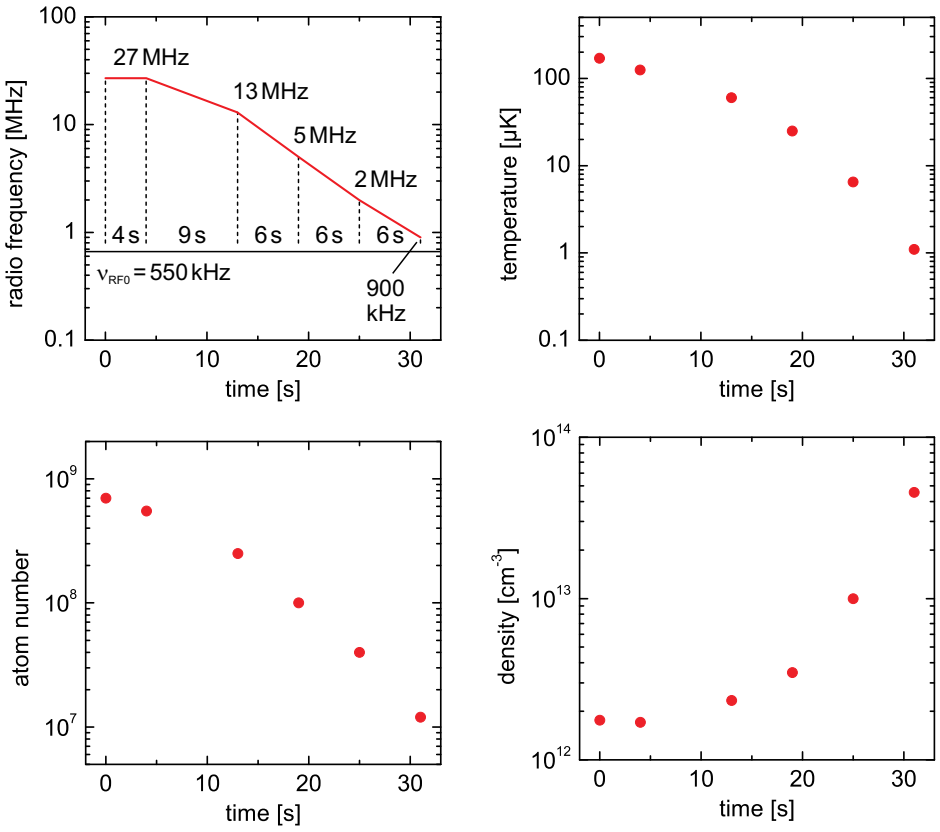

Figure 5.7: *Experimentally optimized RF induced evaporation ramp, measured ^{87}Rb temperatures and atom numbers and calculated peak densities.*

BIODT position. The RF is kept at a constant level of 900 kHz during this process and the trap bottom at the final position is experimentally adjusted to equal the initial value. Without the presence of BIODT potentials, we do not observe any significant change in the ^{87}Rb temperature or atom number induced by the position shift compared to a steady MT.

However, due to imperfect potential cancellation of the BIODT for ^{87}Rb, adiabatic heating leads to ^{87}Rb temperatures of $1.5 \ldots 2 \mu K$ as soon as the ^{87}Rb cloud overlaps with the BIODT. As the ^{87}Rb temperature increase strongly depends on the exact BIODT potential form, this effect is used to experimentally adjust the BIODT beam alignment and the relative beam powers (see Sec. 7.1).

In summary, the sequential loading and preparation of Yb in the BIODT and ^{87}Rb in the MT provides independently trapped cold samples of $1 \ldots 2 \times 10^5$ Yb atoms at $5 \ldots 10\,\mu$K and $1 \ldots 1.5 \times 10^7$ ^{87}Rb atoms at $\approx 1\ \mu$K. These atoms are then used for interspecies interaction studies as described in Chap. 7 and Chap. 8.

6

Trap characterization and modelling of potentials

For a quantitative understanding of the experiments described in Chap. 7 and Chap. 8, it is essential, to know the characteristic parameters of the involved trapping potentials. With the knowledge of measured trap frequencies for the MT and the BIODT, it is possible to simulate the model potentials correspondent to the experimental situation.

This chapter describes the trap frequency measurements of both the magnetic and optical potentials. Furthermore, the procedure which is used to determine the trapping potentials from these measurements is laid out and the simulated potentials for different trapping configurations are shown.

6.1 Trap parameter measurements

Conservative potentials in cold atom experiments are typically characterized by a harmonic approximation which is valid at low energies (see Sec. 3.2). The experimental determination of trap frequencies is a simple and direct way to gain information on this harmonic part of the potentials. In the following, two different methods of trap frequency measurements and the conclusions for the respective potentials are described: In the MT, we directly observe oscillations of an initially deflected ^{87}Rb cloud. In combination with a measurement of the offset magnetic field at the trap bottom, the MT parameters are completely characterized. In contrast, the BIODT trap frequencies are determined using a parametric heating technique. These measurements are performed for different trapping geometries both with ^{174}Yb and ^{87}Rb, in order to achieve comprehensive information on the BIODT potentials.

6.1.1 Trapping parameters of the MT

Trap frequencies

The trap frequency measurement of the MT is based on the idea of directly observing the collective ^{87}Rb atom oscillations in the harmonic regime. In order to probe the harmonic region around the trap center, low temperatures and small oscillation amplitudes are required. Experimentally, it is also important to determine the MT parameters at

the location relevant for further measurements. They slightly depend on the MT center position, which is probably related to off-axis effects.

In order to fulfill these conditions, the following experimental sequence is used: A ^{87}Rb BEC is created by preparing a cloud of ^{87}Rb in the MT and extending the "standard" RF evaporation ramp (see Sec. 5.3.2) by 1 s to a lower final radio frequency of $\approx 100\,\mathrm{kHz}$ above the trap bottom. Simultaneously, the radial MT position is smoothly moved close to the BIODT position using an S-ramp. Finally, the MT center is displaced to the actual BIODT position by applying a hard step to the magnetic compensation fields. This nonadiabatic trap-"jump" collectively excites the ^{87}Rb atoms in the trap leading to radial harmonic oscillations. The actual "jump"-distance is experimentally optimized to $\approx 7\,\mu\mathrm{m}$. In order to measure the axial trap frequency, the trap center is smoothly displaced from the trap center in the axial direction and subsequently set back by a hard step. Axial displacement is achieved by creating an axial magnetic field gradient using the axial compensation fields. Note that the MT trap frequency measurements take place in the absence of the BIODT potentials.

The oscillations of the ^{87}Rb cloud can be described by a damped oscillation, depending on the amplitude A, the damping time constant τ, the trap frequency ω and a phase shift ϕ.

$$\Delta x(t) = A\, e^{-\mathrm{t}/\tau} \sin(\omega t + \phi)\,. \tag{6.1}$$

The damping is attributed to dephasing as a result of the anharmonicity in the trapping potential that smears out the collective cloud movement. Due to the small amplitude, the oscillation inside the trap takes place on a level beyond the resolution of the present imaging system. However, when the atoms are released from the trap after a defined oscillation time, the trajectory depends on the initial velocity $v_0(t)$, which is subject to the same oscillatory behavior:

$$v_0(t) = \Delta\dot{x}(t) = A\, e^{-\mathrm{t}/\tau} \left(\omega \cos(\omega t + \phi) - \frac{1}{\tau} \sin(\omega t + \phi) \right) = A'\, e^{-\mathrm{t}/\tau} \sin(\omega t + \hat{\phi})\,. \tag{6.2}$$

As a result, the position of the cloud center after a free expansion t_{TOF} is given by

$$\Delta x_{\mathrm{TOF}}(t) \approx v_0(t) \cdot t_{\mathrm{TOF}} = \hat{A}\, e^{-\mathrm{t}/\tau} \sin(\omega t + \hat{\phi})\,, \tag{6.3}$$

under the assumption, that the initial cloud displacement $\Delta x(t)$ can be neglected. Experimentally, the cloud is released from the trap after a variable holding time t and an absorption image is taken after $t_{\mathrm{TOF}} = 30\,\mathrm{ms}$ of ballistic expansion. From the absorption images, the center of the cloud is determined. Figure 6.1 (a, b) shows the horizontal and axial oscillations of the cloud center. For the radial measurement, data is taken for an oscillation time $0 \ldots 100\,\mathrm{ms}$ and *camera 1* and *camera 2* (see Sec. 4.3) are simultaneously used to determine horizontal and vertical trap frequencies. Due to the lower trap frequency, the axial measurement uses oscillations times $0 \ldots 400\,\mathrm{ms}$.

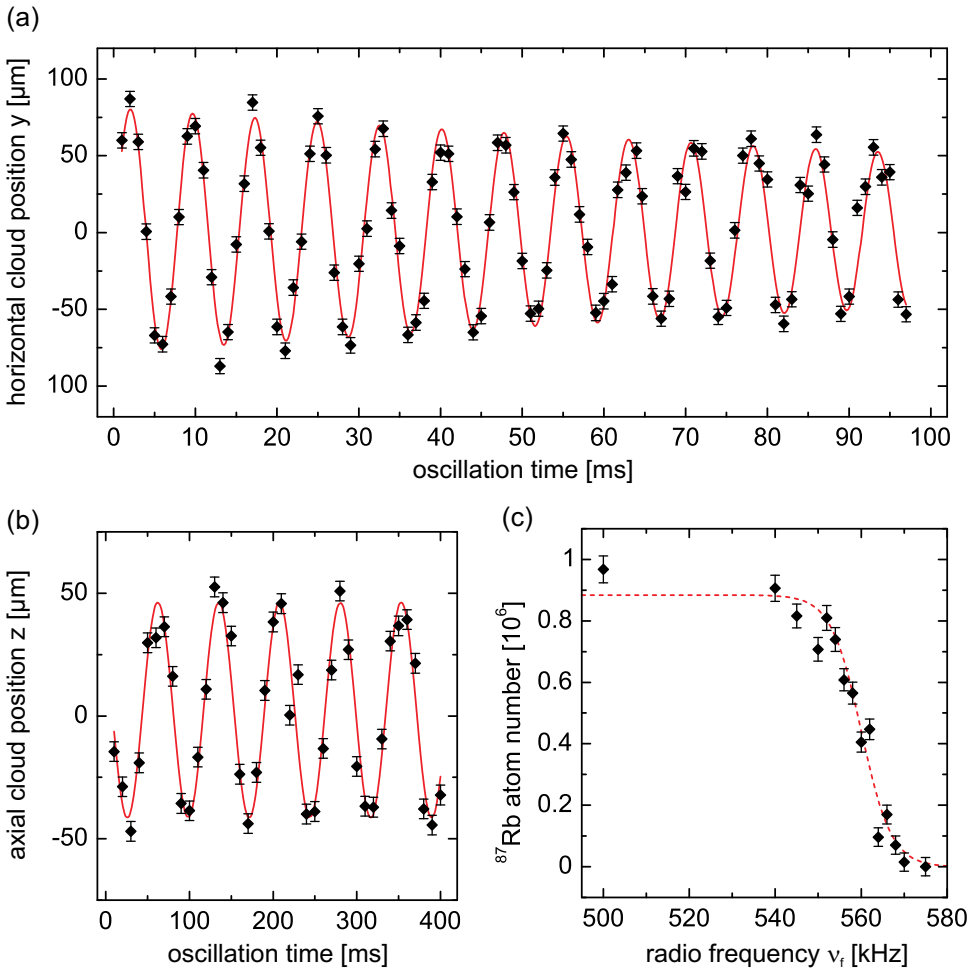

Figure 6.1: *(a, b) Trap frequency measurements of ^{87}Rb in the MT: Horizontal and axial cloud positions as a function of the oscillation time together with a fit to the data. (c) Determination of the trap bottom: Plotted is the steady state number of ^{87}Rb atoms in the MT as a function of the value ν_f of a fixed radio frequency irradiating the atoms. The trap bottom is defined as the lowest value of ν_f for which atom loss is observed. The dashed line is a guide to the eye.*

For a quantitative analysis, the measured cloud positions are fitted to Eq. 6.3 with $\hat{A}$, τ, ω and $\hat{\phi}$ as free parameters. The extracted trap frequencies are summarized in Tab. 6.1 together with results from a previous measurement at this apparatus [9]. The small difference between horizontal and vertical trap frequencies is attributed to an imperfect magnetic field geometry of the Ioffe-Pritchard type MT. Note that for further potential calculations, the mean radial trap frequency $\omega_r = \sqrt{\omega_x\,\omega_y}$ is used.

Trap bottom and MT parameters

An important parameter in a Ioffe-Pritchard type MT is the magnetic offset field B_0, as it defines the strength of the radial confinement and the radial trap frequency (see

parameter	present result	result from [9]
horizontal trap frequency $\omega_y/2\pi$ [Hz]	137.9 ± 0.14	176.0 ± 0.8
vertical trap frequency $\omega_x/2\pi$ [Hz]	131.2 ± 0.19	175.9 ± 1.5
mean radial trap frequency $\omega_r/2\pi$ [Hz]	134.5 ± 0.23	176.0 ± 0.7
axial trap frequency $\omega_z/2\pi$ [Hz]	13.72 ± 0.07	13.47 ± 0.09
magnetic field offset B_0 [G]	$0,79 \pm 0,01$	$0,50 \pm 0,02$
radial field gradient B' [G/cm]	133 ± 1	138 ± 1
axial field curvature B'' [G/cm^2]	231 ± 2	224 ± 3

Table 6.1: *Measured trap frequencies and calculated MT parameters for ^{87}Rb atoms in the $|F = 1, m_F = -1\rangle$ state. The results are compared to previous measurements at this apparatus.*

Eq. 3.16 in Sec. 3.2.1). The present configuration allows a variable adjustment of the so-called trap bottom B_0 by the axial compensation fields. Its magnitude can be determined experimentally (see Fig. 6.1). Together with the trap frequencies, all parameters defining the MT potentials can be deduced.

For a trap bottom measurement, a sample of $\approx 1\,\mu$K cold ^{87}Rb atoms is prepared in the MT and the radio frequency is ramped from zero to a defined final value ν_f within 500 ms. For the case that the radio frequency $\nu_\mathrm{f} = \mu B_0/h$ is in resonance with atoms at the trap center, atom loss is observed. Figure 6.1 (c) shows the ^{87}Rb atom number as a function of the final RF setting ν_f. Atom loss is observed for $\nu_\mathrm{f} > 550 \pm 5$ kHz, resulting in a calculated magnetic offset field $B_0 = 0.8 \pm 0.01$ G.

The radial field gradient B' and the axial field curvature B'' of the present MT are calculated according to Eq. 3.16 and are presented in Tab. 6.1. Note that in comparison to a previous measurement [9], the present configuration is characterized by a significantly larger magnetic offset field resulting in smaller radial trap frequencies. The radial trap frequency as well as B' and B'' are slightly disagreeing with previous measurements, due to a different position of the magnetic trap center.

6.1.2 Trapping parameters of the BIODT

In order to obtain detailed information on the BIODT potentials, trap frequency measurements with ^{174}Yb in the "green" (532 nm) and the "infrared" (1064 nm) ODT as well as in the BIODT are carried out for different beam power ratios. In addition, the 1064 nm ODT- and the BIODT trap frequencies were determined using ^{87}Rb. The measurement conditions are chosen to match typical experimental configurations described in Chap. 7 and Chap. 8.

a) Trap frequency measurements using ^{174}Yb

For trap frequency measurements we prepare a cold sample of ^{174}Yb in the respective ODT/BIODT potential using the combined Yb-Rb-preparation sequence described in Chap. 5. In order to probe the harmonic part of the potential, the ^{174}Yb atoms are

sympathetically cooled by ^{87}Rb to temperatures of $1 \ldots 2\,\mu$K, well below the temperatures obtained by evaporative cooling (see Chap. 7 for details). For trap frequency measurements the Rb atoms are removed.

Radial direction In contrast to the MT trap frequency measurement, a direct observation of the radially oscillating atomic cloud is experimentally impractical for the BIODT in the present configuration. The main difficulty is, to excite an oscillation at a well-determined starting time.

Instead, the radial BIODT trap frequencies are measured using the parametric excitation method [132]. According to the classical description of a parametrically driven harmonic oscillator, the equation for the parametric oscillations can be written as [133]

$$\ddot{x}(t) + \omega^2(t)\, x(t) = 0, \tag{6.4}$$

where $\omega(t)$ represents the time-dependent frequency of the oscillator. For parametric excitation, a modulated frequency according to

$$\omega(t) = \omega_0(1 + A\sin(\omega_m t))\,, \tag{6.5}$$

with the natural frequency of the oscillator ω_0, the modulation frequency ω_m and the modulation amplitude A is assumed. When the modulation frequency ω_m is close to twice the trap frequency $2\omega_0$ or close to subharmonic frequencies $2\omega_0/n$ ($n \in \mathbb{N}$), the energy of the oscillator increases exponentially. The presence of damping in the oscillation introduces a threshold for the modulation amplitude A, which has to be exceeded, for the resonant enhancement to occur. This result also holds in a fully quantum mechanical description. [134].

Experimentally, the ODT beam power is modulated with a variable modulation frequency. When this frequency equals twice the trap frequency $2\omega_0$ or subharmonics $2\omega_0/n$, trapped atoms are heated and eventually lost from the atom trap.

For trap frequency measurements using 174Yb, we modulate the ODT beams for 2 s and subsequently determine the ^{174}Yb temperature[1]. We use the single-image method as described in Sec. 4.3.4 for temperature determination. Parametric heating is observed in the range between 300 Hz and 2500 Hz and the temperature peaks can be assigned to twice the trap frequency and one subharmonic frequency. The modulation amplitude is experimentally optimized in order to detect resonance peaks in the ^{174}Yb temperature without major atom loss. This limits the influence of anharmonic contributions to the trap frequency measurement, as the atomic clouds remains "deep" in the trapping potential. We use a modulation depth of $\approx 4\,\%$ around the main parametric resonance at twice the trap frequency $2\omega_0$ and $\approx 8\,\%$ for the weaker resonance at ω_0. Figure 6.2 (a) shows trap frequency measurements of the single-color ODTs and the BIODT. Each of the measurements consists of several frequency sweeps with a total number of $50 \ldots 110$ single data points. For the temperature plots, the data is scaled by the modulation depth and the relative

[1] For measurements in the BIODT, only the 532 nm beam is modulated, which still determines the BIODT trap frequency.

used element	trap type	beam power	radial measurement peak 1 [Hz]	radial measurement peak 2 [Hz]	radial measurement $\omega_r/2\pi$ [Hz]	axial $\omega_z/2\pi$ [Hz]
^{174}**Yb**	532 nm ODT	$P_{532} = 343\,\mathrm{mW}$ $P_{1064} = 0$	960 ± 48	1945 ± 103	$\mathbf{964 \pm 44}$	$\mathbf{7.5 \pm 0.49}$
	1064 nm ODT	$P_{532} = 0$ $P_{1064} = 135\,\mathrm{mW}$	539 ± 20	1074 ± 57	$\mathbf{538 \pm 19}$	$\mathbf{7.4 \pm 0.43}$
	BIODT	$P_{532} = 343\,\mathrm{mW}$ $P_{1064} = 88\,\mathrm{mW}$	1039 ± 20	2092 ± 64	$\mathbf{1040 \pm 19}$	$\mathbf{9.3 \pm 0.22}$
	BIODT	$P_{532} = 343\,\mathrm{mW}$ $P_{1064} = 118\,\mathrm{mW}$	1091 ± 24	2165 ± 61	$\mathbf{1089 \pm 22}$	$\mathbf{10.5 \pm 0.16}$
^{87}**Rb**	1064 nm ODT	$P_{532} = 0$ $P_{1064} = 135\,\mathrm{mW}$	– –	2922 ± 191	$\mathbf{1461 \pm 96}$	$\mathbf{20.0 \pm 0.77}$
	BIODT	$P_{532} = 172\,\mathrm{mW}$ $P_{1064} = 135\,\mathrm{mW}$	1247 ± 64	2418 ± 177	$\mathbf{1239 \pm 60}$	– –
	BIODT	$P_{532} = 229\,\mathrm{mW}$ $P_{1064} = 135\,\mathrm{mW}$	1093 ± 37	2231 ± 154	$\mathbf{1094 \pm 36}$	– –
	BIODT	$P_{532} = 343\,\mathrm{mW}$ $P_{1064} = 135\,\mathrm{mW}$	801 ± 39	– –	$\mathbf{801 \pm 39}$	– –

Table 6.2: *Summarized results for ODT/BIODT trap frequency measurements.*

offset is adjusted. Error bars of the individual data points include uncertainties from the temperature determination as well as shot-to-shot fluctuations. Gaussian shaped fitting functions are used to extract resonance frequencies, which are summarized in Tab. 6.2.

Determination of axial trap frequencies from the cloud size Axial trap frequencies for the ODT/BIODT can directly be determined from the axial ^{174}Yb cloud size σ_z of atomic samples at known temperature T according to

$$\omega_z = \frac{1}{\sigma_z}\sqrt{\frac{k_\mathrm{B}T}{m}}\,. \tag{6.6}$$

Due to the low axial trap frequencies $\omega_z/\omega_r = \sigma_r/\sigma_z \approx 1/100$ (see Eq. 3.49), the axial cloud size $\sigma_z(t_\mathrm{TOF})$ after a time t_TOF of ballistic expansion does not differ significantly from the initial cloud size $\sigma_z(0)$, if t_TOF is small. For $t_\mathrm{TOF} = 3.5\,\mathrm{ms}$, as it is used for ^{174}Yb temperature measurements in the present experiments, the relative cloud expansion is approximated to be $< 3\,\%$ of the initial cloud size, which is still below the fitting uncertainties of the axial cloud size.

The measured axial trap frequencies slightly depend on the present ^{174}Yb temperature, which is demonstrated in Fig. 6.2 (b). This effect is attributed to anharmonicities of the trapping potentials that increasingly contribute for higher temperatures. The flatter potential on the outside results in disproportionately larger cloud sizes and thus an underestimation of the trap frequencies. To account for this, the measured trap frequencies are linearly extrapolated to zero temperature. Figure 6.2 (b) shows the respective linear fit

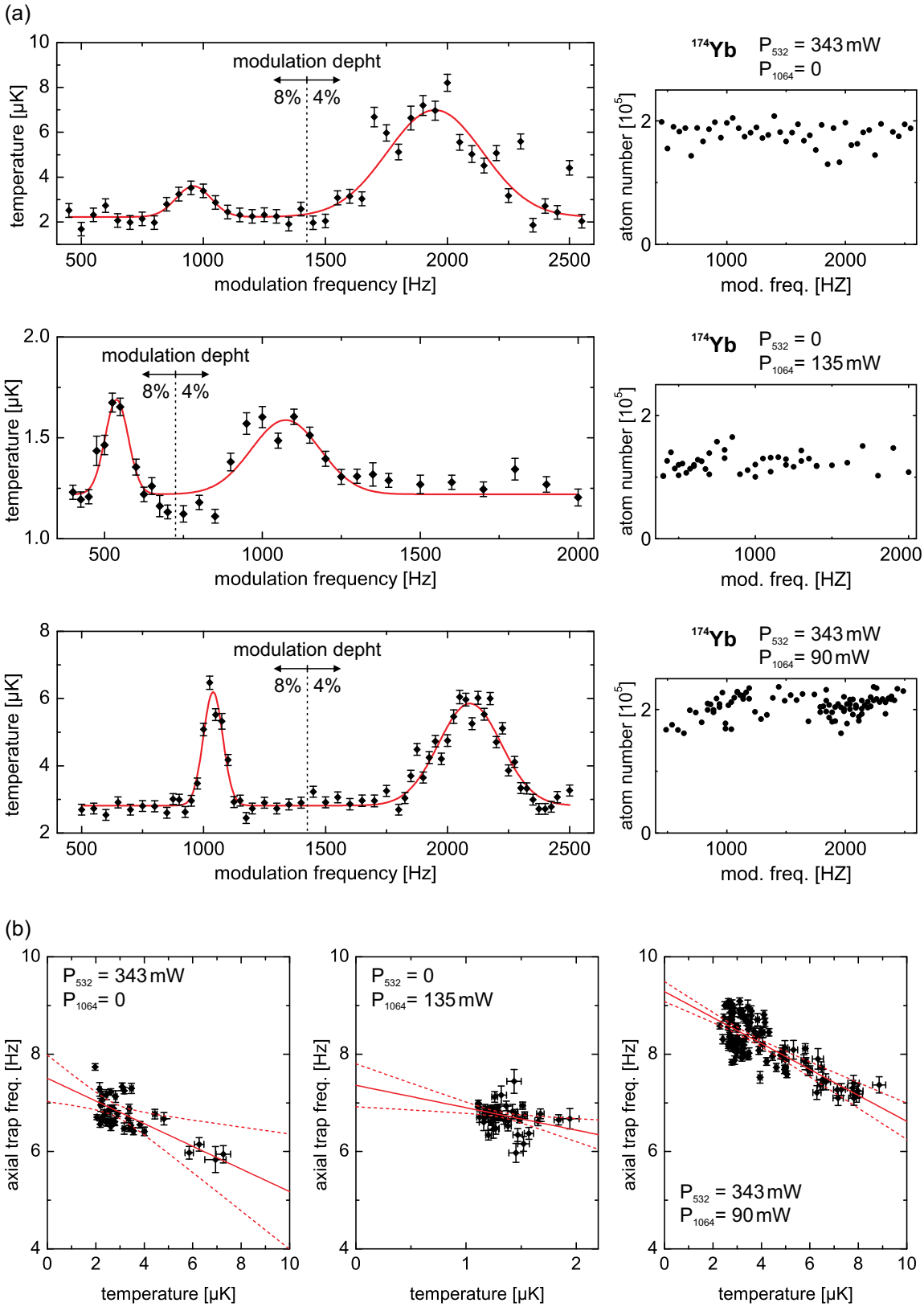

Figure 6.2: *(a) radial- and (b) axial trap frequency measurements of the 532 nm ODT, the 1064 nm ODT and the BIODT using ^{174}Yb.*

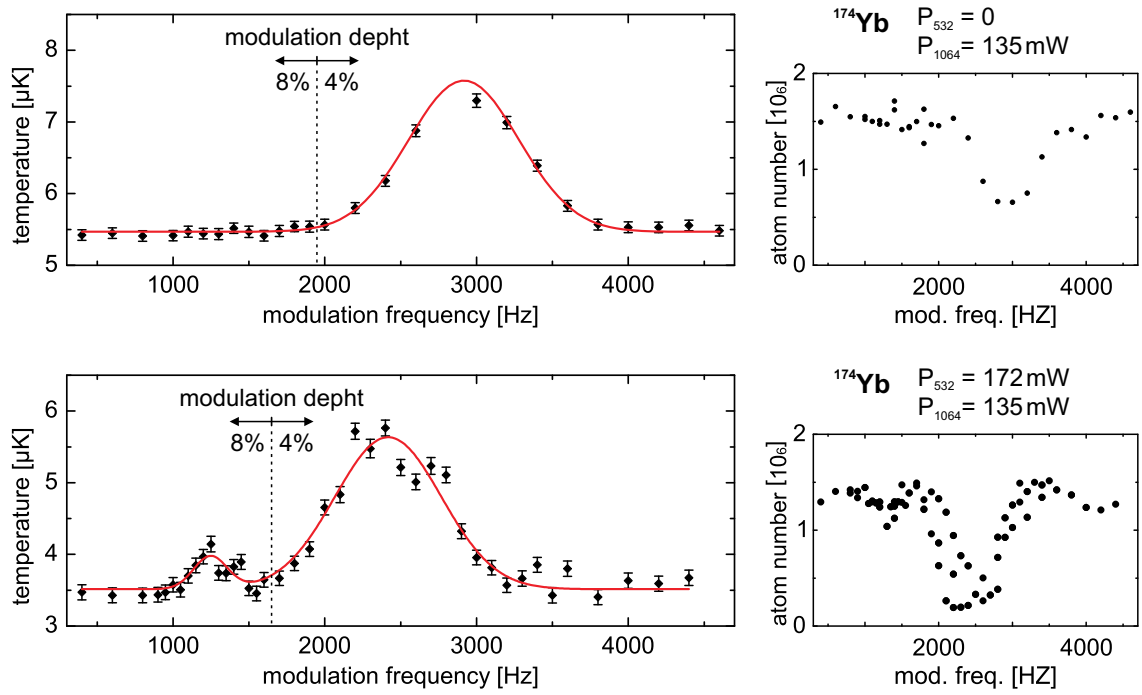

Figure 6.3: *Radial trap frequency measurements of the 1064 nm ODT and the BIODT using ^{87}Rb.*

(red lines) together with the 95 % confidence interval (dashed red lines). Results for the different trap geometries are summarized in Tab. 6.2.

b) Trap frequency measurements using ^{87}Rb

Additional trap frequency measurements of the 1064 nm ODT and the BIODT are performed using ^{87}Rb in order to complement the ^{174}Yb results. Measurements of the "pure" 532 nm ODT are impossible, as this light field does not yield an attractive potential for ^{87}Rb.

For radial trap frequency measurements, a ^{87}Rb cloud at a temperature of $1 \ldots 2\,\mu$K is prepared in the MT and successively moved to the BIODT potential. The transfer to the optical potential is subject to heating due to adiabatic compression to temperatures of $3 \ldots 6\,\mu$K depending on the actual trapping geometry. The MT is turned off and after a short time of 1 s of plain evaporation the ODT/BIODT beam power is modulated for 2 s. Unlike for ^{174}Yb, no further cooling method is available for ^{87}Rb, in order to lower the initial temperature in the optical potentials. Figure 6.3 shows ^{87}Rb temperatures and atom numbers as a function of the modulation frequency for two different trapping geometries.

Due to the initially higher temperatures with respect to the trap depth, parametric heating is inevitably accompanied by atom loss. Note that for the "pure" 1064 nm ODT, no peak at the first subharmonic of $2\omega_r$ is observed at the used modulation depth. In addition to the measurements presented in Fig. 6.3, the trap frequencies of two additional

BIODT configurations are determined using ^{87}Rb. The quantitative analysis of the data is carried out analogously to the ^{174}Yb measurements and the results are also summarized in Tab. 6.2.

In contrast to the ^{174}Yb trap frequency measurement, the data obtained with ^{87}Rb is not useful to determine the axial trap frequency. The cloud expansion during the TOF used for the ^{87}Rb temperature determination ($t_{\mathrm{TOF}} = 10 \ldots 30\,\mathrm{ms}$) can not be neglected compared to the initial cloud size. Hence, dark contrast intratrap images of ^{87}Rb at a known temperature of $\approx 5\,\mu$K are used to extract the axial trap frequency. This additional measurement is performed for the 1064 nm ODT only and the result is included in Tab. 6.2.

c) Systematic effects

According to the classical theory of parametric heating [133], the displacement of an oscillator $x(t)$ and hence the energy $E(t) \propto x^2(t)$ increases exponentially with time in the case of a parametric resonance:

$$x(t) \propto e^{t/T} \qquad \text{and} \qquad E(t) \propto e^{2t/T}\,. \tag{6.7}$$

Here, $T = 2\pi/\omega_m$ represents the modulation period. In order to insert a constant amount of energy in the system, the modulation time t_{mod} in a parametric heating experiment should be adjusted to include a constant number of oscillation periods: $t_{\mathrm{mod}} \propto 1/\omega_m$. The measurements presented here, however, are carried out at a constant modulation time. Experimentally, this does not change the measured position of parametric resonances, but it affects the relative weighting of the data points around a resonance. The influence on the peak shape increases with the peak width. Hence, this effect is taken into account in the data analysis by including a peak width dependent error in the final error budget presented in Tab. 6.2.

Another systematic effect is attributed to the anharmonicity of the actual trapping potential. Its influence depends on the atomic temperature compared to the trap depth U_0, which significantly differs for measurements with ^{174}Yb and ^{87}Rb: Due to the possibility of sympathetic cooling, the ^{174}Yb experiments are carried out at $k_{\mathrm{B}}T_{\mathrm{Yb}}/U_0 = 4 \ldots 6\,\%$, whereas the ^{87}Rb clouds are characterized by $k_{\mathrm{B}}T_{\mathrm{Rb}}/U_0 = 9 \ldots 15\,\%$[2]. For a quantitative analysis, the (amplitude dependent) radial oscillation frequency in the full potential is calculated as a function of the ratio of the praticel energy E and the trap depth U_0 in a one-dimensional model potential corresponding to the radial potential at the axial trap center. This is illustrated in Fig. 6.4 (a). In contrast to the harmonic potential, the oscillation frequency decreases for higher particle energies in a Gaussian-shape potential, which mimicks the potential in a single-beam optical trap.

The energy distribution of a thermal atomic cloud is generally given by the Maxwell Boltzmann energy distribution [67]:

$$N(E)dE \propto E^2\, e^{-E/k_{\mathrm{B}}T}\, dE \tag{6.8}$$

[2]These numbers are calculated assuming a beam waist $w_0 = 15\,\mu$m.

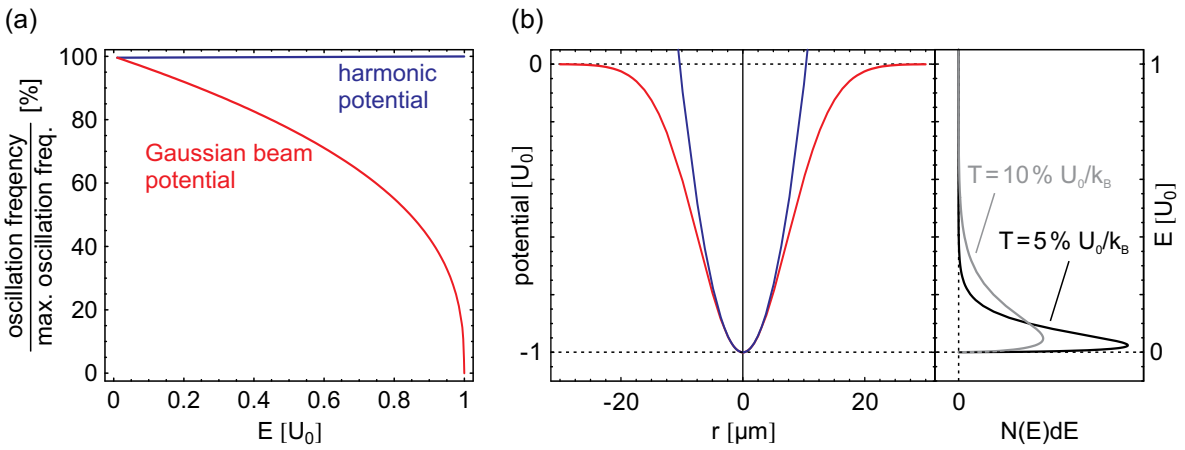

Figure 6.4: *One-dimensional approximation of anharmonic effects for trap frequency measurements. (a) Calculated oscillation frequency dependence on the relative particle energy. (b) Comparison between the harmonic- and the Gaussian-shape potential and Maxwell Boltzmann energy distribution $N(E)dE$ for different cloud temperatures*

Figure 6.4 (b) shows calculated Maxwell Boltzmann energy distributions $N(E)dE$ for $k_\mathrm{B}T/U_0 = 5\,\%$ and $k_\mathrm{B}T/U_0 = 10\,\%$. Combining this distribution with the calculated energy dependence of the oscillation frequency, one obtains a distribution of oscillation frequencies. For $k_\mathrm{B}T/U_0 = 5\,\%$, the peak of this distribution is shifted by $\approx 0.5\,\%$ with respect to the harmonic oscillation frequency and for $k_\mathrm{B}T/U_0 = 10\,\%$ by $\approx 2\,\%$.

In the three-dimensional optical potential, the radial oscillation frequency also depends on the axial position, which can be taken into account by the following approximation: The light intensity $I(z)$ of a Gaussian beam decreases for $|z| > 0$ as $w(z)$ increases according to Eq. 3.40 and at the Rayleigh length $z = z_\mathrm{R} = \pi w_0^2/\lambda$, the intensity is reduced by half. The radial oscillation frequency ω_r depends on the intensity as $\omega_r \propto \sqrt{I(z)}$. Making use of the fact, that trap frequency measurements are typically carried out with atom clouds with an axial size $\sigma_z/z_\mathrm{R} \approx 15\,\%$ for ^{174}Yb and $\sigma_z/z_\mathrm{R} \approx 25\,\%$ for ^{87}Rb, one can estimate that, the radial oscillation frequency varys at level of $\approx 1\,\%$ for ^{174}Yb and $\approx 4\,\%$ for ^{87}Rb.

In summary, the anharmonicity of the trapping potential affects the ODT/BIODT trap frequency measurements performed with ^{174}Yb on a level beyond the experimental uncertainty. Due to the higher temperatures with respect to the trap depth, the ^{87}Rb measurement results tend to produce slightly lower values than the actual harmonic trap frequency. However, the rough approximations presented here are not sophisticated enough to provide a correction factor for the ^{87}Rb data. Hence, the limits set by this approximation are treated as errors and for the calculation of the BIODT potential parameters the results obtained with ^{174}Yb are used.

d) Determination of beam parameters

Beam waist In general, the intensity distribution around the focus of a Gaussian laser beam is completely described by one single parameter, the beam waist w_0. This parameter

can be calculated with the knowledge of the radial trap frequency ω_r. It follows from a solution of equations (3.45), (3.43) and (3.41):

$$w_0 = \sqrt{\frac{4U_0}{m\omega_r^2}} \quad \text{with} \tag{6.9}$$

$$U_0 = \sum_i -\frac{3\pi c^2}{2\omega_{0i}^3}\left(\frac{\gamma_i}{\omega_{0i}-\omega}+\frac{\gamma_i}{\omega_{0i}+\omega}\right)\frac{2P}{\pi w_0^2}\,. \tag{6.10}$$

This calculation, however, involves the theoretical determination of the optical dipole potential $U_0 = U_{\mathrm{dip}}(\vec{r}=0)$. According to the descriptions on multi-level atoms in Sec. 3.2.3, the optical dipole potential is given as the sum of the individual contributions of all relevant atomic levels. For atomic states with fine structure splitting, the contributions of each fine structure transition are weighted by the corresponding oscillator strength in order to calculate a mean effective transition frequency and line width. A detailed discussion on relevant atomic levels included in the calculation for the case of ^{87}Rb and Yb can be found in [9]. All atomic transitions, which contribute to the total dipole potential by more than 1% of the major transition are summarized in Tab. 6.3.

Using the radial trap frequency measurements with ^{174}Yb for the individual ODTs and the BIODT, the following beam waists for the 532 nm- and 1064 nm ODT beams are obtained:

$$w_{532\mathrm{ODT}} = (15.78 \pm 0.20)\,\mu\mathrm{m}$$

$$w_{1064\mathrm{ODT}} = (14.71 \pm 0.25)\,\mu\mathrm{m}$$

Validity of trap frequency results Figure 6.5 (a) shows measured trap frequencies of the 532 nm ODT and the BIODT obtained with ^{174}Yb as a function of the 1064 nm ODT power. This plot also includes calculated trap frequencies using the specified beam parameters. For the BIODT, the trap frequency is determined by the individual trap frequencies according to

$$\omega_i^{\mathrm{BIODT}} = \sqrt{\left(\omega_i^{532\mathrm{ODT}}\right)^2 + \left(\omega_i^{1064\mathrm{ODT}}\right)^2} \qquad i = r, z\,. \tag{6.11}$$

A comparison of measured 1064 nm ODT and BIODT radial trap frequencies using ^{87}Rb and calculations based on $w_{532} = 15.78\,\mu$m and $w_{1064} = (14.71 \pm 0.25))\,\mu$m is displayed in Fig. 6.5 (b). The small deviation, especially for the "pure" 1064 nm ODT, can be attributed to the larger contribution of anharmonic effects present for the ^{87}Rb experiments (see discussion above).

Rayleigh length For a Gaussian beam, the Raleigh length z_{R} is determined by the beam waist according to $z_{\mathrm{R}} = {}^{\pi \mathrm{w}_0^2}/_{\lambda}$ and the axial trap frequency is related to the Raleigh length through

$$\omega_{\mathrm{z}} = \omega_{\mathrm{r}}\frac{w_0}{\sqrt{2}\,z_{\mathrm{R}}} = \omega_{\mathrm{r}}\frac{\lambda}{\pi\sqrt{2}\,w_0}\,. \tag{6.12}$$

^{87}Rb				
excited state	transition wavelength λ_{vac} [nm]	transition probability A_{ij} [s^{-1}] $\equiv \gamma$	line width $\gamma/2\pi$ [Hz]	oscillator strength f_i
$5^2P_{3/2}$	780,237	$3,81 \cdot 10^7$	$6,06 \cdot 10^6$	0,695
$5^2P_{1/2}$	794,975	$3,61 \cdot 10^7$	$5,75 \cdot 10^6$	0,342
$6^2P_{3/2}$	420,295	$1,77 \cdot 10^6$	$2,82 \cdot 10^5$	$9,37 \cdot 10^{-3}$
$6^2P_{1/2}$	421,669	$1,50 \cdot 10^6$	$2,39 \cdot 10^5$	$4,00 \cdot 10^{-3}$
excited state	effective transition wavelength $\bar{\lambda}_{\mathrm{vac}}$ [nm]	effective transition probability $\bar{A}_{ij}$ [s^{-1}] $\equiv \bar{\gamma}$	effective line width $\gamma/2\pi$ [Hz]	
5^2P	785.037	$3,74 \cdot 10^7$	$5,96 \cdot 10^6$	
6^2P	420.705	$1,69 \cdot 10^6$	$2,69 \cdot 10^5$	
Yb				
excited state	transition wavelength λ_{vac} [nm]	transition probability A_{ij} [s^{-1}] $\equiv \gamma$	line width $\gamma/2\pi$ [Hz]	
6^1P_1	398,910	$1,76 \cdot 10^8$	$2,80 \cdot 10^7$	
7^1P_1	246,521	$9,10 \cdot 10^7$	$1,45 \cdot 10^7$	
$6(^7/_2, ^5/_2)_1$	346,534	$6,20 \cdot 10^7$	$9,87 \cdot 10^6$	
$4f^{13}5d6s^2$	267,272	$1,18 \cdot 10^7$	$1,88 \cdot 10^6$	
6^3P_1	555,798	$1,14 \cdot 10^6$	$1,81 \cdot 10^5$	

Table 6.3: *Relevant ground state transitions in ^{87}Rb and Yb used for the BIODT potential calculations. Wavelength λ_{vac} from [135, 136], A_{ki} from [135] and f_i calculated according to (3.38). Effective $\bar{\lambda}_{vac}$ and $\bar{A}_{ki}$ for the $n^2P_{3/2\,(1/2)}$ $(n = 5, 6)$ fine structure doublets in ^{87}Rb are calculated according to (3.37).*

Experimentally, however, deviations of the trapping laser beam from a "perfect" Gaussian beam and astigmatism effects can lead to an increased Rayleigh length for a given beam waist, which we will characterize by an axial expansion factor f_r according to:

$$z_{\mathrm{R,exp}} = f_{\mathrm{R}} \cdot \frac{\pi w_0^2}{\lambda} \,. \tag{6.13}$$

The axial expansion factor f_{R} can be determined by comparing measured axial trap frequencies with results obtained from Eq. 6.12. Using the data from axial trap frequency measurements with ^{174}Yb for the individual ODTs, the expansion factors are:

$$f_{\mathrm{R},532} = 0.96 \pm 0.07$$

$$f_{\mathrm{R},1064} = 1.19 \pm 0.07 \,.$$

The axial trap frequency measurement performed with ^{87}Rb for the 1064 nm ODT leads to $f_{\mathrm{R},1064} = 1.34 \pm 0.07$.

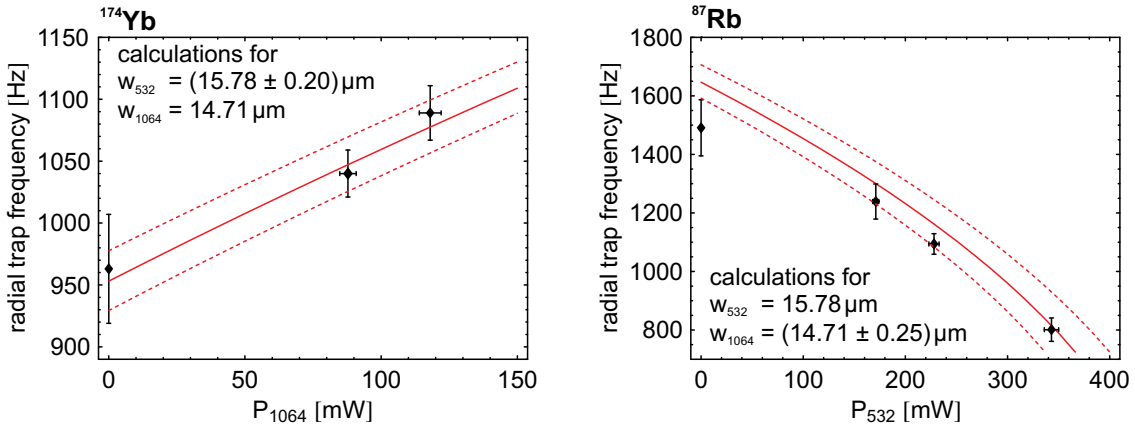

Figure 6.5: *Measured radial ODT/BIODT trap frequencies for different trapping geometries using (a) ^{174}Yb and (b) ^{87}Rb and comparison to calculations based on the specified trap parameters.*

While the results for the 532 nm ODT are consistent with a Gaussian beam, the 1064 nm ODT beam is obviously not a perfect Gaussian beam as its experimentally determined Rayleigh length is $\approx 20\%$ larger than expected.

6.2 Model potentials

With the knowledge of experimentally obtained MT and BIODT parameters, it is possible to model the potentials of various trapping configurations both for ^{87}Rb and Yb. Density distributions of thermal atomic clouds in the presence of these potentials can in turn be calculated according to Eq. 3.17 and Eq. 3.18.

General approach In the most general case, the total potentials for ^{87}Rb and Yb are given by:

$$U_{\mathrm{tot}}^{\mathrm{Rb}} = U_{\mathrm{MT}}^{\mathrm{Rb}} + U_{532\mathrm{ODT}}^{\mathrm{Rb}} + U_{1064\mathrm{ODT}}^{\mathrm{Rb}} + U_{\mathrm{grav}}^{\mathrm{Rb}} \tag{6.14}$$

$$U_{\mathrm{tot}}^{\mathrm{Yb}} = U_{532\mathrm{ODT}}^{\mathrm{Yb}} + U_{1064\mathrm{ODT}}^{\mathrm{Yb}} + U_{\mathrm{grav}}^{\mathrm{Yb}} \tag{6.15}$$

The magnetic potential $U_{\mathrm{MT}}^{\mathrm{Rb}}$ is specified by Eq. 3.14 and the parameters presented in Sec. 6.1.1. For the calculation of optical potentials $U_{532\mathrm{ODT}}^{\mathrm{i}}$ and $U_{1064\mathrm{ODT}}^{\mathrm{i}}$ (i = Rb, Yb), Eq. 3.40 is used including beam parameters given in Sec. 6.1.2. For this calculation, the atomic transitions presented in Tab. 6.3 are taken into account. The gravitational potential is given by $U_{\mathrm{grav}}^{\mathrm{i}} = m_i \cdot g \cdot x$ (i = Rb, Yb), where g is the gravitational acceleration and x represents the vertical direction. Note that experimentally the optical axis of both ODT beams as well as the weak axis of the MT potential are aligned with the horizontal (z) axes. Figure 6.6 shows calculated potentials $U_{\mathrm{tot}}^{\mathrm{Rb}}$ and $U_{\mathrm{tot}}^{\mathrm{Yb}}$ for the case that all individual potential centers spatially coincide. The BIODT beam powers in this plot are chosen to $P_{532} = 343\,\mathrm{mW}$, $P_{1064} = 115\,\mathrm{mW}$, which results in almost perfect cancellation for ^{87}Rb.

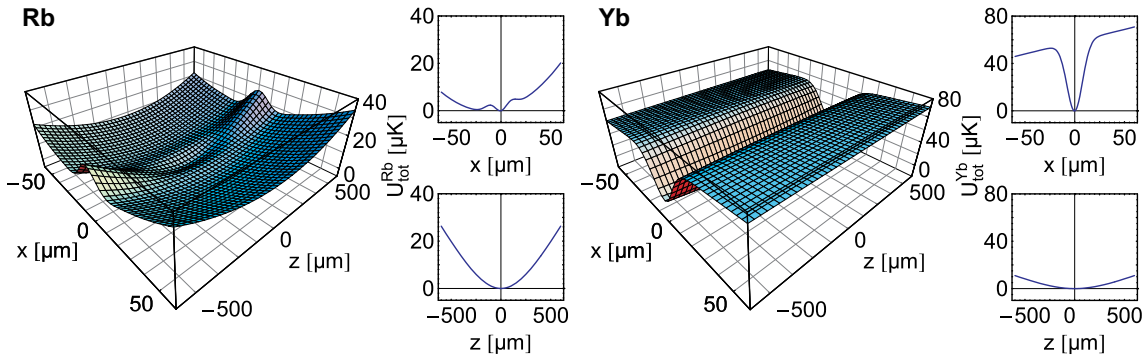

Figure 6.6: *Calculated potentials for Rb and Yb for a BIODT power adjustment of almost perfect potential cancellation for Rb: $P_{532} = 343\,mW$, $P_{1064} = 115\,mW$. Three-dimensional diagram of the x-z-plane and radial and axial cuts of the respective potentials.*

Resulting from unequal waists of the individual ODT beams, an absolute perfect potential cancellation in the trap center, as depicted in Fig. 5.1 of Sec. 5.1 can not be achieved in our real experimental situation. Note that the actual ODT beam power ratio is optimized experimentally as will be described in Sec. 7.1.2.

Harmonic approximation Due to the low ^{87}Rb temperatures ($k_B T_{Rb} \ll \mu B_0$) in the relevant experiments, the use of the harmonic MT approximation (Eq. 3.15) for U_{MT}^{Rb} is justified. Furthermore, the ODT potentials for Yb U_{532ODT}^{Yb} and $U_{1064ODT}^{Yb}$ can be replaced by the harmonic form (3.44) for Yb temperatures well below the total trap depth ($k_B T_{Yb} \ll U_0$). The use of harmonic approximations for the ^{87}Rb BIODT potentials U_{532ODT}^{Rb} and $U_{1064ODT}^{Rb}$ depend on the actual trapping geometry and are discussed in detail for the respective cases (see Sec. 8.2.1).

Gravity The presence of the gravitational potential leads to small displacements of trap centers and trapped atom clouds. However, for the experiments presented in the scope of this thesis, the influence of gravity is negligible for the following reasons:

- Within the harmonic regime, the linear gravitational potential generally does not alter the shape of the potential, but leads only to a shift of the trap center denoted as "gravitational sag". The trapping frequencies remain constant.
- Due to the strong radial confinement of the optical potentials, the gravitational sag for Yb is small compared to the cloud dimensions: For typical experimental parameters ($P_{532} = 343\,\mathrm{mW}$, $P_{1064} = 115\,\mathrm{mW}$), the radial cloud displacement is $\approx 0.2\,\mu$m, which is equivalent to $\approx 4\,\%$ of the $1/e^2$-diameter of an Yb cloud at a temperature of $1.5\,\mu$K.
- During interspecies interaction experiments with ^{87}Rb and ^{174}Yb (see Chap. 8), the relative BIODT beam powers are adjusted in a way to create an attractive potentials for ^{87}Rb ($P_{532} = 343\,\mathrm{mW}$, $P_{1064} = 135\,\mathrm{mW}$). The ^{87}Rb cloud trapped in this BIODT

potential is shifted by $\approx 0.3\,\mu$m, due to the gravitational potential. The gravity related relative displacement of the ^{87}Rb- and the simultaneously trapped ^{174}Yb cloud is well below the accuracy achieved in the spatial overlap of both ODT beams.

- For interspecies interaction experiments, the MT position is experimentally optimized to achieve maximum overlap of the ^{87}Rb- and the Yb cloud. The gravitational sag of $\approx 14\,\mu$m for ^{87}Rb trapped in the MT is hereby compensated by additional offset fields. Unlike the situation present in Fig. 6.6, the MT center does then not spatially coincide with the BIODT center.

As a result, the gravitational potential is omitted in further model potentials, which leads to a cylindrically symmetric trapping geometry for the important case of spatially overlapping potentials.

7

Interspecies interaction I: thermalization

While Chap. 5 describes the successive preparation ^{87}Rb and Yb in their independent trapping potentials, the following chapter focuses on elastic interactions between the two species, which lead to thermalization of various Yb isotopes with the colder ^{87}Rb cloud.

The first part of the chapter describes the dependence of the thermalization process on relative alignment and power ratio of the ODT beams. These effects are used in the day-to-day alignment process in order to provide stable experimental conditions. The second part of this chapter is devoted to thermalization rate measurements which have been performed with 5 different Yb isotopes. These measurements allow for a determination of the isotope-dependence of the scattering cross section between Yb and ^{87}Rb.

7.1 Basic properties of ultracold Yb-Rb mixtures in the combined trap

Starting point The experiments described in the following are based on the preparation process for ^{87}Rb and Yb as described in Chap. 5. As a starting point for interspecies interaction experiments, the successive loading sequence provides $0.3 \ldots 2 \times 10^5$ Yb atoms at a temperature of $5 \ldots 8\,\mu$K and $1 \ldots 1.5 \times 10^7$ ^{87}Rb atoms at $\approx 1\,\mu$K. After the individual preparation of these two ultracold clouds, the ^{87}Rb atom cloud is moved by the use of a 500 ms long, S-shaped MT ramp to the BIODT position. Due to adiabatic heating resulting from residual optical potentials, the ^{87}Rb temperature is slightly increased to $\approx 1.5\,\mu$ K as soon as the ^{87}Rb cloud overlaps with the BIODT.

Isotopic dependence Elastic interactions between ^{87}Rb and Yb manifest themselves in thermalization of the two species: Depending on the BIODT light power ratio and -alignment and the Yb isotope, the Yb temperature decreases reaching approximately the ^{87}Rb temperature. The isotope ^{174}Yb plays an outstanding role compared to the other Yb isotopes as it is characterized by an exceptionally large elastic cross section with ^{87}Rb in the present temperature range. Under the conditions of our experiments, this results in almost instantaneous thermalization with ^{87}Rb. Studies on the relative alignment and power ratio of the ODT beams are hence typically performed with this Yb isotope.

7.1.1 Thermalization model

Sympathetic cooling of Yb by colder ^{87}Rb can be described by a simple thermalization model [9]. This model is used for qualitative conclusions related to the influence of relative alignment and power ratio of the ODT beams. In addition, the data analysis of measured thermalization rates described in Sec. 7.2 is also based on this model.

When Yb is brought into contact with ^{87}Rb (temperature: T_{Rb}, atom number N_{Rb}), the temporal evolution of its temperature T_{Yb} is given by:

$$\frac{dT_{\mathrm{Yb}}}{dt} = -\gamma_{\mathrm{th}} \cdot \Delta T + \dot{T}_{\mathrm{Yb}}^{\mathrm{heat}} \qquad \text{with} \quad \Delta T = T_{\mathrm{Yb}} - T_{\mathrm{Rb}} \tag{7.1}$$

Here,γ_{th} is the thermalization rate and $\dot{T}_{\mathrm{Yb}}^{\mathrm{heat}}$ is a constant heating rate of Yb, which is predominantly caused by scattering of ODT light. For the conditions of the experiments described in this and the following chapter, it is experimentally determined to be $(175 \pm 16)\,{}^{\mathrm{nK}}/_{\mathrm{s}}$ (see Sec. 7.2.2). Note that Eq. 7.1 assumes a constant ^{87}Rb atom number and temperature, independent of the presence of Yb. Experimentally, no additional heating of ^{87}Rb due to the presence of Yb could be found, which is explained by the large atom number difference $N_{\mathrm{Rb}} \gg N_{\mathrm{Yb}}$. However, during the quantitative thermalization measurements described in Sec. 7.2, a small constant ^{87}Rb heating rate is observed, which is accounted for in the respective data analysis.

The thermalization rate γ_{th} is directly proportional to the elastic collision rate γ_{coll}. It depends on the number of collisions α required for thermalization and on a mass-dependent reduction factor ξ [137, 138]:

$$\gamma_{\mathrm{th}} = \frac{\xi}{\alpha} \cdot \gamma_{\mathrm{coll}} \qquad \text{with} \quad \xi = \frac{4 m_{\mathrm{Yb}} m_{\mathrm{Rb}}}{(m_{\mathrm{Yb}} + m_{\mathrm{Rb}})^2} \approx 0,89\,. \tag{7.2}$$

The collision rate $\gamma_{\mathrm{coll}} = n_{\mathrm{YbRb}}\, \sigma_{\mathrm{tot\,YbRb}}\, \bar{v}_{\mathrm{YbRb}}$ is connected to the total elastic collision cross-section $\sigma_{\mathrm{tot\,YbRb}}$ by:

$$\sigma_{\mathrm{tot\,YbRb}} = \frac{\alpha}{\xi} \frac{\gamma_{\mathrm{th}}}{n_{\mathrm{YbRb}} \cdot \bar{v}_{\mathrm{YbRb}}}\,. \tag{7.3}$$

Here,

$$\bar{v}_{\mathrm{YbRb}} = \sqrt{\frac{8 k_{\mathrm{B}}}{\pi} \left(\frac{T_{\mathrm{Yb}}}{m_{\mathrm{Yb}}} + \frac{T_{\mathrm{Rb}}}{m_{\mathrm{Rb}}} \right)} \tag{7.4}$$

is the mean thermal relative velocity of the two species and

$$n_{\mathrm{YbRb}} = \left(\frac{1}{N_{\mathrm{Yb}}} + \frac{1}{N_{\mathrm{Rb}}} \right) \int n_{\mathrm{Yb}}(\vec{r}) n_{\mathrm{Rb}}(\vec{r})\, d^3\vec{r} \tag{7.5}$$

is the overlap density. It depends on the density distribution of both atomic clouds and their relative spatial overlap. The absolute value of this quantity is difficult to determine for the present geometry of the potential. Very small deviations from the assumed trapping potential may lead to dramatic changes of the ^{87}Rb density, in particular for conditions

where the light shifts of the two light fields almost cancel for ^{87}Rb. However, for the given case of $N_{\mathrm{Rb}} \gg N_{\mathrm{Yb}}$, the overlap density can be approximated as

$$n_{\mathrm{YbRb}} \approx N_{\mathrm{Rb}} \cdot f_g, \tag{7.6}$$

with a proportionality factor f_g that takes into account the details of the trap geometry.

In summary, the thermalization process described by this model has the following properties:

- Under the assumption of a negligible heating rate ($\dot{T}_{\mathrm{Yb}}^{\mathrm{heating}} \ll \dot{T}_{\mathrm{Yb}}$), the Yb temperature exponentially approaches the ^{87}Rb temperature with a time constant $\tau_{\mathrm{th}} = 1/\gamma_{\mathrm{th}}$.
- A significant Yb heating rate slows the thermalization process and the equilibrium state $\mathrm{d}T_{\mathrm{Yb}}/\mathrm{d}t = 0$ is characterized by a nonzero temperature difference between the two species:

$$\Delta T = \frac{\dot{T}_{\mathrm{Yb}}^{\mathrm{heating}}}{\gamma_{\mathrm{th}}}\,. \tag{7.7}$$

- The thermalization rate γ_{th} depends on the isotope-dependent ^{87}Rb-Yb scattering properties and the overlap integral n_{YbRb}. In a qualitative picture, n_{YbRb} is proportional to the ^{87}Rb density at the position of the Yb cloud. Experimentally, this parameter strongly depends on the ODT beam alignment and the power ratio.

7.1.2 Influence of trap parameters on the thermalization

a) BIODT light power ratio

In order to study the influence of the BIODT light power ratio, ^{87}Rb and ^{174}Yb atoms are prepared and brought into contact as described above. After a defined contact time of $t_{\mathrm{contact}} = 300\,\mathrm{ms}$, the temperature of both atomic species is simultaneously determined. During the contact time, the RF used for ^{87}Rb evaporative cooling remains on. The final 532 nm ODT power is kept at a constant level of $P_{532} = 343\,\mathrm{mW}$, while the 1064 nm ODT power P_{1064} is varied in a range of $65 \ldots 95\,\mathrm{mW}$. Figure 7.1 shows measured temperatures and atom numbers of ^{87}Rb and ^{174}Yb as a function of P_{1064}.

Below a threshold level of $P_{1064} \approx 80\,\mathrm{mW}$, the ^{174}Yb temperature remains at a level independent on the presence of ^{87}Rb (indicated by the dashed line in Fig. 7.1). This temperature is slightly lower than the initial ^{174}Yb temperature, which is related to plain evaporative cooling during the contact time $t_{\mathrm{contact}} = 300\,\mathrm{ms}$. For P_{1064} greater than this threshold , ^{174}Yb thermalizes with the colder ^{87}Rb cloud and reaches its temperature. Furthermore, an increase in P_{1064} is accompanied by a slight ^{87}Rb temperature rising and ^{174}Yb atom loss. Above $P_{1064} \approx 100\,\mathrm{mW}$, almost no ^{174}Yb atoms are left after the contact time $t_{\mathrm{contact}} = 300\,\mathrm{ms}$

The qualitative results of this experiment can be understood using calculated model potentials and density distributions[1]: By increasing P_{1064}, the BIODT potential is grad-

[1]The model potentials used here include the harmonic approximation for $U_{\mathrm{MT}}^{\mathrm{Rb}}$ according to Eq. 3.15 and the "full" form of the BIODT potentials $U_{532\mathrm{ODT}}^{\mathrm{i}}$ and $U_{1064\mathrm{ODT}}^{\mathrm{i}}$ (i = Rb, Yb) according to Eq. 3.40. Gravity is neglected, which in total results in a clyindrical symmetric potential.

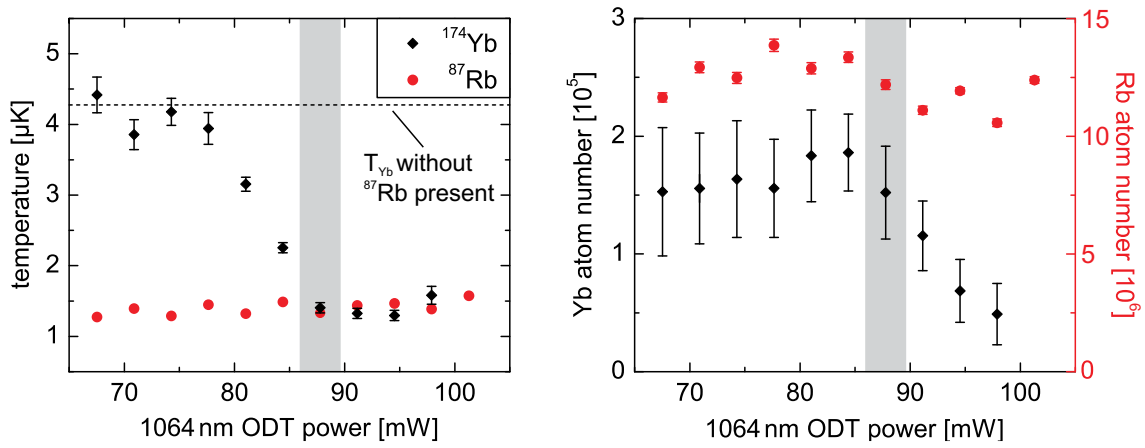

Figure 7.1: *Measured ^{87}Rb and ^{174}Yb temperatures and atom numbers depending on the 1064 nm ODT Power. The gray areas indicate the optimized 1064 nm BIODT power used for further experiments. The data is obtained at the following parameters: P_{532} = 343 mW, t_{contact} = 300 ms.*

ually changed from being repulsive to being attractive for ^{87}Rb in the trap center. This is illustrated in Fig. 7.2. At P_{1064} = 70 mW (Fig. 7.2 (a)), the attractive effect of the 1064 nm light is not strong enough to compensate the 532 nm ODT potential and a repulsive residual 532 nm ODT potential remains. As a result, the ^{87}Rb atoms are arranged in a hollow cylinder around the trap center, where the ^{174}Yb cloud is located. This is shown in Fig. 7.2 (c), which presents axial cuts of calculated Rb and Yb density distributions for $T_{\mathrm{Rb,Yb}} = 1.5\,\mu$K for different settings of P_{1064}.

At P_{1064} = 120 mW (Fig. 7.2 (b)), however, the 1064 nm ODT overcompensates the repulsive effect of the 532 nm light and creates a small "dimple" for ^{87}Rb at the trap center. As a result, the calculated ^{87}Rb density at the trap center rises by up to 6 orders of magnitude during an increase of the 1064 nm ODT power from 70 mW to 120 mW (see Fig. 7.3). Note that in the transition region between a repulsive and an attractive potential for ^{87}Rb, the calculated density n_{Rb} strongly depends on the ODT beam waists $w_{532\mathrm{ODT}}$, $w_{1064\mathrm{ODT}}$ used for the model potential. As a result, uncertainties in these parameters lead to large errors for n_{Rb} up to one order of magnitude. Furthermore, deviations of the actual potential from our model due to imperfect experimental conditions, like non-Gaussian beam shapes, have to be considered. Hence, only a limited quantitative analysis involving the ^{87}Rb density is possible in this trapping geometry. However, qualitative conclusions based on these calculations are well justified, in particular if properties of different Yb isotopes are compared.

The experimental data shows, that the ^{87}Rb density reached at $P_{1064} \approx 88$ mW is high enough to sympathetically cool the ^{174}Yb cloud within the chosen contact time t_{contact} = 300 ms. For further increase of the ^{87}Rb density, the thermalization process is accompanied by rapid atom loss of ^{174}Yb, resulting from inelastic three-body collisions. For ^{87}Rb, no additional loss is observed, which is related to the much higher atom number $N_{\mathrm{Rb}} \gg N_{\mathrm{Yb}}$.

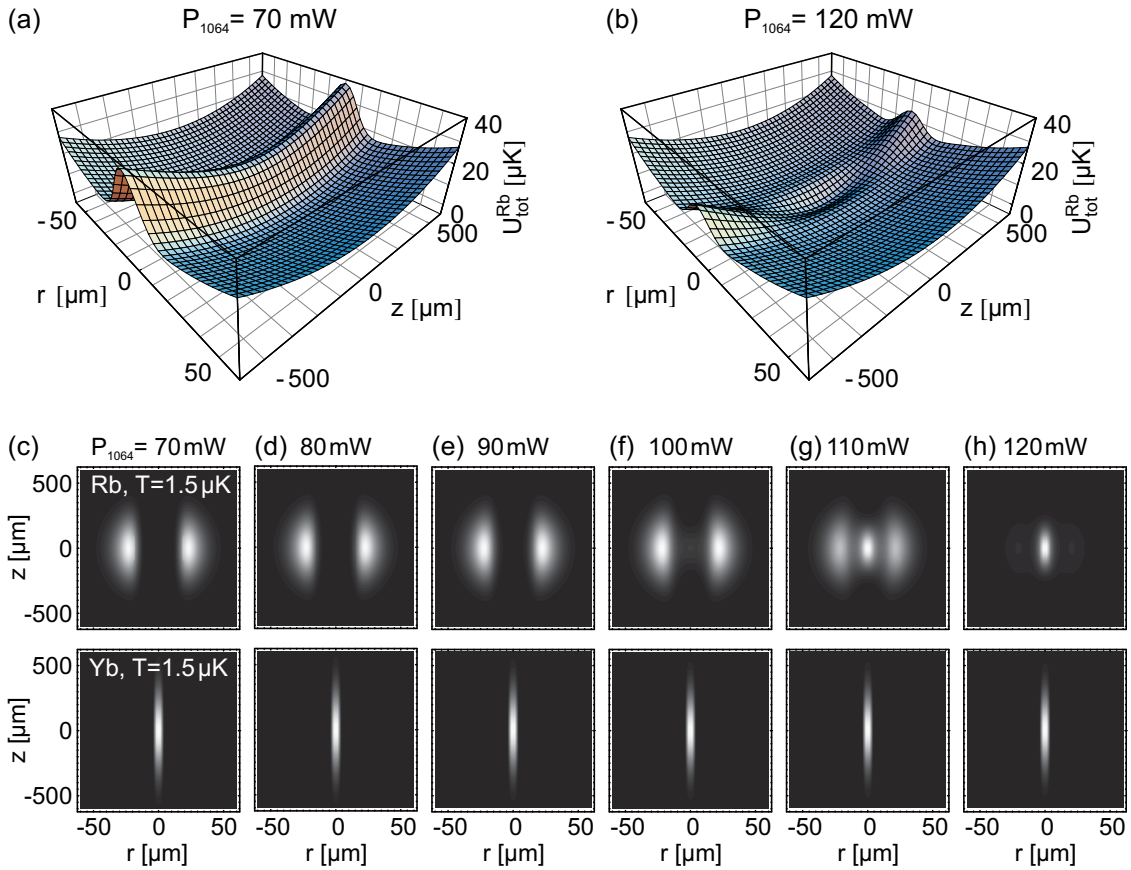

Figure 7.2: *(a, b) Calculated potentials for ^{87}Rb for different settings of the 1064 nm ODT power. (c-h) Axial cuts of calculated density distributions for both species at $T_{\mathrm{Rb,Yb}} = 1.5\,\mu K$. Note that the scales in this series of plots can not be compared directly as they are chosen to match the peak density in each plot.*

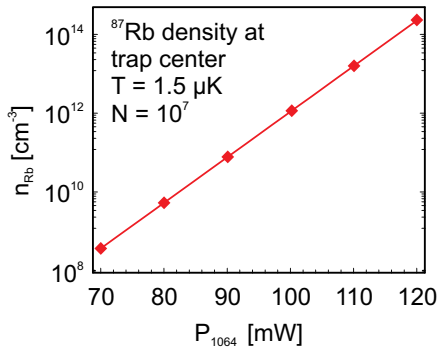

Figure 7.3: *Calculated ^{87}Rb peak density N_{Rb} in the trap center ($r = 0$, $z = 0$) for $T_{\mathrm{Rb}} = 1.5\,\mu K$ and $N_{\mathrm{Rb}} = 10^7$. The calculations strongly depend on the used ODT beam waists $w_{532\mathrm{ODT}}$, $w_{1064\mathrm{ODT}}$. Errors of n_{Rb} resulting from uncertainties of $w_{532\mathrm{ODT}}$, $w_{1064\mathrm{ODT}}$ are approximately one order of magnitude.*

This particular behavior of ^{174}Yb is due to peculiarities of the interatomic potential (and will be detailed in Sec. 8.4.2). All other Yb isotope do not exhibit atom loss due to the presence of ^{87}Rb. The slight ^{87}Rb temperature increase is related to adiabatic heating caused by the increasingly attractive potential for ^{87}Rb.

Ideal BIODT power ratio The results from the measurements described here, are used to optimize the BIODT light power ratio experimentally. For a fixed 532 nm ODT power of $P_{532} = 343\,\mathrm{mW}$, the ideal setting for P_{1064} is on the order of $\approx 88\,\mathrm{mW}$ for ^{174}Yb, as indicated by the gray areas in Fig. 7.1. Here, the ^{87}Rb density at the position of the ^{174}Yb cloud is high enough to warrant complete thermalization. At the same time, no significant ^{174}Yb atom loss caused by ^{87}Rb is observed for this 1064 nm ODT power. The measurements for BIODT power optimization as presented in this section are generally performed after the relative ODT beam position is adjusted to the best possible overlap (see below).

Due to the different scattering properties with ^{87}Rb, the BIODT light power ratio required for thermalization depends on the specific Yb isotope, and is for each case determined experimentally.

The BIODT light power optimization is part of the daily adjustment routine, in order to ensure constant conditions for further experiments described in Sec. 7.2 and Chap. 8. Figure 7.4 shows experimentally optimized 1064 nm ODT powers $P_{1064,\mathrm{ideal}}$ ($P_{532} = 343\,\mathrm{mW} = const.$) as a function of the day of measurement. All experiments

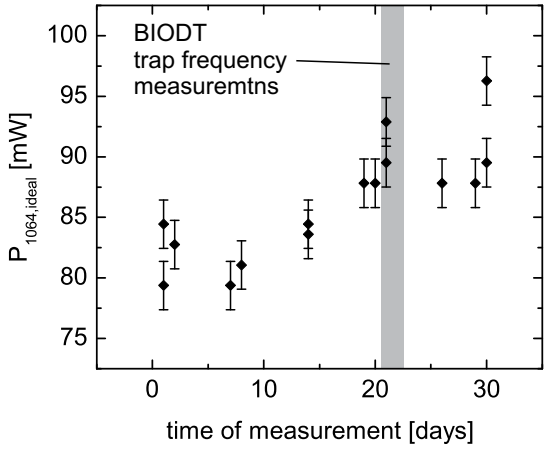

Figure 7.4: *Experimentally determined 1064 nm powers $P_{1064,\mathrm{ideal}}$ optimized for thermalization of ^{174}Yb and ^{87}Rb using a fixed 532 nm power of $P_{532} = 343\,mW$. Within the relevant period for experiments described in Chap. 8, a slight drift from 80 mW to95 mW is observed.*

are performed using ^{174}Yb. Within a time range of several weeks, we observe a slight drift of the ideal power ratio. This is related to long term changes in the 532 nm ODT beam parameters caused by the switching AOM (see Sec. 4.2.3). Taking this into account, the experimentally determined ODT parameters presented in Sec. 6.1.2 are strictly speaking only valid at the day of the frequency measurement. However, the information obtained by this long term analysis is used as a correction factor for the comparison of data measured at different dates.

Note that the experimentally determined BIODT power ratio of $P_{1064}/P_{532} \approx 0.26$ is significantly below the calculated power ratio required for maximum potential cancellation for ^{87}Rb in the trap center. This trapping geometry, as shown in Fig. 6.6 in Sec. 6.2 is characterized by $P_{1064}/P_{532} \approx 0.34$. This result is in good agreement with data from previous measurements [9], that were performed using different BIODT beams and significantly higher absolute ODT powers. For this trapping geometry, the calculated power

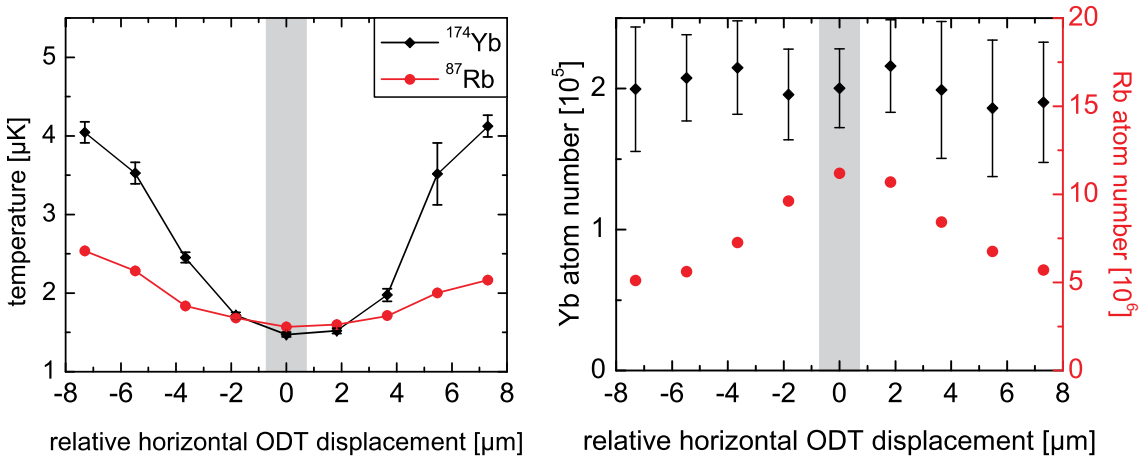

Figure 7.5: *Measured ^{87}Rb and ^{174}Yb temperatures and atom numbers depending on the relative BIODT beam alignment. The data is obtained at the following parameters: $P_{532} = 343\,mW$, $P_{1064} = 88\,mW$.*

ratio of $P_{1064}/P_{532} \approx 0.39$ for ^{87}Rb potential cancellation differs from the experimentally determined ratio of $P_{1064}/P_{532} \approx 0.29$, that provides the lowest ^{174}Yb temperatures. In a qualitative picture, enough contact between the atom clouds of both species is provided for thermalization, although a residual repulsive potential for ^{87}Rb is present.

b) BIODT beam alignment

Radial BIODT alignment The relative position of the individual ODT beams at the trap center is a crucial parameter for experiments in the BIODT potential. Hence, the present setup includes an active stabilization and -control system for the relative radial BIODT position. This system allows the spatial manipulation of the optical trapping potentials on a μm level. However, a direct determination of the radial beam positions by imaging of the atoms trapped in the individual ODTs is limited by the resolution of the present imaging systems to $\approx 5\,\mu$m. For a BIODT beam alignment beyond this level, we make use of its influence on the thermalization process between trapped ^{87}Rb and ^{174}Yb atoms.

In analogy to the experiments focused on the BIODT power ratio, both atomic species atoms are prepared and brought into contact for a fixed contact time $t_{\text{contact}} = 300\,$ms. Subsequently, we determine the temperature and atom number of the trapped ^{87}Rb and ^{174}Yb atoms. The radial 532 nm ODT beam position is manipulated independently in the horizontal and vertical direction using the active position control system. Figure 7.5 shows measured ^{87}Rb and ^{174}Yb data as a function of the relative horizontal ODT displacement. This series of measurements is performed at BIODT powers $P_{532} = 343\,$mW and $P_{1064} = 88\,$mW, which lead to full thermalization of the ^{174}Yb cloud with the ^{87}Rb cloud for perfectly overlapping optical potentials. If the BIODT beams are gradually separated, the following effects are observed:

- The ^{87}Rb temperature increases and the atom number is significantly reduced.

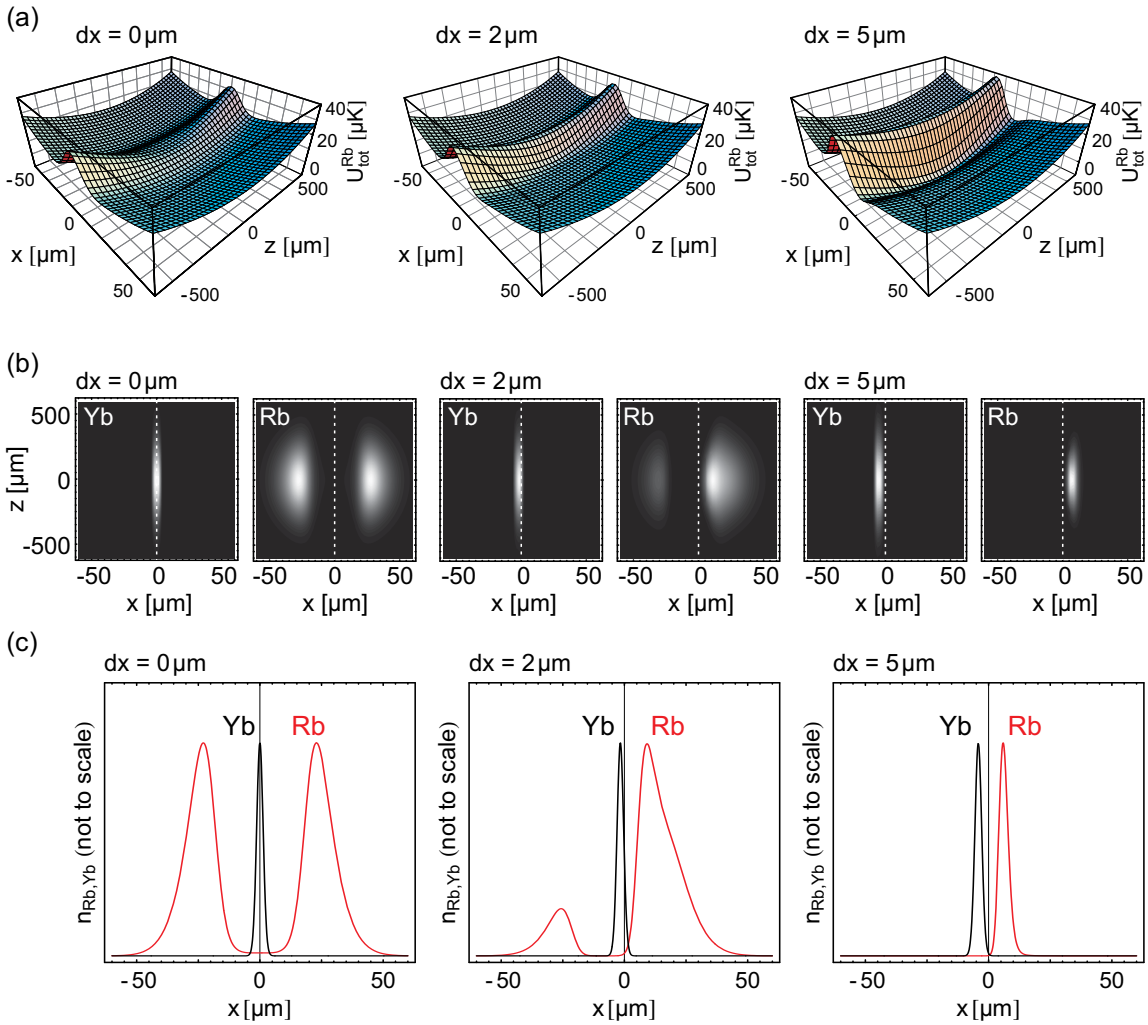

Figure 7.6: *Calculated (a) model potentials and (b,c) density distributions for different beam displacement settings* $dx = 0\,\mu m, 2\,\mu m, 5\,\mu m$. *(b) shows densities* n_{Rb} *and* n_{Yb} *in the* $x-z$ *plane at* $y = 0$ *and (c) along the x-axis* ($y = z = 0$). *Scales are individually adjusted to* $0...n_{\mathrm{RbMAX}}$ *and* $0...n_{\mathrm{YbMAX}}$. *Used parameters:* $P_{532} = 343\,mW$ $P_{1064} = 88\,mW$, $T_{\mathrm{Rb}} = T_{\mathrm{Yb}} = 1.5\,\mu m$.

- Sympathetic cooling of the ^{174}Yb cloud is suppressed.

Model potentials and density distributions calculated for different beam displacements of $dx = 0\,\mu$m, $2\,\mu$m, $5\,\mu$m, as displayed in Fig. 7.6, describe the experimental situation:

When the ODT beams are radially displaced, the total potential for ^{87}Rb contains stronger repulsive as well as attractive regions. The ^{87}Rb cloud is arranged in the attractive parts (see Fig. 7.6 (b,c)) of the potential, which leads to heating due to adiabatic compression. As the RF used for evaporative cooling of ^{87}Rb in the MT is still present during this experimental phase, hot ^{87}Rb atoms are removed from the trap and a temperature increase is ultimately translated into atom loss. Simultaneously, the spatial overlap

between the ^{87}Rb- and ^{174}Yb cloud is reduced, as the BIODT beam displacement dx is increased. As the overlap density is reduced, thermalization between both species decelerates (see Eq. 7.3 and 7.2). Calculation of the individual density distributions show, that for $dx > 5\,\mu$m, both atom clouds are basically located next to each other without contact. This results in an increased temperature difference after a fixed contact time $t_{\mathrm{contact}} = 300\,$ms.

The relative BIODT beam alignment is experimentally adjusted to achieve the lowest ^{87}Rb and ^{174}Yb temperatures and maximum ^{87}Rb atom numbers (indicated by the gray area in Fig. 7.5). Horizontal and vertical axis are optimized individually in order to find the global maximum in this two-dimensional parameter space. This adjustment procedure is included in the daily routine preceding further experiments.

Beam alignment at lower 1064 nm ODT power When the experiments on the relative BIODT beam alignment are performed at lower 1064 nm ODT power, the observed results significantly differ from the results described above. Figure 7.7 presents data obtained at $P_{532} = 343\,$mW and $P_{1064} = 80\,$mW. ^{87}Rb exhibits the same characteristics as in

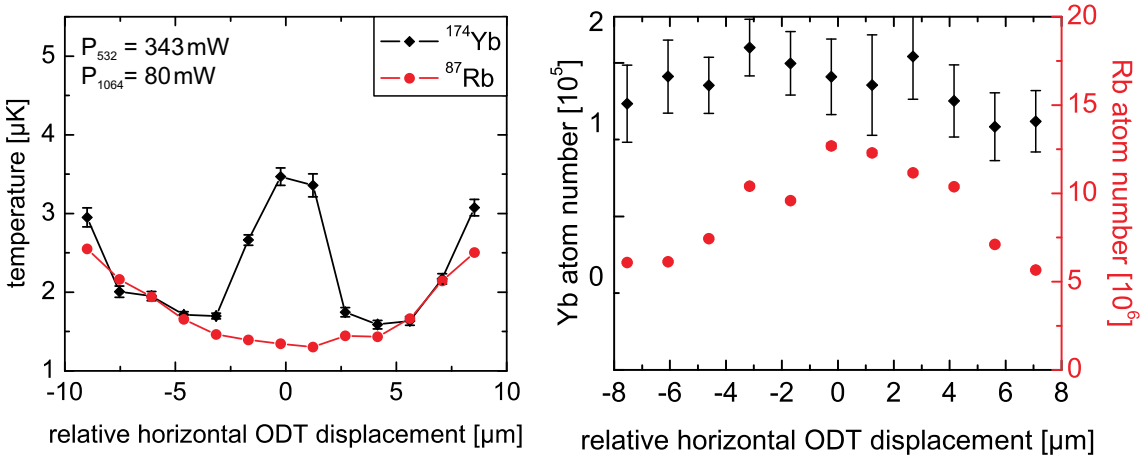

Figure 7.7: *Measured ^{87}Rb and ^{174}Yb temperatures and atom numbers depending on the relative BIODT beam alignment. The data is obtained at the following parameters: $P_{532} = 343\,mW$, $P_{1064} = 80\,mW$.*

experiments performed at $P_{1064} = 88\,$mW: A clear minimum in ^{87}Rb temperature and maximum in atom number is observed, which coincides with the case of best possible overlap of the individual ODT beam foci. However, at this BIODT power configuration, the ^{87}Rb density at the ^{174}Yb cloud position is not sufficient to provide full thermalization of ^{174}Yb (see also Fig. 7.1). For a relative beam displacement $3\,\mu\mathrm{m} < |dx| < 7\mu$m however, the ^{174}Yb atoms are sympathetically cooled to the ^{87}Rb temperature. This effect is related to the overlap of both atom clouds depending on the relative ODT position at this light power ratio. For a more quantitative description, the overlap density n_{YbRb} is calculated according to Eq. 7.5 using the present trapping parameters. These calculations are displayed in Fig. 7.8 for $P_{1064} = 80\,$mW (black) and $P_{1064} = 88\,$mW (gray). At a trapping geometry

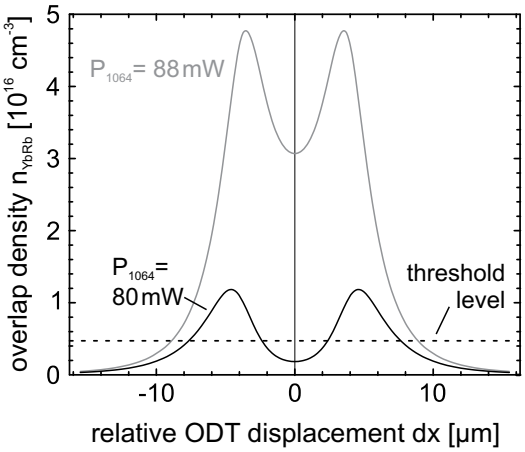

Figure 7.8: *Calculated overlap density n_{YbRb} according to Eq. 7.5 as a function of the relative ODT beam displacement dx. Used parameters: $P_{532} = 343\,mW$, $P_{1064} = 80\,mW$ (black), $P_{1064} = 88\,mW$ (gray) $T_{\mathrm{Rb}} = 1.5\,\mu K$, $N_{\mathrm{Rb}} = 10^7$, $T_{\mathrm{Yb}} = 3\,\mu K$, $N_{\mathrm{Yb}} = 2 \times 10^5$.*

corresponding to the experiments presented in Fig. 7.7 ($P_{1064} = 80\,\mathrm{mW}$), the overlap density increases for $|dx| > 0$ and reaches its maxima at $|dx| \approx 4\,\mu\mathrm{m}$. For larger beam displacements, the overlap density trends to zero. Taking this into consideration, the observed ^{174}Yb temperature dependence can be qualitatively explained: While the overlap density for perfectly superimposed beams is not sufficient to provide full thermalization of ^{174}Yb with colder ^{87}Rb within the chosen contact time $t_{\mathrm{contact}} = 300\,\mathrm{ms}$, thermalization is achieved around the calculated overlap density maxima at $|dx| \approx 4\,\mu\mathrm{m}$. For higher 1064 nm powers ($P_{1064} = 88\,\mathrm{mW}$), the overlap shows a less distinctive structure at a generally higher level. Here, enough overlap between the clouds for full thermalization is present in the complete range $|dx| < 5\,\mu\mathrm{m}$ matching the results described in Fig. 7.5. Note that absolute calculated values of n_{YbRb} are subject to large error bars related to uncertainties in the model potentials. The qualitative characteristics of n_{YbRb} and the relative results for different trapping geometries, however, are not significantly affected by this.

Axial BIODT alignment The axial focus positions of the ODT beams are determined by analyzing the axial position of Yb clouds trapped in the individual ODTs. They are adjusted on a level of $\approx 25\,\mu\mathrm{m}$ by moving lenses in the respective optical systems, that are mounted on micrometer translation stages (see Sec. 4.2.3). Due to the elongated trapping geometry, and resulting axial cloud dimensions in the order of several $100\,\mu\mathrm{m}$, the precision achieved by this adjustment procedure is sufficient for the relevant experiments.

7.2 Thermalization rate studies

The following describes thermalization rate measurements performed with ^{87}Rb and 5 different isotopes of Yb. A quantitative analysis of the dynamics of this process allows conclusions on relative scattering properties of the respective species. In the case of ^{170}Yb and ^{87}Rb, we could also estimate an absolute value of the interspecies scattering length

7.2.1 Experiment

For measurements of the thermalization rate, the two atom clouds are prepared in their individual trapping potentials as described in Chap. 5. The ideal BIODT parameters are adjusted as described in Sec. 7.1.2. After the Yb atoms are brought into contact with the colder ^{87}Rb atoms, their temperature is determined as a function of a defined contact time t_{contact}. Additional measurements of Yb without the presence of ^{87}Rb are performed in order to clearly isolate interspecies interaction effects. In order to have a well defined starting point for the thermalization, the ^{87}Rb atoms are moved to the Yb cloud position using a 500 ms long, linear magnetic field ramp. During the contact period, the RF is turned off to avoid ^{87}Rb atom loss induced by evaporation. Depending on the Yb isotope, the maximum contact time varies from 120 ms (^{174}Yb) to 3000 ms (^{170}Yb). Temperatures of the individual species are determined from single images (see Sec. 4.3.4) after well-defined ballistic expansion times $t_{\mathrm{TOF}} = 3.5$ ms for Yb and $t_{\mathrm{TOF}} = 30$ ms for ^{87}Rb.

a) Yb isotopes ^{172}Yb, ^{173}Yb and ^{176}Yb

Figure 7.9 shows typical thermalization curves for the isotopes ^{172}Yb, ^{173}Yb, ^{176}Yb with ^{87}Rb. It includes temperatures of Yb, measured with (black) and without (blue) the presence of ^{87}Rb and measured ^{87}Rb temperatures (red) as well as the corresponding atom numbers. The thermalization process has the following general characteristics:

- When initially colder ^{87}Rb atoms are present during the measurement, the Yb atoms are sympathetically cooled. The ^{87}Rb temperature is reached after a characteristic contact time, which depends on the Yb isotope.
- Without the presence of ^{87}Rb, the Yb atoms constantly remain at their initial temperature, which is indicated by the dashed blue line in Fig. 7.9. Temperature differences between the individual Yb isotopes are related to their different single-species scattering properties [57], which determine the efficiency of evaporative cooling in the BIODT (see Sec. 5.2.3).
- Yb isotopes with fast thermalization rates, i.e. ^{173}Yb and ^{176}Yb, are significantly cooled by ^{87}Rb already at $t_{\mathrm{contact}} = 0$. This is consistent with the fact that the effective contact between the two species is established before the ^{87}Rb cloud reaches its final position due to the finite size of the atomic clouds.
- The ^{87}Rb atoms are subject to a small constant heating rate of $\dot{T}^{\mathrm{Rb}}_{\mathrm{heat}} \approx 500$ nK/s, attributed to photon scattering and position noise of the BIODT. The measured heating rate is taken into account for quantitative data analysis using a linear fit for the ^{87}Rb temperature.
- Atom numbers of ^{87}Rb and Yb remain constant during the thermalization process, clearly indicating the effect of sympathetic cooling of Yb by colder Rb. The observed atom loss in ^{172}Yb, is related to increased three-body losses due to the large (intraspecies) scattering length $|a_{172}| = 599\,\mathrm{a_0}$ [57].

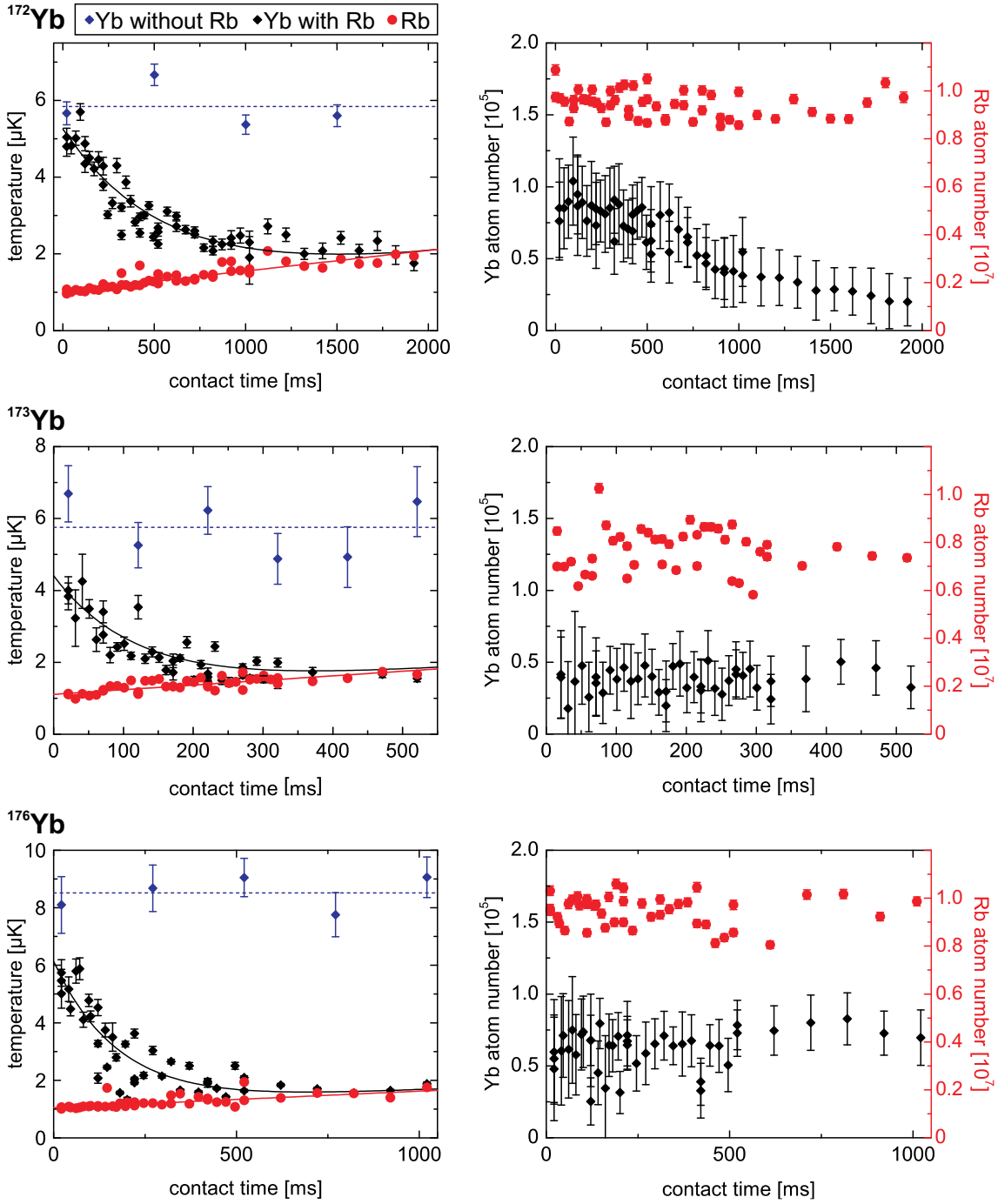

Figure 7.9: *Thermalization curves of ^{87}Rb and ^{172}Yb, ^{173}Yb, ^{176}Yb. Left side: Temperatures of Yb with (black) and without (blue) the presence of ^{87}Rb and ^{87}Rb temperatures (red) as a function of contact time. An exponential fit according to Eq. 7.9 to the Yb temperature (black line) and a linear fit to the ^{87}Rb temperature (red line) is included. Right side: corresponding atom numbers.*

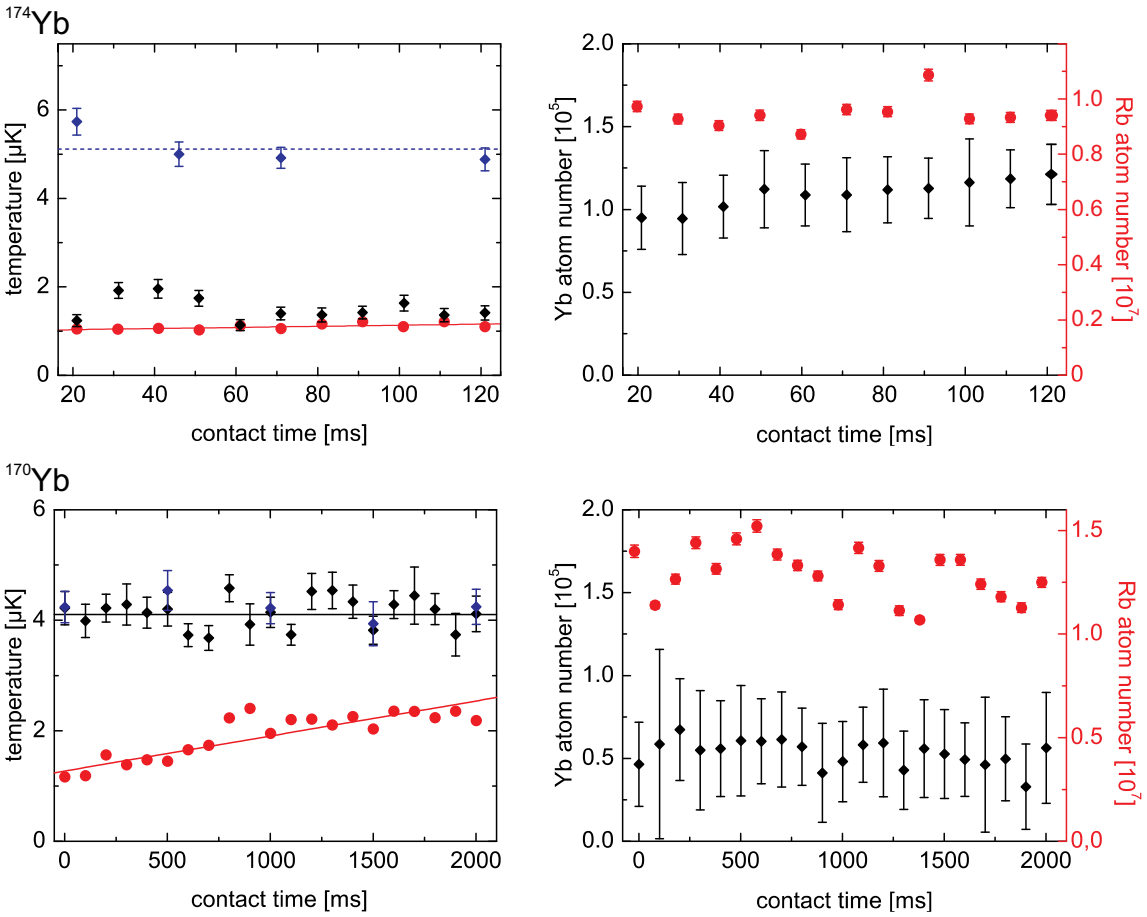

Figure 7.10: *Thermalization curves of ^{87}Rb and ^{174}Yb, ^{170}Yb. While ^{174}Yb shows almost instantaneous thermalization with ^{87}Rb, no thermalization between ^{170}Yb and ^{87}Rb is observed.*

b) Yb isotopes ^{174}Yb and ^{170}Yb

The isotopes ^{174}Yb and ^{170}Yb play an exceptional role regarding thermalization with ^{87}Rb, which is shown in Fig. 7.10.

^{174}Yb atoms thermalize almost instantaneously with the colder ^{87}Rb atoms, indicating a large interspecies scattering length. Results from phase separation experiments performed with this isotope clearly confirm this conclusion (see Chap. 8). The dynamics of the thermalization process can not be resolved in the current experimental setup as it is already finished at $t_{\mathrm{contact}} = 20\,\mathrm{ms}$. For $t_{\mathrm{contact}} < 20\,\mathrm{ms}$, no reliable data can be obtained with our experimental procedure.

On the contrary, in the described trapping geometry, ^{170}Yb shows no thermalization with ^{87}Rb at all. Its temperature remains constant at the initial level of $\approx 4.1\,\mu$K, independent of the presence of ^{87}Rb atoms.

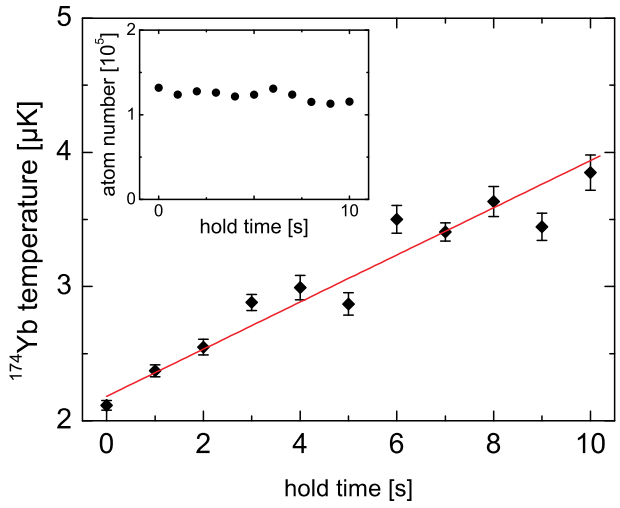

Figure 7.11: *Heating rate measurement of ^{174}Yb in the BIODT. Temperatures and atom numbers (inset) are determined after thermalization with ^{87}Rb and removal of ^{87}Rb as a function of an additional hold time. The red line indicates a linear fit to the data, which yields $\dot{T}_{\mathrm{Yb}}^{heat} = (176 \pm 15)\,\mathrm{nK/s}$.*

7.2.2 Quantitative data analysis

The quantitative analysis of thermalization data is based on the thermalization model described in Sec. 7.1.1. According to Eq. 7.1, the time dependence of the Yb temperature is generally defined by:

$$\frac{dT_{\mathrm{Yb}}}{dt} = -\gamma_{\mathrm{th}} \cdot \Delta T + \dot{T}_{\mathrm{Yb}}^{\mathrm{heat}} \qquad \text{with} \quad \Delta T = T_{\mathrm{Yb}} - T_{\mathrm{Rb}} \tag{7.8}$$

Assuming a linear time dependence of the Rb temperature, $T_{\mathrm{Rb}} \equiv T_{\mathrm{Rb}}(t) = T_{\mathrm{Rb},0} + \dot{T}_{\mathrm{Rb}}^{\mathrm{heat}} t$, consistent with experimental observation, the differential equation Eq. 7.8 is solved by the following function for $T_{\mathrm{Yb}}(t)$:

$$T_{\mathrm{Yb}}(t) = T_{\mathrm{Rb},0} + \dot{T}_{\mathrm{Rb}}^{\mathrm{heat}} t + \frac{\dot{T}_{\mathrm{Yb}}^{\mathrm{heat}} - \dot{T}_{\mathrm{Rb}}^{\mathrm{heat}}}{\gamma_{\mathrm{th}}} + C\, e^{-\gamma_{\mathrm{th}} t}\,. \tag{7.9}$$

Here, C is a free constant factor. In order to use Eq. 7.9 as a fitting function for the Yb temperature data, the parameters $T_{\mathrm{Rb},0}$, $\dot{T}_{\mathrm{Yb}}^{\mathrm{heat}}$ and $\dot{T}_{\mathrm{Yb}}^{\mathrm{heat}}$ have to be determined. While $T_{\mathrm{Rb},0}$ and $\dot{T}_{\mathrm{Rb}}^{\mathrm{heat}}$ are extracted from a linear fit to the ^{87}Rb temperature data in each thermalization series, the Yb heating rate $\dot{T}_{\mathrm{Yb}}^{\mathrm{heat}}$ is determined from an independent measurement: After a fixed contact time $t_{\mathrm{contact}} = 300\,\mathrm{ms}$, where ^{174}Yb atoms are sympathetically cooled to the ^{87}Rb temperature, the ^{87}Rb atoms are removed and the ^{174}Yb temperature is measured as a function of an additional hold time t_{hold}. Fig. 7.11 shows ^{174}Yb temperatures and corresponding atom numbers as a function of t_{hold} together with a linear fit, which yields a constant heating rate of $\dot{T}_{\mathrm{Yb}}^{\mathrm{heat}} = (175 \pm 16)\,\mathrm{nK/s}$. This heating rate is equal for all Yb isotopes as it results from photon scattering in the BIODT (see Sec. 3.2.3) and from laser intensity noise and beam-pointing fluctuations [139].

For the extraction of relative scattering properties from thermalization experiments described above, two different methods are used:

a) Direct Fit The first method uses Eq. 7.9 as a fitting function with the free parameters C and γ_{th} in order to extract the thermalization rate γ_{th} from the Yb temperature data.

Equations 7.2 and 7.3 generally connect the thermalization rate γ_{th} with the scattering cross section:

$$\gamma_{\mathrm{th}} = \frac{\xi}{\alpha}\, n_{\mathrm{YbRb}} \cdot \bar{v}_{\mathrm{YbRb}} \cdot \sigma_{\mathrm{tot\,YbRb}} \tag{7.10}$$

This method is a first order approximation, as it assumes a constant thermalization rate γ_{th} during the thermalization process. It neglects changes in the mean relative velocity $\bar{v}_{\mathrm{YbRb}}$, which in the present experiments decreases by $5 \ldots 15\,\%$ during the thermalization, depending on the ^{87}Rb- and Yb temperatures. In addition, it does not take into account possible temperature dependent variations of the overlap density n_{YbRb} during the thermalization process. However, this method still provides good comparability of thermalization properties for different Yb isotopes, as the discussed simplifications are similar for all measured thermalization curves. Fits to the Yb temperature data according to this method are included in Fig. 7.9 and results for extracted thermalization rates are presented in Tab. 7.1.

b) Initial cooling rate The second method for the extraction of quantitative results from thermalization measurements is adapted from [9]: Fist, an exponential curve is fitted to the Yb temperature data. For further analysis, only the initial cooling rate

$$\dot{T}_{\mathrm{Yb}}^{\mathrm{cool}} = \left.\frac{dT_{\mathrm{Yb}}}{dt}\right|_{t=0} \tag{7.11}$$

at $t_{\mathrm{contact}} = 0$ is used to determine γ_{th}. For ^{170}Yb-^{87}Rb thermalization data, a linear fit is used, which directly yields the respective slope.

This method has the following advantages: At the beginning of each thermalization series, the temperature difference between Yb and ^{87}Rb, which is included in the thermalization model, is large, minimizing the influence of absolute errors in the Yb and ^{87}Rb temperature determination. Furthermore, this procedure reduces effects connected to changes in $\bar{v}_{\mathrm{YbRb}}$ and n_{YbRb} at increased contact times. Results based on this method are also included in Tab. 7.1.

Method b) yields somewhat larger error bars then method a) and generally gives $10 \ldots 20\,\%$ larger results for γ_{th}. Within their uncertainties, however, both data analysis methods are consistent.

7.2.3 Relative isotope-dependent scattering properties

Thermalization measurements as described above are performed at a BIODT power ratio, which provides reliable thermalization between ^{172}Yb, ^{173}Yb, ^{176}Yb and ^{87}Rb at low ^{87}Rb temperatures. As discussed in Sec. 7.1.2, the BIODT potentials are typically set to be in the transition regime between a repulsive and an attractive potential for ^{87}Rb. In this trapping geometry, it is impossible to reliably determine ^{87}Rb densities in the trap center. Thus, due to the unknown absolute overlap density, it is unfeasible to derive absolute scattering cross sections from the measured thermalization rates γ_{th} according to Eq. 7.10. However, for the case of $N_{\mathrm{Rb}} \gg N_{\mathrm{Yb}}$, the overlap density can be approximated as

$$n_{\mathrm{YbRb}} \approx N_{\mathrm{Rb}} \cdot f_g, \tag{7.12}$$

Yb mass number	thermalization rate γ_{th} [s^{-1}] method a)	method b)	β [10^{-6} m^{-1}] method a)	method b)
170	$(0.15 \pm 4.73) \times 10^{-3}$	$(0.53 \pm 5.48) \times 10^{-3}$	$(0.5 \pm 25.5) \times 10^{-3}$	$(1.6 \pm 81.0) \times 10^{-3}$
172	1.78 ± 0.22	2.35 ± 0.40	6.4 ± 0.78	8.19 ± 1.39
173	13.2 ± 2.5	17.9 ± 12.7	56.6 ± 12.2	75.5 ± 52.1
176	5.60 ± 0.86	6.79 ± 2.26	19.4 ± 3.0	22.6 ± 7.5

Table 7.1: *Comparison of extracted thermalization rates γ_{th} and scattering parameters $\beta \propto \sigma_{\mathrm{tot\,YbRb}}$ from thermalization experiments with ^{87}Rb and ^{170}Yb, ^{172}Yb, ^{173}Yb, ^{176}Yb (see Fig. 7.9 and 7.10) using the two analysis methods (see text).*

with an unknown proportionality factor f_g depending on the trap geometry. In order to compare relative collision properties for different Yb isotopes, it is convenient, to define a scattering parameter

$$\beta = \frac{\gamma_{\mathrm{th}}}{\bar{v}_{\mathrm{YbRb}} \cdot N_{\mathrm{Rb}}} \,. \tag{7.13}$$

Under the reasonable assumption, that the geometric parameters (which are included in f_g) are comparable for all datasets, this quantity is proportional to $\sigma_{\mathrm{tot\,YbRb}}$. Hence, it is possible to compare relative interspecies scattering properties of different Yb isotopes with ^{87}Rb.

Thermalization rate measurements performed with the same isotope combination on different days show, that results somewhat depend on the specific BIODT beam adjustment and light power settings. Hence, to ensure relative comparability of the data, the data for different Yb isotopes were either taken in consecutive measurements with fixed conditions or the results are scaled with respect to a calibration measurement using ^{172}Yb, which is performed each time the measurement conditions are changed.

Table 7.1 summarizes results from thermalization rate measurements using ^{87}Rb and the Yb isotopes ^{170}Yb, ^{172}Yb, ^{173}Yb, ^{176}Yb. A comparison of magnitudes for $\beta \propto \sigma_{\mathrm{tot\,YbRb}}$ shows, that the scattering cross section rises for increasing Yb isotope mass numbers from ^{170}Yb to ^{173}Yb. ^{174}Yb continues this trend as it exhibits even larger interaction with ^{87}Rb resulting in almost instantaneous thermalization and, depending on the ^{87}Rb density, phase separation between the two species (see Chap. 8). The scattering cross section for ^{176}Yb and ^{87}Rb is in the range between ^{172}Yb - ^{87}Rb and ^{173}Yb - ^{87}Rb (see also Sec. 9.2).

Detailed discussion on ^{170}Yb - ^{87}Rb

The isotope combination ^{170}Yb - ^{87}Rb plays an outstanding role, as no interaction between the two species can be observed at the trapping geometry used here, which quantitatively yields a parameter β_{87-170} consistent with zero.

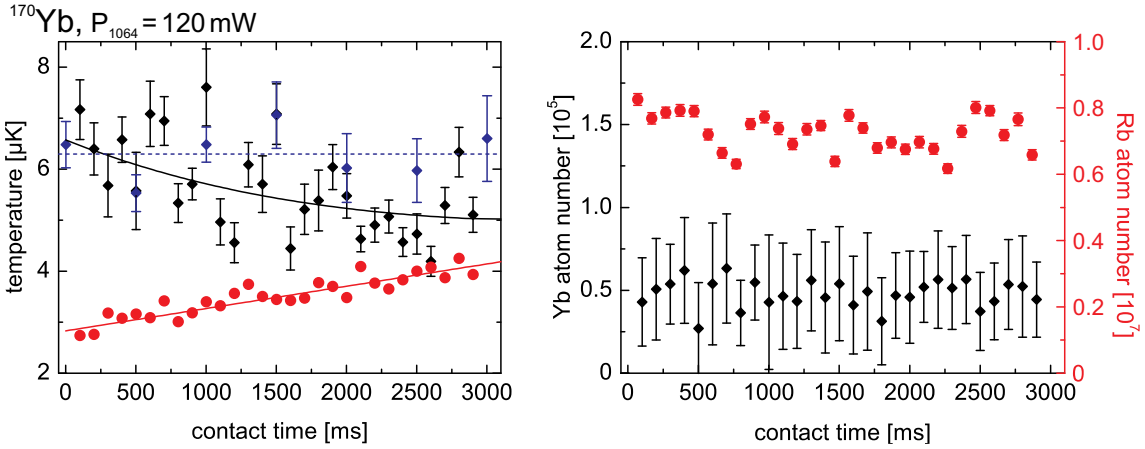

Figure 7.12: *Thermalization curves of ^{87}Rb and ^{170}Yb, measured at significantly higher ^{87}Rb densities due to increased 1064 nm ODT power $P_{1064} \approx 120\,mW$.*

Comparison with ^{172}Yb The parameter $\beta_{87-170} \propto \sigma_{\mathrm{tot\,YbRb}}$ for ^{170}Yb-^{87}Rb, as obtained from thermalization measurements, is smaller by a factor of at least 280 compared to β_{87-172}. Using the relation $\sigma_0 = 4\pi a^2$, which connects the scattering cross section σ_0 in the low energy limit with the s-wave scattering length a (see Sec. 2.1.4), the interspecies s-wave scattering length $|a_{87-170}|$ is thus by a factor of at least 17 smaller compared to $|a_{87-172}|$. This comparison with ^{172}Yb is made, as ^{172}Yb shows the next weakest elastic interaction with ^{87}Rb among the Yb isotopes used in this work. This indicates an extraordinarily small absolute value for $|a_{87-170}|$.

Thermalization measurements of ^{170}Yb at higher ^{87}Rb density All thermalization measurements discussed so far are performed at typical BIODT power settings of $P_{1064} \approx 88\,\mathrm{mW}$ and $P_{532} = 343\,\mathrm{mW}$.

As discussed in 7.1.2, the ^{87}Rb density is significantly increased for larger values of P_{1064}, where the repulsive 532 nm ODT potential is overcompensated by the 1064 nm ODT (see Fig. 7.2), leading to stronger ^{87}Rb confinement. As the thermalization rate is linear in the ^{87}Rb density, we have repeated the measurements with ^{170}Yb under these conditions in order to be able to detect even smaller cross sections. For these measurements, the BIODT power settings were $P_{1064} \approx 120\,\mathrm{mW}$ and $P_{532} = 343\,\mathrm{mW}$. Measured ^{170}Yb and ^{87}Rb temperatures as a function of the contact time are shown in Fig. 7.12. In this trapping geometry, the ^{87}Rb temperature is generally higher due to adiabatic compression in the effectively attractive BIODT potential. The main result is the observation of slow thermalization of ^{170}Yb with colder ^{87}Rb. Both data analysis methods described above yield consistent thermalization rates: a) $\gamma_{\mathrm{th}} = 0.37 \pm 0.12\,\mathrm{s}^{-1}$, b) $\gamma_{\mathrm{th}} = 0.42 \pm 0.40\,\mathrm{s}^{-1}$. Note that the result obtained from method a) may be subject to additional systematic uncertainties, as it does not take into account changes in the overlap density n_{YbRb} and the mean relative velocity $\bar{v}_{\mathrm{YbRb}}$ during the thermalization process (see discussion above).

In the present case of an effectively attractive BIODT potential for ^{87}Rb, it is possible

to estimate the Yb-Rb overlap integral n_{YbRb} according to Eq. 7.5. Through Eq. 7.3, this allows conclusions on the absolute magnitude of $\sigma_{\mathrm{tot\,YbRb}}$ and thus on $|a_{87-170}|$ for this isotope combination. Note that n_{YbRb} strongly depends on the BIODT beam parameters used in the model potential, which leads to large uncertainties in the resulting quantities. A detailed analysis of the ^{87}Rb density error, which depends on identical experimental uncertainties, is presented in Sec. 8.2.1. Using the measured thermalization rate, the low energy s-wave scattering length between ^{170}Yb and ^{87}Rb can be approximated as

$$|a_{170-87}| = 6.6\,^{+3.5}_{-2.9}\,\mathrm{a_0}\,.$$

This result includes uncertainties from γ_{th} and, dominantly, from the overlap integral n_{YbRb}. Both parameters might be subject to additional systematic effects due to the insufficient control of the trapping potentials or imperfect description of the thermalization process (see discussion above). Taking this into account, the absolute value for the interspecies length between ^{170}Yb and ^{87}Rb presented here has to be taken as a first approximation. However, the obtained value is consistent with the results on relative scattering properties, as for the isotope combinations ^{172}Yb-^{87}Rb, ^{173}Yb-^{87}Rb and ^{176}Yb-^{87}Rb, scattering lengths in the range of $100 \ldots 300\,\mathrm{a_0}$ are expected. These predictions are based on a theoretical analysis of the NIST group [15], which is discussed in Sec. 9.2.

8

Interspecies interaction II: phase separation

This chapter discusses the observation of phase separation in a thermal mixture of ^{174}Yb and ^{87}Rb which is the major scientific result of the PhD work presented here. A careful analysis of this effect allows quantitative conclusions on the interaction between ^{174}Yb and ^{87}Rb.

The following describes the experimental sequence and shows typical data from these measurements. It discusses temperature and atom number measurements relevant for the understanding of the observed phase separation process. Furthermore, the data analysis which includes modeling of the interaction potentials and the fitting procedure is presented: The first approach assumes a linear relation between the interaction and the ^{87}Rb density. On the basis of this quantitative analysis, the next part of this chapter focuses on systematic tests performed in order to study the influence of different experimental parameters on the interaction between ^{174}Yb and ^{87}Rb.

Subsequently, the quantitative results on the interaction potential are interpreted in terms two-body scattering properties of the respective atoms. A "naive" mean field approach and thermal averaging of the energy dependent scattering length lead to conclusions inconsistent with experimental observations.

In the light of this discrepancy between observations and theory, the following part discusses possible experimental issues, which may lead to incorrect results for the interspecies interaction potential. Subsequently, the validity of the standard mean field theory in the present case is discussed on the basis of a simple comparison of relevant length scales. Finally, a more sophisticated theoretical model, which involves nonlinear density dependent corrections to the interaction potential, is introduced and results for the interpsecies s-wave scattering length are presented.

8.1 Phase separation experiments

Starting point The experiments described in the following are based on the experimental situation discussed in Chap. 7: ^{174}Yb and ^{87}Rb atoms are loaded and prepared in their individual trapping potentials and brought into contact. Within a fixed contact time $t_{\mathrm{contact}} = 300\,\mathrm{ms}$, the ^{174}Yb cloud is sympathetically cooled to the ^{87}Rb temperature $T_{\mathrm{Rb}} \approx 1.5\,\mu\mathrm{K}$. Atom numbers at this experimental stage are determined to be $N_{\mathrm{Rb}} \approx 10^7$ and $N_{\mathrm{Yb}} = 1.5 \ldots 2 \times 10^5$. The ideal BIODT beam power ratio and the beam alignment is adjusted as described in sections 7.1.2 and 7.1.2.

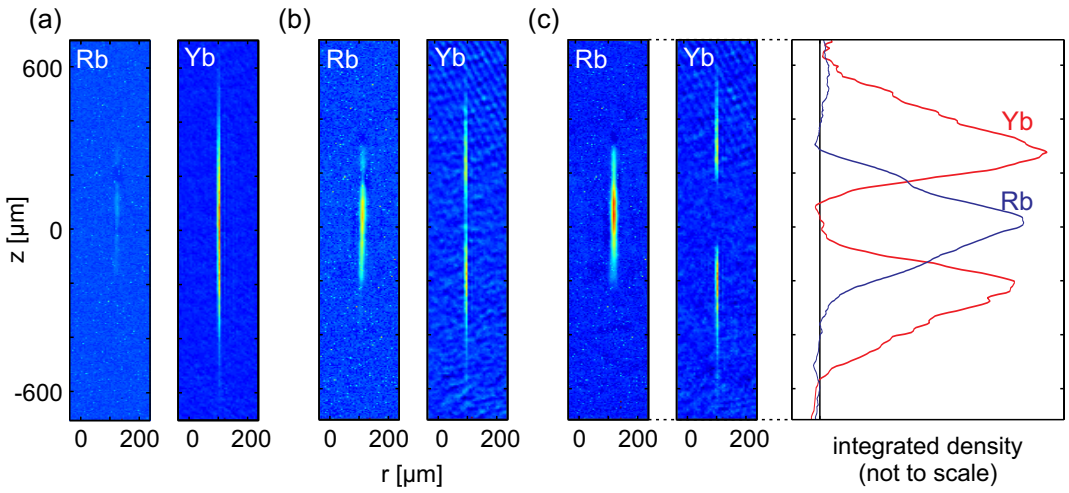

Figure 8.1: *False color intra-trap images of ^{87}Rb and ^{174}Yb clouds at BIODT beam powers $P_{532} = 343\,mW$ and $P_{1064} = 135\,mW$. The ^{87}Rb atom number increases from (a) $\approx 7.0 \times 10^5$ to (b) $\approx 3.6 \times 10^6$and to (c) $\approx 6.9 \times 10^6$. (c) displays the radially integrated density in the relevant regions in a combined plot.*

Increase of ^{87}Rb confinement Subsequently after the thermalization process, we increase the 1064 nm ODT power within 100 ms to a level of 120...145 mW creating an attractive potential for ^{87}Rb. The 532 nm ODT power is kept at a constant level of $P_{532} = 343$ mW. A calculated model potential for ^{87}Rb and density distributions for both species have been shown in the previous chapter in Fig. 7.2 for the case of $P_{1064} = 120$ mW. In this trapping geometry, both the ^{87}Rb cloud and the axially larger ^{174}Yb clouds are overlapping in the trap center and the ^{87}Rb density at the ^{174}Yb cloud position is increased to $\approx 10^{14}$ cm^{-3}. Due to adiabatic compression [130], the 1064 nm ODT power ramp up is accompanied by an increase in the ^{87}Rb temperature to $2 \ldots 3.5\,\mu$K.

Observation of phase separation After the increase of the ^{87}Rb density, we observe a spatial separation of the two species, which depends on the number of ^{87}Rb atoms, the ^{87}Rb density distribution and the temperature (see below). If the optical- and the magnetic traps are perfectly overlapping, the cloud of ^{174}Yb is separated into two parts enclosing the shorter ^{87}Rb atomic cloud which is located in the center of the trapping potentials. An inverse effect on the ^{87}Rb cloud, i.e. an axial compression is expected to be much weaker due to the significantly smaller ^{174}Yb atom number. Hence it is beyond the detection resolution of our experiment.

Unless otherwise stated, the phase separation is detected by taking images of the individual atom clouds 20 ms after the 1064 nm ODT power ramp up is completed. In order to obtain information on ^{87}Rb and ^{174}Yb density distributions and their relative orientation, we simultaneously image both atom clouds inside the trap using absorption imaging for ^{174}Yb and the method of dark contrast imaging for ^{87}Rb (see Sec. 4.3.3 for details on imaging techniques). A typical series of simultaneously created intra-trap images is shown

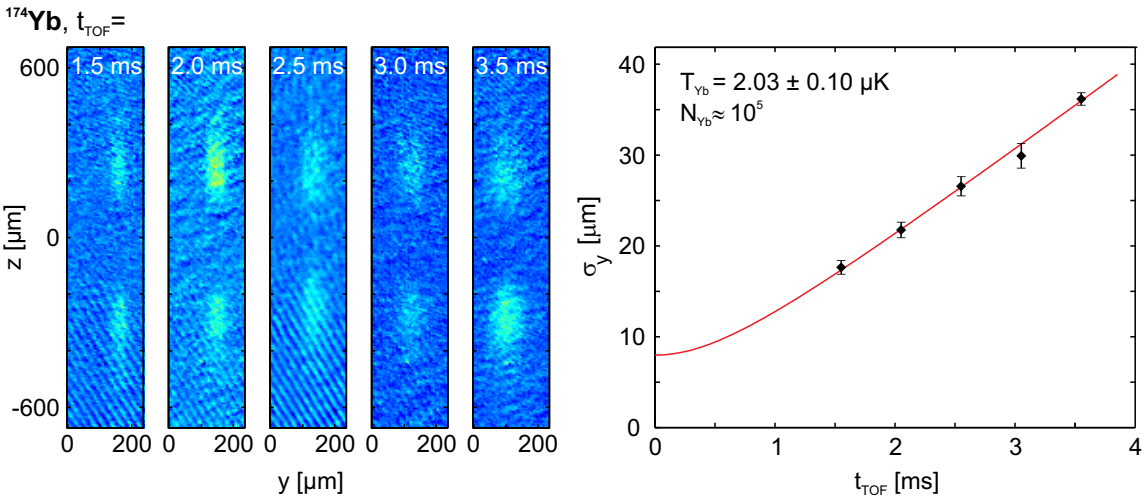

Figure 8.2: *TOF-series of ^{174}Yb under phase separation conditions (BIODT beam powers: $P_{532} = 343\,mW$ and $P_{1064} = 135\,mW$). The temperature is extracted from the expansion of the radial cloud size σ_y according to Eq. 4.15.*

in Fig. 8.1. In this series, we varied the ^{87}Rb atom number through well-defined atom loss induced by an RF sweep with controlled RF amplitude after the thermalization of the two atomic species (see Sec. 8.3.1). In Fig. 8.1 (c), the radial sum of pixels of both images is combined in a single plot pointing out the relative spatial configuration of the atom clouds. This data demonstrates a clear correlation between the ^{87}Rb density and the ^{174}Yb distribution: In a simple picture, the ^{174}Yb atoms are repelled from the position of highest ^{87}Rb density implying a repulsive interaction potential between the two species, which acts in addition to the external trapping potentials.

Note that the ^{87}Rb cloud is imaged in the horizontal plane using *camera 1* whereas ^{174}Yb is imaged by *camera 2* in the vertical plane (see Fig. 4.14). The relative axial positions in the respective images are calibrated by analyzing additional images of ^{87}Rb clouds simultaneously taken with both cameras.

Temperature ^{87}Rb temperatures and atom numbers are extracted from additional absorption images taken after a controlled TOF. In order to determine the temperature of ^{174}Yb, we analyze the radial size of atom clouds imaged after a defined TOF as indicated in Fig. 8.2. This figure shows a series of ^{174}Yb images with an increasing TOF $t_{\mathrm{TOF}} = 1.5 \ldots 3.5\,\mathrm{ms}$ using an experimental configuration, where phase separation occurs. The radial cloud sizes are determined by summing pixels in the axial direction and fitting a one-dimensional Gaussian curve to this data. A fit to the obtained $1/\sqrt{e}$-radii σ_r according to Eq. 4.15 results in a temperature $T_{\mathrm{Yb}} = 2.03 \pm 0.10\,\mu\mathrm{K}$. The corresponding ^{87}Rb temperature in this series is $\approx 2.1\,\mu\mathrm{K}$.

We compared the temperatures of both species under conditions, which lead to phase separation for different ^{87}Rb temperatures, which is shown in Fig. 8.3. In this series, the ^{87}Rb temperature is adjusted within a range of $2.5 \ldots 7\,\mu\mathrm{K}$ by a variation of the final RF

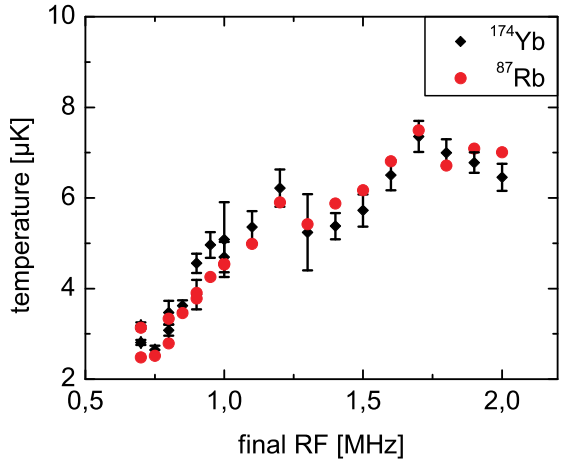

Figure 8.3: *Measured ^{87}Rb and ^{174}Yb temperatures for different settings of the final radio frequency level used for evaporative cooling of ^{87}Rb.*

level before both atomic clouds are brought into contact. In order to determine the individual temperatures of both species, single images at $t_{\mathrm{TOF}} = 3.5\,\mathrm{ms}$ (^{174}Yb) and $t_{\mathrm{TOF}} = 30\,\mathrm{ms}$ (^{87}Rb) are analyzed according to the description in Sec. 4.3.4. The data experimentally confirms, that $T_{\mathrm{Rb}} = T_{\mathrm{Yb}} \equiv T$ is a valid assumption for phase separation measurements. This result is related to the nearly instantaneous thermalization of ^{87}Rb and ^{174}Yb at the present ^{87}Rb density.

^{174}Yb atom loss The observed effect of phase separation between the two atomic species is accompanied by a rapid loss of ^{174}Yb atoms. This is attributed to inelastic collisions with ^{87}Rb due to the strong interspecies interaction [79]. In order to quantitatively analyze this effect, an additional holding time after the final 1064 nm ODT power ramp up is introduced in the experimental sequence. Figure 8.4 shows intra-trap images and extracted ^{174}Yb atom numbers at the configuration, where phase separation occurs, as a function of the holding time. The ^{174}Yb atom loss 1/e-time-constant is $\approx 210\,\mathrm{ms}$ for typical ^{87}Rb peak densities of $\approx 3 \times 10^{14}\,\mathrm{cm}^{-3}$. For ^{87}Rb, the atom number remains at an almost constant level (see inset in Fig. 8.4). A comparison with data from experiments without ^{174}Yb shows, that no additional loss which is attributed to the presence of ^{174}Yb can be observed.

The effect of ^{174}Yb atom loss at phase separation conditions is discussed in detail in Sec. 8.4.2. The following quantitative analysis of phase separation data, however, does not take ^{174}Yb atom loss into account.

8.2 Quantitative data analysis – a basic linear approach

In the following, we will develop a simple model which describes the observed phase separation quantitatively. In this model, the experimentally discovered phase separation of ^{174}Yb and ^{87}Rb is treated as a result of an additional interaction potential on ^{174}Yb. This potential $U_{\mathrm{YbRb}}(\vec{r}, T)$ is created by the interaction with the ^{87}Rb atoms and in this first

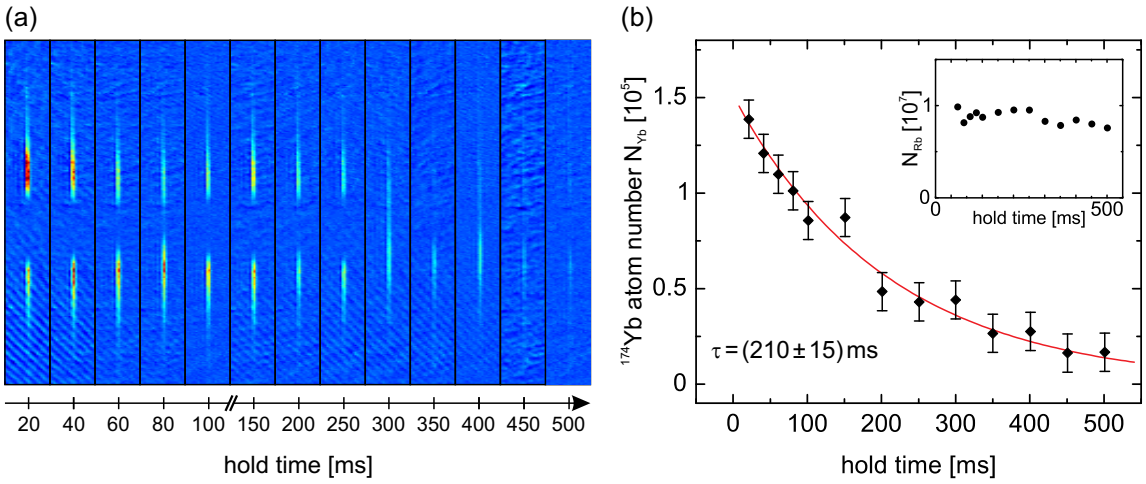

Figure 8.4: *(a) False color intra-trap images and (b) extracted ^{174}Yb atom numbers as a function of the holding time at phase separation conditions. An exponential fit to the data yields a $1/e$-decay time of $\tau \approx 210$ ms. The inset in (b) shows the corresponding ^{87}Rb atom number. Note that the lack of complete phase separation at 300 ms and 400 ms is attributed to fluctuations in the radial ODT beam alignment.*

order approach is assumed to be proportional to the ^{87}Rb density distribution $n_{\mathrm{Rb}}(\vec{r}, T)$:

$$U_{\mathrm{YbRb}}(\vec{r}, T) = n_{\mathrm{Rb}}(\vec{r}, T) \cdot \tilde{U}(T) \tag{8.1}$$

Here, $\tilde{U}(T)$ represents a normalized interaction parameter which may depend on the temperature T.

In the following, the calculated model potential for ^{87}Rb and the resulting density distribution $n_{\mathrm{Rb}}(\vec{r}, T)$ is discussed for the given experimental situation. The interaction term $U_{\mathrm{YbRb}}(\vec{r}, T)$ is subsequently included in the total potential for ^{174}Yb. For a quantitative analysis of the observed effect, modeled density distributions resulting from the total potential for ^{174}Yb are used as a fitting function for measured ^{174}Yb density distributions. Consequently, this allows the extraction of $\tilde{U}(T)$.

8.2.1 ^{87}Rb model potential and density distribution

The total potential for ^{87}Rb at BIODT beam powers typically used for phase separation measurements ($P_{532} = 343\,\mathrm{mW}$ and $P_{1064} = 135\,\mathrm{mW}$) is characterized by the comparatively flat MT contribution and a small, approximately $12\,\mu$K deep dimple created by the BIODT part (see Fig. 8.5 (a, b)). The model potentials shown here include the harmonic approximation for $U^{\mathrm{Rb}}_{\mathrm{MT}}$ according to Eq. 3.15 and the "full" form of the BIODT potentials $U^{\mathrm{Rb}}_{532\mathrm{ODT}}$ and $U^{\mathrm{Rb}}_{1064\mathrm{ODT}}$ according to Eq. 3.42:

$$U^{\mathrm{Rb}}_{\mathrm{tot}} = U^{\mathrm{Rb}}_{\mathrm{MT}} + U^{\mathrm{Rb}}_{532\mathrm{ODT}} + U^{\mathrm{Rb}}_{1064\mathrm{ODT}} \tag{8.2}$$

$$U^{\mathrm{Yb}}_{\mathrm{tot}} = U^{\mathrm{Yb}}_{532\mathrm{ODT}} + U^{\mathrm{Yb}}_{1064\mathrm{ODT}} \tag{8.3}$$

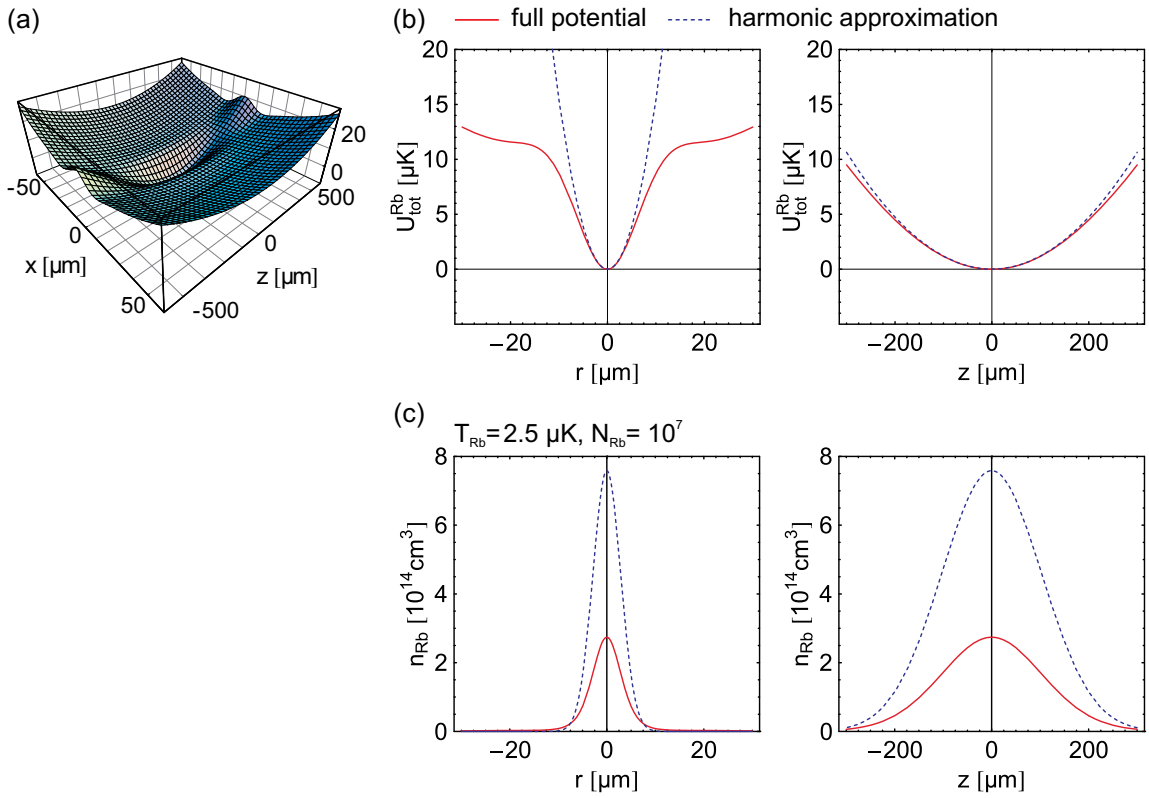

Figure 8.5: *Calculated ^{87}Rb potentials U_{tot}^{Rb} and density distributions n_{Rb} at parameters typically used for phase separation measurements: $P_{532} = 343\,mW$ and $P_{1064} = 135\,mW$. (a) shows the x-z-plane, whereas (b) compares radial and axial cuts of U_{tot}^{Rb} (red) with the harmonic approximation $U_{\mathrm{tot,harm.}}^{Rb}$ (blue dashed). (c) compares density distributions at $T_{\mathrm{Rb}} = 2.5\,\mu K$ and $N_{\mathrm{Rb}} = 10^7$ using U_{tot}^{Rb} (red) and $U_{\mathrm{tot,harm.}}^{Rb}$ (blue dashed).*

The density distribution $n(\vec{r}, T)$ of a thermal cloud trapped in any potential $U(\vec{r})$ at a defined temperature T is generally given by Eq. 3.17 and 3.18. This calculation, however, involves the volume integral of $U(\vec{r})$, which in the present case can only be solved numerically. In order to determine an analytical fitting function, however, the representation of the interaction potential according to Eq. 8.1 requires an analytic form of $n(\vec{r})$. This is achieved by a harmonic approximation of $U_{\mathrm{tot}}^{\mathrm{Rb}}$, resulting in a Gaussian shaped ^{87}Rb density distribution.

At the trap center, the potential $U_{\mathrm{tot}}^{\mathrm{Rb}}$ can be approximated by a harmonic potential according to

$$U_{\mathrm{harm.}}^{\mathrm{Rb}}(r, z) = \frac{1}{2} m_{\mathrm{Rb}} \omega_r^2 r^2 + \frac{1}{2} m_{\mathrm{Rb}} \omega_z^2 z^2 \,. \tag{8.4}$$

For the given BIODT configuration, the calculated radial and axial trap frequencies are $\omega_r = 2\pi \times 863\,\mathrm{Hz}$ and $\omega_z = 2\pi \times 23.9\,\mathrm{Hz}$. As shown in Fig. 8.5 (b), the harmonic potential (blue dashed line) matches the central part of the "BIODT dimple", but differs significantly from the full form of $U_{\mathrm{tot}}^{\mathrm{Rb}}$ (red line) in the radially outer regions, which are dominated by

the MT potential. The imperfect description of $U_{\mathrm{tot}}^{\mathrm{Rb}}$ by the harmonic approximation is also reflected in calculated density distributions, which are presented in Fig. 8.5 (c) for a typical ^{87}Rb temperature of $T_{\mathrm{Rb}} = 2.5\,\mu$K and a ^{87}Rb atom number $N_{\mathrm{Rb}} = 10^7$: Although the shapes of both distributions are nearly identical, the absolute calculated peak densities vary by a factor of ≈ 2.8. From a physical point of view, this difference is attributed to the fact that for the given trapping geometry and ^{87}Rb temperature, a significant fraction of the ^{87}Rb atoms are located outside the "BIODT dimple", which is not taken into account by the harmonic potential approximation.

In order to compensate for this insufficient description by the harmonic potential, a temperature dependent correction factor for the density is introduced:

$$\hat{f}(T) = \frac{n_{\mathrm{harm.}}^{\mathrm{Rb}}(\vec{r}=0,T)}{n_{\mathrm{tot}}^{\mathrm{Rb}}(\vec{r}=0,T)} \tag{8.5}$$

This factor compares calculated ^{87}Rb densities in the trap center using the full potential $U_{\mathrm{tot}}^{\mathrm{Rb}}$ and the harmonic approximation $U_{\mathrm{tot,harm}}^{\mathrm{Rb}}$. The corrected ^{87}Rb density distribution $\hat{n}_{\mathrm{Rb}}(\vec{r},T)$ consequently includes $\hat{f}(T)$ according to

$$\hat{n}_{\mathrm{Rb}}(\vec{r},T) = \frac{1}{\hat{f}(T)} \cdot n_{\mathrm{harm.}}^{\mathrm{Rb}}(\vec{r},T)\,. \tag{8.6}$$

Figure 8.6 (a) shows calculated values of $\hat{f}(T)$ at the present trapping geometry for $T = 0 \ldots 4.5\,\mu$K together with a fit using a polynomial of degree 4 (red line). At low tem-

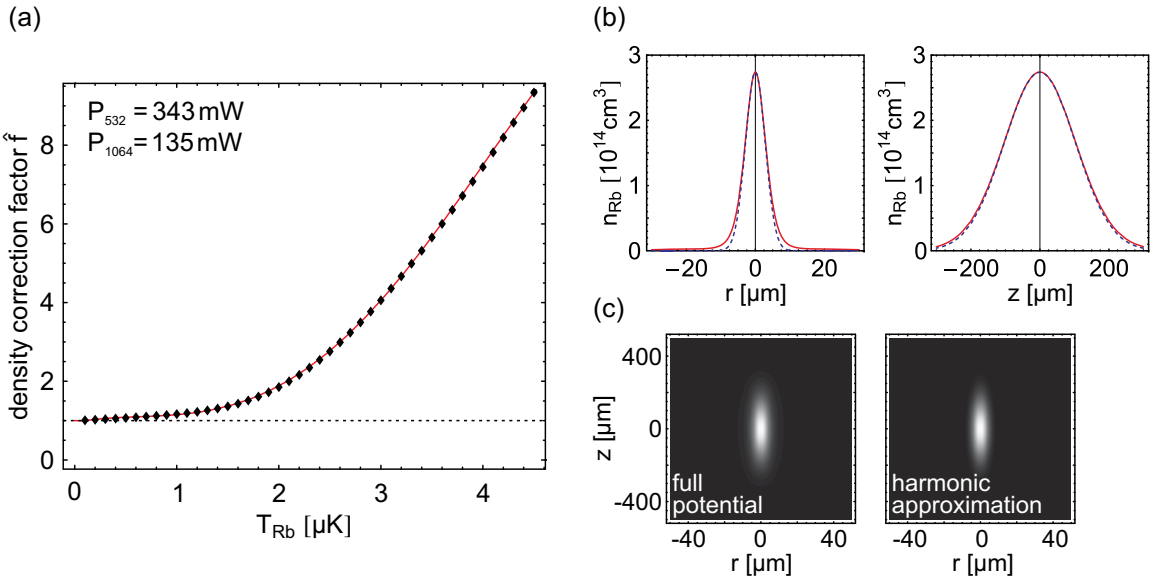

Figure 8.6: *(a) Correction factors for the ^{87}Rb density depending on the temperature for $P_{532} = 343\,mW$ and $P_{1064} = 135\,mW$. (b,c) Comparison of cuts along the radial and axial direction of resulting density distributions using U_{tot}^{Rb} and $U_{\mathrm{tot,harm.}}^{Rb}$ including $\hat{f}(T)$ for $T_{\mathrm{Rb}} = 2.5\,\mu K$ and $N_{\mathrm{Rb}} = 10^7$.*

peratures $T < 1\,\mu$K, $\hat{f}(T)$ can be neglected in density distribution calculations, whereas for typical temperatures used in the present experiments ($T = 2 \ldots 3.5\,\mu$K), it plays a significant role. The increase of $\hat{f}(T)$ with temperature is due to the fact that more and more ^{87}Rb atoms are accumulated outside the harmonic region in the trap center. However, by including $\hat{f}(T)$, calculated Gaussian shaped ^{87}Rb density distributions $\hat{n}_{\mathrm{Rb}}(\vec{r}, T)$ using the harmonic potential according to Eq. 8.4, describe the experimental situation with sufficient accuracy as illustrated in Fig. 8.6 (b,c). Over the complete trapping region, the density distributions agree within 5 % of the ^{87}Rb peak density. They differ slightly in the radial direction for $z = 0$ and $|r| > 5\,\mu$m, where $\hat{n}_{\mathrm{Rb}}(\vec{r}, T)$ tends to underestimate the "real" ^{87}Rb density. In phase separation measurements however, the ^{174}Yb cloud is split into two parts, which are axially separated by the ^{87}Rb cloud located in the trap center. These experiments probe the parts of the interaction potential, where both clouds overlap. Hence, the relevant regions are typically located at axial positions $|z| > 100 \ldots 200\,\mu$m. In this region, $\hat{n}_{\mathrm{Rb}}(\vec{r}, T)$ differs from the density distribution based on the full potential $U_{\mathrm{tot}}^{\mathrm{Rb}}$ at a level below < 2 % of the ^{87}Rb peak density.

Note that for different BIODT beam powers, the temperature dependent correction factor $\hat{f}(T)$ changes. For a quantitative analysis of the data, $\hat{f}(T)$ is calculated each time using the respective trapping parameters.

Absolute ^{87}Rb density

The calculation of absolute values for the ^{87}Rb peak density $n_{0,\mathrm{Rb}}$ at a given temperature T strongly depends on the BIODT beam parameters used in the model potential (see discussion in Sec. 7.1.2). As a result, uncertainties in the BIODT beam waists w_{532} and w_{1064} are the dominating contribution for the error of $n_{0,\mathrm{Rb}}$[1]. Additionally, the experimental determination of the ^{87}Rb atom number is subject to systematic uncertainties (see Sec. 4.3.5). Table 8.1 summarizes the error budget of the ^{87}Rb peak density $n_{0,\mathrm{Rb}}$ assuming a 5 % error in the ^{87}Rb temperature on a 10 % error in the atom number. For the determination of the total error σ_n^{tot}, the error contributions σ_n^i resulting from the uncertainties of the respective parameters i ($i = w_{532}, w_{1064}, T, N_{\mathrm{Rb}}$) are calculated independently. Consequently, σ_n^{tot} is obtained according to [140]:

$$\frac{\sigma_n^{\mathrm{tot}}}{n_{0,\mathrm{Rb}}} = \sqrt{\sum_i \frac{\sigma_n^i}{n_{0,\mathrm{Rb}}}} \qquad \text{with} \qquad i = w_{532}, w_{1064}, T, N_{\mathrm{Rb}} \tag{8.7}$$

This model calculation uses only one set of typical experimental parameters. Further analysis however shows, that within the relevant range of BIODT beam powers and ^{87}Rb temperatures, the final relative error bars of $^{+85\%}_{-61\%}$ for the ^{87}Rb density are practically unchanged.

From a physical point of view, the large error bars for $n_{0,\mathrm{Rb}}$ result from the fact, that the BIODT consists of two potentials with small uncertainties in their parameters. In

[1] Beam waists are obtained from trap frequency measurements (see Sec. 6.1.2), assuming perfect Gaussian beam shapes. Possible deviations from this case are not accounted for in the respective error bars. However, the relevant parameter for ^{87}Rb density calculations is the relative error of both ODT beam waists, which can be well assumed to be in the specified error range.

parameter	value & error	calculated ^{87}Rb density $[10^{14}\,\mathrm{cm}^{-3}]$	absolute error contribution	relative error contribution
532 nm ODT beam waist w_{532}	$15.78\,^{+0.20}_{-0.20}\,\mu$m	2.73	$^{+1.01}_{-0.85}$	$^{+37\%}_{-31\%}$
1064 nm ODT beam waist w_{1064}	$14.71\,^{+0.25}_{-0.25}\,\mu$m	2.73	$^{+1.94}_{-1.23}$	$^{+71\%}_{-45\%}$
^{87}Rb atom number N_{Rb}	$1\,^{+0.10}_{-0.10}\times 10^7$	2.73	$^{+0.27}_{-0.27}$	$^{+10\%}_{-10\%}$
^{87}Rb temperature T	$2.5\,^{+0.13}_{-0.13}\,\mu$K	2.73	$^{+0.54}_{-0.43}$	$^{+20\%}_{-16\%}$
^{87}Rb density $\mathbf{n}_{0,\mathrm{Rb}}$ and total error $\sigma^{\mathrm{tot}}_{\mathbf{n}}$:		**2.73**	$\mathbf{^{+2.32}_{-1.66}}$	$\mathbf{^{+85\%}_{-61\%}}$

Table 8.1: *Error budged for determination of the ^{87}Rb density for typical BIODT parameters used in phase separation experiments: $P_{532} = 343\,mW$ and $P_{1064} = 135\,mW$*

the case of ^{87}Rb, a repulsive and attractive contribution are added resulting in a small attractive total potential. This process strongly increases the relative uncertainty in the BIODT potential, which is used for calculations of $n_{0,\mathrm{Rb}}$.

Note that the relative comparability of data based on constant trapping geometry is not subject to the large errors in the absolute ^{87}Rb density. For fixed BIODT parameters, the relative errors only involve uncertainties from ^{87}Rb temperature and atom number determinations.

8.2.2 ^{174}Yb potential and density distribution including the interaction term

The total potential for ^{174}Yb including the interaction term $U_{\mathrm{YbRb}}(\vec{r},T)$ is given by

$$\begin{aligned} U^{\mathrm{Yb}}_{\mathrm{tot}}(\vec{r},T) &= U^{\mathrm{Yb}}_{\mathrm{BIODT}}(\vec{r},T) + U_{\mathrm{YbRb}}(\vec{r},T) \\ &= U^{\mathrm{Yb}}_{\mathrm{BIODT}}(\vec{r},T) + \frac{1}{\hat{f}(T)}\cdot n^{\mathrm{Rb}}_{\mathrm{harm.}}(\vec{r},T)\cdot\tilde{U}(T)\,. \end{aligned} \tag{8.8}$$

This representation uses the Gaussian shaped form for the ^{87}Rb density distribution according to Eq. 8.6. For a more convenient description, the magnitude of the interaction potential in the trap center,

$$U_0 \equiv U_{\mathrm{YbRb}}(\vec{r}=0,T)\,, \tag{8.9}$$

is introduced. Figure. 8.7 (a-d) shows calculated axial cuts of the ^{174}Yb potentials and the resulting density distributions for a cloud of $N_{\mathrm{Yb}} = 10^5$ ^{174}Yb atoms at $T = 2.5\,\mu$K. The plots (a) and (b) present the unperturbed case, while in (c) an interaction potential U_{YbRb}, proportional to the ^{87}Rb density distribution at $T = 2.5\,\mu$K and with a maximum value of $U_0/k_{\mathrm{B}} = 12\,\mu$K is added to the BIODT potential. The resulting ^{174}Yb distribution is shown in (d). In addition, Figure. 8.7 (e) illustrates ^{174}Yb distributions in the r-z-plane

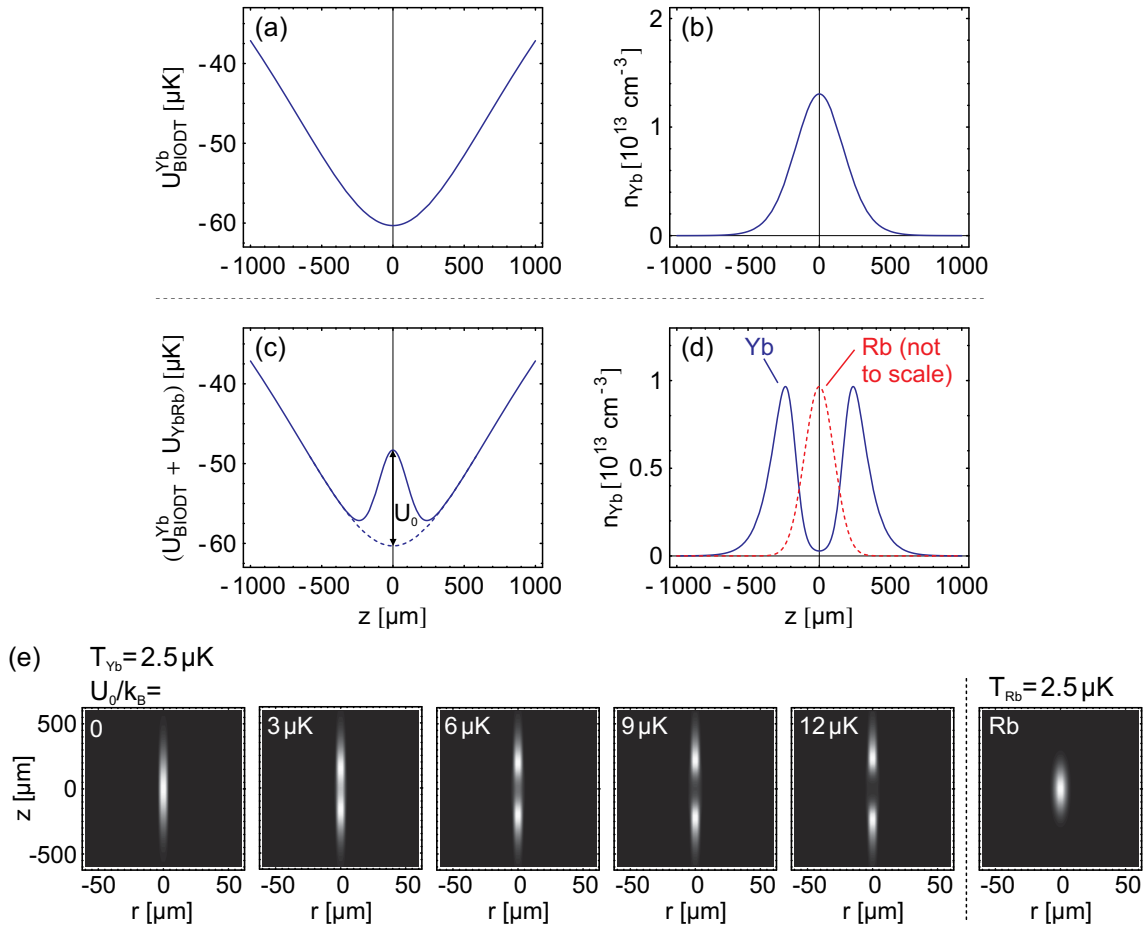

Figure 8.7: *Calculated axial potentials (a, c) and density distributions (b, d, e) for* ^{174}Yb *for* $T = 2.5\,\mu K$ *and* $N_{\mathrm{Yb}} = 10^5$*. For a direct comparison, the calculated* ^{87}Rb *density distribution at* $T = 2.5\,\mu K$ *is included in (d, e).*

at $T = 2.5\,\mu$K for increasing interaction potentials $U_0/k_{\mathrm{B}} = 0 \ldots 12\,\mu$K. Subfigures (d) and (e) also contain calculated ^{87}Rb density distributions, allowing a direct comparison of the two distributions. The model potentials used in these calculations include the full form of $U^{\mathrm{Yb}}_{532\mathrm{ODT}}$ and $U^{\mathrm{Yb}}_{1064\mathrm{ODT}}$ according to Eq. 3.40 and the Gaussian shaped ^{174}Yb-^{87}Rb interaction potential as discussed above. Calculated ^{174}Yb density distributions presented here, qualitatively match the observations from phase separation measurements: For an increasing repulsive interaction potential, the ^{174}Yb density in the trap center is reduced. Finally, the cloud is separated into two parts that are axially well separated from each other, enclosing the ^{87}Rb cloud in the trap center.

8.2.3 Quantitative analysis of the interspecies interaction

In order to quantitatively characterize the interaction potential between ^{174}Yb and ^{87}Rb, we use the calculated ^{174}Yb density distribution as a fitting function on the experimental

data. The magnitude of $\tilde{U}(T)$ is a free parameter, while the temperature and the ^{87}Rb density distribution are experimentally determined.

a) Auxiliary fitting function

The ^{174}Yb density distribution in phase separation measurements is identified by intra-trap images of the atomic cloud. At the present temperatures of $\approx 2.5\,\mu$K, the radial dimension of atomic cloud ($1/e^2$-radius $\sigma_r \approx 3\,\mu$m) is beyond the resolution of our imaging system (see Sec. 4.3.1). As a result, the image of the ^{174}Yb cloud extends radially over a range of only a few pixels (see Fig. 8.9), which does not allow the extraction of any usable information on the density distribution in this direction. Hence, the pixel values are summed over the relevant range in the radial direction, resulting in an integrated *linear density*, which depends only on the axial coordinate z.

In order to compare this data with calculated density distributions, the *linear density* $\hat{n}_{\mathrm{Yb}}(z)$ of the model distribution has to be calculated by integrating over the radial direction:

$$\hat{n}_{\mathrm{Yb}}(z) = \int_0^\infty n_{\mathrm{Yb}}(\vec{r}) \cdot 2\pi r dr = \int_0^\infty n_0 \cdot \exp\left(-\frac{U_{\mathrm{tot}}^{\mathrm{Yb}}(\vec{r},T)}{k_{\mathrm{B}}T}\right) \cdot 2\pi r dr \tag{8.10}$$

This equation includes the volume integral in cylindrical coordinates assuming axial symmetry and Eq. 3.17. However, for $U_{\mathrm{tot}}^{\mathrm{Yb}}(\vec{r},T)$ according to Eq. 8.8, this integral can not be solved analytically. Therefore, Eq. 8.10 can not be used as an analytic fitting function for the data.

In order to solve this problem, an auxiliary fitting function is introduced, that matches the relevant characteristics of the "real" function (8.10) and is analytic. In the automated fitting process, the auxiliary function is used and subsequently the corresponding parameters of $\hat{n}_{\mathrm{Yb}}(z)$ are determined.

Due to the cylindrical symmetry of the density distribution, the distribution of $n_{\mathrm{Yb}}(\vec{r})$ along the z-axis, $n_{\mathrm{Yb}}(r=0,z)$ exhibits similar characteristics as the integral $\int_0^\infty n_{\mathrm{Yb}}(\vec{r}) \cdot 2\pi r dr$. Hence, $n_{\mathrm{Yb}}(r=0,z)$ is used as an auxiliary fitting function for the data. However, depending on the magnitude of the interaction potential U_0 included in $U_{\mathrm{tot}}^{\mathrm{Yb}}(\vec{r},T)$ and the temperature T, the shapes of both functions do not exactly match in the relevant region. Hence, a scaling factor $\xi(U_0,T)$, which takes this into account, is introduced according to:

$$\int_0^\infty n_{\mathrm{Yb}}(\vec{r},U_0) \cdot 2\pi r dr = \text{const.} \cdot n_{\mathrm{Yb}}(r=0,z,\xi(U_0,T)\cdot U_0)\,. \tag{8.11}$$

Note that the right side of this equation also includes a constant factor that adjusts the absolute magnitude of both functions[2]. Figure 8.8 shows both the auxiliary function including the correction factor $\xi(U_0,T)$ (red line) and the "real" ^{174}Yb density distribution (8.10) (black dots) for increasing values of U_0. Within the relevant parameter range

[2]The unit of this factor is m^2 in order to match the left side of Eq. 8.11, which represents the physical meaning of a *linear density*.

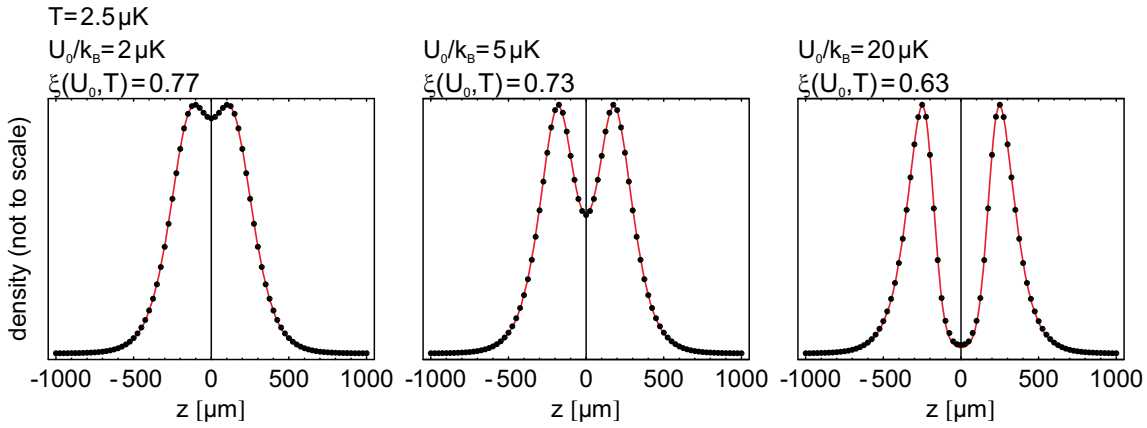

Figure 8.8: *Comparison of the auxiliary fitting function* $n_{\mathrm{Yb}}(r=0,z,\xi(U_0,T)\cdot U_0)$ *(red line) and* $\int_0^\infty n_{\mathrm{Yb}}(\vec{r},U_0)\cdot 2\pi r dr$ *(black dots) for different values of the interaction potential* U_0 *at a fixed temperature* $T = 2.5\,\mu K$

($T = 1\ldots7\,\mu$K, $U_0/k_{\mathrm{B}} = 0\ldots25\,\mu$K), the values of $\xi(U_0,T)$ are determined by numerically solving the integral in Eq. 8.10 and comparing this data with the auxiliary function $n_{\mathrm{Yb}}(r=0,z)$. Subsequently, a two-dimensional polynomial fit with a maximum order of 2 in T and U_0 is applied to the data for $\xi(U_0,T)$ in order to obtain an analytical correlation between the auxiliary fitting function and $\hat{n}_{\mathrm{Yb}}(z)$ according to (8.10). Typical values of the correction factor $\xi(U_0,T)$ are in the range of $0.6\ldots0.8$ and the fit deviates from the numerically calculated values of $\xi(U_0,T)$ by less than 2 % across the relevant parameter range for T and U_0.

The extraction of the interaction potential magnitude U_0 based on ^{174}Yb density distributions from phase separation measurements includes two steps: First, the data is fitted using the auxiliary function $n_{\mathrm{Yb}}(r=0,z)$, which yields a parameter $U_{0,\mathrm{fit}}$. The peak interaction potential U_0 is then determined by solving the equation

$$U_{0,\mathrm{fit}} = \xi(U_0,T)\cdot U_0\,, \tag{8.12}$$

where T acts as a fixed parameter, which is obtained experimentally.

The validity of this indirect determination of U_0 has been verified by numerically creating test data for variable parameter sets and using the fitting procedure described above.

b) Fitting procedure

The following section summarizes the fitting procedure used for the phase separation measurements, including the methods described above.

The experimental data are based on intra-trap images of the ^{174}Yb cloud. By summing over relevant pixel values in the radial direction, a 1-dimensional distribution of *linear densities* along the z-axis is obtained. Figure 8.9 illustrates this step according to three typical examples. The background level of all data sets is adjusted by averaging pixel

values within a defined region, where no ^{174}Yb atoms are present. This mean background value is then subtracted from all pixel values of the respective data set.

Fitting parameters The fitting function used for this data is given by Eq. 8.11, and with the use of (8.8), (6.15) and (3.17), it can be written as

$$n_{\mathrm{Yb}}(r=0,z,\Delta z_1,\Delta z_2,T,U_{0,\mathrm{fit}}) = \hat{n}_0 \cdot \exp\left(-\frac{U^{\mathrm{Yb}}_{\mathrm{tot}}(r=0,z,\dots)}{k_{\mathrm{B}}T}\right) \quad \text{with}$$

$$U^{\mathrm{Yb}}_{\mathrm{tot}}(r=0,z,\dots) = U^{\mathrm{Yb}}_{532\mathrm{ODT}}(r=0,z-\Delta z_1-\Delta z_2,T) + U^{\mathrm{Yb}}_{1064\mathrm{ODT}}(r=0,z-\Delta z_1,T) + \frac{\hat{n}_{\mathrm{Rb}}(r=0,z-\Delta z_1,T)}{\hat{n}_{\mathrm{Rb}}(r=0,z=0,T)} \cdot U_{0,\mathrm{fit}}\,. \tag{8.13}$$

It includes a variable amplitude (here: $\hat{n}_0$) and a free parameter Δz_1, which is used to determine the center of the interaction potential in the z-direction.

As shown in Fig. 8.9, the summed density distributions are typically not perfectly symmetric in the z-direction. This effect is attributed to an imperfect axial alignment of the two independent ODT beams (see Sec. 7.1.2) and residual relative movement of the two clouds. It results in axially different positions of the ^{87}Rb- and ^{174}Yb cloud centers as the (attractive) potential for ^{87}Rb is defined by the 1064 nm ODT beam whereas the ^{174}Yb potential is dominated by the 532 nm ODT beam. In order to take this into account, the relative axial position of the optical potentials is treated as an additional free parameter Δz_2 in the fit.

The only other free fitting parameter is the interaction potential magnitude $U_{0,\mathrm{fit}}$, which determines the shape of the ^{174}Yb density distribution in the center region.

On the contrary, the temperature T included in the fit is extracted from the corresponding ^{87}Rb image (see discussion in Sec. 8.1) and acts as a fixed parameter.

Automated fitting routine A set of data from multiple ^{174}Yb images can be processed in an automated fitting routine using the programming language *Mathematica 5*. The determination of the optimum fitting parameters is based on a nonlinear least square algorithm using a method according to Levenberg-Marquardt [141, 142].

Figure 8.9 shows typical examples of experimental data and the corresponding fit together with the residual of the fit. These data sets all originate from a series of phase separation experiments, where the ^{87}Rb atom number was changed in a controlled way, while the temperature was kept approximately constant. As the ^{87}Rb atom number is increased from 1.7×10^6 in Fig. 8.9 (a) to 3.9×10^6 in (b) and 9.8×10^6 in (c), the magnitude of the peak interaction potential U_0 also increases. As a result, a greater number of ^{174}Yb atoms are repelled from the center region of the trap, creating a larger and larger dip in the integrated density distribution.

The quality of the fit can be estimated by the χ^2-test, which compares all n measured data points m_i with the corresponding values h_i calculated by the fitting function according

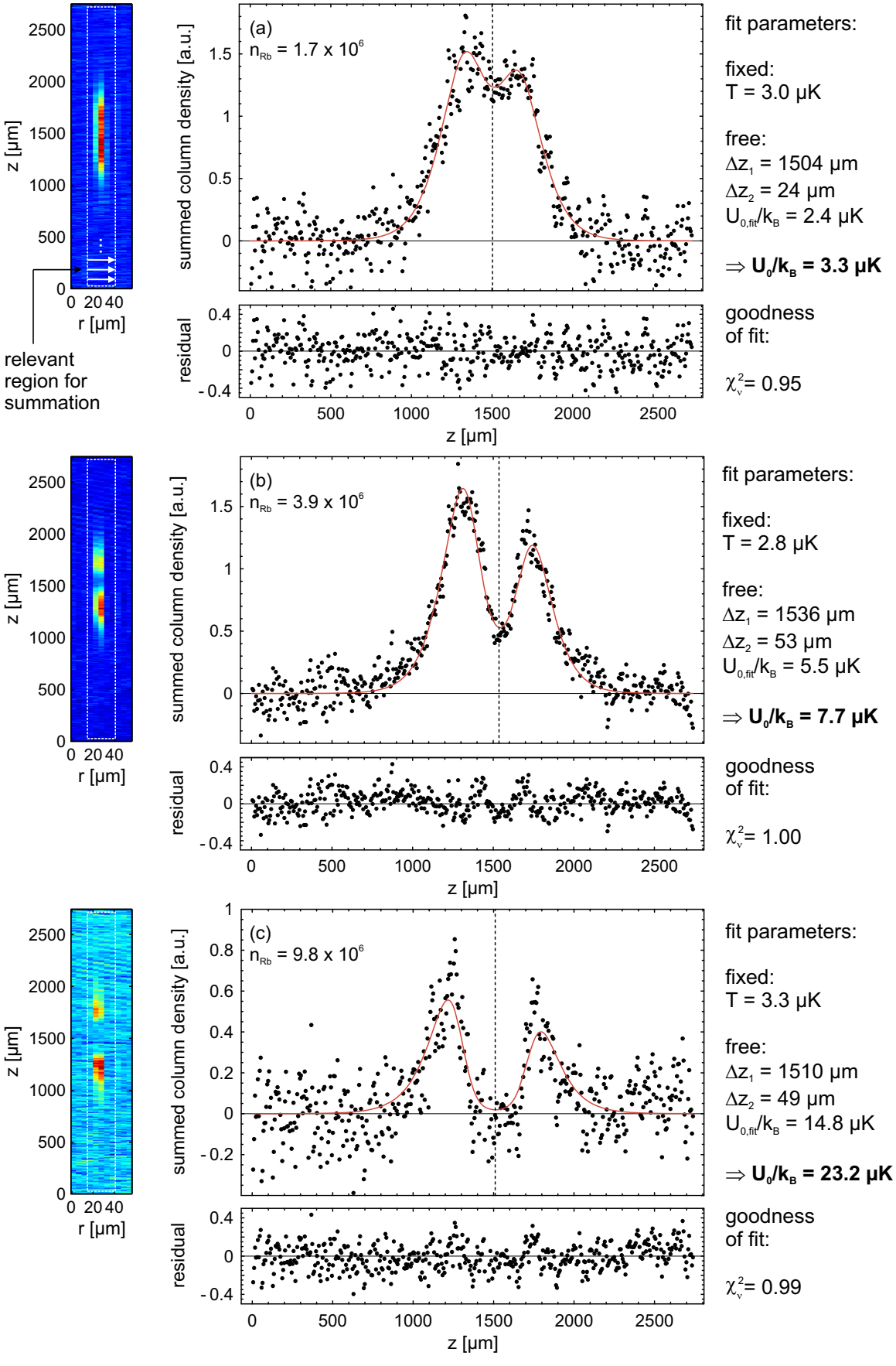

Figure 8.9: *Illustration of the fitting procedure according to 3 typical examples.*

to [140]

$$\chi^2 = \sum_{i=1}^{n} \frac{(h_i - m_i)^2}{\sigma_i^2} \,. \tag{8.14}$$

Here, $\sigma_i \equiv \sigma$ represents the (constant) error of each data point, which in the present case is estimated by calculating the standard deviation of the data points in the background region, where no ^{174}Yb atoms are present. It is convenient to define the reduced χ^2 as $\chi^2_\nu = \chi^2/\nu$ (where ν is the number of degrees of freedom), with the general expectation value $\langle \chi^2_\nu \rangle = 1$. Typical fits on ^{174}Yb distributions as displayed in Fig. 8.9 yield reduced χ^2-values $\chi^2_\nu = 1.0 \pm 0.1$, indicating that the fitting function describes the experimental data very well.

Statistical error of the fitting parameters The statistical error of the magnitude of the interaction potential U_0 obtained by the described fitting routine is determined in a first order approximation using the signal-to-noise ratio of the respective data set. This quantity itself is calculated as $\sigma/\max(h_i)$ and results in typical relative errors for U_0 on the order of $10 \ldots 20\%$.

Note that generally, errors in fitting parameters are obtained by finding the change in each parameter to produce a change of χ^2 of 1 from the minimum value after reoptimizing the fit. This method is manually applied to selected test data sets and the resulting error bars for U_0 are consistent with the results from the signal-to-noise method. Due to its complexity, however, this more sophisticated approach is not implemented in the automated fitting routine. Taking into consideration, that the dominating error contribution for further analysis of this data is given by the large uncertainty in the ^{87}Rb density (see Sec. 8.2.1), this simplification seems legitimate.

8.3 Results and Systematic tests

This section describes the quantitative results from phase separation measurements with ^{174}Yb and ^{87}Rb. According to the fitting method described above, the magnitude of the interaction potential is extracted from ^{174}Yb density distributions based on intra-trap images.

The interaction potential according to Eq. 8.1 assumes a linear dependence on the ^{87}Rb density. This prediction is tested experimentally using several series of data with controlled ^{87}Rb atom numbers at fixed temperatures. These results are combined in order to obtain a final value for the normalized interaction parameter $\tilde{U}(T)$.

Additional data sets probe the temperature dependence of the interaction in a range of $1.5 \ldots 6.5\,\mu$K. Furthermore, experiments are performed using pure optical potentials and ^{87}Rb in the $|F = 2, m_F = 2\rangle >$ spin state. Finally, the properties of different Yb isotopes are tested under conditions, where phase separation occurs with ^{174}Yb.

8.3.1 Density dependence

The quantitative analysis of phase separation experiments as described in the previous section is based on the basic assumption, that the interaction potential affecting the ^{174}Yb atoms is directly proportional to the ^{87}Rb density:

$$U_{\mathrm{YbRb}}(\vec{r},T) = n_{\mathrm{Rb}}(\vec{r},T)\cdot\tilde{U}(T) \tag{8.15}$$

This dependency is experimentally tested by several different methods:

a) Variation of the ^{87}Rb confinement: As described in Sec. 7.1.2, the ^{87}Rb density in the trap center strongly depends on the power ratio of the two ODT beams. Using a fixed power level of 343 mW for the 532 nm ODT beam, the ^{87}Rb density in phase separation experiments is controlled by changing the 1064 nm ODT beam power at the end of the final ramp up within a range of 100 . . . 145 mW. This experimental sequence is illustrated in Fig. 8.11 (a), further details can also be found in Sec. 8.1. Figure 8.10 shows combined results of 6 different data sets for U_0 and the respective measured temperature T_{Rb} as a function of the present ^{87}Rb density n_{Rb}. The results are in qualitative agreement with the

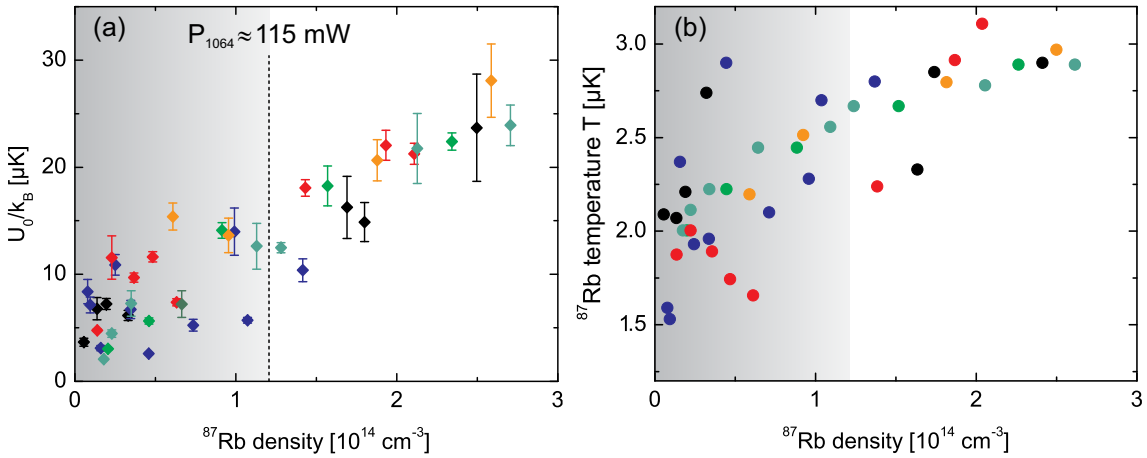

Figure 8.10: *(a) Fitted interaction potential magnitudes U_0 depending on the present ^{87}Rb density. This plot combines 6 data sets, which are characterized by different colors. Note that the absolute ^{87}Rb density is subject to large error bars of $^{+85\%}_{-61\%}$. The dashed line indicates $P_{1064} \approx 115\,\mathrm{mW}$. Data points below this level are additionaly liable to relative errors, as the total ^{87}Rb potential tends to be unclearly defined for lower 1064 nm ODT powers. (b) Corresponding measured ^{87}Rb temperatures.*

assumed proportionality. However, the following experimental issues for these data sets have to be carefully considered:

- The ^{87}Rb density in the trap center is calculated for each data point in Fig. 8.10 using the measured ^{87}Rb temperature and -atom number and the model potential based on the particular BIODT beam powers. As discussed in Sec. 8.2.1, the error bars of this quantity are large due to uncertainties in the BIODT beam waists.

- Despite the large errors of n_{Rb}, the relative comparability of these data points is valid, as long as the respective BIODT beam powers lead to defined attractive optical potentials for ^{87}Rb. For lower 1064 nm ODT powers (indicated by the gray area in Fig. 8.10), the ^{87}Rb potential is closer to the case, where the effects of the attractive 1064 nm beam and the repulsive 532 nm beam cancel (see Fig. 7.2). In this regime, the calculated ^{87}Rb density in the trap center is even more sensitive to the underlying beam parameters. Furthermore, experimental imperfections such as relative misalignment of the ODT beams tend to have greater relative effect on measured values of U_0 for lower 1064 nm ODT powers. As a result, data points below $P_{1064} \approx 115\,\mathrm{mW}$ exhibit larger spread. Hence, they are not included in further quantitative analysis.
- In the experimental sequence used for phase separation measurements, the ^{87}Rb temperature rises within the 1064 nm ODT power ramp up due to adiabatic compression (see Sec. 8.1) to a level, which depends on the final 1064 nm ODT power. Hence, altering the 1064 nm ODT power within a series of measurements simultaneously changes T. As shown in Fig. 8.10 (b), the temperature connected to the present data sets ranges from $\approx 1.5\,\mu\mathrm{K}$ for low 1064 nm ODT power settings up to $\approx 3.1\,\mu\mathrm{K}$ for high 1064 nm ODT powers and ^{87}Rb densities.

In summary, the variation of the final 1064 nm ODT power in phase separation measurements provides an experimentally simple way to change the ^{87}Rb density in the trap center and the results qualitatively confirm the assumed linear n_{Rb}-dependence of the interspecies interaction potential. Especially for lower 1064 nm ODT beam powers, however, the present ^{87}Rb density is subject to increased relative fluctuations and its absolute determination leads to large error bars. Furthermore, altering the final 1064 nm ODT power simultaneously changes a second experimental parameter, namely the temperature of both atomic species.

b) Variation of the ^{87}Rb atom number Since for large ^{87}Rb densities the clouds are already separated, the ^{174}Yb only probes the ^{87}Rb density at the edge, which is lower than the peak density. Hence, deviations of the linearity cannot be observed for large ^{87}Rb densities (using the method described above) alone. In order to overcome these limitations, an experimental sequence is designed, which exclusively changes the ^{87}Rb density while leaving all other experimental parameters constant. The basic idea is, to include a controlled ^{87}Rb atom loss procedure without interfering with the temperature and the ^{174}Yb atoms right before phase separation conditions are established. This approach is realized by the following sequence, which is illustrated in Fig. 8.11 (b):

Starting from the point, where both species are in contact and the interspecies thermalization process is finished, the 1064 nm ODT power is not directly ramped up to create the experimental situation required for phase separation measurements. Instead, we ramp the 1064 nm ODT beam power down to 0 within 50 ms, leaving behind only the MT and the 523 nm ODT, which represents a repulsive potential for the ^{87}Rb atoms. This ramp down temporarily separates the two atomic species, allowing a controlled removal of ^{87}Rb with-

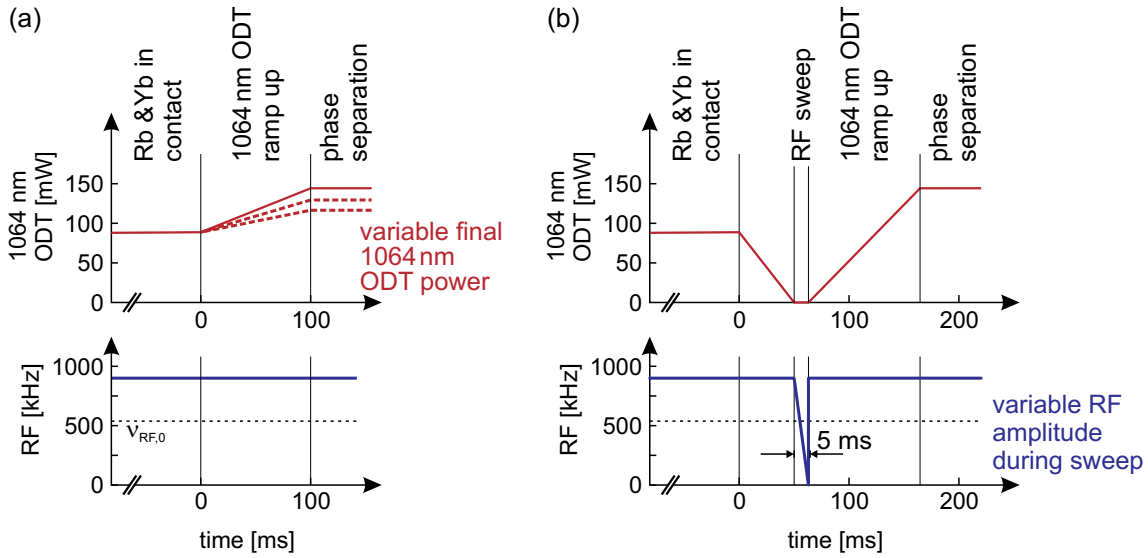

Figure 8.11: *Comparison of different experimental procedures used to control the ^{87}Rb density in phase separation measurements. (a) Sequence used for variation of the ^{87}Rb confinement; (b) sequence for variation of the ^{87}Rb atom number.*

out significantly affecting the present ^{174}Yb atoms. The ^{87}Rb atom loss itself is induced by a 5 ms long RF sweep from 900 kHz to 0. As this RF sweep takes place on a time scale much smaller than required for effective rethermalization of atoms in an evaporative cooling ramp, the temperature of the ensemble remains approximately constant. This is also confirmed experimentally. The RF sweep can rather be seen as an non-adiabatic removal of ^{87}Rb atoms of all energy classes. The fraction of ^{87}Rb atoms removed from the trap is determined by the RF amplitude used during the sweep. Subsequently, the RF is set back to its original level and phase separation conditions are achieved by ramping up the 1064 nm ODT beam power to a fixed level.

Resulting peak interaction potentials U_0 and measured temperatures are shown as a function of the ^{87}Rb atom number in Fig. 8.12. This plot includes typical data, which is obtained using the following experimental parameters for the phase separation measurements: $P_{532} = 343\,\mathrm{mW}$, $P_{1064} = 143\,\mathrm{mW}$. As shown in Fig. 8.12 (b), the data is taken at a temperature of $3.3 \pm 0.2\,\mu\mathrm{K}$, independent of the actual ^{87}Rb atom number. The dashed red line in Fig. 8.12 (a) indicates the direct proportionality between U_0 and the ^{87}Rb atom number, which itself is proportional to n_{Rb} for the given case where all other experimental parameters are kept constant. Hence, the assumption on the interaction potential $U_{\mathrm{YbRb}} \propto n_{\mathrm{Rb}}$ as given in Eq. 8.15 is qualitatively verified within the uncertainties of the present measurements.

8.3.2 Temperature dependence

The results from density tests presented in the previous section do not show a significant temperature dependence of the normalized interaction parameter $\tilde{U}(T)$ within the probed

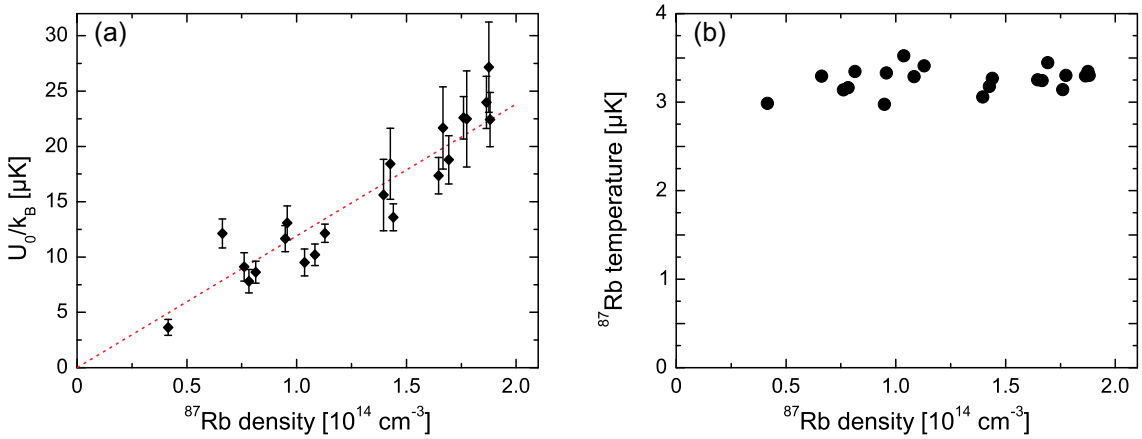

Figure 8.12: *Fitted (a) interaction potential magnitudes U_0 and (b) corresponding temperatures depending on the ^{87}Rb density The dashed red line indicates the direct proportionality.*

temperature range of $T = 1.5 \ldots 3.5\,\mu$K (see Sec. 8.3.4). The different temperatures in these measurements, however, result from variations in the trapping potentials present in the respective experiments.

In order to obtain better defined information on the temperature characteristics, we performed additional phase separation measurements at different temperature settings using fixed parameters for the trapping potentials. The ^{87}Rb temperature is controlled by a variation of the final RF level ν_{RF} before both atomic clouds are brought into contact. After the thermalization time, conditions for phase separation measurements are created by ramping up the 1064 nm ODT power to a fixed level. A change of $\nu_{\mathrm{RF}} = 2.0 \ldots 0.65$ MHz reduces the temperature $T_{\mathrm{Rb}} = T_{\mathrm{Yb}} \equiv T$ during phase separation experiments from $\approx 7\,\mu$K to $\approx 2.5\,\mu$K. In general, a temperature reduction obtained by further evaporative cooling is accompanied by a loss of atoms. In the present case, the ^{87}Rb atom number ranges from $\approx 3.5 \times 10^7$ at $7\,\mu$K to $\approx 5 \times 10^6$ at $2\,\mu$K. Nonetheless, the peak ^{87}Rb density in the trap center rises during the temperature decrease from $\approx 1 \times 10^{14}\,\mathrm{cm}^{-3}$ to $\approx 2 \times 10^{14}\,\mathrm{cm}^{-3}$.

Using the present trapping geometry, the temperature range for phase separation measurements is limited due to the following experimental issues: The lowest obtainable ^{87}Rb temperatures are limited by the temperature increase due to adiabatic compression to $\approx 2\,\mu$K. Lowering the total potential for ^{87}Rb would reduce the temperature, but this would also lead to a more sensitive experimental situation and larger statistical spread in the fitted interaction parameters (see Sec. 8.3.1). On the other hand, the qualitative analysis of phase separation measurements at higher temperatures is limited as the ^{87}Rb density lowers below a treshold level. At $T > 7 \ldots 8\,\mu$K, the reduction of the ^{174}Yb density in the trap center due to the repulsive interaction with the ^{87}Rb cloud becomes hard to detect at the given signal-to-noise ratio. As a result, the fitting routine yields unreliable and strongly fluctuating results.

Figure 8.13 shows extracted normalized interaction parameters $\tilde{U}(T)$ as a function of the

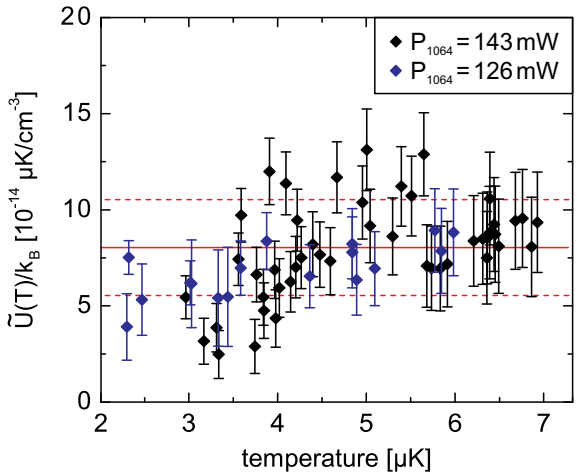

Figure 8.13: *Extracted normalized interaction parameters as a function of corresponding measured temperature. This plot combines results obtained with different 1064 nm ODT power settings and shows the mean (red line) and standard deviation (dashed res lines) of all data points.*

measured temperature within $2\,\mu\text{K} < T < 7\,\mu\text{K}$. Each data point is obtained by dividing fitted values of U_0 by the corresponding calculated ^{87}Rb peak density n_{Rb}. The majority of the data included in this plot results from phase separation measurements performed at a final 1064 nm ODT power $P_{1064} = 143\,\text{mW}$. Additional sets using $P_{1064} = 126\,\text{mW}$ complement this experimental series. Error bars of the individual data points contain fitting uncertainties and take into account the statistical spread. They do not include the uncertainty of n_{Rb}, as it is irrelevant for a relative comparison of the data. The red line in Fig. 8.13 indicates the weighted mean of all data points and the dashed red lines represent the standard deviation.

The most important conclusion of these measurements is, that phase separation between ^{87}Rb and ^{174}Yb is unambiguously observed at temperatures up to $\approx 7\,\mu\text{K}$. Furthermore, the results for U_0 do not show a significant temperature dependence in the range of $T = 2.5 \ldots 7\,\mu\text{K}$ within experimental uncertainties. Despite the slight overall increase between $3\,\mu\text{K}$ and $4\,\mu\text{K}$, the distribution of data points is consistent with a temperature independent interaction potential.

Note that the additional temperature dependence measurements are performed after a complete readjustment of the BIODT optical system. It is probable, that this process involved changes of the ODT beam parameters on a significant level. Although the results of these complementary measurements are consistent with results from original experiments, they are not included in the final value for $\tilde{U}(T)$ presented in Sec. 8.3.4. The relative comparability of the results based on these separate experiments, however is still justified.

8.3.3 Pure optical potentials

All results presented in this section so far are based on experiments using the BIODT potentials as well as the MT potential. Additional measurements described in the following show, that the effect of phase separation is also observed when the MT is turned off.

Omitting the MT alters the conditions used for the qualitative analysis of the data. Hence, adapting the calculated model potentials to the new experimental situation probes

their validity and robustness under parameter changes.

Furthermore, the pure optical approach probes the interaction between ^{87}Rb and ^{174}Yb under a small variation of the magnetic field. In the trap center, the magnetic field is changed by the amount of the offset $B_0 \approx 0.8\,\mathrm{G}$ (see Sec. 4.1), when the MT is turned off.

Experimentally, phase separation measurements in pure optical potential are based on the sequence for ^{87}*Rb atom number series* (see Sec. 8.3.1 and Fig. 8.11 (b)). After the final 1064 nm ODT power ramp up, the MT is shut down within 5 ms. This situation is then kept constant for a total holding time of 70 ms before images of both the ^{174}Yb- and the ^{87}Rb cloud are taken. The RF used for evaporative cooling of ^{87}Rb is turned off simultaneously with the MT.

During the ramp down of the magnetic potential, all (high energetic) ^{87}Rb atom located outside the potential "dimple" created by the BIODT are lost from the trap. At the present BIODT parameters $P_{532} = 343\,\mathrm{mW}$ and $P_{1064} = 143\,\mathrm{mW}$, the ^{87}Rb atom number is reduced by a factor of ≈ 2.1. Simultaneously, the measured temperature of the remaining ^{87}Rb atoms is decreased to $\approx 1.6\,\mu$K by plane evaporation. In a rough description, turning off the MT can be seen as a hard step in an evaporative cooling ramp.

The analysis of data from these measurements is nearly equivalent to the usual procedure. The main difference is, that the correction factor (8.5) for the ^{87}Rb density, which takes into account ^{87}Rb atoms located outside the "BIDOT dimple", is omitted in the calculation of the fitting function. As only the optical potentials are present, the harmonic approximation for the ^{87}Rb density given in Eq. 8.4 describes the situation with sufficient accuracy.

Phase separation measurements using pure optical potential involved 2 series with varied ^{87}Rb atom numbers at fixed ODT parameters $P_{532} = 343\,\mathrm{mW}$ and $P_{1064} = 143\,\mathrm{mW}$. Extracted normalized interaction parameters $\tilde{U}(T)$ are consistent with the results based on measurements with the both optical and magnetic potentials. At the given accuracy level, no effect of the magnetic field change on interaction properties between ^{87}Rb and ^{174}Yb can be observed. Hence, the data is included in the combined results shown in Fig. 8.14 (data points labeled (1)).

8.3.4 Combined results for $\tilde{U}(T)$

On the basis of a linear dependence between $U_{\mathrm{YbRb}}(\vec{r}, T)$ and $n_{\mathrm{Rb}}(\vec{r}, T)$, the normalized interaction parameter $\tilde{U}(T) = U_{\mathrm{YbRb}}(\vec{r}, T)/n_{\mathrm{Rb}}(\vec{r}, T)$ generally describes the interaction energy of ^{87}Rb and ^{174}Yb atoms at a given temperature T. It can be extracted from the present data by dividing fitted values of U_0 by the corresponding measured ^{87}Rb peak density n_{Rb}. Figure 8.14 combines results for $\tilde{U}$ from different experimental series as a function of the mean temperature of the respective series. Data points labeled as (2) and (4) originate from ^{87}Rb density tests according to method b) described in Sec. 8.3.1 with fixed final 1064 nm ODT beam powers $P_{1064} = 126\,\mathrm{mW}$ and $P_{1064} = 143\,\mathrm{mW}$. Lower mean temperatures in (2) compared to (4) are connected to the smaller ^{87}Rb temperature increase during the 1064 nm ODT power ramp up. The results (1) are based on ^{87}Rb atom number series using pure optical potentials without the MT potential (see Sec. 8.3.3). Finally the blue data point (3) combines results from density tests according to method

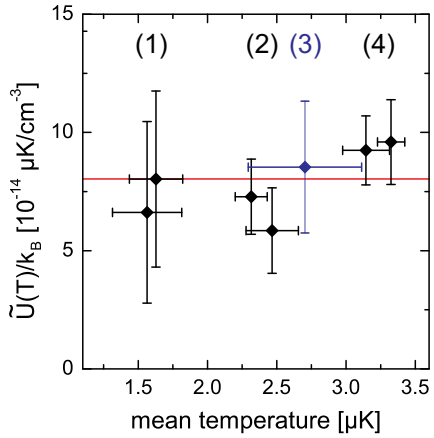

Figure 8.14: *Combined results for $\tilde{U}(T)$ depending on the mean temperature of the corresponding series. See text for details.*

b) described in Sec. 8.3.1 for $P_{1064} > 115\,\mathrm{mW}$. Data point (3), originating from the series, where the 1064 nm ODT power is altered, has a larger error bar in the x-direction, due to the temperature variation within this data set.

In general, the error bars of the individual results take into account fitting errors of individual data points and the statistical spread of data points within the respective measurement series. In order to compare the relative results from the individual series, the systematic error of the absolute ^{87}Rb density is not included in the data points shown in Fig. 8.14.

As results from data sets with different temperature overlap within their error bars, they have been combined to give a single mean value of the interaction parameter $\tilde{U}(T)$. Indicated by the red line in Fig. 8.14, the weighted mean of the results presented here is $\langle\tilde{U}(T)\rangle = 8.06 \times 10^{-14}\,\mu\mathrm{K/cm^{-3}}$. Taking the large error of $^{+85\%}_{-61\%}$ of n_{Rb} into account, the normalized interaction parameter results in

$$\langle\tilde{\mathbf{U}}(\mathbf{T})\rangle = (\mathbf{8.06}\ ^{\mathbf{+12.7}}_{\mathbf{-4.06}}) \times \mathbf{10^{-14}}\,\boldsymbol{\mu}\mathbf{K/cm^{-3}}$$

for the given temperature range of $T = 1.5 \ldots 3.5\,\mu\mathrm{K}$.

Note that a total number of 80 single measurements from 6 series according to method a) in Sec. 8.3.1 and 6 series according to method b) contribute to this result. The fact that measurements performed with different experimental parameters yield consistent results, indicates that the underlying model potentials used for the extraction of this data describe the experimental situation correctly.

8.3.5 ^{87}Rb in the $F = 2$ spin state

Another way to learn more about the nature of the strong interaction between ^{87}Rb and ^{174}Yb is to change the hyperfine state occupied by the ^{87}Rb atoms. Besides the $|5^2\mathrm{S}_{1/2}, F = 1, m_F = -1\rangle$ state, which is used in the majority of experiments presented here, the $|5^2\mathrm{S}_{1/2}, F = 2, m_F = 2\rangle$ state is also a low field seeking and hence magnetically trappable state for ^{87}Rb atoms (see Sec. 3.2.1). Figure 8.15 illustrates ground state potentials of YbRb molecules involving the ^{87}Rb ground state hyperfine splitting. Comparing interac-

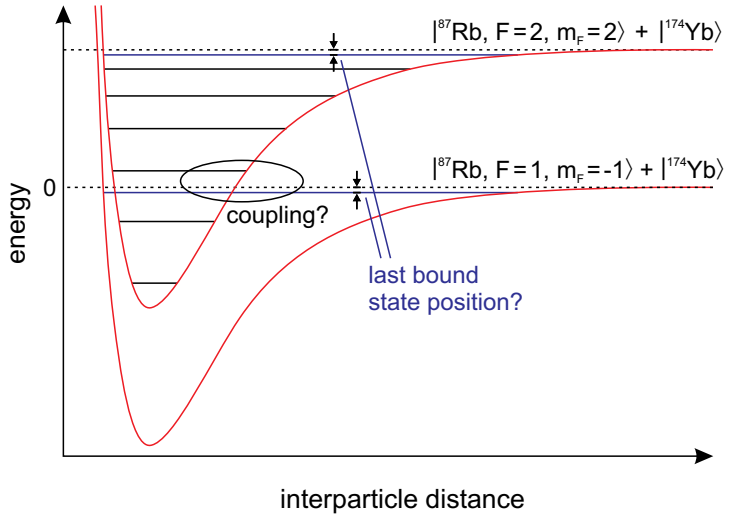

Figure 8.15: *Basic diagram of YbRb molecular ground state potentials. In this first order approximation, the ^{87}Rb ground state hyperfine splitting translates in a simple energy shift of the molecular potential without changing its shape. Feshbach resonances are only possible in the lower hyperfine state. Only atoms in this state could resonantly couple to a closed bound level belonging to an energetically higher molecular potential. If no Feshbach resonances are involved, interaction properties are determined by the energy position of the molecular bound state closest to the dissociation limit. This parameter itself depends on the potential characteristics, which can be probed by phase separation measurements using different ^{87}Rb hyperfine levels.*

tion properties of ^{87}Rb and ^{174}Yb using different ^{87}Rb hyperfine states probes two effects: First, the involvement of a Feshbach resonance in the interspecies interaction is tested, as it is only possible in the lower $|F = 1, m_F = -1\rangle$ hyperfine state[3]. Second, information obtained by these experiments allows conclusions on the relative form of the molecular potentials, which are distinguished by the ^{87}Rb hyperfine level. A first order approximation, as illustrated in Fig. 8.15 assumes, that the molecular potential connected to the ^{87}Rb $|F = 2, m_F = 2\rangle$ state is simply shifted in energy by the amount of the atomic ^{87}Rb hyperfine splitting with respect to the $|F = 1, m_F = -1\rangle$ potential. However, higher order effects like coupling to excited state potentials could slightly change the potential. In this case, the relative energetic position of the last molecular bound state with the dissociation limit, could be different, leading to a dramatic change in the ^{87}Rb-^{174}Yb interaction properties.

Experimentally, ^{87}Rb atoms are prepared in the $|F = 2, m_F = 2\rangle$ state by turning on the repumper 2 laser for 50 μs during the MT loading phase (see Sec. 5.3 for details on the ^{87}Rb preparation process). As this light is resonant with the $|F = 2\rangle \rightarrow |F' = 3\rangle$ transition of the D2 line, it optically pumps the ^{87}Rb atoms into the desired state. The

[3]In the system YbRb, Feshbach resonances are generally suppressed, as the lowest order coupling mechanism requires a selection rule $\Delta m_F = 0$ between the entry channel and the closed channel. Due to the absence of magnetic moment in (bosonic) Yb in the ground state, this condition can not be fulfilled.

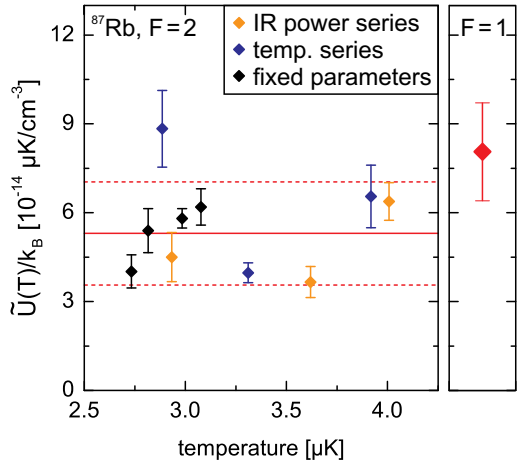

Figure 8.16: *Extracted normalized interaction parameters depending on the corresponding measured temperature. The weighted mean (red line) and standard deviation (dashed res lines) of all data points as well as the combined results of all experiments using ^{87}Rb in the $|F = 1, m_F = -1\rangle$ state is shown.*

correct m_F-sublevel is preferentially populated using a defined circular light polarization with respect to the magnetic field direction. This parameter is optimized experimentally in order to obtain the maximum ^{87}Rb atom number in the MT. Nonetheless, the resulting ^{87}Rb atom number in the $|F = 2, m_F = 2\rangle$ state is a factor of ≈ 2 smaller compared to corresponding $|F = 1, m_F = -1\rangle$ state experiments.

We performed different series of phase separation measurements with varied 1064 nm ODT powers and ^{87}Rb temperatures using ^{87}Rb in the $|F = 2, m_F = 2\rangle$ state. Phase separation of ^{87}Rb and ^{174}Yb is clearly observed. The quantitative data analysis takes into account the different magnetic potential, which especially in the axial direction leads to significantly higher confinement of the ^{87}Rb cloud. Figure 8.16 presents combined results of extracted normalized interaction parameters $\tilde{U}(T)$ using $|F = 2, m_F = 2\rangle$ state ^{87}Rb atoms. The data covers a temperature range of $2.7 \ldots 4\,\mu$K, arising from varied optical potential parameters or final RF levels during the individual measurements. The weighted mean value of these results including their standard deviation overlaps with the combined results of measurements with ^{87}Rb in the $|F = 1, m_F = -1\rangle$ state.

Hence, our experimental results indicate that the adiabatic potentials for $^{87}\mathrm{Rb}_{F=1}{}^{174}$Yb and $^{87}\mathrm{Rb}_{F=2}{}^{174}$Yb are identical. The assumption, that both molecular potentials are simply shifted in energy by the amount of the atomic ^{87}Rb ground state hyperfine splitting seems correct. In addition, it can be ruled out, that Feshbach resonances play an important role for the observed extraordinarily strong interaction.

8.3.6 Different Yb isotopes

The interaction properties of ^{87}Rb and Yb strongly depend on the respective Yb isotope, which is experimentally demonstrated in thermalization measurements of both species (see Sec. 7.2 and [9]). This behavior is attributed to mass-dependent changes in the $^{x}\mathrm{Yb}^{87}$Rb ground state molecular potential and hence the energetic position of its last bound state.

As indicated by thermalization measurements in the temperature range below $10\,\mu$K, the interaction between ^{174}Yb and ^{87}Rb is exceptionally large compared to all other trappable

Yb isotopes. As a result, the effect of phase separation of the two species is only observed with ^{174}Yb. Experiments performed at conditions resulting in phase separation of ^{174}Yb and ^{87}Rb do not show any sign of phase separation when the isotopes ^{172}Yb, ^{173}Yb and ^{176}Yb are used. The isotopes ^{170}Yb and ^{171}Yb are not explicitly tested under phase separation conditions, as thermalization measurements with ^{87}Rb already demonstrate negligibly small interaction between these species and ^{87}Rb (see Sec. 7.2). Figure 8.17 compares ^{173}Yb and ^{174}Yb intratrap images resulting from identical experimental conditions. This

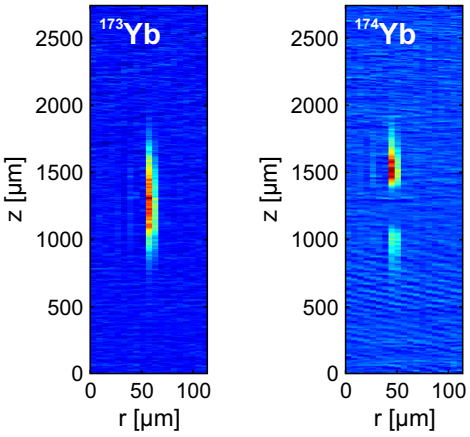

Figure 8.17: *False color intratrap images of ^{173}Yb and ^{174}Yb clouds under identical experimental conditions: BIODT beam powers $P_{532} = 343\,mW$ and $P_{1064} = 143\,mW$; ^{87}Rb atom number $N_{\mathrm{Rb}} \approx 9 \times 10^6$; ^{87}Rb temperature $T_{\mathrm{Rb}} = T_{\mathrm{Yb}} \equiv T \approx 3.3\,\mu K$.*

data is taken as an example for the described situation and is representative for all other Yb isotopes used in the present experiments.

8.4 Theoretical interpretation of ^{174}Yb - ^{87}Rb phase separation

8.4.1 "Naive" mean field approach

A basic zero order approach to infer a fundamental scattering parameter from the observed interaction potential is to apply the standard mean-field s-wave interaction potential (Eq. 2.48):

$$U_{\mathrm{YbRb}}(\vec{r},T) = n_{\mathrm{Rb}}(\vec{r}) \cdot \tilde{U}(T) = n_{\mathrm{Rb}}(\vec{r},T) \cdot \frac{4\pi\hbar^2 a}{2m_r}\,. \tag{8.16}$$

The interspecies scattering length a can directly be obtained using the combined result for the normalized interaction parameter $\langle\tilde{U}(T)\rangle = (8.06\ ^{+12.7}_{-4.06}) \times 10^{-14}\,\mu K/cm^{-3}$, given above. The temperature independent mean field approach (8.16) leads to the enormous s-wave scattering length of

$$\mathbf{a} \;=\; (\,\mathbf{29100}\ ^{\mathbf{+45800}}_{\mathbf{-14500}}\,)\ \mathbf{a_0}\,,$$

where a_0 is the Bohr radius.

Temperature dependence – thermal averaging

So far, the interpretation of the observed phase separation between ^{147}Yb and ^{87}Rb assumes a temperature independent interaction potential. Following a more careful treatment (e.g. according to [143]), the scattering length a in Eq. 8.16 is replaced by the energy dependent effective range expansion (see Sec. 2.3)

$$\frac{1}{a_E(k)} \approx -\frac{1}{a} + \frac{1}{2} r_{\text{eff}} k^2 \qquad \Longleftrightarrow \qquad a_E(k) = \frac{a}{1 - \frac{1}{2} k^2 r_{\text{eff}} a} \tag{8.17}$$

The effective range parameter r_{eff} depends on a and can be obtained using Eq. 2.43. In the system of ^{174}Yb and ^{87}Rb, $r_{\text{eff}} \approx 218\,\text{a}_0$ for $a \to \infty$. Assuming $T_{\text{Yb}} = T_{\text{Rb}} \equiv T$, the relative wave vector k is connected to the temperature T via $E = k_{\text{B}}T = \hbar^2 k^2/(2m_r)$.

Thus, the interaction potential becomes energy dependent:

$$U_{\text{YbRb}}(\vec{r}, E) = n_{\text{Rb}}(\vec{r}) \cdot \frac{4\pi\hbar^2 a_E(E)}{2m_r} = n_{\text{Rb}}(\vec{r}) \cdot \frac{4\pi\hbar^2}{2m_r} \frac{a}{1 - \frac{m_r E}{\hbar^2} r_{\text{eff}} a} \,. \tag{8.18}$$

The mean interaction between the atomic clouds of ^{174}Yb and ^{87}Rb is obtained by averaging over all present relative collision energies E [15]. The thermal energy distribution at a defined temperature T is given by the Maxwell-Boltzmann distribution [67]

$$f(E,T)\,\mathrm{d}E = \frac{2}{\sqrt{\pi (k_{\text{B}}T)^3}} \sqrt{E}\, e^{-\frac{E}{k_{\text{B}}T}}\,\mathrm{d}E \,. \tag{8.19}$$

Hence, the mean effective scattering length and the corresponding mean interaction potential are determined by the following integral:

$$\langle a_E \rangle(T) = \frac{2}{\sqrt{\pi (k_{\text{B}}T)^3}} \int_0^\infty \sqrt{E}\, e^{-\frac{E}{k_{\text{B}}T}} \cdot \frac{a}{1 - \frac{m_r E}{\hbar^2} r_{\text{eff}} a}\,\mathrm{d}E \qquad \text{and} \tag{8.20}$$

$$\langle U_{\text{YbRb}} \rangle(\vec{r}, T) = n_{\text{Rb}}(\vec{r}) \cdot \frac{4\pi\hbar^2 \langle a_E \rangle(T)}{2m_r} \tag{8.21}$$

Note that this approach assumes that collisions with all possible relative particle energies contribute to the effective potential. The integral (8.20) must be taken as a principal part in order to properly treat the singularity at $E = \hbar^2/(r_{\text{eff}} a\, m_r)$. Furthermore, at temperatures $T \lesssim 0.5\,\mu\text{K}$, the thermal distribution (8.19) is inappropriate, as the ^{87}Rb atoms will be Bose condensed in this temperature regime.

Figure 8.18 (a) shows the temperature dependence of $a_E(k_{\text{B}}T)$ and (b) of the effective scattering length $\langle a_E \rangle(T)$ for different values of the zero energy limit a. The most prominent feature of $a_E(k_{\text{B}}T)$ is the singularity at $E = k_{\text{B}}T\hbar^2/(r_{\text{eff}} a\, m_r)$, where the scattering length changes sign. The larger the scattering length a, the closer this divergence moves toward zero energy. Note, that in general, the effective range theory underlying these calculations works very well at large scattering length, even across the divergence (see Sec. 2.3). The result from this temperature dependence of $a_E(k_{\text{B}}T)$ is, that at finite temperature, the averaged effective scattering length $\langle a_E \rangle(T)$ includes a significant contribution from negative scattering lengths. Depending on the zero energy scattering length

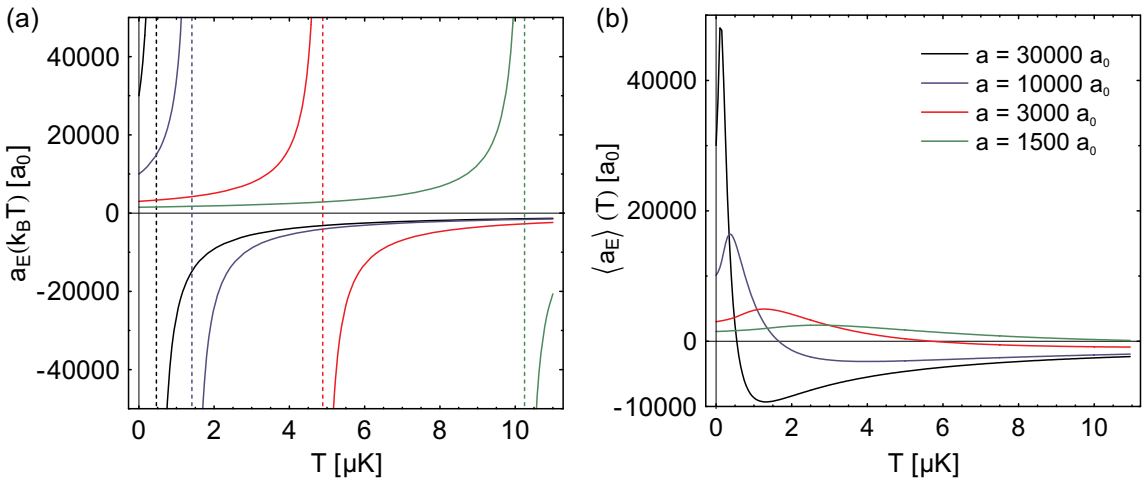

Figure 8.18: *(a) Calculated temperature dependence of $a_E(k_BT)$ according to Eq. 8.17 for the system of ^{174}Yb and ^{87}Rb and different zero energy scattering lengths a. (b) Averaged mean effective scattering length $\langle a_E \rangle(T)$ (Eq. 8.20) as a function of the atomic sample temperature $T_{Yb} = T_{Rb} \equiv T$ assuming corresponding values for a.*

a, the mean effective interaction even changes from being repulsive ($\langle a_E \rangle > 0$) to being attractive ($\langle a_E \rangle > 0$) as the temperature T increases.

In the temperature regime $T = 2 \ldots 6\,\mu$K, we observe phase separation of ^{174}Yb and ^{87}Rb, which can be attributed to a repulsive interaction potential. As described above, the quantitative analysis of this data based on the mean field approach, yields a corresponding mean averaged scattering length $\langle a_E \rangle = (29100\ ^{+45800}_{-14500})\ a_0$. However, Fig. 8.18 (b) clearly shows, that no zero energy scattering length a can be found, which is consistent with this result: Experimental observations indicate a strong and temperature independent repulsive interaction in the range of $2 \ldots 6\,\mu$K. Qualitatively, this only occurs for $a < 1500\ a_0$. However, assuming such a value for a, $\langle a_E \rangle$ would have to be $1000\ a_0 \ldots 2500\ a_0$ in the relevant temperature regime, disagreeing by a factor of ≈ 20 with experimental results.

The discrepancy between observations and this theoretical model can be related to the following issues:

- **Experimental issues:** Large values for the interaction potential underlying the phase separation of ^{174}Yb and ^{87}Rb could be attributed to an underestimation of the ^{87}Rb density. In contrast to the reliable and accurate temperature measurement, this quantity is generally more difficult to determine (see Sec. 8.2.1). Furthermore, the effect of strong ^{174}Yb loss present in the phase separation experiments could also lead to an overestimation of the repulsive interaction potential. These topics are discussed in the following Sec. 8.4.2.
- **Theoretical issues:** Under the assumption of an evidently large ^{174}Yb - ^{87}Rb interspecies scattering length a, the basic model based on mean field theory and effective scattering length is questionable. Based on a simple comparison of relevant length scales, Sec. 8.5 discusses the applicability of the standard mean field approach and

introduces a higher order correction. However, a complete theoretical description of the present observations goes beyond the scope of this thesis.

8.4.2 Experimental considerations

a) ^{87}Rb density determination

The correct determination of the ^{87}Rb density plays an important role for the interpretation of the observed phase separation effect between ^{174}Yb and ^{87}Rb, as this parameter directly enters the mean field interaction potential (see Eq. 8.16). Error bars for this quantity, which is calculated using measured ^{87}Rb atom numbers and the respective model potentials are generally large: detailed considerations described in Sec. 8.2.1 result in final relative error bars of $^{+85\%}_{-61\%}$ for n_{Rb}.

The following approach independently provides an upper limit for the ^{87}Rb density at the present experiments: The line of argument is based on the fact, that all phase separation experiments are performed with *thermal* ^{87}Rb clouds. Indeed, quantum degeneracy of ^{87}Rb in the described experiments can be ruled out experimentally. In general, the regime of quantum degeneracy is reached, when the mean thermal de Broglie wavelength, $\lambda_{\mathrm{dB}} = h/\sqrt{2\pi m\, k_{\mathrm{B}}\, T}$ approaches the mean inter atomic distance $d = n^{-1/3}$. Quantitatively, the BEC transition temperature T_c is given by [62]

$$n\,\lambda_{\mathrm{dB}}^3 = \zeta\left(\frac{3}{2}\right) \qquad \Longleftrightarrow \qquad k_{\mathrm{B}} T_c \approx 3.31\,\frac{\hbar^2 n^{2/3}}{m}\,. \tag{8.22}$$

Here, $\zeta(x)$ is the Riemann Zeta function with $\zeta(3/2) \approx 2.612$. Figure 8.19 shows the inverse function of Eq. 8.22, i.e. the ^{87}Rb density n required for quantum degeneracy as a function of the temperature, together with measured peak densities at different phase separation experiments. ^{87}Rb densities above the blue line lead to the formation of a BEC, while below this line, the cloud is in the thermal regime.

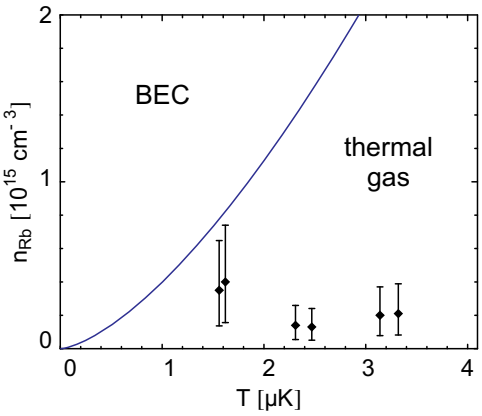

Figure 8.19: *Calculated temperature dependence of critical ^{87}Rb density necessary for quantum degeneracy together with measured ^{87}Rb densities.*

The measurement performed at the lowest temperature of $\approx 1.6\,\mu$K exhibit ^{87}Rb densities, which are only a factor of ≈ 2 below quantum degeneracy. Hence, an underestimation

of the ^{87}Rb density by more than a factor of ≈ 2 in the data analysis of phase separation experiments is impossible, as all observed ^{87}Rb clouds clearly show pure thermal characteristics.

In summary, for the case that the standard ^{87}Rb density determination method fails on a level beyond the obtained error bars, these considerations provide a hard limit for the maximum possible ^{87}Rb density. Consequently, the lower limit for the interaction parameter is results in $\tilde{U}_m in = 3.7 \times 10^{-14}\,\mu K/cm^{-3}$.

b) ^{174}Yb atom loss

As described in Sec. 8.1, the observed effect of phase separation is accompanied with ^{174}Yb atom loss, which is related to inelastic three-body collisions with ^{87}Rb due to the strong interspecies interaction (see Sec. 2.6). The measured ^{174}Yb atom loss 1/e-time-constant is ≈ 210 ms for typical ^{87}Rb peak densities of $\approx 3 \times 10^{14}$ cm^{-3}.

In principle, large interspecies losses could also lead to a spatial atom distribution which is very similar to the one observed in the present experiments. The reduction of the ^{174}Yb density at the position of maximum ^{87}Rb density (see Fig. 8.1 (c)) could result from the local removal of ^{174}Yb atoms in the trap center by inelastic collisions with ^{87}Rb. The following section discusses the possibility of loss-induced separation of the two clouds taking into account different experimental consideration.

^{174}Yb Loss rate at phase separation conditions The measured loss rate under phase separation conditions is characterized by a 1/e-time-constant of ≈ 210 ms.

In the case of pure loss-induced separation, however, all ^{174}Yb atoms would be lost after less than half an oscillation period of the atoms in this trap (at least under experimental conditions, where the ^{174}Yb density drops to almost zero at the location of the ^{87}Rb cloud). At a measured axial trap frequency of $\omega_z/2\pi = \nu_z \approx 10.5$ Hz, this time span is below 50 ms, contradicting the data presented above, where phase separation is still clearly observed after a holding time of up to 500 ms (see Fig. 8.4). Hence, pure loss-induced separation of the two clouds is not compatible with our observations.

Assuming a repulsive potential with magnitude U_0 for ^{174}Yb in the trap center, caused by the presence of ^{87}Rb atoms, the total radial potential for ^{174}Yb has the form of a double well potential. Even for small values of U_0, the axial trap frequency in each of the wells is larger than ν_z for $U_0 = 0$, which is illustrated in Fig. 8.20. Note that for $U_0/kB < 2\,\mu$K, no clear double well exists, hence a description by trap frequencies in the individual wells fails. In this case, the system is defined by the optical trapping potentials and their respective trap frequencies.

This additional discussion shows, that the original considerations comparing loss time constants and trap frequencies are still valid for the case of an additional repulsive interaction potential.

^{174}Yb loss rate at lower ^{87}Rb densities Experiments performed in order to adjust the optimum BIODT power ratio for thermalization of both species also exhibit strong ^{174}Yb

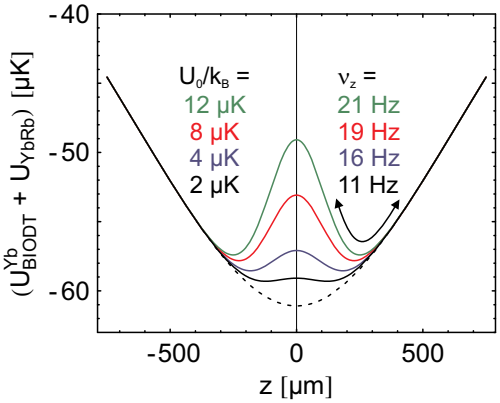

Figure 8.20: *Calculated trap frequencies in each well of the double well potential for ^{174}Yb, which is created by an additional repulsive part in the trap center with magnitude U_0.*

atom loss, when the ^{87}Rb density is increased (see Fig. 7.1 in Sec. 7.1.2). As already mentioned, these losses can be attributed to inelastic three-body collisions involving either one ^{174}Yb and two ^{87}Rb atoms or collisions with one ^{87}Rb and two ^{174}Yb atoms. The rate coefficients for these two processes, α_1 and α_2, can in general be different, with one process dominating over the other. The event rate for an ^{174}Yb atom to be involved in a three body event, is therefore given by

$$L_{\mathrm{Yb}} = 2n_{\mathrm{Rb}}n_{\mathrm{Yb}}\alpha_1 + n_{\mathrm{Rb}}^2\alpha_2 = n_{\mathrm{Rb}}(2n_{\mathrm{Yb}}\alpha_1 + n_{\mathrm{Rb}}\alpha_2)\,. \tag{8.23}$$

The factor of 2 in the first term is related to the loss of 2 ^{174}Yb atoms caused by an Yb-Yb-Rb event. Assuming the rate coefficients α_1 and α_2 to be in the same range, the dominating process is governed by the density ratio of the two species.

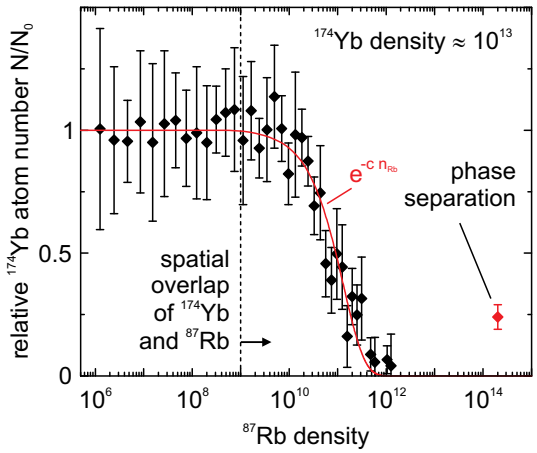

Figure 8.21: *^{174}Yb atom number as a function of the ^{87}Rb density after a fixed contact time $t_{\mathrm{contact}} = 300\,ms$.If phase separation is observed, the ^{174}Yb atom loss is greatly suppressed, as the spacial overlap of the atom clouds is reduced.*

Figure 8.21 shows ^{174}Yb atom loss N/N_0 in thermalization experiments, measured after a fixed contact time $t_{\mathrm{contact}} = 300\,\mathrm{ms}$ as a function of the calculated ^{87}Rb density n_{Rb} in the trap center. The assumption $T_{\mathrm{Yb}} = T_{\mathrm{Rb}}$ is valid for $n_{\mathrm{Rb}} > 10^9 \ldots 10^{10}\,\mathrm{cm}^{-3}$. The temperature increases from $\approx 1.1\,\mu$K at $n_{\mathrm{Rb}} = 10^{10}\,\mathrm{cm}^{-3}$ to $\approx 1.5\,\mu$K at $n_{\mathrm{Rb}} = 10^{12}\,\mathrm{cm}^{-3}$. In this range, the corresponding ^{174}Yb density $n_{\mathrm{Yb}} \approx 10^{13}\,\mathrm{cm}^{-3}$ is slightly decreasing as the temperature changes. In the regime of thermalization experiments, $n_{\mathrm{Yb}} > n_{\mathrm{Rb}}$, hence

for comparable loss coefficients and under the rough approximation of constant ^{174}Yb density, Eq. 8.23 yields a linear dependence on the ^{87}Rb density: $L_{\mathrm{Yb}} \approx 2 n_{\mathrm{Yb}} n_{\mathrm{Rb}} \alpha_1$. The red line represents a fit to the data according to $N/N_0 = \exp(-c\, n_{\mathrm{Rb}})$, where c is the only fitting parameter. This yields an approximate value for the rate coefficients $\alpha_1 = c/(2\, t_{\mathrm{contact}}\, n_{\mathrm{Yb}}) \approx 1 \times 10^{-24}\,\mathrm{cm^6/s}$. Using Eq. 2.52 with the constant $C = 1$, the interspecies scattering length $|a|$ at $T \approx 1.5\,\mu$K, related to the observed three-body loss rate α_1 results in

$$|a| \approx \left(\frac{\alpha_1 m_r}{C\hbar}\right)^{\frac{1}{4}} \approx 3500\,\mathrm{a_0}\,. \tag{8.24}$$

Note that this rough approximation gives lower limits for α_1 and $|a|$ as it neglects the reduced densities of both species outside the trap center.

Phase separation experiments are performed at ^{87}Rb densities, which are $2 \ldots 3$ orders of magnitude larger than ^{87}Rb densities during thermalization measurements. Still assuming a loss rate $\propto \alpha_1 n_{\mathrm{Rb}}$, the 1/e-time-constant for ^{174}Yb atom loss would be in the range of $\tau \approx 2\,$ms. Hence all atoms would be lost after the same contact time $t_{\mathrm{contact}} = 300\,$ms. In this regime, $n_{\mathrm{Rb}} > n_{\mathrm{Yb}}$, which increases the second term in Eq. 8.23, enhancing the loss rate even more. The measured atom loss time constant at phase separation conditions, however, $\tau \approx 210\,$ms, yields remaining ^{174}Yb atoms $N(t = 300\,\mathrm{ms})/N_0 \approx 0.24$, which is included in Fig 8.21. This result clearly states, that the observed phase separation is not dominantly loss-induced. On the contrary, ^{174}Yb atom loss is greatly suppressed, as the overlap between both atom clouds is reduced due to the repulsive interspecies interaction potential leading to phase separation.

Radial distortion in ^{174}Yb clouds Another indication, that the interaction between ^{87}Rb and ^{174}Yb involves a repulsive potential, comes from experiments performed with radially misaligned BIODT beams. According to Sec. 7.1.2, the relative BIODT beam alignment dr is experimentally adjusted to achieve the lowest ^{87}Rb and ^{174}Yb temperatures and maximum ^{87}Rb atom numbers after both species are brought into contact for a thermalization time of 300 ms. Figure 8.22 (a) shows false color images of ^{176}Yb after a fixed TOF $t_{\mathrm{TOF}} = 3.5\,$ms as a function of the relative radial beam displacement dr. A clear temperature minimum, indicated by the tightest cloud distribution can be detected for perfect beam alignment. An identical experimental series using ^{174}Yb is presented in Fig. 8.22 (b). In addition to the expected temperature dependence, the ^{174}Yb density distributions exhibit a non-Gaussian, "banana-shaped" characteristic, depending on dr. This behavior can be attributed to the presence of ^{87}Rb, which is respectively located at the inside position of the bent ^{174}Yb cloud. After simultaneously switching off all potentials before the TOF, the ballistic ^{174}Yb cloud expansion is distorted by the repulsive force from the ^{87}Rb atoms, leading to the observed density distributions. These observations verify the presence of a repulsive interaction potential, as they could not be explained by three-body loss processes.

Summary The different experimental observations discussed above doubtlessly verify that phase separation of ^{174}Yb and ^{87}Rb is dominantly resulting from a repulsive interaction

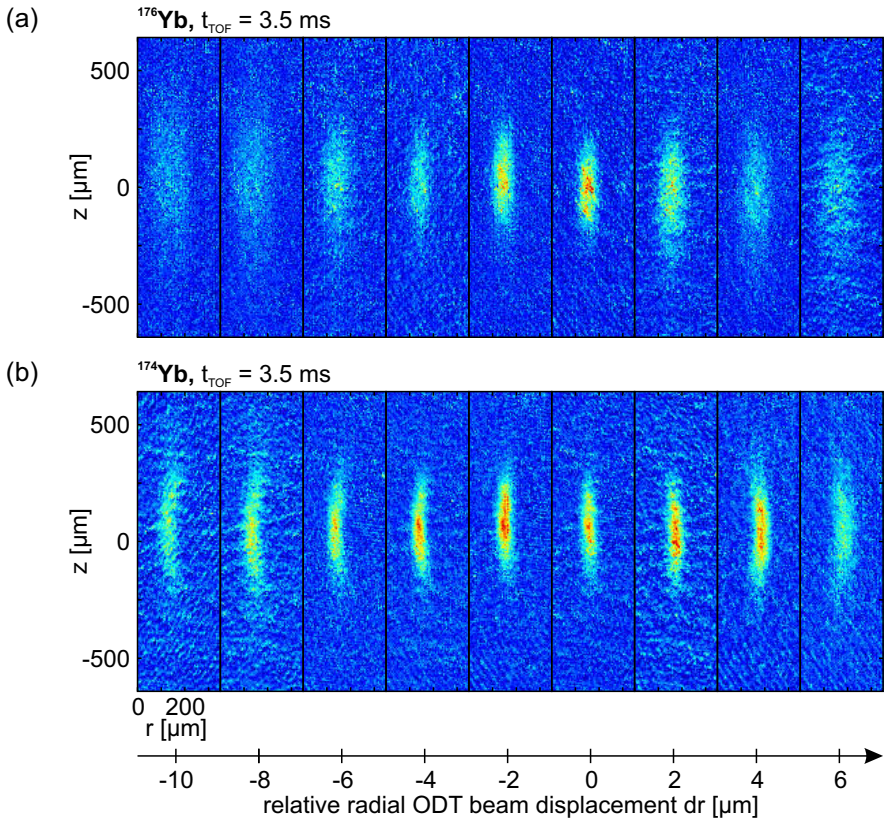

Figure 8.22: *Comparison of false color (a) ^{176}Yb and (b) ^{174}Yb images after thermalization depending on the relative radial beam displacement. The ^{174}Yb clouds for $|dr| \geq 2 \ldots 4\,\mu m$ clearly show distortions attributed to repulsive interactions with the present ^{87}Rb atoms.*

potential between the two species. Still, the effect of ^{174}Yb loss contributing to the observed spatial density distributions is hard to quantify and may lead to an overestimation of the normalized interaction parameter $\tilde{U}(T)$ extracted from this data.

8.5 Corrections to the mean field theory

8.5.1 Comparison of relevant length scales

As discussed in Sec. 2.4, the mean field theory describes the collective behavior of gases in the ultracold, dilute regime. It is based on the assumption, that the interparticle separation $d = 1/n^3$ is much larger than the range of interatomic forces: In this regime, the effective interaction between particles is dominated by two body s-wave scattering. Here, the scattering length a defines the low energy scattering cross section $\sigma_0 = 4\pi a^2$ (see Sec. 2.1.4), which determines the range of interparticle interaction. Hence, the condition for the mean field description of a gaseous system is

$$n|a|^3 \ll 1 \qquad \Longleftrightarrow \qquad |a| \ll d \tag{8.25}$$

Table 8.2 shows relevant length scales for our experiments, where phase separation between ^{174}Yb and ^{87}Rb was observed. Note, that the relative de Broglie wavelength $\lambda_{\mathrm{dB,r}} = h/\sqrt{2\pi m_r k_\mathrm{B} T}$ is related to the center of mass system describing a ^{174}Yb-^{87}Rb collision with reduced mass $m_r = \frac{m_\mathrm{Yb} m_\mathrm{Rb}}{m_\mathrm{Yb}+m_\mathrm{Rb}}$. The interspecies scattering length a is calculated from results of phase separation measurements on the basis of the temperature independent mean field approach described in Sec. 8.4.1.

relative interspecies de Broglie wavelength ($T_\mathrm{Rb} = T_\mathrm{Yb} \approx 3\,\mu$K)	$\lambda_{\mathrm{dB,r}}$	≈ 2400
^{87}Rb atom-atom distance (for $n_\mathrm{Rb} = (2.0\,^{+1.7}_{-1.2}) \times 10^{14}\,\mathrm{cm}^{-3}$)	$d_\mathrm{Rb} = n_\mathrm{Rb}^{-1/3}$	$3200\,^{+1200}_{-600}$
interspecies scattering length according to Eq. 8.16	a	$29100\,^{+45800}_{-14500}$

Table 8.2: *Characteristic length scales for the typical phase separation measurement conditions. All parameters are given in atomic units.*

The comparison of length scales shows, that the assumption (Eq. 8.25) is clearly violated, since $a \gg d_\mathrm{Rb}$, if we assume the results from the mean field theory (Eq. 8.16) to be correct. In this regime, the basic mean field theory becomes invalid, as higher order effects, like three body (and ultimately n-body) collisions significantly contribute to the effective interaction.

8.5.2 The LHY correction

Lee, Huang and Yang. [144] have first investigated corrections to the mean field theory for larger values of na^3. Their calculation is related to the ground state energy of a Bose gas consisting of N particles. This approach uses hard sphere interactions between the atoms where the s-wave scattering length a equals the hard sphere radius[4]. The correction term, which is denoted as the *LHY*-term, is the first order in a power series expansion of the parameter $\sqrt{na^3}$:

$$\frac{E_0}{N} = \frac{4\pi\hbar^2 na}{m}\left[1 + \frac{128}{15\sqrt{\pi}}\sqrt{na^3} + \mathcal{O}(na^3)\right] \tag{8.26}$$

Without the correction, Eq. 8.26 reproduces the standard mean field energy. From a physical point of view, the additional average particle energy is related to *quantum depletion* of the Bose gas: This is the fraction of the many-body wave function which cannot be represented by the macroscopic single particle wave function. In a homogeneous BEC, it consists of admixtures of higher momentum states into the ground state of the system. Quantum depletion is related to strong interactions and has been observed with a BEC of Na atoms [145]. Beyond mean field effects connected to the LHY-correction also alter the compressibility of strongly interacting Bose gases [146]. Higher order terms, which add

[4] This implies $a > 0$.

to the series in Eq. 8.26, are attributed to three-body (and higher order) collision pseudo potentials and depend on the respective interatomic potential [147].

The additional energy E_{LHY} related to the LHY term in Eq. 8.26 becomes significant as the scattering length a becomes comparable to the mean interatomic separation $d = 1/n^3$, which is shown in Fig. 8.23. Although this regime strictly speaking violates the assumptions

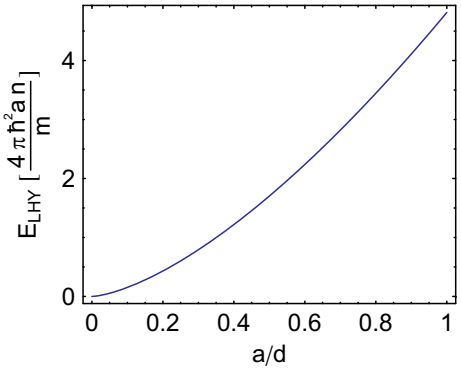

Figure 8.23: *Calculated additional energy E_{LHY} related to the LHY term in Eq. 8.26 given in units of the mean field energy $4\pi\hbar^2 na/m$ as a function of on the ratio between the scattering length a and the mean interatomic distance $d = 1/n^3$.*

underlying the mean field description, in the case of the energy per particle, the universal LHY term in Eq. 8.26 correctly reproduces results from a diffuse Monte Carlo simulation on the BEC ground state energy up to $d/a \approx 0.6$ [148]. The work of Braaten et al. [149] extends beyond-mean-field corrections based on the power series in Eq. 8.26 to various properties of the Bose gas: For example, the interaction energy becomes:

$$U = \frac{4\pi\hbar^2 na}{m}\left[1 + \frac{128}{15\sqrt{\pi}}\sqrt{na^3} + \mathcal{O}(na^3)\right] = E_0 + E_{\mathrm{LHY}} + \mathcal{O}(na^3) \tag{8.27}$$

Inclusion in the present data analysis

Fitting process Data analysis from phase separation measurements as described in Sec. 8.2, is based on the basic assumption of an interaction potential, which is directly proportional to the ^{87}Rb density n_{Rb}.

An inclusion of the LHY-correction, alters the form of the interaction potential $U_{\mathrm{YbRb}}(\vec{r}, T)$ involved in the fitting function according to

$$U_{\mathrm{YbRb,LHY}}(\vec{r}, T) = \frac{4\pi\hbar^2 a\, n_{\mathrm{Rb}}(\vec{r}, T)}{2m_r}\left[1 + \frac{128}{15\sqrt{\pi}}a^{3/2}\left(n_{\mathrm{Rb}}(\vec{r}, T)\right)^{1/2}\right] \tag{8.28}$$

As the ^{87}Rb density distribution is approximated by a Gaussian with radial width σ_z (see Sec. 8.2.1), the altered interaction potential is qualitatively given by

$$U_{\mathrm{YbRb,LHY}}(r = 0, z) \propto c_1 \exp\left(-\frac{z^2}{2\sigma_z^2}\right) + c_2 \exp\left(-\frac{3}{2}\frac{z^2}{2\sigma_z^2}\right). \tag{8.29}$$

Hence, $U_{\mathrm{YbRb,LHY}}(r = 0, z)$ is simply a sum of the original function and another Gaussian shaped function with reduced width, depending on the relation between the parameters c_1

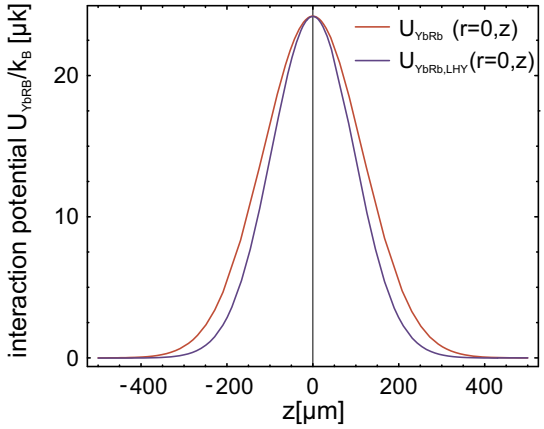

Figure 8.24: *Comparison between* $U_{\mathrm{YbRb}}(r=0,z)$ *and* $U_{\mathrm{YbRb,LHY}}(r=0,z)$ *for typical experimental parameters:* $T = 3\,\mu K$; $n_{\mathrm{Rb,max.}} = 2.5 \times 10^{14}$ cm^{-3}; *scattering lengths* a *and* a_{LHY} *are chosen to obtain equal magnitudes* U_0*:* $a = 35000$ a$_0$, $a_{\mathrm{LHY}} \approx 4700$ a$_0$.

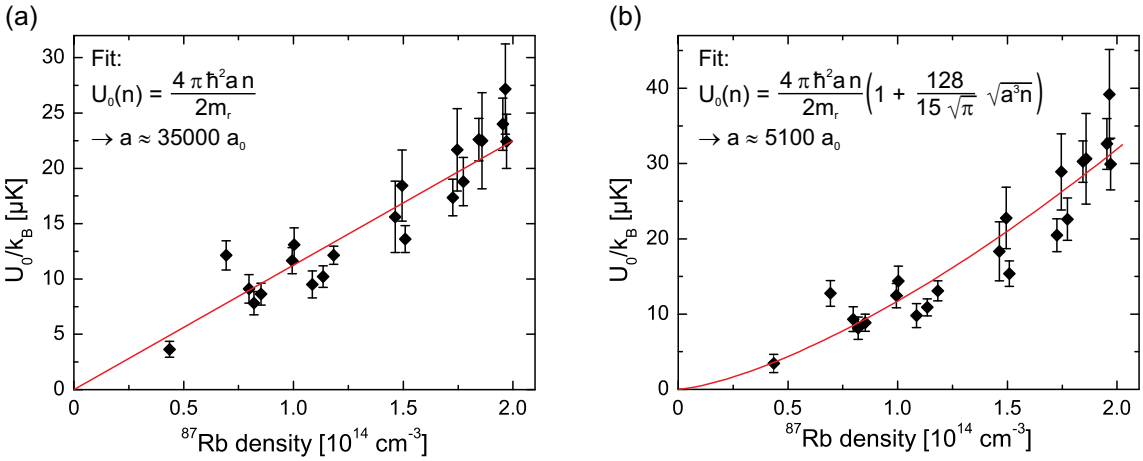

Figure 8.25: *Fitted interaction potential magnitudes* U_0 *depending on the* ^{87}Rb *density. A linear fit (a) using the standard mean field potential yields a scattering length* $a \approx 35000\,a_0$*, while the LHY correction (b) leads to* $a \approx 5100\,a_0$.

and c_2. As shown in Fig. 8.24 for our experimental parameters, the shape of $U_{\mathrm{YbRb,LHY}}(r = 0,z)$ does not significantly differ from $U_{\mathrm{YbRb}}(r=0,z)$, which is linear in $n_{\mathrm{Rb}}(\vec{r})$.

The LHY correction is included in the fitting function used to extract interaction potential magnitudes U_0. As expected from the qualitative considerations discussed above, the results at lower n_{Rb} are almost unchanged ($c_1 > c_2$ in Eq. 8.29), while at high ^{87}Rb densities, typically $20\% \ldots 30\%$ larger values for U_0 are obtained.

Quantitative results Figure 8.25 compares results for U_0 from typical experimental data with fixed temperature $T \approx 3.3\,\mu$K using (a) the standard mean field approach and (b) the nonlinear LHY correction. The red line represents a fit used to obtain the respective interspecies scattering length a, (a) without and (b) with the LHY-correction term. The large difference of extracted scattering lengths is related to the ^{87}Rb density of up to $n_{\mathrm{Rb}} = 2\times10^{14}\mathrm{cm}^{-3}$, which corresponds to a mean interatomic distance $d = 1/n^3 \approx 3200\mathrm{a}_0$.

In this parameter regime of n and a, the LHY term plays a dominating role.

The modified data analysis including the LHY-correction is applied to 6 experimental series with varied ^{87}Rb density, that are obtained according to method b) described in Sec. 8.3.1. This data includes various trapping potential parameters and temperatures $T = 1.5 \ldots 3.5\,\mu$K and represents the main contribution to the combined result for $\tilde{U}(T)$, in Sec. 8.3.4.

Results from all relevant experimental series yield consistent results within their error bars. The combined result for the interspecies scattering length in the temperature regime $T = 1.5 \ldots 3.5\,\mu$K is

$$\mathbf{a_{LHY}} \;=\; (\,\mathbf{4710}\,{}^{\mathbf{+3970}}_{\mathbf{-1520}}\,)\;\mathbf{a_0}\,.$$

This number includes fitting uncertainties as well as the large error of $^{+85\%}_{-61\%}$ for n_{Rb}, which is treated the following way: As the fitting function and hence the results for U_0 in each data point depend on the underlying ^{87}Rb density, a simple error propagation calculation is incorrect in this case. Therefore, the fitting process is repeated assuming lower and upper bounds for n_{Rb} and the individual results for a_{LHY} are treated as its uncertainty limits.

Temperature dependence and the LHY approach The original calculations underlying the LHY approach [144], assume the limit $k \to 0$, which is experimentally achieved in BEC systems. At low but nonzero temperatures, the effective range expansion can be used to describe the temperature dependence of the scattering length (see Sec. 2.3):

$$\frac{1}{a_E(k)} \approx -\frac{1}{a} + \frac{1}{2} r_{\mathrm{eff}} k^2 \qquad \Longleftrightarrow \qquad a_E(k) = \frac{a}{1 - \frac{1}{2} k^2 r_{\mathrm{eff}} a} \tag{8.30}$$

In the LHY potential, the scattering length a can not simply be replaced by its energy dependent counterpart $a_E(k)$: Assuming a positive scattering length a, $a_E(k)$ becomes negative for $k > \sqrt{1/2 r_{\mathrm{eff}} a}$ (a negative scattering length remains negative for all values of k). The LHY term, however gives imaginary results for $a < 0$. This is not surprising taking into account the assumptions underlying the LHY approach: The LHY expansion is originally based on interactions between hard spheres with radius $R_0 = a$, which intrinsically postulates $a > 0$. The LHY correction simply does not describe interactions with $a < 0$.

The publication of Fu et al. [150] presents a modified Gross-Pitaevskii (GP) equation including both quantum fluctuation (i.e. the LHY term) and temperature dependence corrections. This calculation – namely the approximation made before Eq. 10 in [150] – is valid only for $k^2 \ll 1/2 r_{\mathrm{eff}} a$. Hence, it does not extend to a region, where $a_E(k)$ becomes negative.

8.5.3 Diffusion model

In collaboration with E. Tiesinga and S. Maxwell from the atomic theory group at NIST [15], a diffusion model described in the following was developed. I takes into account the dynamics of a thermal ^{174}Yb atom in a cloud of ^{87}Rb resulting from diffusion assuming a

large elastic cross section. In connection with local three-body loss of ^{174}Yb, this approach qualitatively reproduces the ^{174}Yb density distribution experimentally observed at phase separation conditions:

While pure mean field theory does not provide a satisfactory explanation for the observed phase separation, the results do suggest that the interactions between ^{87}Rb and ^{174}Yb are strong and that the elastic cross section is large. Correspondingly, the mean free path of a thermal ^{174}Yb atom in a cloud of ^{87}Rb will be much smaller than the size of the cloud. Thus, the trapped system can be modeled using the time-dependent diffusion equation including loss due to three-body recombination. The diffusion equation is

$$\dot{n}(\vec{r},t) = -\nabla \cdot \vec{j}(\vec{r},t) - K_3 n_{\mathrm{Rb}}^2(\vec{r}) n(\vec{r},t), \tag{8.31}$$

where $n(\vec{r},t)$ is the ^{174}Yb distribution, K_3 is the three-body loss rate coefficient, $n_{\mathrm{Rb}}(\vec{r})$ is the ^{87}Rb density, which will be assumed to follow a Boltzmann distribution and is independent of time, and the current density is

$$\vec{j}(\vec{r},t) = -\frac{k_B T \tau(\vec{r})}{m} \nabla n(\vec{r},t) + \frac{\tau(\vec{r})}{m} \left(\nabla V(\vec{r})\right) n(\vec{r},t), \tag{8.32}$$

which describes diffusion and drift. Here $\tau(\vec{r})$ is the spatially dependent mean collision time and m is the ^{174}Yb mass.

The mean collision time is determined by Yb+Yb and Yb+Rb collisions and satisfies $\tau(\vec{r})^{-1} = \tau_{\mathrm{YbRb}}(\vec{r})^{-1} + \tau_{\mathrm{YbYb}}(\vec{r})^{-1}$. Here $\tau_{\mathrm{YbRb}}(\vec{r})^{-1} = \langle v_{\mathrm{rel}} \sigma_{\mathrm{YbRb}} \rangle \, n_{\mathrm{Rb}}(\vec{r})$, where σ_{YbRb} is the interspecies collision cross section, and v_{rel} is the relative velocity. The angle brackets represent a thermal average. Similarly, self-diffusion is governed by $\tau_{\mathrm{YbYb}}(\vec{r})^{-1} = \langle v_{\mathrm{rel-Yb}} \sigma_{\mathrm{YbYb}} \rangle \, n(\vec{r})$.

By looking for the solution $n(\vec{r},t) = e^{-\Gamma t} n(\vec{r})$, the diffusion equation becomes an eigenvalue equation for Γ. The smallest eigenvalue corresponds to the longest lived eigenfunction. This eigenfunction is the spatial distribution that would be observed in an experiment at long times. For $K_3 = 0$ in a trap deep compared to the temperature, this solution is a Boltzmann distribution, $n_{\mathrm{Yb}} \propto e^{-V(\vec{r})/k_B T}$, with $\Gamma = 0$.

Rather than solving the full 3-D equation including the self-diffusion, which depends on the Yb density and is nonlinear, the equation is reduced to 1-D. The reduction is justified by the cylindrical symmetry of the cigar-shaped trapping potential, taken to be harmonic, and the larger radial extent of the ^{87}Rb cloud and have simplified the treatment of self-diffusion. Then the radial distribution of the Yb is independent of axial position and is gaussian. For simplicity, an axially uniform distribution of ^{174}Yb in $\tau_{\mathrm{YbYb}}(\vec{r})$ is substituted and the radial distribution is taken to be the same as that for ^{87}Rb, thus turning $\tau(\vec{r})$ into a separable function of radial and axial coordinates and removing the nonlinearity. Finally, the transverse (x, y) coordinates are integrated to obtain the 1-D equation. After the trap geometry has been set, the adjustable inputs to the theory are $\langle v_{\mathrm{rel}} \sigma_{\mathrm{YbRb}} \rangle$, the three-body rate coefficient K_3, and the approximation used for the Yb density in the collision time.

Because the interactions appear to be stronger than has been seen in any other thermal gas, the interspecies cross section is taken to be unitarity limited, $\sigma_{\mathrm{YbRb}} = 4\pi\hbar^2/(\mu v_{rel})^2$. Then the collision time can be computed analytically.In this simulation a temperature of

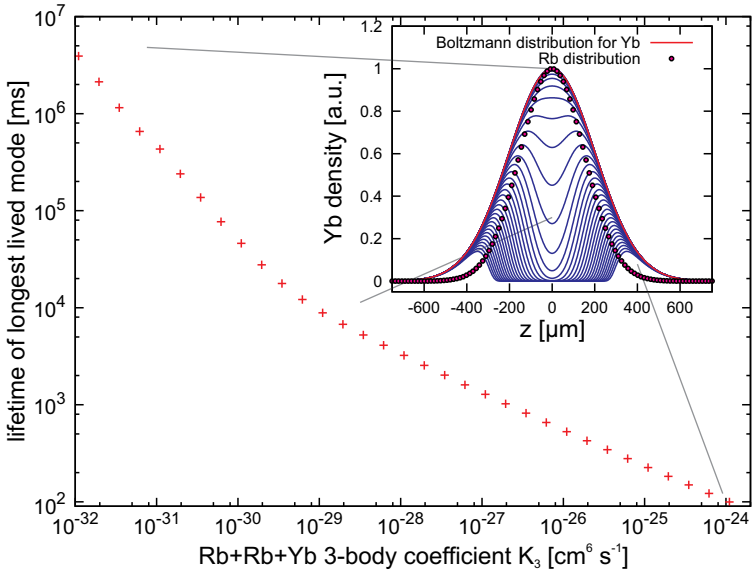

Figure 8.26: *Asymptotic lifetime of trapped ^{174}Yb versus the Rb+Rb+Yb 3-body loss rate coefficient, K_3. Inset shows the axial profile of ^{174}Yb for varying K_3 (thin blue lines). The thick red profile is the Boltzmann distribution for ^{174}Yb. Pink points are the ^{87}Rb distribution. Lines connect key points on the lifetime plot to the corresponding distribution in the inset. From [15].*

$T = 3\,\mu$K and a peak density of $n_{Rb}(0) = 3 \times 10^{14}\text{cm}^{-3}$ is used resulting in $\tau_{\text{YbRb}}(\vec{0}) = 5.7\,\mu$s. The Yb+Yb cross section is $\sigma_{\text{YbYb}} = 7 \times 10^{-11}$ cm^2 and is constant over the range of energies here [57]. A density of 10^{13} cm^{-3} ^{174}Yb atoms gives $\tau_{\text{YbYb}} = 6.1$ ms.

Figure 8.26 shows solutions of the 1-D equation, giving the lifetime $1/\Gamma$ of the longest lived eigenfunction and the eigenfunctions for a range of values of K_3. For small K_3, the ^{174}Yb distribution is roughly gaussian and the lifetime is $\propto 1/K_3$. With increasing K_3, a kink in the lifetime occurs where the ^{174}Yb is excluded from the ^{87}Rb. The reduced overlap of the clouds results in a weaker dependence of lifetime on K_3. The next longest-lived diffusion mode has a lifetime that is nearly ten times shorter.

For a 3-body rate coefficient of $\approx 10^{-25}\text{cm}^6\text{s}^{-1}$, $1/\Gamma \approx 200$ ms and the ^{174}Yb distribution peaks around 320 μm from the center of the trap. This is consistent with the measured locations of the maxima shown in Fig. **??**. As a test of the limitations of our model, τ_{YbYb} is decreased to 0.1×6.1 ms and a 40% increase in lifetime is observed. Increasing τ_{YbYb} causes no significant effect. Hence, improving the treatment of self-diffusion would only modestly improve the accuracy of the model.

The coefficient K_3 is also constrained by a unitarity condition. This imposes a maximum thermally averaged K_3 which is $\propto T^{-2}$ and is $\approx 6 \times 10^{-25}$ cm^{6}s^{-1} at 3 μK. The value reported above is consistent with this limit. One may ask whether the model constrains the interspecies scattering length. We have assumed that $\langle v_{\text{rel}}\sigma_{\text{YbRb}}\rangle$ is given by the value at unitarity, which at $T = 3\,\mu$K implies a scattering length with magnitude $> 1000a_0$. However, if we choose a smaller cross section, a reduced K_3 allows $1/\Gamma = 200$ ms. Thus,

a bound on the scattering length can not be extracted. If lifetimes are measured under more conditions, for example, by varying the ^{87}Rb density, then it will be possible extract a cross section and K_3.

In conclusion, a pure mean-field model cannot fit the observations quantitatively, although it suggests that the interspecies interactions are large. A diffusive model including the effects of three-body recombination can reproduce the experimental observations with physically reasonable parameters. However, a thermally averaged scattering length with a magnitude of $\sim 10^3 a_0$ gives a mean-field potential comparable to $k_B T$, so that a complete understanding will require the inclusion of both a mean field and the diffusion dynamics.

9

Conclusion and interpretation of Rb-Yb interaction results

The previous chapters 7 and 8 described experiments characterizing the interaction of different Yb isotopes with ^{87}Rb at temperatures in the low $10\,\mu K$ range. The most prominent feature, which I have investigated, is the large repulsive interaction between ^{174}Yb and ^{87}Rb leading to phase separation of the two species in a thermal mixture.

The first part of the following chapter summarizes the results from ^{174}Yb - ^{87}Rb phase separation measurements, which represent the essential outcome of the PhD work presented here.

The second part of this chapter introduces theoretical model calculations on the YbRb molecular ground state potential based on the experimental results presented in this PhD thesis. E. Tiesinga and S. Maxwell from the atomic theory group at NIST [15] determined a Lennard-Jones potential, which quantitatively reproduces the experimental observations.

9.1 Conclusive results of ^{174}Yb - ^{87}Rb phase separation measurements

As described in Chap. 8, we experimentally observe phase separation in a thermal mixture of ^{174}Yb and ^{87}Rb. The occurrence of phase separation depends on the number of ^{87}Rb atoms, the ^{87}Rb density distribution and the temperature. This effect is clearly observed in a temperature regime $T = 2 \ldots 6\,\mu$K (see Sec. 8.3.2) and it is independent of the ^{87}Rb ground state hyperfine level (see Sec. 8.3.5).

Phase separation of ^{174}Yb and ^{87}Rb is accompanied by rapid ^{174}Yb atom loss, which is discussed in detail in Sec. 8.4.2: It's contribution to the spatial atom distribution observed in the present experiments can not be fully quantified. Purely loss-induced phase separation, however, can be excluded.

A basic qualitative interpretation of the data assumes a repulsive interaction potential between ^{174}Yb and ^{87}Rb, which is given by the standard mean-field s-wave interaction potential with large positive scattering length a. In a temperature dependent approach, the scattering length a is replaced by the energy dependent effective range expansion $a_E(k)$ (see Sec. 8.4.1). The mean effective interaction potential is obtained by thermal averaging over all possible collision energies. Results from this approach are inconsistent

with experimental observations.

As described in Sec. 8.5.1, a comparison of relevant length scales clearly shows, that theoretical models beyond the simple mean field description are required to correctly treat the observed phase separation between ^{174}Yb and ^{87}Rb.

The LHY correction extends the mean field theory into a regime of larger interactions and higher densities. An inclusion of the LHY correction in the quantitative data analysis is discussed in Sec. 8.5.2 and yields an interspecies scattering length of

$$\mathbf{a_{LHY}} \;=\; (\,\mathbf{4710}\,{}^{+\mathbf{3970}}_{-\mathbf{1520}}\,)\;\mathbf{a_0}\,.$$

The LHY correction term successfully describes effects like quantum depletion, which are attributed to large interactions in Bose Einstein condensates [145] in the limit $k \to 0$. It's complete validity in the present case, where the scattering length exceeds the interatomic distance $d = 1/n^{-3}$ is still questionable. Furthermore, the case of finite temperatures beyond the point, where $a_E(k)$ diverges and changes its sign is not taken into account by this approach. A proper treatment of higher order effects emerging in this regimes will require theories that differ much more substantially from the mean field description.

Assuming that the elastic cross section between ^{174}Yb and ^{87}Rb is large, the mean free path of a thermal ^{174}Yb atom in a cloud of ^{87}Rb will be much smaller than the size of the cloud. Thus, the trapped system can be modeled using the time-dependent diffusion equation including loss due to three-body recombination. A diffusive model including the effects of three-body recombination, which is developed by E. Tiesinga and S. Maxwell [15] and described in detail in Sec. 8.5.3 can reproduce the experimental observations with physically reasonable parameters. However, for a quantitative description of the observed phase separation by diffusion and three-body recombination, further experimental and theoretical investigations are needed.

While a complete theoretical understanding of the observed phase separation will require the inclusion of both a repulsive potential and the diffusion dynamics, the results presented here are the first observation of phase separation in a thermal mixture of ultracold atoms. Our analysis indicates that the scattering length between ^{174}Yb and ^{87}Rb is the largest interspecies scattering length in any mixture of ultracold atoms investigated to date (magnetically tunable Feshbach resonances excluded).

9.2 Conclusions on the Yb Rb molecular ground state potential

On the basis of the results regarding the low energy scattering properties of different Yb isotopes and ^{87}Rb, which are presented in this PhD thesis, E. Tiesinga and S. Maxwell have calculated a model potential for the Yb Rb molecular ground state [15]. These calculations are based on a Lennard-Jones potential and a semiclassical approximation according to [151], in order to compute the zero-energy s-wave scattering lengths.

As described in Sec. 2.2.2 the low energy interaction between atoms is determined by the energetic position of the bound states close to the dissociation limit. Hence, scattering experiments allow conclusions mainly on the long range part of the interatomic potential,

which can be well approximated by a Lennard-Jones potential:

$$U_{\mathrm{LJ}}(r) \propto \frac{C_n}{r^n} - \frac{C_6}{r^6} \tag{9.1}$$

The first term with a high power of n (here: $n = 12$) describes the Pauli repulsion at short ranges due to overlapping electron orbitals and the r^{-6} term describes attraction at long ranges (van der Waals force, see Sec. 2.1.4).

The C_6 dispersion coefficient used in this calculation is $C_6 \approx 2740 \pm 140$ a.u.. It is determined using the dynamic polarizability at imaginary frequencies of Yb (and Rb) [15]. This method gives a slightly lower value than the approximation based on [60], which is presented in Sec. 2.2.2.

The input parameters for the model potentials based on the present experimental results are:

- The interspecies s-wave scattering length $|a_{87-170}|$ is below $\approx 10\,\mathrm{a_0}$.
- The interspecies s-wave scattering length between ^{87}Rb and ^{174}Yb is large and positive ($a_{87-174} > 3000\,\mathrm{a_0}$) , indicating a zero-energy resonance for this isotope combination.

Calculations indicate, that potentials supporting $60 \ldots 70$ bound states can reproduce these experimental observations. Table. 9.1 summarizes calculated interspecies scattering length and binding energies (E_B/h in units of MHz) of the three bound states closest to the dissociation limit. The underlying model potential supports 63 bound states for all isotope combinations except ^{87}Rb-^{174}Yb and ^{87}Rb-^{176}Yb, where one more bound state enters the potential. These calculated result are shown in Fig. 9.1 as a function of the reduced mass $m_r = \frac{m_{\mathrm{Yb}} m_{\mathrm{Rb}}}{m_{\mathrm{Yb}} + m_{\mathrm{Rb}}}$. Note that although the blue lines indicate a continuous distribution, only the black and/or red dots are physical.

The characteristics of the scattering length and binding energies qualitatively match the situation discussed in Sec. 2.2.2 on the basis of a square well potential: Generally, a change in the reduced mass alters the position of the last bound states in the potential. The larger the binding energy of the last bound state, the smaller is the scattering length. Finally, a crosses zero and just before a new bound state enters the potential, a becomes large and negative. In this case, the potential is said to have a virtual state close to the dissociation energy.

The scattering length diverges and changes sign as a new bound state enters the Lennard Jones potential. In the case of Yb-Rb, the zero energy resonance, which is indicated by the dashed blue line in Fig. 9.1, is located at a reduced mass m_r slightly below the ^{87}Rb-^{174}Yb point leading to a large and positive a for this combination. In the case of a bound state close to resonance, its binding energy E_b is related to the scattering length through Eq. 2.34:

$$E_b \cong \frac{\hbar^2}{2 m_r a^2} \tag{9.2}$$

Using the calculated ^{87}Rb-^{174}Yb scattering length $a = 7355\,\mathrm{a_0}$, the binding energy of the last bound state $E_b/h \approx 570\,\mathrm{Hz}$ is extremely low.

Rb isotope	Yb isotope	scattering length [a_0]	number of bound states	1st bound state [MHz]	2nd bound state [MHz]	3rd bound state [MHz]
85	168	227.6	63	1.4	304.1	1769.4
85	170	140.5	63	7.0	402.2	2066.3
85	171	118.3	63	11.6	457.2	2223.9
85	172	101.0	63	17.7	516.3	2387.3
85	173	85.9	63	25.4	579.6	2556.9
85	174	71.9	63	34.8	647.1	2732.1
85	176	42.6	63	59.5	794.8	3100.7
87	168	42.8	63	59.3	794.0	3098.5
87	170	-2.4	63	96.0	975.6	3529.0
87	171	-41.2	63	118.6	1074.5	3754.8
87	172	-113.9	63	144.1	1178.5	3987.2
87	173	-330.0	63	172.6	1287.8	4226.9
87	174	7355.2	64	0.0	204.3	1402.4
87	176	255.9	64	1.2	277.4	1647.6

Table 9.1: *Calculated interspecies scattering length and binding energies based on a Lennard Jones model potential, which qualitatively reproduces our experimental observations [15].*

At even larger values of the reduced mass, the binding energy increases again, reproducing the situation below $m_r = 56.5\,\mathrm{u}$.

Comparison with measured relative scattering properties Calculated interspecies s-wave scattering length based on the model potential discussed here can be used to infer low energy scattering cross sections according to

$$\sigma_0 = 4\pi a^2 \,. \tag{9.3}$$

It allows a qualitative comparison with experimental results on relative scattering properties between ^{87}Rb and various Yb isotopes, which are obtained from thermalization measurements as described in Sec. 7.2.

Thermalization measurements are performed in the low μK regime, where the assumption of pure s-wave scattering is well justified (see discussion in Sec. 2.1.4). Due to unknown absolute interspecies overlap densities, no absolute scattering cross sections could be extracted from measured thermalization rates. However, the determination of a scattering parameter $\beta \propto \sigma_{\mathrm{tot\,YbRb}}$ allows conclusions on relative scattering properties of different Yb isotopes with ^{87}Rb. Figure 9.2 compares calculated scattering cross sections based on the model potential with experimental results $C \cdot \beta \propto \sigma_{\mathrm{tot\,YbRb}}$ for different Yb isotopes, where the constant C is chosen to fit the theoretical data. Note that due to the smaller uncertainties, results for β obtained with data analysis method a) from thermalization rate studies (see Sec. 7.2.2) are chosen for this comparison.

The theoretical model, which is purely based on measured scattering properties of ^{170}Yb - ^{87}Rb and ^{174}Yb - ^{87}Rb, correctly reproduces measured relative scattering cross sections

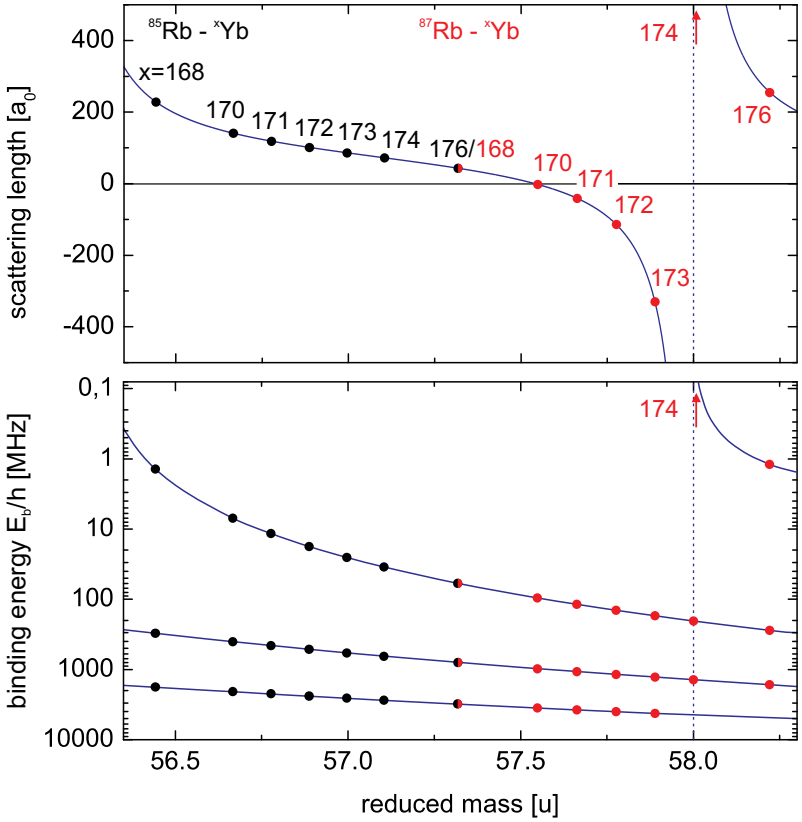

Figure 9.1: *Graphic representation of the calculated result presented in Tab. 9.1 as a function of the reduced mass (given in atomic mass units u).*

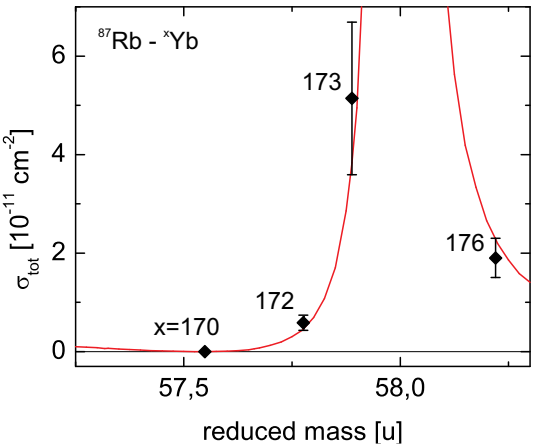

Figure 9.2: *Calculated elastic scattering cross section σ_{tot} as a function of the reduced mass (red line) together with experimental results from thermalization measurements with ^{87}Rb and ^{170}Yb, ^{172}Yb, ^{173}Yb, ^{176}Yb. Note that the experimental data points, which are obtained using method a) described in Sec. 7.2.2, include a free common scaling factor chosen to match the theoretical results.*

for the combinations ^{172}Yb - ^{87}Rb, ^{173}Yb - ^{87}Rb and ^{176}Yb - ^{87}Rb within their experimental uncertainties. This supports the theoretical model and the underlying assumptions for the YbRb molecular potential.

10

Outlook on future experiments

The experimental studies on interspecies interaction between different Yb isotopes and ^{87}Rb, which are described in this PhD work, have greatly increased the knowledge of low energy properties of this novel mixture. This is a major step towards the long term goal of this research project, which is the production of ultracold YbRb molecules in the rovibronic ground state. The future developments required to achieve this goal can be divided into two areas: One will be the continuation of studies on the YbRb molecular potentials, which already resulted in the successful production of excited state YbRb molecules by photoassociation [16]. The other will be to realize a quantum degenerate mixture of both species, which would be an ideal starting point for the creation of ground state YbRb molecules.*

The following chapter briefly outlines the consequential future developments of this research project on the basis of present experimental results. First, it focuses on two color photoassociation spectroscopy on the YbRb molecular ground state potential. The second part of this chapter summarizes the present developments on efficient cooling of Yb and points out a promising pathway towards a combined degenerate mixture of Rb and Yb.

10.1 Two-color photoassociation spectroscopy

The current plan for the formation of rovibronic ground state molecules consisting of Rb and Yb involves two consecutive tow-photon processes, which is illustrated in Fig. 10.1 (a). The first two-photon process involves a transition to an excited YbRb* molecular state (1) followed by de-excitation to a high-lying vibrational level of the electronic ground state (2). The second process ((3) and (4)) then couples this state to the rovibrational molecular ground state through an intermediate excited state in a lower vibrational level. Note that this complex scheme is necessary, as the efficient production of ground state molecules requires good Franck-Condon overlap between the nuclear wave functions for all molecular transitions. The simplified Franck-Condon principle states, that transitions between different electronic states can be driven most efficiently without directly changing interatomic distance and kinetic energy at the turning points. These conditions are met by "vertical" transitions in Fig. 10.1 (a). A detailed theoretical discussion of possible routes towards absolute ground state YbRb molecules can be found in [11].

The first experimental step in this direction, i.e. the formation of excited state YbRb* molecules by photoassociation, has already been observed successfully in our apparatus [16].

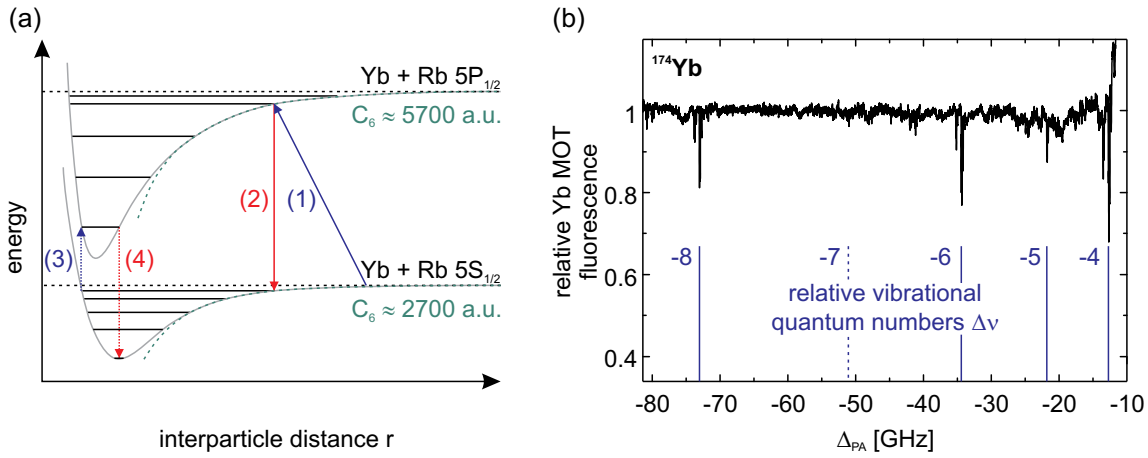

Figure 10.1: *(a) Possible scheme for production of YbRb rovibronic ground state molecules: (1) A well-defined excited YbRb* molecular state is accessed with the first photon. Step (2), connects this state with molecules in the stable but weakly bound vibrational level of the ground state. This will be the first two-photon process. A second tow-photon scheme (3) involves a more deeply bound excited molecular state with good Franck-Condon overlap to the absolute ground state (4). (b) Trap loss photoassociation spectrum from a combined MOT of ^{87}Rb and ^{174}Yb, correspondent to step (1). Assigned peaks are labeled by their vibrational quantum number relative to the level closest to the dissociation limit. Adapted from [11].*

Detailed knowledge on YbRb molecular ground state potentials and the energetic positions of weakly bound states is the first thing that is required in order to accomplish the first tow-photon process. Experimental results described within this PhD work allow predictions for the energies of weakly bound states of different Yb and Rb isotopic combinations through a calculated model potential (see Chap. 9 and [15]). The direct observation of the respective molecular levels using two-color photoassociation spectroscopy, which is currently being prepared, will represent an independent measurement, which complements and tests the current results on a highly improved accuracy level.

Photoassociation spectroscopy

Photoassociation spectroscopy of YbRb* molecules was performed in a combined MOT consisting of ^{87}Rb and ^{174}Yb (^{176}Yb) atoms at temperatures in the range of several 100 μK. We have been using a photoassociation laser at frequencies slightly below the 795 nm D1 transition from the rubidium ground state to the $5^2P_{1/2}$ state. In that experiment, spectra were taken by monitoring the reduction of trap fluorescence due to molecule formation and subsequent loss from the trap. Fig. 10.1 (b) shows parts of the resulting photoassociation spectrum for ^{174}Yb as a function of the frequency detuning Δ_{PA} from the atomic ^{87}Rb D1 transition. The individual lines could be clearly attributed to high vibrational levels of the molecular potential with a dissociation limit equal to the ground state of ^{174}Yb and the excited $5^2P_{1/2}$ state of ^{87}Rb. For this potential, an accurate long-range dispersion

coefficient $C_6 = 5700 \pm 100$ a.u. could be extracted from the experimental data.

Autler Townes spectroscopy

The next step will be a study of the molecular YbRb ground state by Autler-Townes spectroscopy. The use of Autler-Townes spectroscopy [152] makes it possible, to spectroscopically probe a level that is not directly accessible from the initial state. This method is based on the AC stark effect, which leads to splitting of atomic energy levels in the presence of a (strong) light field, depending on its intensity the frequency detuning from a coupling transition.

Experimentally, the photoassociation laser is operated on resonance for a transition between the unbound ground state continuum and a bound excited molecular state as described above. An additional *Raman laser* is then used to couple this state with a (weakly) bound level of the molecular ground state (corresponding to transition (2) in Fig. 10.1 (a)). When the Raman laser is resonant (or close to resonance) with the bound-bound transition, it will induce Autler-Townes splitting of the original photoassociation transition into two components. The splitting between the components $\Delta\nu_{\mathrm{AT}}$ is identical to the Rabi frequency Ω, which depends on the frequency ν_R and intensity I_R of the Raman laser and the bound-bound transition rate Γ_{bb} according to [153]

$$\Delta\nu_{\mathrm{AT}} = \frac{\Omega}{2\pi} = \sqrt{\frac{3c^2 I_R \Gamma_{\mathrm{bb}}}{16\pi^3 h \nu_R^3}}\,. \tag{10.1}$$

Autler-Townes spectroscopy in combination with photoassociation has been performed e.g. in the triplet system of magnetooptically trapped ^{6}Li [153]. In this experimental scheme, the Raman laser is tuned on resonance with the bound-bound transition and the photoassociation laser is scanned. Transition rates could be inferred from measured Autler-Townes splittings of the trap loss peaks.

For the identification of ground state vibrational levels, two-color photoassociation spectroscopy in our experimental setup, will first require a variation of the standard scheme: The photoassociation laser will be set on resonance with a vibrational line, resulting in constant trap loss due to excited state YbRb* molecule production. Then, the Raman laser will be scanned. When it is in resonance (or close to resonance) with a bound-bound transition, reduction in the trap loss will be observed, as it shifts the photoassociation laser out of resonance from the original transition.

The required light power for the Raman laser can be roughly approximated using Eq. 10.1. In order to observe a significant reduction of trap loss, the Autler-Townes splitting should be on the order of the measured line width of the photoassociation lines, which is $\approx 30\,\mathrm{MHz}$ [11]. The bound-bound transition rate Γ_{bb} is approximated as

$$\Gamma_{\mathrm{bb}} = \Gamma_{\mathrm{atom}} \cdot f_{\mathrm{FC}}, \tag{10.2}$$

where Γ_{atom} is the atomic ^{87}Rb D1 transition rate. The Franck-Condon factor f_{FC} depends on the overlap of the nuclear wave functions ψ_n and ψ'_n of the initial and final state of the

molecular transition according to $f_{\mathrm{FC}} = |\langle\psi_n|\psi'_n\rangle|^2$. Assuming a combined Yb-Rb MOT diameter of ≈0.4 mm [11] and a photoassociation laser beam of identical size, the required Raman laser power P_R is roughly given by

$$P_R \approx \frac{0.1\,\mathrm{mW}}{f_{\mathrm{FC}}}. \tag{10.3}$$

Hence, for perfect overlap of the nuclear wave functions of the bound-bound molecular transition ($f_{\mathrm{FC}} = 1$), only 0.1 mW of Raman laser light would be required to obtain a significant Autler-Townes splitting. Assuming (more realistic) Franck-Condon factors of 10^{-2} to 10^{-3}, the Raman laser power should be in the range of several $10 \ldots 100$ mW.

Based on the simplified Franck-Condon principle, the energy range of most easily accessible bound levels in the molecular ground state can be approximated: Assuming "vertical" transitions between the classical outer turning points ($r = r'$) in the long range approximation of the potential, the relation between binding energies in the ground and excited state, E and E', is given by:

$$E(r) = \frac{C_6}{r^6} \quad \text{and} \quad E'(r') = \frac{C'_6}{r'^6} \quad \underset{r=r'}{\Longleftrightarrow} \quad E = \frac{C_6}{C'_6} \cdot E' \approx 0.5 \cdot E'\,. \tag{10.4}$$

Here, the known dispersion coefficients of the ground and excited state molecular potentials are included. In a qualitative description, this result means, that for an excited state level with binding energy E' the best Franck-Condonon overlap is realized for a ground state level of halve the excited state binding energy. Generally, this simple "rule of thumb" can be helpful in the choice of excited state levels suited for two-photon photoassociation spectroscopy.

In order to probe the energetic position of calculated molecular ground state levels presented in Tab. 9.1, which are in the regime $E < h \cdot 5\,\mathrm{GHz}$, an excited state level very close to the atomic resonance should be chosen. In terms of good Franck-Condon overlap, the strong $\Delta\nu = -4$ line at $\Delta_{\mathrm{PA}} \approx -13\,\mathrm{GHz}$ in the ^{174}Yb-^{87}Rb mixture (see Fig. 10.1 (b)) could be an appropriate candidate for the study of the bound ground state levels closest to the dissociation energy. However, further experimental issues, e.g. ^{87}Rb loss due to Rb-Rb molecule creation, which preferably occurs close to the atomic resonance, have to be considered. Above $\Delta_{\mathrm{PA}} \approx -10\,\mathrm{GHz}$, the strong photoassociation laser is too close to the atomic ^{87}Rb D1-transition causing sufficient heating and depletion of the rubidium trap to obscure the photoassociation lines.

A detailed discussion on possible candidate lines suited for the first two-photon process to create ground state YbRb molecules is given in [11].

10.2 Combined Yb Rb quantum gas

The realization of a combined quantum gas consisting of a ^{87}Rb BEC and a Yb BEC or a Yb degenerate Fermi-gas will open new possibilities for interspecies studies in this mixture.

While large condensates of ^{87}Rb ($N_{\mathrm{Rb}} \approx 10^6$) can reliably be produced in our apparatus, quantum degeneracy has not been observed for Yb. The present approach involves sympathetic cooling of Yb trapped in the BIODT by magnetically trapped and evaporatively cooled ^{87}Rb.

In the course of this thesis, new insights on physical parameters of the system Yb-^{87}Rb as well as on intrinsic technical limitations of the current experimental setup have been gained. This additional knowledge leads to the conclusion, that successful sympathetic cooling of Yb to the regime of quantum degeneracy, is very hard to achieve with our current approach. The reasons are discussed in this section a possible alternative route towards a YbRb-double BEC using a novel trapping geometry for Yb is sketched

10.2.1 Yb BEC by sympathetic cooling?

In cold trapped gases, the transition from the thermal regime to the regime of quantum degeneracy can be clearly observed, when a stable BEC is produced. The transition to Bose Einstein condensation typically creates a region of dramatically increased density in a trapped cloud, which leads to a bimodal density distribution with a characteristic "BEC-peak", when it is imaged after a defined time of ballistic expansion (see e.g. [121, 62]). On the contrary, degenerate Fermi gases are experimentally much harder to distinguish from the thermal sample [154]. Hence, our present experimental studies on the achievement of lower Yb temperatures have so far focused on bosonic Yb isotopes.

Table 10.1 summarizes relevant physical properties of Yb-^{87}Rb mixtures and states resultant obstacles for the creation of an Yb BEC by means of sympathetic cooling with ^{87}Rb. This roundup shows, that either the low energy scattering properties of each Yb isotope itself or its interaction with ^{87}Rb prevents the formation of a stable BEC using the present approach.

Besides these physical aspects, further studies with ^{176}Yb and ^{87}Rb have demonstrated, that the present experimental setup makes it difficult to gain sufficient control over the trapping geometry, to reach the BEC transition temperature for ^{176}Yb. This isotope has a negative scattering length and an emerging BEC would collapse instantly due to the effective attractive atom-atom interaction in the cloud. Hence, temperature dependent ^{176}Yb atom loss from the trap could indicate quantum degeneracy for this isotope.

The experimental sequence used in these studies is based on the thermalization measurements presented in Chap. 7. The BIODT potentials were gradually reduced, while the forced evaporation ramp for ^{87}Rb was continued. We were able to produce ^{176}Yb clouds consisting of $\approx 5 \times 10^4$ atoms at temperatures of $300 \ldots 400\,\mathrm{nK}$, while ^{87}Rb formed a BEC. Calculated transition temperatures for ^{176}Yb in the present trapping geometry, however, are still lower by a factor of 3 to 4. Increasing the confinement for ^{176}Yb by using higher BIODT powers generally led to higher ^{87}Rb temperatures and ^{87}Rb atom loss. Although these studies showed promising results, they led to the following conclusion: In the current experimental setup, the level of control over the BIODT beam parameters is not sufficient, to simultaneously reduce disturbances of the potential for ^{87}Rb while providing enough confinement for ^{176}Yb and maintaining contact between both species.

Yb isotope	boson/ fermion	relative abundance[1]	$a_{\mathrm{Yb-Yb}}$ $[a_0]$ [2]	$\lvert a_{\mathrm{Yb-^{87}Rb}}\rvert$ $[a_0]$ [3]	obstacles for Yb-^{87}Rb double BEC through sympathetic cooling
^{168}Yb	b	0.13%	252 ± 3	43	low relative abundance; small interspecies scattering length
^{170}Yb	b	3.05%	64 ± 2	<10	insufficent thermalization with ^{87}Rb due to very small interspecies scattering length
^{171}Yb	f	14.3%	-2.8 ± 3.6	41	fermion; small interspecies scattering length
^{172}Yb	b	21.9%	-599 ± 64	114	(large) negative intraspecies scattering length ⇒ BEC unstable; (intraspecies) three body loss
^{173}Yb	f	16.1%	199 ± 2	330	fermion; (however, possible candidate for degenerate bose-fermi mixture, due to reasonably large intraspecies scattering length)
^{174}Yb	b	31.8%	105 ± 2	>3000	large interspecies interaction ⇒ phase separation; strong (interspecies) three body loss
^{176}Yb	b	12.7%	-24 ± 4	256	negative intraspecies scattering length ⇒ BEC unstable

[1] from [116]
[2] from [57]
[3] for ^{170}Yb and ^{174}Yb: measured values; otherwise: calculated as described in Chap. 9 and [15]

Table 10.1: *Summary of physical Yb-^{87}Rb properties relevant for the creation of a combined quantum gas through sympathetic cooling.*

10.2.2 A novel approach for a combined trap

In order to circumvent the technical and physical problems that have been encountered in the course of this thesis, we have developed a new strategy for the creation of mixed quantum gases with Yb and Rb which will be implemented in the near future. This strategy involves a single-color crossed beam optical dipole trap, the independent creation of Yb and Rb quantum gases and subsequent realization of a spatial overlap of the two independent traps.

Near-resonant "green" trap for Yb

As discussed in Sec. 5.1, the basic idea of the bichromatic ODT is, to provide independent trapping potentials for Yb, without affecting the ^{87}Rb atoms. However, even for perfect Gaussian ODT beams with equal waists, this condition is fulfilled only in the trap center due to the different Raleigh lengths. Experimentally, the control of the size and the spatial

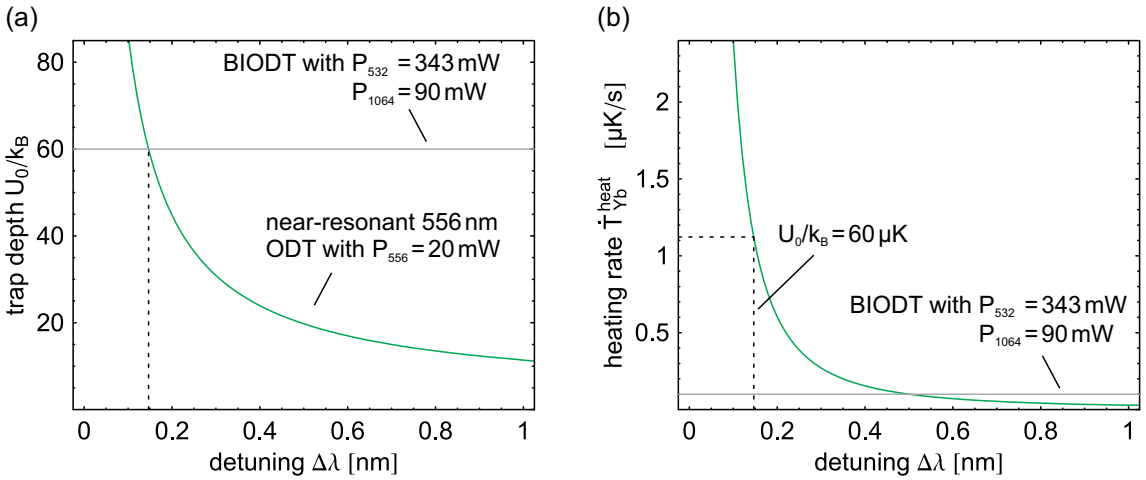

Figure 10.2: *(a) Calculated trap depths U_0/k_B and (b) heating rates for Yb for a single beam ODT with detuning $\Delta\lambda$ from the "green" 555.8 nm intercombination transition in Yb. Beam parameters: waist $w_0 = 15\,\mu m$ and light power $P_{556} = 20\,mW$. The gray lines indicate BIODT parameters in the present experiments: For comparable trap depth $U_0/k_B \approx 60\,\mu K$, the corresponding heating rate is increased by a factor of ≈ 10.*

overlap of the two ODT beams involves a high level of complexity.

The particular electronic level structure of Yb, however, allows for a similar independent trapping approach, using only a single beam ODT. Due to the narrow line width of $\gamma_{556} = 2\pi \times 181$ kHz of the $^1S_0 \rightarrow {}^3P_1$ intercombination line at 555.8 nm, a light field, which is tuned close to the "red" side of this transition, creates a strong dipole potential whereas photon scattering is on a reasonably low level (see Eqn. 3.33 and 3.34)

Figure 10.2 shows calculated trap depths and heating rates as a function of the detuning of the trap light from the $^1S_0 \rightarrow {}^3P_1$ transition for a single beam trap with beam waist $w_0 = 15\,\mu$m and light power of only $P_{556} = 20\,$mW. A trap depth of $U_0/k_B \approx 60\,\mu$K, which is equal to the value in the experiments presented here, is obtained at a detuning $\Delta\lambda \approx 0.15\,$nm from resonance. At this detuning, the heating rate is by a factor of ≈ 10 larger than the current BIODT, but still small enough to avoid significant Yb heating within the required times scales. Due to the much lower light power $P_{556} = 20\,$mW, the repulsive optical potential for ^{87}Rb is greatly reduced to only $k_B \times 4\,\mu$K.

In parallel to the writing of this thesis, different Yb isotopes were successfully trapped in such a near-resonant ODT. A DPSS laser pumped dye laser served as a source for $\approx 20\,$mW of 556 nm light, which was superimposed on the 532 nm ODT beam (see Fig. 4.11 for a schematic of the current laser system). Yb atoms were first prepared in a strong 532 nm ODT, before they were transferred to the near-resonant trap with a transfer efficiency of $\approx 70\,\%$. Sympathetic cooling and phase separation between ^{174}Yb and ^{87}Rb could be observed in this potential geometry. The preparation of a ^{87}Rb BEC in a phase separated mixture with ^{174}Yb demonstrated, that interspecies contact is maintained even at temperatures low enougth to reach quantum degeneracy in ^{87}Rb. In this experiment, the light power of the

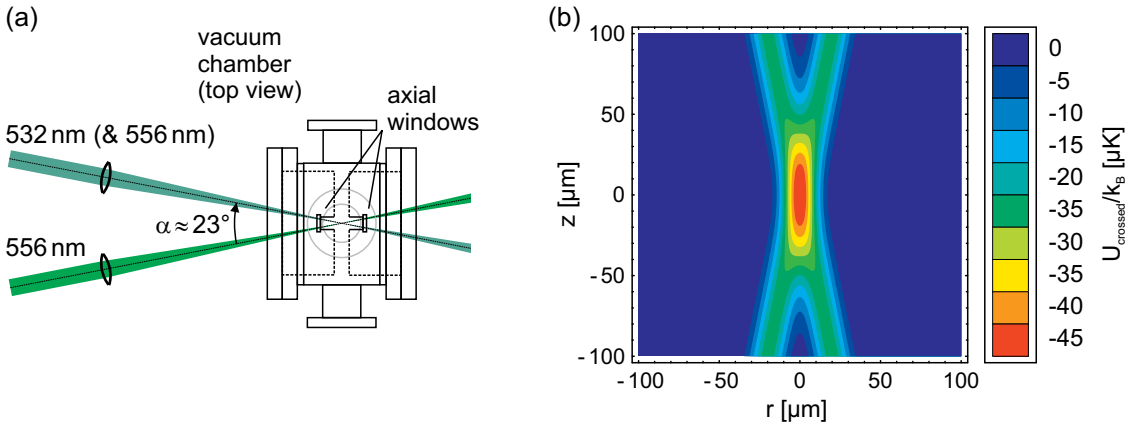

Figure 10.3: *(a) Possible implementation of a crossed ODT in the existing experimental setup. The axial windows of the vacuum chamber allow for a maximum trap angle* $\alpha \approx 23°$*. (b) Calculated horizontal cut of the potential* U_{crossed} *for this geometry assuming identical trap depths* $U_0/k_{\mathrm{B}} \approx 26\,\mu K$ *for the individual single beam potentials and beam waists* $w_0 = 15\,\mu m$*.*

near-resonant ODT was reduced to levels below 2 mW. However, no indications of quantum degeneracy for ^{174}Yb or ^{176}Yb could been observed during these preliminary experiments, probably due to the weak confinement in the single beam near-resonant ODT leading to low Yb transition temperatures.

Crossed beam ODT

As discussed in Sec. 3.2.3, the use of dipole traps consisting of two crossed red detuned laser beams enhances the confinement in all three dimensions. This trapping configuration, which allows for effective evaporative cooling of trapped atoms, is used in many cold atom experiments. As a result, the all optical formation of quantum degenerated gases in crossed dipole traps is now an established technique (see e.g.[110]), which has also successfully been applied to different Yb isotopes by the group in Kyoto [1, 111].

While a crossed geometry for the BIODT which has been used so far, would be an experimentally very challenging task, the implementation of a single color "green" ODT for Yb should be straightforward. In the existing experimental setup, both ODT beams of the crossed trap will enter the vacuum chamber trough of the axial windows, as illustrated in Fig. 10.3 (a). Due to the geometry of the vacuum chamber, the maximum angle between the two ODT beams will then be limited to $\alpha \approx 23°$. Fig. 10.3 (b) shows a horizontal cut of the resulting trapping potential for Yb. The calculation is based on two identical single beam ODTs with trap depths $U_0/k_{\mathrm{B}} \approx 26\,\mu$K and beam waists $w_0 = 15\,\mu$m. Trapping parameters of crossed beam ODTs with different trap angles α are summarized in Tab. 10.2 and compared to a single beam ODT with identical trap depth.

These model calculations clearly show, that in the crossed ODT geometry, even for small beam angles α, the axial trap frequency ω_z and hence the axial confinement is

beam parameters: $\lambda = 532\,\text{nm}$; $w_0 = 15\,\mu\text{m}$; $P_{\text{total}} = 340\,\text{mW}$;	single beam trap	crossed beam trap with beam angle $\alpha = 5°$	$\alpha = 10°$	$\alpha = 23°$
trap depth U_0/k_B	$\approx 52\,\mu\text{K}$			
axial trap freq. $\omega_z/(2\pi)$ [Hz]	8.4	47	93	211
radial trap freq. $\bar{\omega}_r/(2\pi)$ [Hz][1]	1055	1054	1053	1044
aspect ratio $\sigma_z/\bar{\sigma}_r = \bar{\omega}_r/\omega_z$	125	23	11	4.9
relative trap volume[2] $V = \sigma_z\bar{\sigma}_r^2$	1	0.18	0.09	0.04
relative density[2,3] $n \propto 1/V$	1	5.5	11	24

[1] geometric mean of both radial trap frequencies $\bar{\omega}_r = \sqrt{\omega_x\omega_y}$
[2] compared to the single beam trap
[3] assuming identical atom numbers and temperatures

Table 10.2: *Comparison of calculated trapping parameters between a single beam ODT and a crossed beam trap with different trap angles α.*

dramatically increased. The aspect ratio $\sigma_z/\bar{\sigma}_r = \bar{\omega}_r/\omega_z$ of an atomic cloud trapped in the respective potentials is changed from a nearly 1-dimensional geometry in the single beam trap to a "cigar shaped" geometry in crossed ODTs. Consequently, the trap volume is reduced, which, under the assumption of identical atom numbers and temperatures, results in significantly larger atom densities $n \propto 1/V$ compared to a single beam trap.

For the creation of degenerate quantum gases by means of evaporative cooling, an increase in the atom density has two major advantages: First, the method of evaporative cooling becomes more efficient, as the thermalization rate (Eq. 3.23) is directly proportional to n. Second, the transition temperature for Bose Einstein condensation also depends on the density (see Eq. 8.22): $T_c \propto n^{2/3}$.

Towards a combined Yb-^{87}Rb BEC

In the present experimental setup, the creation of a combined Yb-^{87}Rb BEC could be realized by an approach, which includes a near-resonant crossed beam "green" ODT as described above: As shown in Fig. 10.3 (a), one arm of the crossed trap will consist of a superposition of the (far detuned) 532 nm ODT with $P_{532} > 3\,\text{W}$ and a small portion ($P_{556a} \approx 1\,mW$) of the near-resonant 556 nm ODT ($\Delta\lambda \approx 0.15\,\text{nm}$). Preliminary measurements have demonstrated, that the strong 532 nm ODT potential is required for efficient transfer of Yb atoms from the MOT to the near-resonant 556 nm ODT. The second arm, which will be created by another 556 nm light field with $P_{556b} \approx 20\,\text{mW}$, increases the axial confinement of the trapped atoms. Subsequently, after loading Yb atoms from the MOT, forced evaporative cooling of Yb will be realized by ramping down the light powers P_{532} to 0 and P_{556b} to $\approx 1\,mW$. After this evaporation ramp, which should result in a Yb BEC for appropriate Yb isotopes, the crossed ODT will be created by two near-resonant beams with identical power. In analogy to the present experiments (see Chap. 5), ^{87}Rb atoms can

then independently be prepared and evaporatively cooled to quantum degeneracy in the spatially separated MT, while Yb is stored in the optical potentials. Finally, interaction between both quantum degenerate species can be studied by spatially superimposing both atomic clouds.

The most promising Yb isotope for creating a combined BEC with ^{87}Rb, will be ^{170}Yb, due to its small scattering length with ^{87}Rb. The realization of a Yb-^{87}Rb Bose-Fermi mixture could be achieved with ^{173}Yb, which is better suited for evaporative cooling than ^{171}Yb.

Note that this proposed experimental sequence only roughly sketches the pathway towards a combined quantum gas consisting of Yb and ^{87}Rb. Many parameters, e.g. the evaporation ramp and the actual ODT beam parameters will have to be optimized experimentally. However, preliminary measurements using the near-resonant "green" ODT and the successful use of crossed ODT geometries in numerous cold atom experiment indicate, that a combination of both techniques will be a very promising approach.

Bibliography

[1] Y. Takasu, K. Maki, K. Komori, T. Takano, K. Honda, M. Kumakura, T. Yabuzaki, and Y. Takahashi, *Spin-Singlet Bose-Einstein Condensation of Two-Electron Atoms*, Phys. Rev. Lett. **91**, 040404 (2003).

[2] M. H. Anderson, J. R. Ensher, M. R. Matthews, C. E. Wieman, and E. A. Cornell, *Observation of Bose-Einstein-Condensation in a Dilute Atomic Vapor*, Science **269**, 198–201 (1995).

[3] F. Lang, K. Winkler, C. Strauss, R. Grimm, and J. H. Denschlag, *Ultracold Triplet Molecules in the Rovibrational Ground State*, Phys. Rev. Lett. **101**, 133005– (2008).

[4] J. G. Danzl, E. Haller, M. Gustavsson, M. J. Mark, R. Hart, N. Bouloufa, O. Dulieu, H. Ritsch, and H.-C. Nagerl, *Quantum Gas of Deeply Bound Ground State Molecules*, Science **321**, 1062–1066 (2008).

[5] S. Knoop, F. Ferlaino, M. Berninger, M. Mark, H.-C. Nägerl, R. Grimm, J. P. D'Incao, and B. D. Esry, *Magnetically Controlled Exchange Process in an Ultracold Atom-Dimer Mixture*, Phys. Rev. Lett. **104**, 053201– (2010).

[6] K.-K. Ni, S. Ospelkaus, M. H. G. de Miranda, A. Pe'er, B. Neyenhuis, J. J. Zirbel, S. Kotochigova, P. S. Julienne, D. S. Jin, and J. Ye, *A High Phase-Space-Density Gas of Polar Molecules*, Science **322**, 231–235 (2008).

[7] G. K. Brennen, A. Micheli, and P. Zoller, *Designing spin-1 lattice models using polar molecules*, New Journal of Physics **9**, 138 (2007).

[8] A. Batär, *Erzeugung und Charakterisierung ultrakalter Rubidium- und Ytterbiumatome – auf dem Weg zu einem gemischten Quantengas*, Dissertation, Universität Düsseldorf (2005).

[9] S. Tassy, *Sympathetische Kühlung von Ytterbium mit Rubidium*, Ph.D. thesis, Universität Düsseldorf (2007).

[10] S. Tassy, N. Nemitz, F. Baumer, C. Höhl, A. Batär, and A. Görlitz, *Sympathetic cooling in a mixture of diamagnetic and paramagnetic atoms*, Preprint-Archiv arXiv:0709.0827 (2007).

[11] N. Nemitz, *Production and spectroscopy of ultracold YbRb* molecules*, Ph.D. thesis, Universität Düsseldorf (2008).

[12] D. S. Hall, M. R. Matthews, J. R. Ensher, C. E. Wieman, and E. A. Cornell, *Dynamics of Component Separation in a Binary Mixture of Bose-Einstein Condensates*, Phys. Rev. Lett. **81**, 1539– (1998).

[13] S. B. Papp, J. M. Pino, and C. E. Wieman, *Tunable Miscibility in a Dual-Species Bose-Einstein Condensate*, Phys. Rev. Lett. **101**, 040402– (2008).

[14] Y. Shin, A. Schirotzek, C. H. Schunck, and W. Ketterle, *Realization of a Strongly Interacting Bose-Fermi Mixture from a Two-Component Fermi Gas*, Phys. Rev. Lett. **101**, 070404– (2008).

[15] S. E. Maxwell and E. Tiesinga, *Ultracold Rb + Yb collisions and near-threshold bound states*, in preparation (2010).

[16] N. Nemitz, F. Baumer, F. Münchow, S. Tassy, and A. Gorlitz, *Production of heteronuclear molecules in an electronically excited state by photoassociation in a mixture of ultracold Yb and Rb*, Phys. Rev. A **79**, 061403–4 (2009).

[17] J. V. Prodan, W. D. Phillips, and H. Metcalf, *Laser Production of a Very Slow Monoenergetic Atomic Beam*, Phys. Rev. Lett. **49**, 1149 (1982).

[18] W. Phillips and H. Metcalf, *Laser Deceleration of an Atomic Beam*, Phys. Rev. Lett. **48**, 596–599 (1982).

[19] W. D. Phillips, *Nobel Lecture: Laser cooling and trapping of neutral atoms*, Rev. Mod. Phys. **70**, 721– (1998).

[20] The Official Web Site of the Nobel Foundation, *The Nobel Prize in Physics 1997*, URL `http://nobelprize.org/nobel_prizes/physics/laureates/1997/index.html`.

[21] C. C. Bradley, C. A. Sackett, J. J. Tollett, and R. G. Hulet, *Evidence of Bose-Einstein Condensation in an Atomic Gas with Attractive Interactions*, Phys. Rev. Lett. **75**, 1687 (1995).

[22] K. B. Davis, M.-O. Mewes, M. R. Andrews, N. J. van Druten, D. S. Durfee, D. M. Kurn, and W. Ketterle, *Bose-Einstein Condensation in a Gas of Sodium Atoms*, Phys. Rev. Lett. **75**, 3969 (1995).

[23] The Official Web Site of the Nobel Foundation, *The Nobel Prize in Physics 2001*, URL `http://nobelprize.org/nobel_prizes/physics/laureates/2001/index.html`.

[24] S. Y. T. van de Meerakker, N. Vanhaecke, M. P. J. van der Loo, G. C. Groenenboom, and G. Meijer, *Direct Measurement of the Radiative Lifetime of Vibrationally Excited OH Radicals*, Phys. Rev. Lett. **95**, 013003– (2005).

[25] D. DeMille, S. B. Cahn, D. Murphree, D. A. Rahmlow, and M. G. Kozlov, *Using Molecules to Measure Nuclear Spin-Dependent Parity Violation*, Phys. Rev. Lett. **100**, 023003– (2008).

[26] E. R. Hudson, H. J. Lewandowski, B. C. Sawyer, and J. Ye, *Cold Molecule Spectroscopy for Constraining the Evolution of the Fine Structure Constant*, Phys. Rev. Lett. **96**, 143004– (2006).

[27] J. J. Hudson, B. E. Sauer, M. R. Tarbutt, and E. A. Hinds, *Measurement of the Electron Electric Dipole Moment Using YbF Molecules*, Phys. Rev. Lett. **89**, 023003– (2002).

[28] E. R. Meyer and J. L. Bohn, *Electron electric-dipole-moment searches based on alkali-metal- or alkaline-earth-metal-bearing molecules*, Phys. Rev. A **80**, 042508– (2009).

[29] T. Lahaye, J. Metz, B. Fröhlich, T. Koch, M. Meister, A. Griesmaier, T. Pfau, H. Saito, Y. Kawaguchi, and M. Ueda, *d-Wave Collapse and Explosion of a Dipolar Bose-Einstein Condensate*, Phys. Rev. Lett. **101**, 080401– (2008).

[30] M. Baranov, L. Dobrek, K. Goral, L. Santos, and M. Lewenstein, *Ultracold dipolar gases – a challenge for experiments and theory*, Physica Scripta **T102**, 74–81 (2002).

[31] G. Pupillo, A. Micheli, H. P. Büchler, and P. Zoller, *Condensed Matter Physics with Cold Polar Molecules*, Preprint-Archiv arXiv: arXiv:0805.1896v1 (2008).

[32] A. Micheli, G. K. Brennen, and P. Zoller, *A toolbox for lattice-spin models with polar molecules*, Nat Phys **2**, 341–347 (2006).

[33] S. Ospelkaus, K.-K. Ni, D. Wang, M. H. G. de Miranda, B. Neyenhuis, G. Quemener, P. S. Julienne, J. L. Bohn, D. S. Jin, and J. Ye, *Quantum-State Controlled Chemical Reactions of Ultracold Potassium-Rubidium Molecules*, Science **327**, 853–857 (2010).

[34] L. D. Carr, D. DeMille, R. V. Krems, and J. Ye, *Cold and ultracold molecules: science, technology and applications*, New Journal of Physics **11**, 055049 (2009).

[35] J. Doyle, B. Friedrich, R. V. Krems, and F. Masnou-Seeuws, *Quo vadis, cold molecules?*, Eur. Phys. J. D **31**, 149 (2004).

[36] T. Köhler, K. Góral, and P. S. Julienne, *Production of cold molecules via magnetically tunable Feshbach resonances*, Rev. Mod. Phys. **78**, 1311– (2006).

[37] K. M. Jones, E. Tiesinga, P. D. Lett, and P. S. Julienne, *Ultracold photoassociation spectroscopy: Long-range molecules and atomic scattering*, Rev. Mod. Phys. **78**, 483– (2006).

[38] K. Bergmann, H. Theuer, and B. W. Shore, *Coherent population transfer among quantum states of atoms and molecules*, Rev. Mod. Phys. **70**, 1003– (1998).

[39] C. J. Myatt, E. A. Burt, R. W.Ghrist, E. A. Cornell, and C. E. Wieman, *Production of Two Overlapping Bose-Einstein Condensates by Sympathetic Cooling*, Phys. Rev. Lett. **78**, 586 (1997).

[40] H. Pu and N. P. Bigelow, *Properties of Two-Species Bose Condensates*, Phys. Rev. Lett. **80**, 1130 (1998).

[41] D. S. Hall, M. R. Matthews, C. E. Wieman, and E. A. Cornell, *Measurements of Relative Phase in Two-Component Bose-Einstein Condensates*, Phys. Rev. Lett. **81**, 1543– (1998).

[42] H. J. Lewandowski, D. M. Harber, D. L. Whitaker, and E. A. Cornell, *Observation of Anomalous Spin-State Segregation in a Trapped Ultracold Vapor*, Phys. Rev. Lett. **88**, 070403– (2002).

[43] S. Ronen, J. L. Bohn, L. E. Halmo, and M. Edwards, *Dynamical pattern formation during growth of a dual-species Bose-Einstein condensate*, Phys. Rev. A **78**, 053613– (2008).

[44] Y. Shin, M. W. Zwierlein, C. H. Schunck, A. Schirotzek, and W. Ketterle, *Observation of Phase Separation in a Strongly Interacting Imbalanced Fermi gas*, Phys. Rev. Lett. **97**, 030401 (2006).

[45] G. Modugno, G. Ferrari, G. Roati, R. J. Brecha, A. Simoni, and M. Inguscio, *Bose-Einstein Condensation of Potassium Atoms by Sympathetic Cooling*, Science **294**, 1320 (2001).

[46] G. Modugno, M. Modugno, F. Riboli, G. Roati, and M. Inguscio, *Two Atomic Species Superfluid*, Phys. Rev. Lett. **89**, 190404– (2002).

[47] J. Dalibard, *Collisional dynamics of ultra-cold atomic gases*, in *Bose-Einstein Condensation in Atomic Gases. Proceedings of The International School of Physics Enrico Fermi - Course CXL*, edited by M. Inguscio, S. Stringari, and C. E. Wieman, p. 321 (IOS Press, Amsterdam, 1999).

[48] L. D. Landau and E. M. Lifschitz, *Quantum Mechanics, Non-relativistic Theory*, vol. 3 of *Course of theoretical physics* (Pergamon Press, Oxford, 1977).

[49] F. Schwabl, *Quantenmechanik QMI* (5. Auflage, Springer–Verlag, Berlin, 1998).

[50] C. J. Joachain, *Quantum collision theory* (North-Holland Publishing Company, Amsterdam, 1975).

[51] N. F. Mott and H. S. W. Massey, *The Theory of Atomic Collisions* (Oxford University Press, Oxford, UK, 1965).

[52] W. Nolting, *Quantenmechanik - Methoden und Anwendungen*, vol. 5/2 of *Grundkurs Theoretische Physik* (Springer, Berlin, Heidelberg, New York, 2002).

[53] C. Cohen-Tannoudji, *Quantum Mechanics* (Hermann, Paris, 1977).

[54] A. Derevianko, W. R. Johnson, M. S. Safronova, and J. F. Babb, *High-Precision Calculations of Dispersion Coefficients, Static Dipole Polarizabilities, and Atom-Wall Interaction Constants for Alkali-Metal Atoms*, Phys. Rev. Lett. **82**, 3589 (1999).

[55] J. Roberts, N. Claussen, J. Burke, C. Greene, E. Cornell, and C. Wieman, *Resonant Magnetic Field Control of Elastic Scattering in Cold* ^{85}*Rb*, Phys. Rev. Lett. **81**, 5109 (1998).

[56] E. G. M. van Kempen, S. J. J. M. F. Kokkelmans, D. J. Heinzen, and B. J. Verhaar, *Interisotope Determination of Ultracold Rubidium Interactions from Three High- Precision Experiments*, Phys. Rev. Lett. **88**, 093201 (2002).

[57] M. Kitagawa, K. Enomoto, K. Kasa, Y. Takahashi, R. Ciurylo, P. Naidon, and P. S. Julienne, *Two-color photoassociation spectroscopy of ytterbium atoms and the precise determinations of s-wave scattering lengths*, Phys. Rev. A **77**, 012719–8 (2008).

[58] P. S. Julienne and M. H, *Collisions of ultracold trapped atoms*, J. Opt. Soc. Am. B **6**, 2257 (1989).

[59] L. K. Sørensen, S. Knecht, T. Fleig, and C. M. Marian, *Four-Component Relativistic Coupled Cluster and Configuration Interaction Calculations on the Ground and Excited States of the RbYb Molecule*, The Journal of Physical Chemistry A **113**, 12607–12614 (2009).

[60] A. Derevianko, J. F. Babb, and A. Dalgamo, *High-precision calculations of van der Waals coefficients for heteronuclear alkali-metal dimers*, Phys. Rev. A **63**, 052704 (2001).

[61] A. Marte, *Feshbach-Resonanzen bei Stößen ultrakalter Rubidiumatome*, Ph.D. thesis, Technische Universiät München, Max-Planck-Institut für Quantenoptik (2003).

[62] C. J. Pethick and H. Smith, *Bose-Einstein-Condensation in Dilute Gases* (Cambridge University Press, 2002).

[63] T. Köhler, K. Góral, and P. S. Julienne, *Production of cold molecules via magnetically tunable Feshbach resonances*, Rev. Mod. Phys. **78**, 1311–1361 (2006).

[64] W. Nolting, *Quantenmechanik - Grundlagen*, vol. 5/1 of *Grundkurs Theoretische Physik* (Springer, Berlin, Heidelberg, New York, 2002).

[65] V. V. Flambaum, G. F. Gribakin, and C. Harabati, *Analytical calculation of cold-atom scattering*, Phys. Rev. A **59**, 1998 (1999).

[66] B. Gao, *Quantum-defect theory of atomic collisions and molecular vibration spectra*, Phys. Rev. A **58**, 4222– (1998).

[67] K. Huang, *Statistical Mechanics* (Wiley, New York, 1987).

[68] F. Dalfovo, S. Giorgini, L. P. Pitaevskii, and S. Stringari, *Theory of Bose-Einstein condensation in trapped gases*, Rev. Mod. Phys. **71**, 463 (1999).

[69] C. C. Bradley, C. A. Sackett, and R. G. Hulet, *Bose-Einstein Condensation of Lithium: Observation of Limited Condensate Number*, Phys. Rev. Lett. **78**, 985 (1997).

[70] E. L. Bolda, E. Tiesinga, and P. S. Julienne, *Pseudopotential model of ultracold atomic collisions in quasi-one- and two-dimensional traps*, Phys. Rev. A **68**, 032702– (2003).

[71] A. J. Moerdijk, B. J. Verhaar, and A. Axelsson, *Resonances in ultracold collisions of Li6, Li7, and Na23*, Phys. Rev. A **51**, 4852– (1995).

[72] C. Chin, R. Grimm, P. Julienne, and E. Tiesinga, *Feshbach Resonances in Ultracold Gases*, Preprint-Archiv arXiv: 0812.1496v2 (2008).

[73] S. Inouye, M. R. Andrews, J. Stenger, H.-J. Miesner, D. Stamper-Kurn, and W. Ketterle, *Observation of Feshbach Resonances in a Bose-Einstein Condensate*, Nature **392**, 151–154 (1998).

[74] S. Jochim, M. Bartenstein, G. Hendl, J. H. Denschlag, R. Grimm, A. Mosk, and M. Weidemüller, *Magnetic Field Control of Elastic Scattering in a Cold Gas of Fermionic Lithium Atoms*, Phys. Rev. Lett. **89**, 273202– (2002).

[75] K. M. Jones, E. Tiesinga, P. D. Lett, and P. S. Julienne, *Ultracold photoassociation spectroscopy: Long-range molecules and atomic scattering*, Rev. Mod. Phys. **78**, 483–535 (2006).

[76] H. Metcalf and P. van der Straten, *Laser Cooling and Trapping* (Springer–Verlag, New York, 1999).

[77] F. H. Mies, C. J. Williams, and P. S. J. und M. Krauss, *Estimating Bounds on Collisional Relaxation Rates of Spin-Polarized ^{87}Rb Atoms at Ultracold Temperatures*, J. Res. Natl. Inst. Stand. Tech. **101**, 521 (1996).

[78] S. Hensler, J. Werner, A. Griesmaier, P. O. Schmidt, A. Görlitz, T. Pfau, S. Giovanazzi, and K. Rzazewski, *Dipolar Relaxation in an ultra-cold Gas of magnetically trapped chromium atoms*, Appl. Phys. B **77**, 765 (2003).

[79] P. O. Fedichev, M. W. Reynolds, and G. V. Shlyapnikov, *Three-Body Recombination of Ultracold Atoms to a Weakly Bound s Level*, Phys. Rev. Lett. **77**, 2921– (1996).

[80] T. Weber, J. Herbig, M. Mark, H.-C. Nägerl, and R. Grimm, *Three-Body Recombination at Large Scattering Lengths in an Ultracold Atomic Gas*, Phys. Rev. Lett. **91**, 123201– (2003).

[81] P. Meystre, *Atom Optics* (Springer–Verlag, New York, 2001).

[82] T. W. Hänsch and A. Schawlow, *Cooling of gases by laser radiation*, Opt. Comm. **13**, 68 (1975).

[83] D. Wineland and W. Itano, *Laser cooling of atoms*, Phys. Rev. **A 20**, 1521 (1979).

[84] S. Kroboth, *Laserkühlung von Ytterbiumatomen*, Diplomarbeit, Universität Stuttgart (2002).

[85] S. Chu, L. Hollberg, J. E. Bjorkholm, A. Cable, and A. Ashkin, *Three-Dimensional Viscous Confinement and Cooling of Atoms by Resonance Radiation Pressure*, Phys. Rev. Lett. **55**, 48 (1985).

[86] P. D. Lett, W. D. Phillips, S. L. Rolston, C. E. Tanner, R. N. Watts, and W. C. I., *Optical molasses*, J. Opt. Soc. Am. B **6**, 2084 (1989).

[87] P. Ungar, D. Weiss, S. Chu, and E. Riis, *Optical Molasses and Multilevel Atoms — Theory*, J. Opt. Soc. Am. B **6**, 2058–2071 (1989).

[88] D.S.Weiss, E.Riis, Y.Shevy, P.J.Ungar, and S.Chu, *Optical molasses and multilevel atoms: experiment*, J. Opt. Soc. Am. B **6**, 2072 (1989).

[89] C. G. Townsend, N. H. Edwards, C. J. Cooper, K. P. Zetie, C. J. Foot, A. M. Steane, P. Szriftgiser, H. Perrin, and J. Dalibard, *Phase-space density in the Magneto-Optical Trap*, Phys. Rev. A **52**, 1423–1440 (1995).

[90] T. Walker, D. Sesko, and C. Wieman, *Collective behavior of optically trapped neutral atoms*, Phys. Rev. Lett. **64**, 408– (1990).

[91] W. Ketterle, K. B. Davis, M. A. Joffe, A. Martin, and D. E. Pritchard, *High densities of cold atoms in a dark spontaneous-force optical trap*, Phys. Rev. Lett. **70**, 2253– (1993).

[92] P. D. Lett, R. N. Watts, C. I. Westbrook, W. D. Phillips, P. L. Gould, and H. J. Metcalf, *Observation of Atoms Laser Cooled below the Doppler Limit*, Phys. Rev. Lett. **61**, 169 (1988).

[93] J. Dalibard and C. Cohen-Tannoudji, *Laser cooling below the Doppler limit by polarization gradients: simple theoretical models*, J. Opt. Soc. Am. B **6**, 2023 (1989).

[94] E. L. Raab, M. Prentiss, A. Cable, S. Chu, and D. E. Pritchard, *Trapping of Neutral Sodium Atoms with Radiation Pressure*, Phys. Rev. Lett. **59**, 2631 (1987).

[95] C.J.Cooper, G.Hillenbrand, J.Rink, C.G.Townsend, K.Zetie, and C.J.Foot, *The Temperature of Atoms in a Magneto-optical Trap*, Europhys. Lett. **28**, 397 (1994).

[96] A. L. Migdall, J. V. Prodan, W. D. Phillips, T. H. Bergemann, and H. J. Metcalf, *First Observation of Magnetically Trapped Neutral Atoms*, Phys. Rev. Lett. **54**, 2596 (1985).

[97] T. Bergeman, G. Erez, and H. J. Metcalf, *Magnetostatic trapping fields for neutral atoms*, Phys. Rev. A **35**, 1535 (1987).

[98] S. Chu, J. E. Bjorkholm, A. Ashkin, and A. Cable, *Experimental Observation of Optically Trapped Atoms*, Phys. Rev. Lett. **57**, 314 (1986).

[99] W. H. Wing, *On neutral particle trapping in quasistatic electromagnetic fields*, Prog. Quant. Electr. **8**, 181 (1984).

[100] W. Petrich, M. H. Anderson, J. R. Ensher, and E. A. Cornell, *Behavior of atoms in a compressed magneto-optical trap*, J. Opt. Soc. Am. B **11**, 1332 (1994).

[101] D. E. Pritchard, *Cooling Neutral Atoms in a Magnetic Trap for Precision Spectroscopy*, Phys. Rev. Lett. **51**, 1336 (1983).

[102] M.-O. Mewes, M. R. Andrews, N. J. van Druten, D. M. Kurn, D. S. Durfee, and W. Ketterle, *Bose-Einstein Condensation in a Tightly Confining dc Magnetic Trap*, Phys. Rev. Lett. **77**, 416 (1996).

[103] N. Masuhara, J. M. Doyle, J. C. Sandberg, D. Kleppner, T. J. Greytak, H. Hess, and G. P. Kochanski, *Evaporative Cooling of Spin-Polarized Atomic Hydrogen*, Phys. Rev. Lett. **61**, 935 (1988).

[104] W. Ketterle and J. van Druten, *Evaporative cooling of trapped atoms*, Advances in Atomic, Molecular, and Optical Physics **31**, 181 (1996).

[105] R. Grimm, M. Weidemüller, and Y. B. Ovchinnikov, *Optical Dipole Traps for Neutral Atoms*, Advances in Atomic, Molecular and Optical Physics **42**, 95–170 (2000).

[106] C. Cohen-Tannoudji, J. Dupont-Roc, and G. Grynberg, *Atom-photon interactions* (John Wiley & Sons, 1992).

[107] J. Dalibard and C. Cohen-Tannoudji, *Dressed-atom approach to atomic motion in laser light: the dipole force revisited*, J. Opt. Soc. Am. B **2**, 1707–1720 (1985).

[108] W. C. Martin and W. L. Wiese, *Atomic Spectroscopy: An Introduction*, National Institute of Standards and Technology, http://sed.nist.gov/Pubs/AtSpec/total.html, urspünglich publiziert als Kapitel 10 in: Atomic, Molecular, and Optical Physics Handbook, G.W.F. Drake, Ed. (AIP Press, Woodbury, NY, 1996).

[109] M. D. Barrett, J. A. Sauer, and M. S. Chapman, *All-Optical Formation of an Atomic Bose-Einstein Condensate*, Phys. Rev. Lett. **87**, 010404 (2001).

[110] J. A. Anglin and W. Ketterle, *Bose-Einstein condensation of atomic gases*, Nature **416**, 211 (2002).

[111] T. Fukuhara, Y. Takasu, M. Kumakura, and Y. Takahashi, *Degenerate Fermi Gases of Ytterbium*, Phys. Rev. Lett. **98**, 030401 (2007).

[112] L. Ricci, M. Weidemüller, T. Esslinger, A. Hemmerich, C. Zimmermann, V. Vuletic, W. König, and T. W. Hänsch, *A compact grating-stabilized diode laser system for atomic physics*, Opt. Comm. **117**, 541 (1995).

[113] K. L. Corwin, Z.-T. Lu, C. F. Hand, R. J. Epstein, and C. E. Wieman, *Frequency-Stabilized Diode Laser with the Zeeman Shift in an Atomic Vapor*, Appl. Opt. **37**, 3295–3298 (1998).

[114] W. Demtröder, *Laserspektroskopie* (Springer Verlag, Berlin, 1993).

[115] D. A. Steck, *Rubidium 87 D Line Data*, Los Alamos National Laboratory, http://george.ph.utexas.edu/~dsteck/alkalidata/rubidium87numbers.pdf (2003).

[116] D. R. Lide, *Handbook of Chemistry and Physics* (CRC Press, 2001), 82nd edn.

[117] W. A. van Wijngaarden and J. Li, *Measurements of isotopic shifts and hyperfine splittings of ytterbium by means of acousto-optic modulation*, J. Opt. Soc. Am. B **11**, 2163 (1994).

[118] T. H. Loftus, *Laser Cooling and Trapping of Atomic Ytterbium*, Ph.D. thesis, University of Oregon (2001).

[119] T. Mayer-Kuckuk, *Atomphysik* (Teubner, Stuttgart, 1985), 3. edn.

[120] B. E. A. Saleh and M. C. Teich, *Fundamentals of Photonics* (John Wiley & Sons, 1991).

[121] W. Ketterle, D. Durfee, and D. Stamper-Kurn, *Making, probing and understanding Bose-Einstein condensates*, in *Proceedings of the International School of Physics - Enrico Fermi*, edited by M. Inguscio, S. Stringari, and C. Wieman, p. 67 (IOS Press, 1999).

[122] G. Modugno, M. Modugno, F. Riboli, G. Roati, and M. Inguscio, *Two Atomic Species Superfluid*, Phys. Rev. Lett. **89** (2002).

[123] Z. Hadzhibabic, C. A. Stan, K. Dieckmann, S. Gupta, M. Zwierlein, A. Görlitz, and W. Ketterle, *Two species mixture of quantum degenerate Bose and Fermi gases*, Phys. Rev. Lett. **88** (2002).

[124] M. Mudrich, S. Kraft, K. Singer, R. Grimm, A. Mosk, and M. Weidemüller, *Sympathetic Cooling with Two Atomic Species in an Optical Trap*, Phys. Rev. Lett. **88**, 253001 (2002).

[125] K. Pilch, A. D. Lange, A. Prantner, G. Kerner, F. Ferlaino, H.-C. Nägerl, and R. Grimm, *Observation of interspecies Feshbach resonances in an ultracold Rb-Cs mixture*, Phys. Rev. A **79**, 042718– (2009).

[126] R. Onofrio and C. Presilla, *Reaching Fermi degeneracy in two-species optical diople traps*, Phys. Rev. Lett. **89** (2002).

[127] T. Kuwamoto, K. Honda, Y. Takahashi, and T. Yabuzaki, *Magneto-optical trapping of Yb atoms using an intercombination transition*, Phys. Rev. A **60** (1999).

[128] R. Maruyama, R. H. Wynar, M. V. Romalis, A. Andalkar, M. D. Swallows, C. E. Pearson, and E. N. Fortson, *Investigation of sub-Doppler cooling in an ytterbium magneto-optical trap*, Phys. Rev. A **68**, 011403 (2003).

[129] H. M. J. M. Boesten, A. J. Moerdijk, and B. J. Verhaar, *Dipolar decay in two recent Bose-Einstein condensation experiments*, Physical Review A **54**, R29–R32 (1996).

[130] P. W. H. Pinkse, A. Mosk, M. Weidemüller, M. W. Reynolds, T. W. Hijmans, and J. T. M. Walraven, *Adiabatically Changing the Phase-Space Density of a Trapped Bose Gas*, Phys. Rev. Lett. **78**, 990 (1997).

[131] L. Zimmermann, *Charakterisierung eines ultrakalten Quantengases aus Rubidiumatomen*, Bachelor's Thesis, Universität Düsseldorf (2008).

[132] S. Friebel, C. D'Andrea, J. Walz, M. Weitz, and T. W. Hänsch, *CO2-laser optical lattice with cold rubidium atoms*, Phys. Rev. A **57**, R20– (1998).

[133] L. D. Landau and E. M. Lifschitz, *Mechanics (Course of theoretical physids; v.1)* (Pergamon Press, Oxford, 1960).

[134] R. Jáuregui, *Nonperturbative and perturbative treatments of parametric heating in atom traps*, Phys. Rev. A **64**, 053408– (2001).

[135] *NIST Atomic Spectra Database*, http://physics.nist.gov/PhysRefData/ASD/index.html.

[136] *NIST Engineering Metrology Toolbox*, http://emtoolbox.nist.gov/Main/Main.asp.

[137] G. Delannoy, S. G. Murdoch, V. Boyer, V. Josse, P. Bouyer, and A. Aspect, *Understanding the production of dual Bose-Einstein condensation with sympathetic cooling*, Phys. Rev. A **63**, 051602 (2001).

[138] A. Mosk, S. Kraft, M. Mudrich, K. Singer, W. Wohlleben, R. Grimm, and M. Weidemüller, *Mixture of ultracold lithium and cesium atoms in an optical dipole trap*, Appl. Phys. B **73**, 791 (2001).

[139] T. A. Savard, K. M. O'Hara, and J. E. Thomas, *Laser-noise-induced heating in far-off resonance optical traps*, Phys. Rev. A **56**, R1095 (1997).

[140] P. R. Bevington, *Data reduction and error analysis for the physical sciences* (McGraw-Hill, 1992), 2nd edn.

[141] K. Levenberg, *A method for the solution of certain problems in least squares*, Quart. Applied Math. **2**, 164–168 (1944).

[142] D. Marquardt, *An Algorithm for Least-Squares Estimation of Nonlinear Parameters*, SIAM Journal on Applied Mathematics **11**, 431–441 (1963).

[143] D. Blume and C. H. Greene, *Fermi pseudopotential approximation: Two particles under external confinement*, Phys. Rev. A **65**, 043613– (2002).

[144] T. D. Lee, K. Huang, and C. N. Yang, *Eigenvalues and Eigenfunctions of a Bose System of Hard Spheres and Its Low-Temperature Properties*, Phys. Rev. **106**, 1135– (1957).

[145] K. Xu, Y. Liu, D. E. Miller, J. K. Chin, W. Setiawan, and W. Ketterle, *Observation of Strong Quantum Depletion in a Gaseous Bose-Einstein Condensate*, Phys. Rev. Lett. **96**, 180405– (2006).

[146] A. Altmeyer, S. Riedl, C. Kohstall, M. J. Wright, R. Geursen, M. Bartenstein, C. Chin, J. H. Denschlag, and R. Grimm, *Precision Measurements of Collective Oscillations in the BEC-BCS Crossover*, Phys. Rev. Lett. **98**, 040401– (2007).

[147] T. T. Wu, *Ground State of a Bose System of Hard Spheres*, Phys. Rev. **115**, 1390– (1959).

[148] S. Giorgini, J. Boronat, and J. Casulleras, *Ground state of a homogeneous Bose gas: A diffusion Monte Carlo calculation*, Phys. Rev. A **60**, 5129– (1999).

[149] E. Braaten, H.-W. Hammer, and S. Hermans, *Nonuniversal effects in the homogeneous Bose gas*, Phys. Rev. A **63**, 063609– (2001).

[150] H. Fu, Y. Wang, and B. Gao, *Beyond the Fermi pseudopotential: A modified Gross-Pitaevskii equation*, Phys. Rev. A **67**, 053612– (2003).

[151] G. F. Gribakin and V. V. Flambaum, *Calculation of the scattering length in atomic collisions using the semiclassical approximation*, Phys. Rev. A **48**, 546– (1993).

[152] S. H. Autler and C. H. Townes, *Stark Effect in Rapidly Varying Fields*, Phys. Rev. **100**, 703– (1955).

[153] U. Schlöder, T. Deuschle, C. Silber, and C. Zimmermann, *Autler-Townes splitting in two-color photoassociation of 6Li*, Phys. Rev. A **68**, 051403– (2003).

[154] S. Giorgini, L. P. Pitaevskii, and S. Stringari, *Theory of ultracold atomic Fermi gases*, Rev. Mod. Phys. **80**, 1215– (2008).

Danksagung

Diese Arbeit ist erst durch die Hilfe und die Geduld Anderer möglich geworden. Neben meiner Familie und all meinen Freunden, die mich während meiner Promotion unterstützt haben, gilt mein Dank natürlich allen Mitarbeitern und Mitarbeiterinnen des Instituts für Experimentalphysik der HHU Düsseldorf.

- Als erster Stelle steht in diesem Zusammenhang Prof. Axel Görlitz, innerhalb dessen junger Arbeitsgruppe diese Promotion entstanden ist. Er hatte immer ein offenes Ohr, wenn es irgendwo "gehakt" hat. Durch seine begeisterte (und begeisternde) Mitarbeit im Labor hat er das Experiment immer wieder vorangetrieben. Zudem habe ich durch seine Erfahrung und sein intuitives Verständnis für Physik sehr viel gelernt. Schließlich bedanke ich mich für das sorgfältige Korrekturlesen dieser Arbeit vor der Abgabe und für die Übernahme des Hauptberichtes.
- Bei Prof. Georg Pretzler bedanke ich mich für die Übernahme des Mitberichtes, insbesondere für die zügige Fertigstellung des Gutachtens.
- Meinen "Vorgängern" Sven Tassy und Nils Nemitz möchte ich danken. Von ihnen habe ich zu Beginn meiner Promotion das "Handwerk" im experimentellen Umgang mit kalten Atomen gelernt. Zudem hat die gemeinsame Arbeit mit ihnen extrem viel Spaß gemacht.
- Gleiches gilt auch für Frank Münchow, meinen Mitstreiter, als es um die entscheidenden Experimente ging. Mit gutem Teamwork haben wir auch einige experimentelle Durststrecken überstanden. Nicht unerwähnt bleiben sollen natürlich auch seine Grill-Künste!
- Wichtigster Mann im Labor ist und bleibt Ralf Stefan, Meister der Elektronik und der innovativen Problemlösungen. Bei ihm möchte ich für den Aufbau zahlreicher Spezialkomponenten und die immer zu Verfügung stehende Soforthilfe bei technischen Problemen bedanken.
- Darüber hinaus danke ich allen weiteren Mitarbeitern unserer Arbeitsgruppe, die mir während meiner Promotion mit Rat und Tat zur Seite gestanden haben: Claudia Höhl, Christian Bruni, Charbel Abou Jaoudeh, Michael Köppinger und Simon Hübner.
- Außerhalb des Labors geht mein besonderer Dank an meine Eltern, die mich während der Zeit meines Studiums und meiner Doktorarbeit immer unterstützt haben.
- Meiner Frau Natascha kann ich nicht genug danken. Ohne ihre Geduld, ihren Rückhalt und ihre Unterstützung wäre diese Arbeit nicht möglich gewesen. Schließlich soll auch unsere Tochter Helene nicht unerwähnt bleiben, die in der Endphase dieser Arbeit auf die Welt gekommen ist und die uns sehr viel Freude bereitet.